Alma Mater Studiorum – Università di Bologna

DOTTORATO DI RICERCA IN

Ingegneria Civile, Chimica, Ambientale e dei Materiali

Ciclo XXX

Settore Concorsuale: 08/B2

Settore Scientifico Disciplinare: ICAR/08 Scienza delle costruzioni

BOND BEHAVIOR BETWEEN FIBER REINFORCED COMPOSITES AND QUASI-BRITTLE MATERIAL INTERFACES

Presentata da: Mattia Santandrea

Coordinatore Dottorato

Prof. Luca Vittuari

Supervisore

Prof. Christian Carloni

Esame finale anno 2018

Contents

List of Figures

List of Tables

Abstract

The present dissertation presents an investigation of the bond behavior of newly developed fiber reinforced composite systems applied to quasi-brittle material interfaces. Direct shear tests were performed on steel reinforced polymer (SRP) and steel reinforced grout (SRG) composite strips applied to both concrete and masonry substrates. Different types of cementitious matrices and different densities of steel fiber sheets were employed. Tests were performed investigating several parameters, i.e. bonded width, bonded length, loading rate, and face to which the composite strip was applied. Failure modes and load responses were presented and discussed. It was observed that the fracture energy G_F of SRP-concrete joints is independent of the composite density but varies as the composite is bonded to different faces of the concrete prism. The width effect was considered in the evaluation of the load-carrying capacity of SRP-concrete joints, while the loading rate influenced the peak load of both SRP and SRG specimens. The behavior of SRP-concrete joints was also investigated through a numerical analysis, using lattice discrete particle model (LDPM), obtaining an excellent match with the experimental results. Some concrete prisms were reinforced and tested using a geopolymer matrix that showed interesting results. Some masonry specimens were subjected to artificially weathering cycles to investigate the durability performances of SRG strips with respect to salt attack. Furthermore, monotonic compressive tests were performed on concrete columns confined with both SRP and SRG composites. Several parameters were investigated, i.e. the density of steel fiber sheets, the concrete corner condition, the overlapping length, the number of confinement layers, the scale effect, and the shape effect. Failure modes and load responses were presented and discussed. Finally, several applications of basalt-fiber reinforced cementitious matrix (B-FRCM) composites bonded to masonry substrates were showed, including full scale tests on existing masonry arches.

1. Introduction

This chapter deals with an introduction on composite materials with an accurate description of the constituents. The main applications of both fiber reinforced polymer (FRP) and fiber reinforced cementitious matrix (FRCM) composites are then presented. Eventually, the aim and objectives together with the disposition of the thesis are presented and new and original contributions are pointed out.

1.1. Composite materials

Composite materials can be defined as a system consisting of two or more elements, whose properties and performances are designed to be superior to those of the constituent materials that act independently. Given the large range of materials that can be considered as composites and the wide range of uses for which composites materials can be designed, it is not easy to agree upon a single definition. However, it is possible to restrict the field of composite materials considering those materials that contain a continuous matrix constituent that binds together and provide form to an array of a stronger and stiffer reinforcement constituent [1]. Composites are engineered materials that have been designed to provide significantly higher specific stiffness and specific strength relative to previously available structural materials. The main property that each individual component must possess in order to constitute a composite material is to maintain the original identity, without mixing or dissolving in another component. A composite can be then considered as a heterogeneous material characterized by distinct phases that can always be separated from each other. In general, a composite consists of a discontinuous phase (reinforcement) dispersed within a continuous phase (matrix). The fiber or particle phase is usually stiffer and stronger than the continuous matrix phase. In the case of structural high-performance composites, the reinforcement is usually made of fibers and it forms the skeleton of the material. The matrix provides protection, support for the fibers and entails the transfer of local stress from one fiber to another and to the substrate to which the composite is applied. The reinforcement is thus able to express its physical and mechanical properties. In general, three phases characterized a composite material (Figure 1):

- *Matrix*: the continuous constituent which, by embedding the reinforcement, guarantees the transfer of external loads and protects the reinforcement from environmental factors, wear and mechanical cutting actions.
- *Reinforcement*: the stiffer and stronger phase, usually in the form of long fibers, short fibers or particles.
- *Interface*: the contact area between the reinforcing material and the matrix.

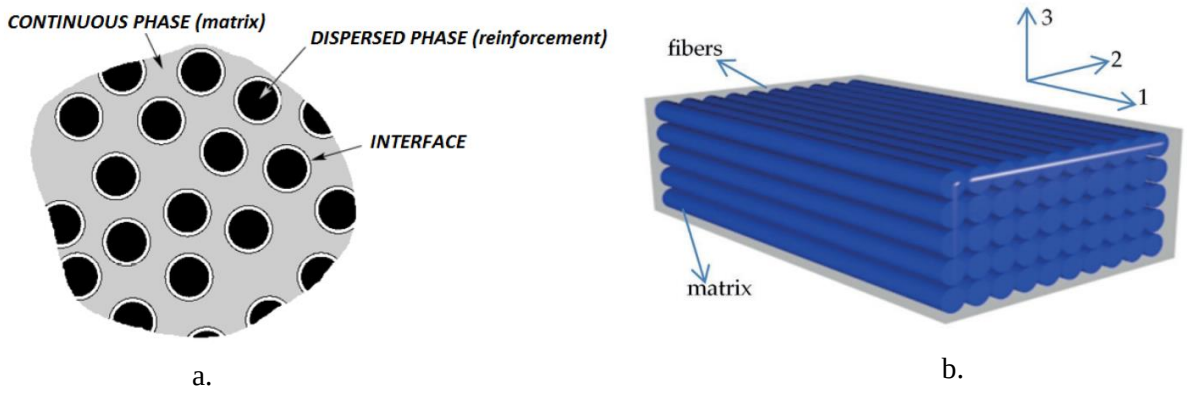

a. b.

Figure 1. Schematic representation of the constituent phases of a composite material (a, b) [2] [3].

The low cost of the raw material, the ease of installation together with the optimization of the manufacturing processes entailed the success of composite materials that has been also successfully employed in the field of construction industry in the last thirty years.

1.2. Fibers

Various fibers are commercially available, with a wide range of material properties. The suitability of the fibers mainly depends on the composite properties which are needed. Fibers are usually characterized by small diameters, relatively high stiffness and strength, and a brittle behavior. Any elongated material that has a ratio between the minimum length and the maximum transverse dimension equal to 10 and a maximum transverse dimension less than one millimeter can be defined as filament. A fiber consists in one or more filaments held together using different configurations. The most common fiber configurations are:

- *Monofilament*: basic filament with a diameter equal to 10 μm.
- *Tow*: untwisted bundle of continuous filaments.
- *Yarn*: Assemblage of twisted filaments and fibers formed into a continuous length that is suitable for use in weaving textile materials.
- *Roving*: a number of yarns or tows collected into parallel bundle with little or no twist.

The different fiber configurations are reported in Figure 2. A part for the configuration filament arrangement, fibers can be classified based on the material. Several types of fibers are currently used in composite materials, i.e. carbon fibers, glass fibers, aramid fibers, basalt fibers, and steel fibers.

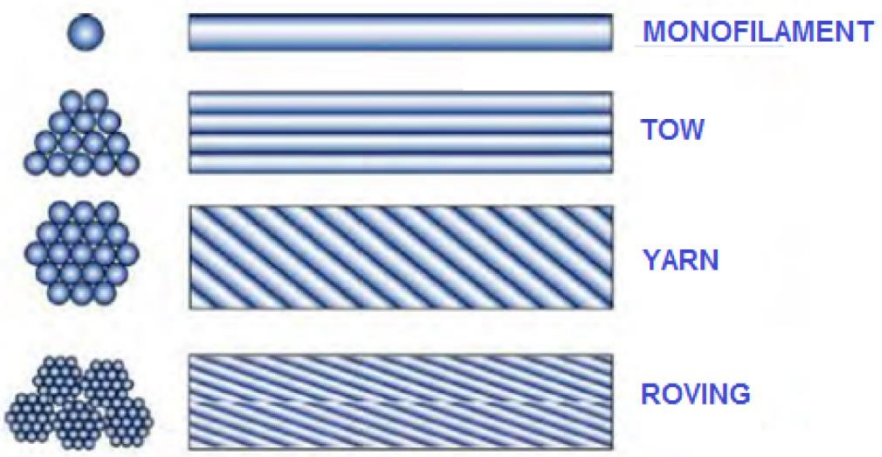

Figure 2. Different fiber configurations [4].

1.2.1. Carbon fibers

Carbon and graphite fibers are produced from polyacrylnitrile (PAN), pitch or rayon. Isotropic pitch and rayon are used to produce low modulus carbon fibers (elastic modulus of about 50 GPa). High elastic modulus (between GPa and 850 GPa) and high strength (between 1900 MPa and 3200 MPa) carbon and graphite fibers are made from PAN or liquid crystalline pitch. PAN fibers are obtained by separating a chain of carbon atoms from polyacrylnitrile through heating and oxidation. Pitch fibers are fabricated by using refined petroleum or coal pitch that is passed through a thin nozzle and stabilized by heating. The molecular structure consists of graphene (hexagonal) layer networks ordered in two or three dimensions. The former is defined as carbon, the latter as graphite. Typically, graphite has a higher tensile modulus than carbon. Although this difference, the term carbon fibre is often used irrespective of the graphitization. Carbon fibers are very resistant against creep and fatigue ad have a very good chemical, UV light and moisture resistance. Hence, carbon fibers are very durable and have excellent mechanical properties. As the fibers are electrically conducting, they can give galvanic corrosion in contact with metals. The wetting of the fibers by resins is not easy, so that surface treatments are normally needed. Thus, carbon fibers are often provided with an epoxy size treatment which protects the fibers against abrasion (improved handling) and offers an epoxy matrix compatible interface. Compared to glass fibers, carbon fibers are much more expensive (approximatively 10 times more expansive).

1.2.2. Glass fibers

Glass fibers are made of silicon oxide with the addition of small amounts of other oxides and are formed by extruding molten glass and fiber stretching. As glass fibers are very surface active and hydrophilic, individual fibers are generally coated by a sizing agent immediately after fiber forming. The sizing also

acts to minimize abrasion damage and to aid coupling with polymer matrices. Depending on their chemical composition, glass fibers can be divided into groups. Most general-purpose and widely used are E-glass fibers, which are based on calcium-aluminoborosilicate glass. These low-cost fibers have a good electrical resistance and strength. S-glass is a magnesium-aluminosilicate formulation which has higher strength, stiffness, and thermal stability. C-glass has a soda-lime-borosilicate composition that is used for its higher chemical stability against acids. Alkali-resistant (AR) glass fibers contain a considerable amount of zirconium oxide to increase resistance against alkalis from cement matrices.

Glass fibers are characterized by high tensile strength (between 2400 and 3500 MPa), good electrical resistivity, good thermal resistance and low price (especially E-glass fibers). Glass fibers have an elastic modulus that ranges from 50 GPa to 85 GPa, and are known to degrade in the presence of water, acid and alkaline solutions. They also exhibit a considerable creep or stress rupture behavior, meaning that the tensile strength gradually decreases under constant stress. Given the low durability of glass fibers, it is important to select a suitable and protective matrix.

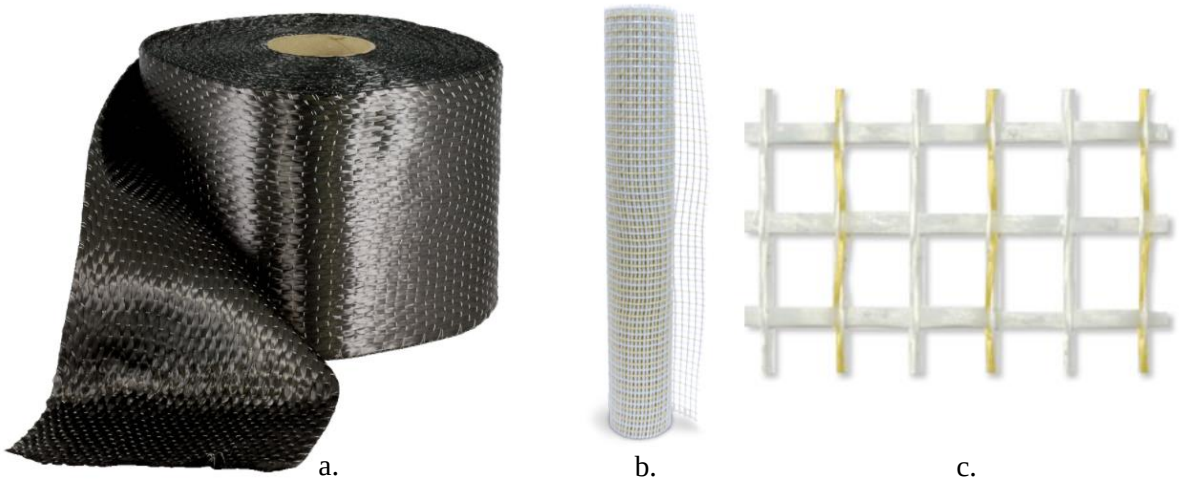

a. b. c.

Figure 3. a) Carbon-fiber roll [5]; b) Glass-fiber roll [6]; c) Detail of a glass-fiber net [6].

1.2.3. Aramid fibers

Aromatic polyamide or aramid fibers are producted from para-phenylene-terephthalamid by extrusion as a liquid crystal polymer and by fibre stretching. These organic fibers have an anisotropic fibrillar structure. In the fiber axis direction they consist of aligned molecular chains with strong covalent bond. In transverse direction these chains are cross-linked by weaker hydrogen bridges, so that higher tensile strength and stiffness are obtained in the longitudinal direction. Besides the high tensile strength, aramid fibers show high energy absorption and toughness, good vibration damping and fatigue resistance, low thermal conductivity, good thermal stability, moderate to fairly good chemical resistance, low

compressive strength and moderate adhesive properties. The aramid fibers respond elastically in tension but exhibit non-linear and ductile behavior under compression.

With respect to durability, aramid fibers generally exhibit a low or moderate resistance against acids, a moderate resistance against alkalis and a poor resistance against ultraviolet radiation. Due to the interaction of water with the polymer structure, they are sensitive to moisture as well. Because of these aspects, the fibers should be embedded in a matrix which is carefully chosen to provide additional protection. To improve the bond between fibers and matrix, surface treatments may be used. The cost prize of aramid fibers is similar to that of carbon fibers.

1.2.4. Basalt fibers

Basalt is a volcanic rock, from which fibers can be drawn by melting (melting point above 1400 °C) crushed basalt stone, giving a single ingredient rock melt, and fiber winding. It is composed of the minerals plagioclase, pyroxene, and olivine. The fibers are very thin filaments of basalt that belong to the category of the mineral fibers together with the carbon fibers and glass fibers but, compared with these fibers, have better mechanical and physical properties. Basalt fibers are a valid alternative to glass fibers, since they possess mechanical characteristics that are comparable in terms of mechanical strength and modulus of elasticity, but with advantageous properties such as the absence of toxic reactions with air or water, incombustibility, a high degree of thermal insulation, and do not produce chemical reactions in contact with other chemical products.

1.2.5. Steel fibers

Steel fibers consisted in high-strength steel wires twisted together in order to form strands. The steel used is derived from the evolution of a pearlitic or hypereutectoid steel (with a carbon content between 0.80% and 0.96%) subjected to a process which can be summarized in a first wire drawing, followed by tempering, plating brass or zinc, thin wire drawing and cutting. Steel fibers reached high tensile strengths (between 2400 MPa and 4000 MPa). The individual wires are produced in diameters of the order of 0.2-0.50 mm. The reduced size of the steel wires allows for obtaining limited thickness of the fiber sheet. Further details about the steel fibers employed in this dissertation are provided in section 3.3.1.

1.3. Matrix

The matrix phase is fundamental in order to define the geometry of a composite material, to incorporate the fibers, to hold the fibers in the desired position and protect them from corrosion or formation of surface defects. The matrix has to distribute, as uniformly as possible, the stresses between the fibers of the

composite material. It also must ensure sufficient adhesion between the composite material and the substrate. Two types of matrix are generally used in the construction field:

- *Organic matrices*: they can be either based on thermosetting or thermoplastic polymers. Thermosetting resins, when cured, are characterized by a high degree of cross-linking of molecules (polymerization) so that it solidifies irreversibly. Upon heating, these cured resins show no melting (at high temperature decomposition occurs). On the other hand, thermoplastic polymers are characterized by more linear macromolecules and can be repeatedly softened when heated and hardened when cooled. Thermosetting polymer matrices allow for good fiber wet-out without applying high pressure or temperature, which makes them very attractive with respect to processability. Compared thermoplastics, thermosets also offer better thermal stability and chemical resistance, as well as reduced creep and stress relaxation. Disadvantages are their limited storage life and failure strain.
- *Inorganic matrices*: they are newly developed matrices that consisted in a lime based or cementitious mortar with the addition of specific additives in order to improve the mechanical and bond performances.

A comparison between the main features of both organic and inorganic matrices is provided in Table 1.

Table 1. Comparison between organic and inorganic matrices [4].

Feature	Organic matrix	High Density
High temperature resistance	Loss of mechanical properties between 60°C and 80 °C	Comparable with the resistance of the support (masonry or concrete).
Workability	Limited to a short-time interval (between 30 and 60 minutes) that depend on the temperature	Extended to a long-time interval (several hours)
Vapor permeability	None	Comparable with that of the support
Viscosity	Low viscosity in the liquid state with consequent ease of impregnation of the fibers	High viscosity in the fluid state with consequent difficulty of impregnation of the fibers
Toxicity	Dangerous both by contact and by inhalation	None

1.4. Fiber reinforced polymer (FRP) composites

Fiber reinforced polymer (FRP) composite materials consist in high strength fibers embedded in an organic matrix (usually a thermosetting epoxy resin). FRP materials have been successfully employed to strengthen existing concrete or masonry buildings over the last thirty years. FRPs are used in the construction field with different types of fabric:

- *Uniaxial*: where fibers are oriented in one main direction;
- *Biaxial*: characterized by an orthogonal fiber texture (with a defined percentage of fibers in each direction);
- *Multiaxial*: where fibers are oriented following several directions.

The fabrics are distributed using rolls in a dry state and are usually applied to a substrate using a "wet" procedure. Composite material can be also available in the form of sheets or bars, obtained by an industrial extrusion process (pultrusion). The main advantages provided by FRP composites are the easy of installation, the height strength-to-weight ratio, and the durability in aggressive environments. On the other hand, the low vapor permeability, the poor behavior at elevated temperatures, and the lack of reversibility of the installation are some disadvantages of FRP materials.
The main applications of FRP systems for restoration purposes include:

- Reinforcements aimed to improve the flexural capacity of concrete slabs or beams (Figure 4a);
- Shear reinforcements of concrete beams (Figure 4a);
- Confinement of concrete or masonry columns and pillars (Figure 4c);

FRP composites are an appealing technique if compared with traditional strengthening systems, since the element to which the composite is applied does not modify significantly its shape and its weight, determining important benefits for interventions in seismic areas. FRP systems can be applied also to prevent local mechanisms of a structure (Figure 4b), such as overturning of the walls.
This dissertation will be mainly focused on the analysis of steel reinforced polymer (SRP) composites that employ high strength steel fibers embedded in a thermosetting epoxy matrix.

Figure 4. Application of FRP composites: a) Flexural and shear strengthening of a concrete beam; b) Strengthening of a masonry wall to prevent local mechanisms; c) Confinement of a column [3].

1.5. Fiber reinforced cementitious matrix (FRCM) composites

Fiber reinforced cementitious matrix (FRCM) composites consist in high strength fibers embedded in a inorganic matrix (usually a cement based or a lime based mortar). FRCM composites are a newly developed material and have gained a tremendous success in several applications that aim to increase the original service life of existing constructions, as an alternative to traditional FRPs. FRCM composites employ an inorganic matrix, instead of epoxy, that is responsible for the stress-transfer mechanism between the composite and the fibers and among the fibers. FRCM composites overcome several drawbacks related to FRPs and appear to be a promising alternative since they offer:

- High resistance to fire and high temperatures;
- Resistance to UV radiation;
- Ease of handling during the application because the inorganic binder is water-based;
- Permeability compatibility with concrete and masonry substrates;
- Unvarying working time (between 4°C and 40°C).

FRCM systems are used as an alternative to FRP composite materials and therefore they can be used to improve the flexural strengthening of concrete members or to confine masonry and concrete structures. In particular, they are used for the rehabilitation of existing masonry structure in order to eliminate local failure mechanism. Figure 5, Figure 6, Figure 7, and Figure 8 show the most common failure mechanisms in historic masonry buildings and the available strengthening solutions using FRCM systems.

The present dissertation will be focused on the investigation of steel reinforced grout (SRG) composites (Figure 9) that employ high strength steel fibers embedded in a cement-based or lime based grout and basalt-FRCM composites that employ basalt fibers embedded in a lime based grout.

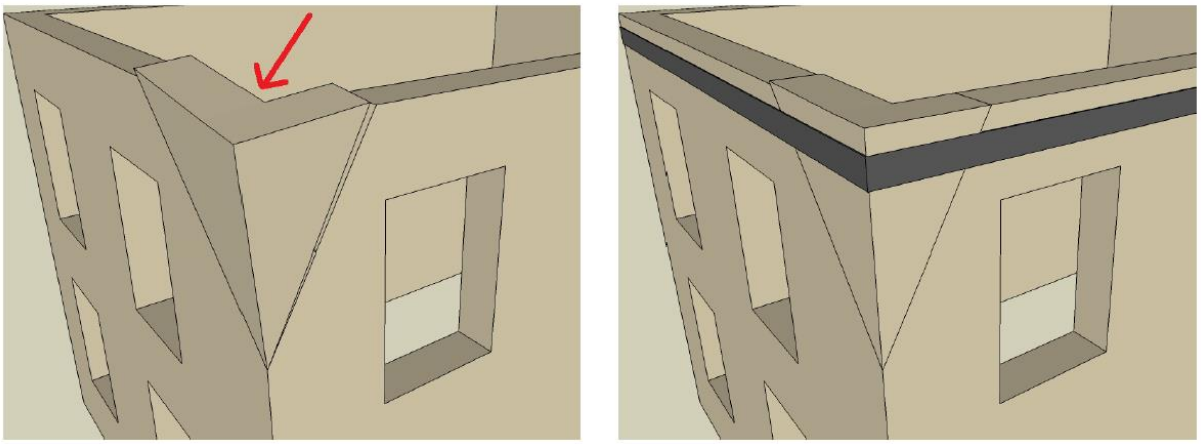

Figure 5. Diagonal cracks close to the corners [4].

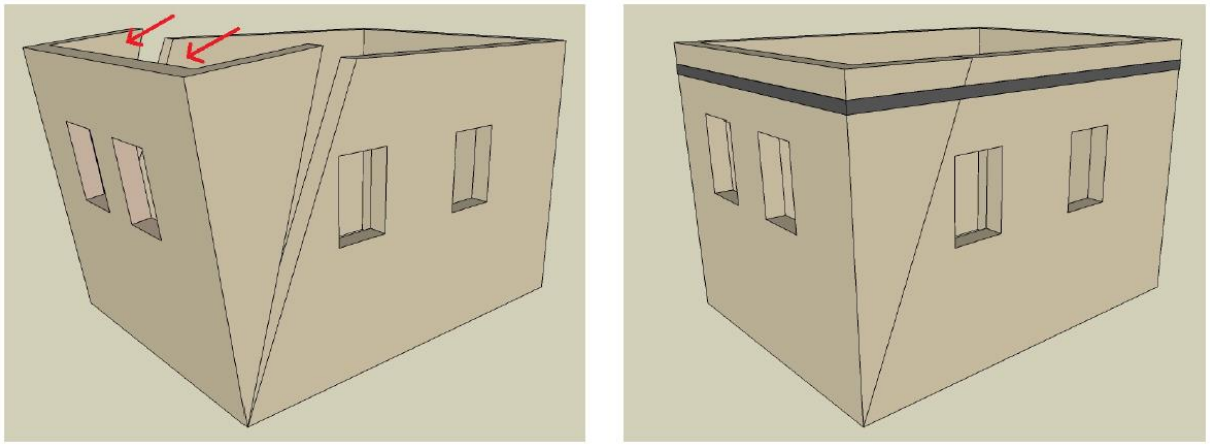

Figure 6. Overturning of masonry walls [4].

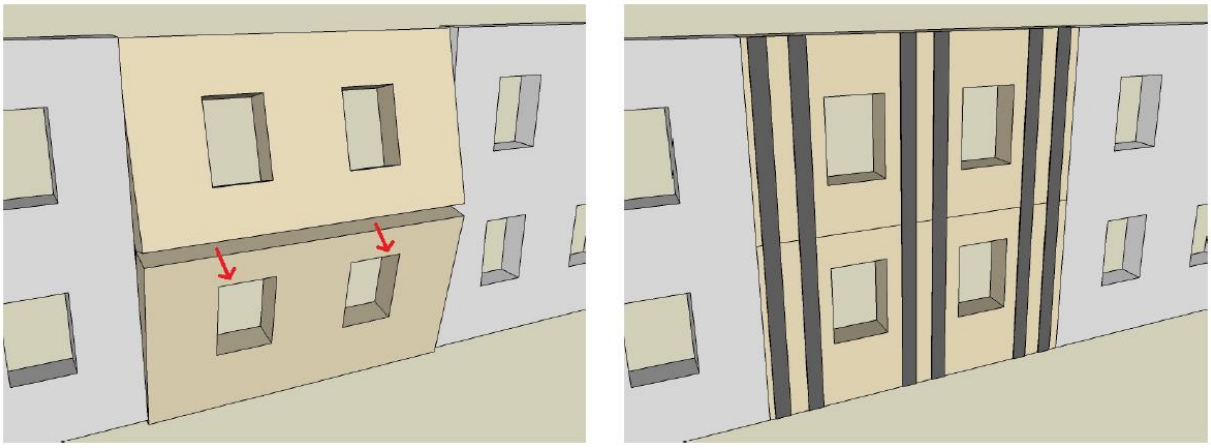

Figure 7. Out-of-plane mechanism [4].

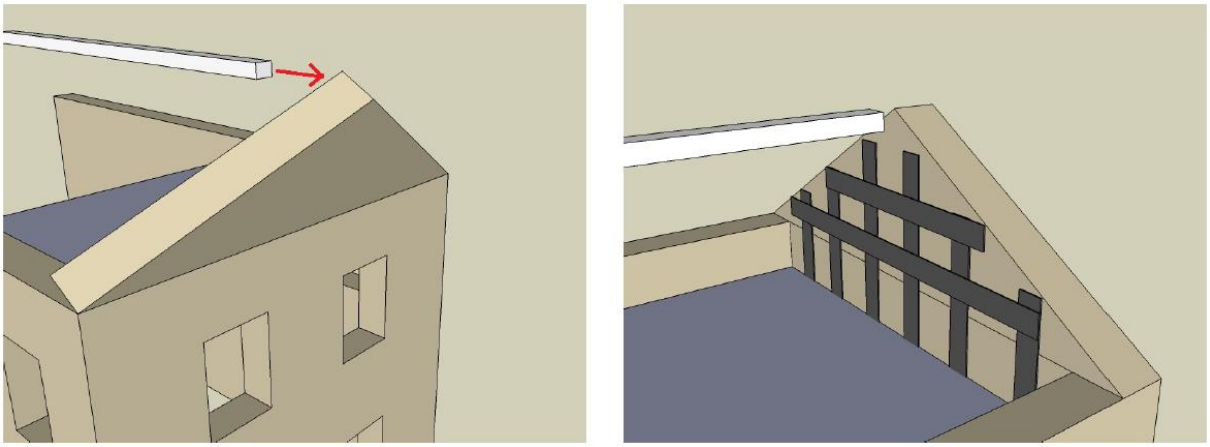

Figure 8. Overturning of the gable [4].

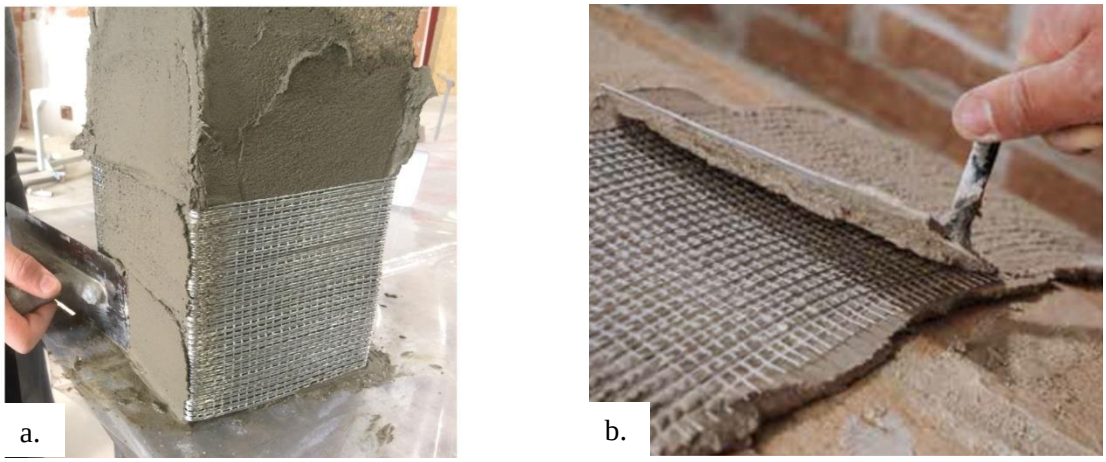

Figure 9. SRG application to a concrete member (a) and to a masonry arch (b) [4].

1.6. Aim and objectives

The aim of this work is to investigate the behavior of newly developed composite materials bonded to concrete or masonry substrates for strengthening applications. A large portion of this dissertation is focused on the study of composite systems that employed steel fibers embedded in an epoxy matrix or a cementitious matrix and known respectively as steel reinforced polymer (SRP) and steel reinforced grout (SRG) composites. The low cost of the steel fibers compared to carbon or aramid fibers makes SRPs and SRGs competitive composite materials with respect to traditional composite systems. The bond between FRP composites and quasi-brittle substrates has been largely investigated in the last decades by the scientific community but few work has been performed on SRP and SRG systems. Therefore, the present study tries to deeply investigate several aspects related to the bond between SRP and SRG composites and concrete or masonry substrate in order to define the cohesive laws that governed the bond behavior and other important features related to composite materials, such as the correct evaluation of the fractur energy, the influence of the width of the composite strip on the load response and the effect of the test rate on the peak load. In addition, the objective of this work is also to take advantage of the experimental results and numerical simulations to suggest some design aspects for these new types of composites. Eventually, this work tries also to find out the main bond properties of Basalt-fiber reinforced cementitious matrix (B-FRCM) composites through a preliminary experimental campaign.

1.7. Organization of the thesis

In Chapter 2 a literature review is presented, showing the main results obtained in the study of the bond behavior between fiber reinforced polymer (FRP) composites and concrete. A description of the bond test set-ups employed in the past, together with the strategies proposed to determine the load carrying capacity and the cohesive material law are showed.

Chapter 3 presents the properties of the materials employed in the experimental work.

In Chapter 4 an investigation of the bond between composite materials and quasi-brittle substrate is presented. The first section is focused on the study of the debonding phenomenon of steel reinforced polymer (SRP), steel reinforced grout (SRG), and fiber reinforced geopolymer matrix (FRGM) composites bonded to a concrete surface and tested using a single-lap shear test set-up. A numerical analysis of SRP-concrete joints is also proposed, modelling the concrete substrate through lattice discrete particle model (LDPM). The second section is focused on the study of the debonding mechanism in SRG-masonry joints. Durability of SRG composites is also investigated.

Chapter 5 presents the results of an experimental study on concrete columns wrapped with SRP or SRG composites, investigating several parameters, i.e. the shape of the cross-section, the size of the specimen,

the density of steel fibers, the number of confinement layers, the corner condition, the number of overlapping faces, and the length of the reinforcement. Digital image correlation (DIC) was also employed to analyze the strains on the composite surface.

Chapter 6 provides a preliminary investigation of the bond between Basalt-fiber cementitious matrix (B-FRCM) composites and a masonry substrate, through bond and confinement tests. Full scale tests on strengthened masonry arches are also presented.

Eventually, Chapter 7 are the concluding remarks and discussions together with proposal to continued research in the topic of bond between new composite materials and quasi-brittle substrates.

1.8. Advancement of the knowledge and original features

In this thesis several new and original features are introduced.

In the study of the bond between SRP and concrete substrates, two new fitting functions are proposed and used to fit the experimental strain profile along the SRP strip. These new fitting functions provide a finite value of the effective bond length, i.e. the length over which the shear stresses are transferred when the load sharing is fully established. This is an important aspect, as most of the cohesive material laws and strain functions are not associated with a finite effective bond length.

The Mode-I fracture energy of concrete, obtained from fracture mechanics tests, is compared with the interfacial fracture energy obtained from bond tests. Most, if not all, of the published work has never tried to compare these two quantities based on experimental data.

A new global approach is proposed to obtain the interfacial fracture energy. This approach could be used without the need of fitting the strain or displacement profiles obtained experimentally.

A new width effect formula, that take into account the face of application of the composite strip, is proposed on the basis of the most recent articles on this subject.

Numerical analysis of the bond between SRP composites and concrete were performed using a meso-scale model that simulates the failure behavior of concrete by modelling the coarse aggregates and the cementitious paste. For the first time, the SRP-concrete joint was modelled without using any interface, since the fracture process developed on the concrete substrate.

The study of the bond between SRG composites and quasi-brittle substrates (both concrete and masonry) is investigated analyzing several parameters and determining some fundamental aspects such as the effective bond length and the cohesive material law that govern the debonding phenomenon. A new accelerated weathering protocol was adopted in this study and used to investigate the durability of SRG systems applied to masonry substrates.

For the first time SRG jackets were applied for the confinement of the concrete columns without any treatment of the corner condition (sharp corner) and a comparison between results obtained with sharp and rounded corners is provided.

Full scale tests on strengthened masonry arches are also presented. These tests show possible practical applications of the Basalt-fiber reinforced cementitious matrix (B-FRCM) strengthening method.

2. Bond behavior between fiber reinforced polymer (FRP) composites and concrete: a state-of-the-art review

Fiber reinforced polymer (FRP) composites have been successfully employed to strengthen, restore, and repair concrete buildings since the 1990s. FRPs were used in several applications, i.e. or for confining of concrete members or for flexural and shear strengthening of existing concrete beams. In particular, when a FRP composite laminate/sheet is applied to the tension side of a beam, the inertial moment capacity of the strengthened section increases. Similarly, when attached to the web of a beam in the high-shear region, the composite improves the nominal shear capacity of the section. Particular attention was paid in the study of the failure modes of beams strengthened with FRP laminates/sheets [7], [8]. Based on existing studies, Teng et al. [8] showed that seven typical failure modes were observed in experimental tests on beams strengthened with FRP composites (Figure 10): (1) flexural failure by FRP rupture; (2) flexural failure by crushing of compressive concrete; (3) shear failure; (4) concrete cover separation; (5) plate end interfacial debonding; (6) intermediate flexural crack induced interfacial debonding; and (7) intermediate flexural-shear crack induced interfacial debonding. Among the different failure modes, particular attention was paid to the debonding phenomenon, that is one of the most dangerous types of failure since it is a brittle phenomenon [9]. In addition, debonding usually occurs with no visible warning at a load level significantly lower than the flexural or shear capacity of the strengthened member corresponding to the rupture of the FRP reinforcement [10]. The available tests from literature showed that the load-carrying capacity of RC beams flexurally-strengthened with an FRP composite bonded to the tension face is often limited by one of the debonding failure modes.

The observed modes of debonding in beams strengthened with FRP composites can be broadly classified into two types: (*i*) those associated with high interfacial stresses near the ends of the bonded plate (failure modes (4) and (5)) which are collectively referred to as end plate debonding (EPD); and (*ii*) those induced by a flexural or flexural-shear crack away from the plate ends (failure modes (6) and (7)) which are collectively referred to as intermediate crack debonding (ICD). The interest of researchers was therefore focused to investigate the intermediate crack debonding (ICD) through simple experimental tests able to reproduce a pure Mode-II debonding process. Based both on the results of experimental tests and on analytical approaches, the scientific community tried to develop several models able to describe the relation between shear stresses (τ) and slips (s) during the debonding process of a FRP strip bonded to a concrete substrate, i.e the cohesive material law $\tau(s)$. In next sections, the most relevant results obtained

from literature and referred to the bond between composite materials and concrete substrates are presented.

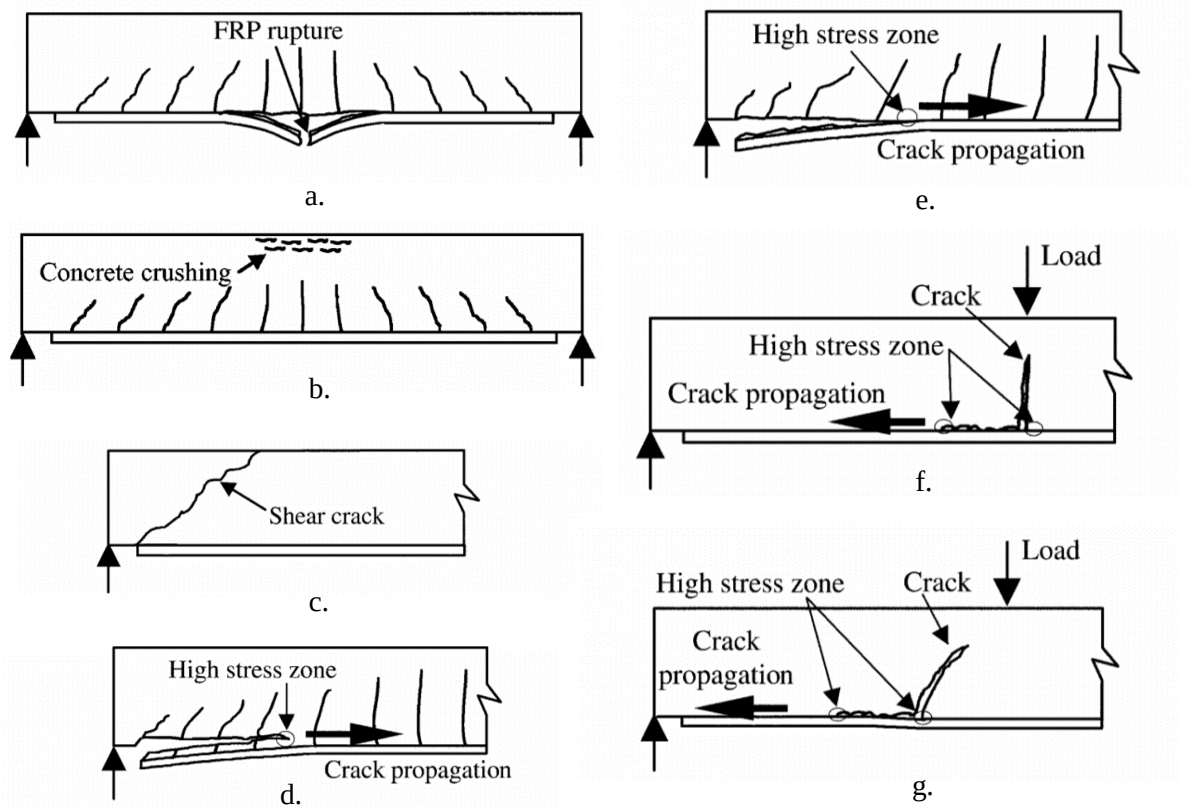

Figure 10. Failure modes of beams strengthened with FRP composites: a) flexural failure by FRP rupture, b) flexural failure by crushing of compressive concrete; c) shear failure; d) concrete cover separation; e) plate end interfacial debonding; f) intermediate flexural crack induced interfacial debonding; g) intermediate flexural-shear crack induced interfacial debonding [8].

2.1. Bond test set-up

The optimal tests to investigate the bond behavior of composite materials bonded to a concrete substrate were, and still are, full-scale beam tests [11] [12]. However, the high cost of the set-up and the complexity of the flexural behavior of a RC strengthened beam, which includes load sharing between internal steel reinforcement and external FRP laminates/sheets, in addition to the quasi-brittle behavior of concrete, and the subsequent formation of a not easily predicted crack pattern, have induced several research groups to develop *ad-hoc* set-up to investigate the FRP-concrete debonding [10]. The first experiments have been carried out using several set-ups, including single lap shear tests [13] [14] [15], double shear tests [16] [17] [18] [19] [20], and modified beam tests [16] [21]. Some of those test set-ups have gained more popularity than others in the last decade, and some others have been proposed or adjusted from the original

ones [22] [23]. Researchers are still debeating the differences among the set-ups in order to identify which one(s) are capable of capturing the debonding phenomenon in beams. It is recognized that among the different set-ups, the single-lap and the double-lap shear test set-ups capture the debonding phenomenon better [10].

2.1.1. Single lap shear test set-up

Chajes et al. [13] in 1996 were among the first researchers to investigate the behavior of composite material plates externally bonded to a concrete substrate through a single lap shear test set-up. The research was aimed to investigate several parameters that affected the bond behavior, i.e the concrete surface preparation prior to bonding, the type of adhesive used, and the concrete strength. The test specime consisted of a 25 mm-wide composite plate bonded to a concrete block (150 mm-wide × 150 mm-high × 225 mm-long) with a 75 mm bond length. In the test set-up, the concrete block was mounted to the bottom crosshead of a 130 kN capacity testing machine with 9.5 mm-thick steel plates and four 12 mm-diameter steel all-thread at the corners of the plate. The top of the composite plate was clamped in a serrated grip that was free to rotate in all directions Figure 11a.

Täljsten in 1997 [15] performed single lap shear tests to investigate the anchor lenghts of steel and carbon fiber reinforced polymer (CFRP) composites bonded to a concrete substrate and to define the critical strain level in the concrete at failure. The test equipment consisted in a strenghtened concrete prism on two supports in place on a steel beam. The tensile force was applied by an hydraulic jack and transferred to the steel plate through a moment-free link. The hydraulick jack can also be moved in the vertical direction to minimize the negative effect of any moment introduced by the angle between the steel plate and the load level arm. All tests were position-controlled by a linear variable differential transformer (LVDT) that was also used to measure the slip Figure 11b.

Bizindavyi and Neale [14] investigated the shear conditions of both glass fiber reinforced polymer (GFRP) composites and carbon fiber reinforced polymer (CFRP) composites bonded to concrete substrate in order to determine the stress and strain distribution profiles in the composite laminates and the bond strengths. The composite material was applied on a 150 mm × 150 mm × 400 mm concrete prism. The test specimen was inserted into a conventional tensile loading frame. The assembly was supported in such a way that there was direct shear at the composite-to-concrete interface. By pulling on the FRP laminate, the face of the upper concrete section came into contact with a bearing plate. The resulting bearing pressure was transmitted to two U-shape steel supports via a upper shear connector plate. Longitudinal steel supports transmitted the applied load to the lower part of the frame via a threaded steel rod and a lower shear connector plate Figure 12.

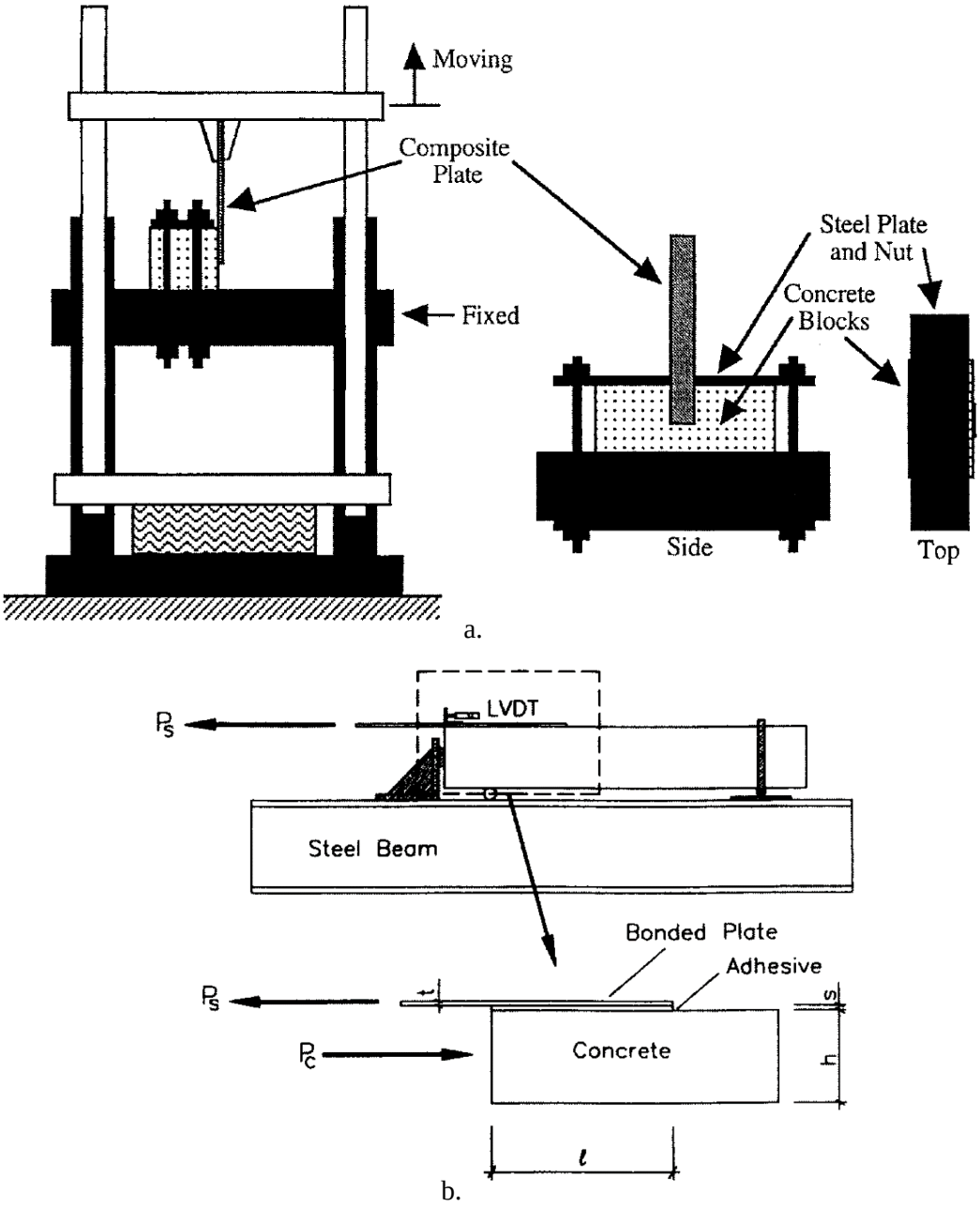

Figure 11. a) Single-lap shear bond test set-up used by Chajes et al. [13]; b) Sketch of the bond set-up used by Täljsten [15].

2.1.2.Double lap shear test set-up

The double shear test was introduced for the first time by Van Gemert in 1980 [16]. Van Gemert investigated the behavior of steel plates bonded to a concrete surface, using 150 mm × 150 mm × 300 mm concrete blocks. Two pairs of steel plates were glued on the opposide sides of each prism. One pair had a width of 100 mm and was used to investigate the debonding phenomenon. The two other plates

were 150 mm width, and served as fixing elements. All the plates were 5 mm thick. To avoid unysimmetrical loading of the plates, the loads were introduced thorugh a universal joint on the upper and lower side of the test piece. A representation of the test set-up is showed in Figure 13a-b.

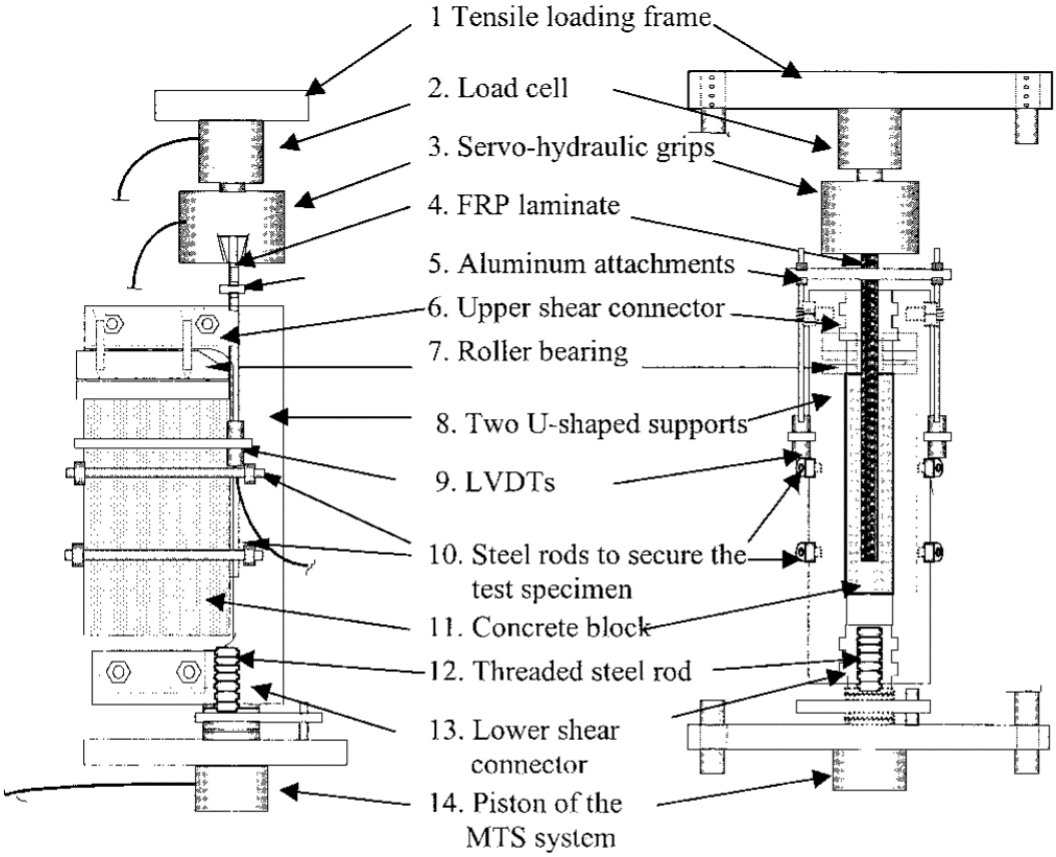

Figure 12. Single-lap shear test set-up used by Bizindavyi and Neale [14].

A similar set-up was adopted by Swamy et al. [17] that bonded 3 mm-thick steel plates on both faces of 60 mm × 60 mm × 150 mm concrete specimens. In this case, one of the two square faces of the concrete prism was restrained by a steel set-up as shown by the scketch of Figure 13c.

Brosens and Van Gemert [18] studied the shear stress distribution and the fracture behavior of carbon reinforced laminates bonded to a concrete surface using a double shear test set-up. Each specimen consisted of two concrete prisms (150 mm × 150 mm × 300 mm) connected by gluing three layers of carbon fiber reinforced polymer (CFRP) laminates at two opposite sides Figure 14a. Each specimen was loaded in a displacement controlled tension machine. Two cardan transmissions assured that the tensile forces acted centrically.

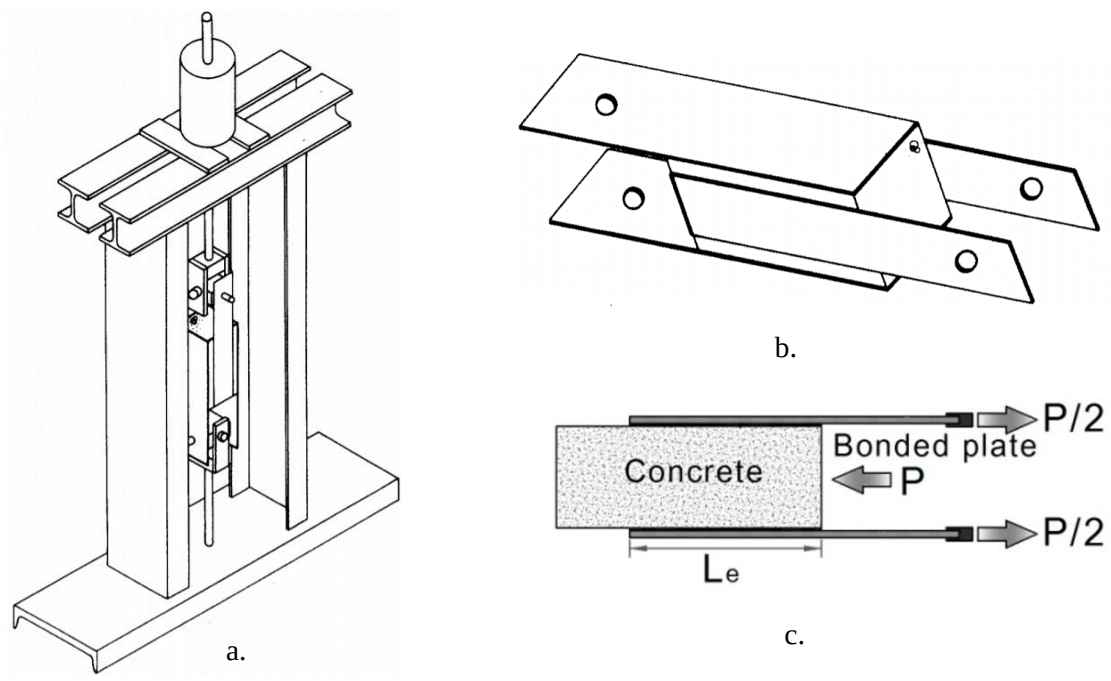

Figure 13. Double-lap shear test set-up employed by Van Gemert [16](a,b). Sketch of the double-lap shear test set used by Swamy et al. [17] (c).

A similar procedure was adopted by Maeda et al. [19], that investigated the bond strength of carbon fiber sheet bonded to a concrete substrate. Each specimen consisted of two concrete prisms with a cross section equal to 100 mm × 100 mm connected by a 50 mm-wide carbon fiber sheet. The specimen was loaded by pulling re-bars which were placed at the center of each concrete prism. In one side of the specimen the carbon fiber sheet was wrapped in order to avoid the bond failure Figure 14b.

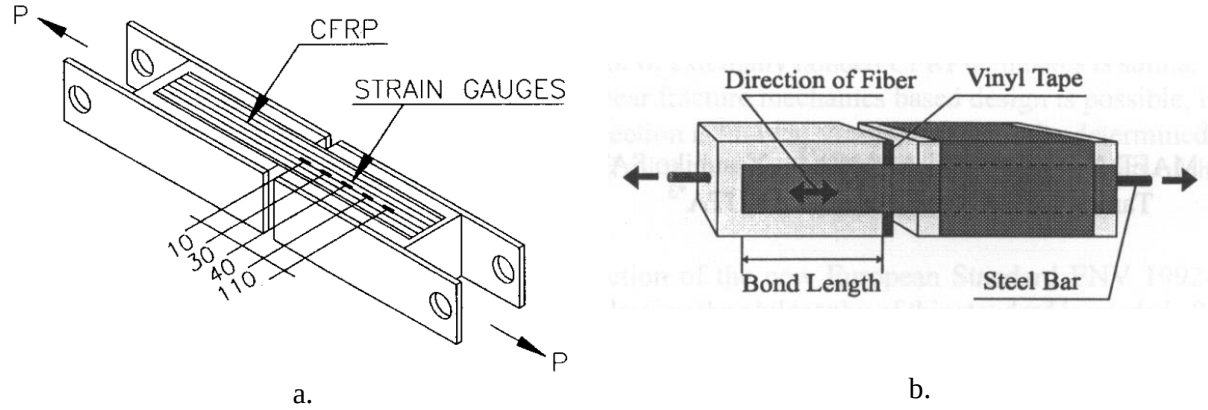

Figure 14. Specimens tested by Brosens and Van Gemert [18] (a) and by Maeda at al. [19] (b).

2.1.3. Beam tests

Since in bending problems the shearing stresses in the adhesive between the external reinforcement and the concrete are partly due to the variation of the bending moments and partly to the introduction of forces in the anchoring zones, Van Gemert in 1980 [16] performed experimental bending tests on beams. The beams were composed of two concrete prisms, linked by a steel plate of 5 mm thickness that was bonded to the lower surface of the prism with an epoxy adhesive. The stresses in the reinforcing plate was measured with strain gages. Figure 15 shows the test set-up adopted by Van Gemert [16].

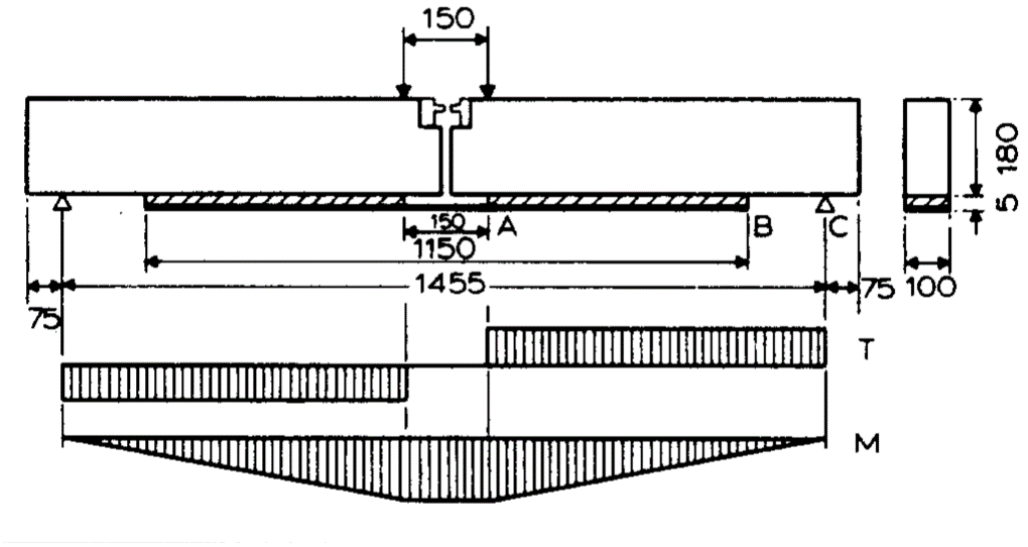

Figure 15. Beam test set-up by Van Gemert [16].

In 1995 Ziraba et al. [21] proposed a new test set-up, using a half-test beam to study the bond properties of epoxy bonded steel-concrete interfaces (Figure 16). Each specimen consisted of a plane concrete prism on the tension side of which a steel plate 3 mm thick and 15 mm wide was bonded. The width of the unglued part of the plate was kept constant of an extra length of 200 mm and then enlarged to 100 mm and secured to the top of a steel I section beam by two bolts. Near the bottom of the concrete prism the two halves were connected through a simple hinge. The whole assembly was subjected to four-point loading in a flexural test [21].

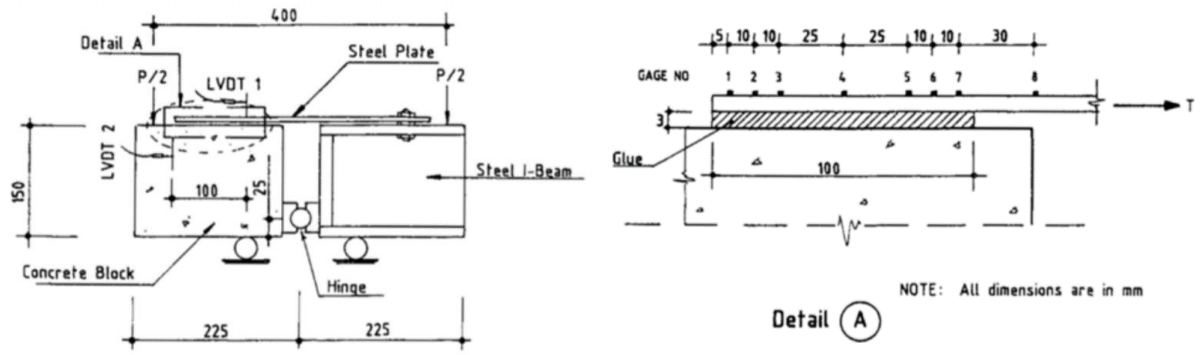

Figure 16. Half beam test details by Ziraba et al. [21].

2.2. Failure modes

Regardless the type of test set-up employed to investigate the bond between FRP composites and concrete substrates, six possible failure modes can be defined, although they may be mixed in an actual failure. The different types of failure modes are:

- Concrete failure;
- Plate tensile failure including FRP rupture or steel yielding;
- Adhesive failure;
- FRP delamination for FRP-to-concrete joints;
- Concrete-to-adhesive interfacial failure;
- Plate-to-adhesive interfacial failure.

The available literature showed that in most of cases failure usually occurred in thin layer of concrete beneath the adhesive layer unless a weak adhesive or a concrete with very high strength have been used. As a result, the concrete strength and the concrete surface condition are two critical parameters when the maximum transferable load is studied. The concrete surface was studied experimentally and analytically. Nowadays, the most common accepted concrete surface treatment is sandblasting.

The interfacial failure between either the adhesive and the concrete or the adhesive and the plate was rarely observed. This was a consequence of the availability of strong adhesives that bonded well to composite materials and concrete. For the same reason, also the adhesive failure was rare.

When the tensile strength of the composite material was reached before the maximum shear in concrete substrate and interlay of FRP was reached, FRP tensile failure occurred.

2.3. Effective bond length

The first researcher that investigated the effective bond length of steel plates externally bonded to a concrete substrate was Van Gemert in 1980 [16] (the test set-up is described in section 2.1.1). In his study, Van Gemert found that the tensile force in the steel plate decayed exponentially toward the anchored end of the plate. At higher loads, the distribution of the tensile force became more and more even in the initial bond zone. This phenomenon meant that no force was transferred from the plate to the concrete in this zon, because the cracking of the concrete close to the applied load shifted the active bond zone to new area farther away from the loading point. This process was confirmed by many researchers that considered both steel and FRP composites bonded to a concrete substrate. The shift of the active bond zone means that when long bonded lengths are considered, during the debonding phenomenon only part of the bonded area is effective. That is, as cracking in the concrete propagates, bond resistance is gradually lost in the zone close to the load, but in the meantime it is activated farther away from the load. The implication is that the anchorage strength cannot always increase with an increase in the bond length, and that the ultimate tensile strength of a plate may never be reached, however long the bond length is. Therefore, in a debonding phenomenon it can be found an effective bond length, i.e. a bond length beyond which any increase in the boned length cannot increase the load carrying capacity or anchorage strength. However, a longer bond length may improve the ductility of the failure process.

The debonding process between FRP composites and concrete substrates is substantially different from the bond behavior of internal reinforcement, for which a bond length can always be designed for its full tensile strength if there is sufficient concrete cover.

2.4. Load carrying capacity

The load carrying capacity or maximum transferable load of a FRP composite bonded to a concrete surface is one of the main aspects that captured the attention of the scientific community. Generally, the parameters that affect the load carrying capacity include interfacial fracture energy, tensile stiffness of FRP plate, effective bond length, width ratio of FRP over the concrete member. Based on different types of interfacial bond shear-slip relationships, Yuan et al. [24] proved that the load carrying capacity was proportional to the square root of the product between the fracture energy, G_F, and the FRP tensile stiffness (load carrying capacity $\propto \sqrt{G_F E_{FRP} t_{FRP}}$). E_{FRP} and t_{FRP} are the elastic modulus and the thickness of the FRP composite. Most of the existing studies focused on the modification of this expression with respect to the interfacial fracture energy, the width radio of the FRP composite over concrete, and the effective bond length. The models aimed to predict the load carrying capacity can be classified into three categories, i.e. empirical models, based directly on the regression of test data, fracture mechanics models,

and design proposals that generally make use of some simple assumptions. Among the fracture mechanics based models, the formula proposed by Täljsten in 1994 [25] was largely used:

$$P_u = b_f \sqrt{\frac{2E_{FRP}t_{FRP}G_F}{1+\alpha_T}} \tag{1}$$

Where:

$$\alpha_T = \frac{E_{FRP}t_{FRP}}{E_c t_c} \tag{2}$$

P_u is the load carrying capacity, b_f is the width of the composite strip, E_c and t_c are the elastic modulus and the thickness of the concrete prism, respectively. Usually the stiffness of the composite is negligible with respect to the stiffness of concrete and the coefficient α_T can be assumed equal to zero, obtaining:

$$P_u = b_f \sqrt{2E_{FRP}t_{FRP}G_F} \tag{3}$$

Täljsten in 1996 [26] was able to determine the load-carrying capacity considering the energy release rate *G*. In particular, the energy release in a single-lap shear test during the advancement of the interfacial crack *a* by an amount *da* was considered (Figure 17). The following assumptions were made:

- The materials are homogeneous, isotropic and linear elastic;
- The adhesive is only exposed to shear forces;
- The thickness of the adherents and the adhesive are constant throughout the bond line;
- The width of the steel plate is constant throughout the bond line.

The energy release rate *G* per unit width b_f of the composite was obtained as:

$$G = \frac{1}{b_f}\left[\frac{d}{da}\left(F - U_e\right)\right] \tag{4}$$

Where *F* is the work done by the external load *P* and U_e is the elastic energy. When debonding propagates, $G = G_F$.

If δ is the displacement of the point of application of the applied force *P* (Figure 17) and *C* is the compliance of the system, then:

$$U_e = \frac{1}{2}P^2 C \tag{5}$$

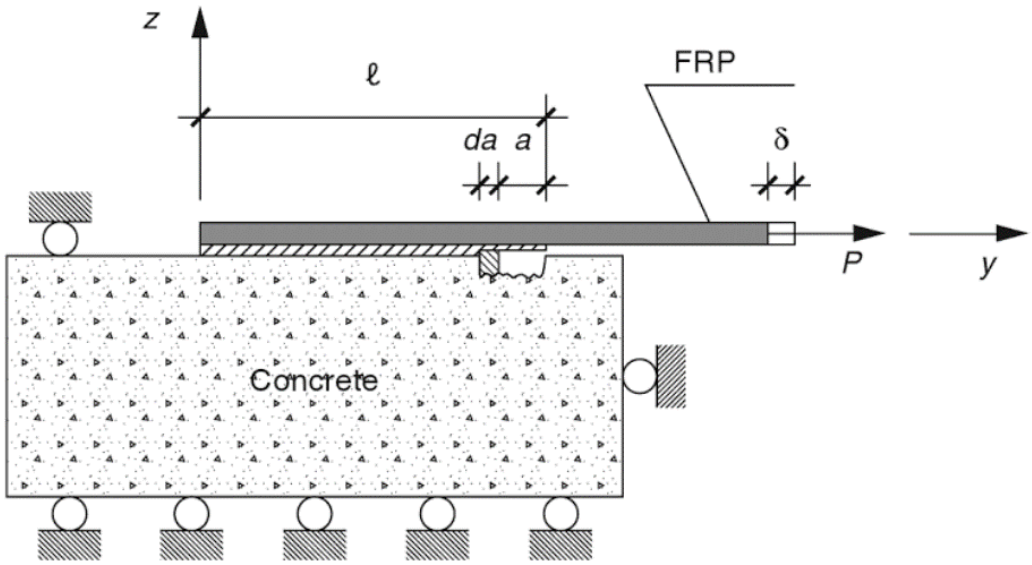

Figure 17. Crack propagation in direct-shear test [10].

And when the interfacial crack propagates:

$$G_F = \frac{1}{b_f}\left[P\frac{d\delta}{da} - \frac{dU_e}{da}\right] = \frac{1}{b_f}\frac{P^2}{2}\frac{\partial C}{\partial a} \tag{6}$$

Therefore:

$$P = \sqrt{\frac{2G_F b_f}{\partial C/\partial a}} \tag{7}$$

If the substrate is considered rigid and the adhesive layer is idealized as a zero-thickness layer:

$$\frac{\partial C}{\partial a} = \frac{1}{E_{FRP} b_f t_{FRP}} \tag{8}$$

Combining Eq. (7) and Eq. (8), the load-carrying capacity defined in Eq. (3) was obtained.

2.5. Cohesive material law

Several researchers attempted to study the debonding process in direct-shear tests as a Mode-II fracture problem where the interface region was idealized to be of zero thickness with well-defined material properties [27] [28] [29]. In other words, researchers aimed to understand the quasi-brittle behavior of the bond between composites and concrete substrates via a constitutive law of a fictitious material that separated the two adherents. The most widespread technique to define the interfacial τ-s relationship consisted in the direct calculation of local bond stress and slip from the variation of the strain measured by a series of strain gages mounted on the external surface of the FRP sheets. This procedure led to an inaccurate evaluation of the bond stresses at the interface due to several causes, among which the high non-linearity natural of local fractures, the random distribution of discrete cracks and aggregates in the concrete and the irregularity in the adhesive layer and surface preparation. In order to overcome the drawbacks of this procedure, Ali-Ahmad et al. [27] established an experimental procedure to directly determine the Mode-II interfacial fracture law using DIC measurements.

Several expressions of the cohesive material law are available in literature. Some of the most fundamental constitutive laws that characterized the bond of FRP sheet-concrete interface are (Figure 18):

- Elastoplastic model by Sato et al. [30] and De Lorenzis et al. [31];
- Bilinear model based on the interfacial fracture energy G_F (Yoshizawa et al. [32]);
- Model based on Popovic's expression by Nakaba et al. [33];
- Shear softening model by Sato et al. [34].

Dai et al. [35] in 2005 made a comparison between these models that configure the shapes of the τ-s relationship in different ways. Dai et al. considered a constant concrete strength equal to 35 MPa in order to compare the models. It was found that although the elastic modulus of adhesives in these studies was similar, big differences existed among the models. These differences can be due to different interfacial material properties (e.g., composite stiffness) or to different bonding skills (the deviations of concrete surface conditions or the adhesive's thickness) used in the different studies. Beside that, the large scatter observed in the experimental bond stress-slip relationships at different interfacial locations may be another factor that affected the shape of the τ-s relationship. Due to these large differences, Dai et al. proposed a more reliable and accurate method in order to describe the behavior at the interface between the FRP strip and the concrete substrate considering the relationship among the strains of the FRP sheets and the slips at the loaded end. This procedure appeared to be more correct because the measurements of the load and slip at the loaded end in a direct-shear test are much more stable that the strain obtained from strain gages along the FRP-strip.

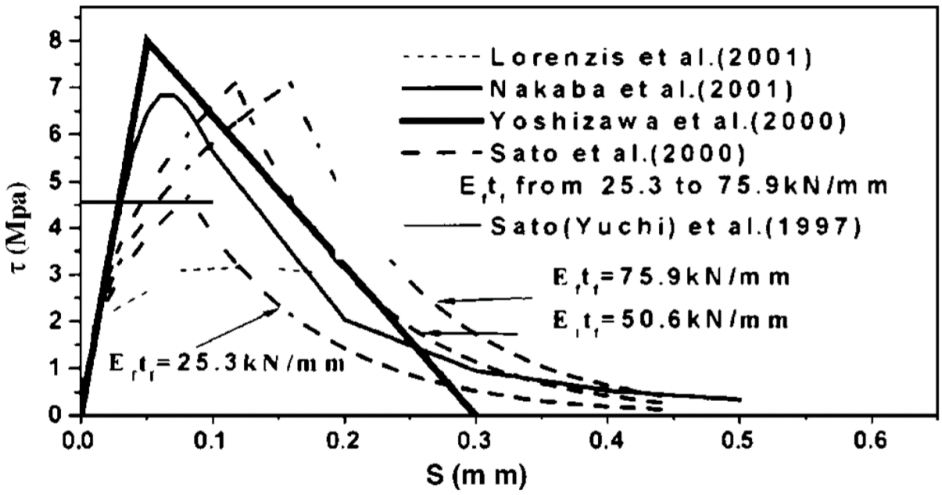

Figure 18. Most popular bond stress-slip relationships of fiber reinforced plastic sheet-concrete interfaces [35].

3. Materials

This chapter presents the material characterization of the composite materials and of the substrates used in the experimental work described in the present dissertation. Composite materials were applied on two different substrates, i.e. concrete substrates and masonry substrates. Four different types of composite materials have been investigated:

- Steel reinforced polymer (SRP) composites, applied on a concrete surface;
- Steel reinforced grout (SRG) composites, applied both on a concrete surface and on a masonry surface. Two different matrices were employed for SRG systems, i.e. a lime based mortar and a cementitious mortar. The lime based mortar was applied both on concrete surfaces and on masonry surfaces, while the cement based mortar was applied only on concrete surfaces;
- Steel-fiber reinforced geopolymer matrix (S-FRGM) composites, applied on a concrete surface.
- Basalt-fiber reinforced cementitious matrix (B-FRCM) composites, applied on a masonry surface.

3.1. Concrete

Each experimental campaign performed to investigate the performances of composite materials applied to a concrete substrate was characterized by a specific concrete mix design, determining different mechanical properties. For these reasons, the material characterization performed on three different types of concrete is herein presented. The three types of concrete were referred to as “Concrete – Type A”, “Concrete – Type B”, and “Concrete – Type C”. The material characterization consisted of compressive tests on concrete cubes and cylinders, splitting tests performed on concrete cylinders, and fracture mechanics tests performed on concrete notched prisms. The fracture mechanics set-up is described in section 3.1.1.1.

3.1.1. Concrete – Type A

All “Concrete – Type A” prisms were cast from the same batch of concrete. Concrete was normalweight with portland cement. The maximum aggregate size was 15 mm. Compressive and tensile splitting strengths of concrete were measured at 21 (only compression), 28, 42, 56, 84, 112, 168, 224, and 420 days after casting using 150 mm side cubes (compression) and 150 mm × 300 mm cylinders (splitting) tested according to [36] and [37], respectively. In addition, 150 mm × 300 mm concrete cylinders were

tested in compression at 84, 112, 168, 224, and 420 days after casting according to [36]. The average values of 3 tests for each day are plotted in Figure 19.

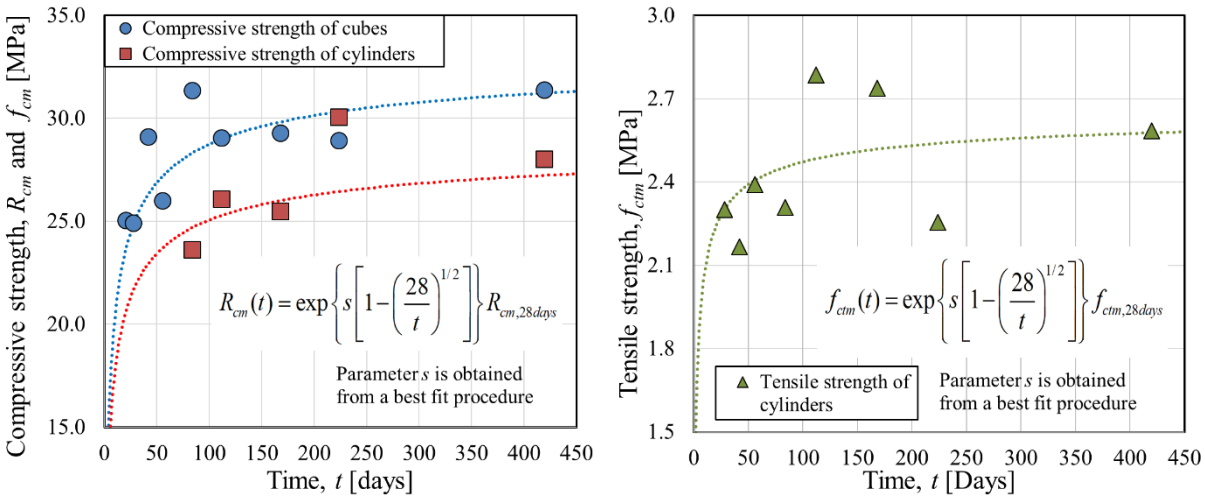

a. b.

Figure 19. Compressive (a) and tensile strength (b) of concrete as a function of time.

The behavior of the cubic compressive strength at different ages was fitted using the formula proposed in Eurocode 2 [38]:

$$R_{cm}(t) = \exp\left\{s\left[1-\left(\frac{28}{t}\right)^{1/2}\right]\right\} R_{cm} \tag{9}$$

where R_{cm} is the mean cubic compressive strength at 28 days obtained from experimental tests, while s is a parameter defined through a non-linear regression. The coefficient s was found to be equal to 0.31, which is slightly higher than prescriptions suggested in Eurocode 2 [38]. The same formula was used to fit the results of tensile tests, using the mean tensile strength at 28 days obtained from splitting tests, f_{ctm}, instead of R_{cm} (coefficient s equal to 0.15). Since the compressive tests on cylinders were not performed until the age of 84 days, the cylinder compressive strength over time behavior was obtained by scaling the curve from cubes in order to best fit the experimental data of cylinders. Since bond tests and confinement tests were performed approximatively 300 days after casting, the compressive strength of cubes and cylinders and the tensile strength at 300 days evaluated from the fitting of experimental data was determined and resulted equal to 30.78 MPa, 26.83 MPa, and 2.56 MPa respectively. The 28 days compressive strength of cubes and the 28 days tensile strength obtained from experimental tests resulted equal to 24.88 MPa and 2.30 MPa, respectively.

The evaluation of the fracture energy for "Concrete – Type A" was performed through a detailed experimental work, that is reported in next sections.

3.1.1.1. Fracture mechanics set-up

Concrete prisms with different widths, depths, and lengths were tested using a three-point bending (TPB) set-up (Figure 20). Concrete specimens were named following the notation FM_X_Y_W_A_Z, where X indicates the specimen depth (d) in mm, Y represents the specimen width (b) in mm, W indicates the specimen free span (S) in mm, A denotes the use of DIC (D = DIC was used, ND = DIC was not used), and Z = specimen number.

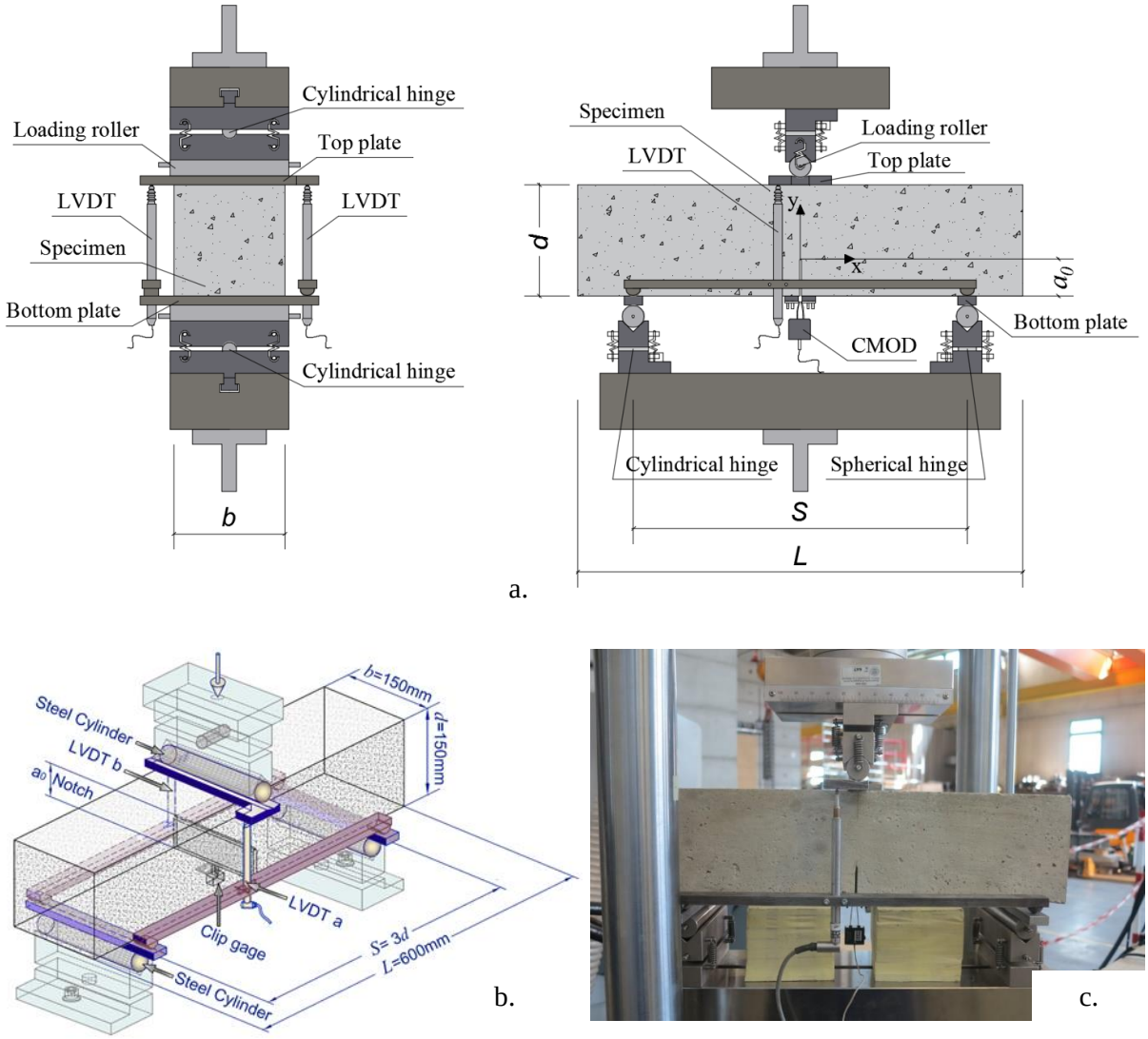

Figure 20. Fracture mechanics set-up: sketch (a), 3D view (b), and photograph (c).

All concrete prisms had a central notch with a V-shaped tip. The notch length a_0 was equal to one third of the prism depth *D*. The net span *S* was equal to three times the depth of the specimen. The loading apparatus consisted of two bottom cylindrical rollers that supported the prism base and a cylindrical roller at the top of the specimen, centered with respect to its length that was used to apply the load. Two steel plates were glued to the bottom face of the specimen and placed on the support rollers to reduce friction. An "S-shaped" steel plate with a central V-shaped section was glued to the top face of the specimen to rest firmly the loading cylindrical roller. Both the top and the bottom plates had a length exceeding the prism width. On both sides of the concrete prism, a steel element, with a semi-spherical and a cylindrical support rested on the bottom plates. Each steel element fastened a linear variable displacement transducer (LVDT) that reacted off of the "S-shaped" top plate. The two LVDTs measured the vertical displacement δ of the prism where the load was applied. Two small steel plates were glued to the bottom face of the prism near each edge of the central notch. Two screws were welded on each small plate in order to fix the knives that provided the fastening of a clip-on gage. The clip-on gage measured the crack mouth opening displacement (CMOD) and was used to control the test. The rate of the test was equal to 0.001 mm/s. The set-up herein presented has been designed to become potentially part of the ACI 446 report on fracture.

3.1.1.2. Evaluation of the fracture energy of "Concrete – Type A"

Twelve "Concrete – Type A" prisms with different widths, depths, and lengths were tested using a TPB set-up (Figure 20) in order to investigate the role of the width and size effects in the evaluation of the fracture mechanics parameters. The dimensions of all concrete prisms obtained as the average of three measurements are presented in Table 2. Two different widths and two different depths of the concrete prisms were considered. Figure 21 shows the load per unit width, *P/b*, plotted versus CMOD (Figure 21a) and displacement δ (Figure 21b) for 75 mm while Figure 22 shows the load per unit width, *P/b*, plotted versus CMOD (Figure 22a) and displacement δ (Figure 22b) for 150 mm depth specimens.

All load responses exhibit a similar trend. Concrete notched specimens show an initial linear branch, followed by a non-linear portion until the peak load is reached. At peak load, the maximum tensile strength of concrete is reached near the crack tip and part of the FPZ has formed [39]. Crack propagation occurs after the peak in the descending branch of the load response, which is characterized by a long tail until the specimen finally breaks at a value of the load close to zero. Few specimens failed prematurely at a value of the load approximately equal to 15% of the peak load, therefore the tail of the response was incomplete. In those specimens, the fracture surface was similar to those that exhibited a long tail. A typical cohesive crack pattern of a specimen tested (FM_75_150_210_D_2) and the relative crack surfaces are shown in Figure 23a and Figure 23b, respectively.

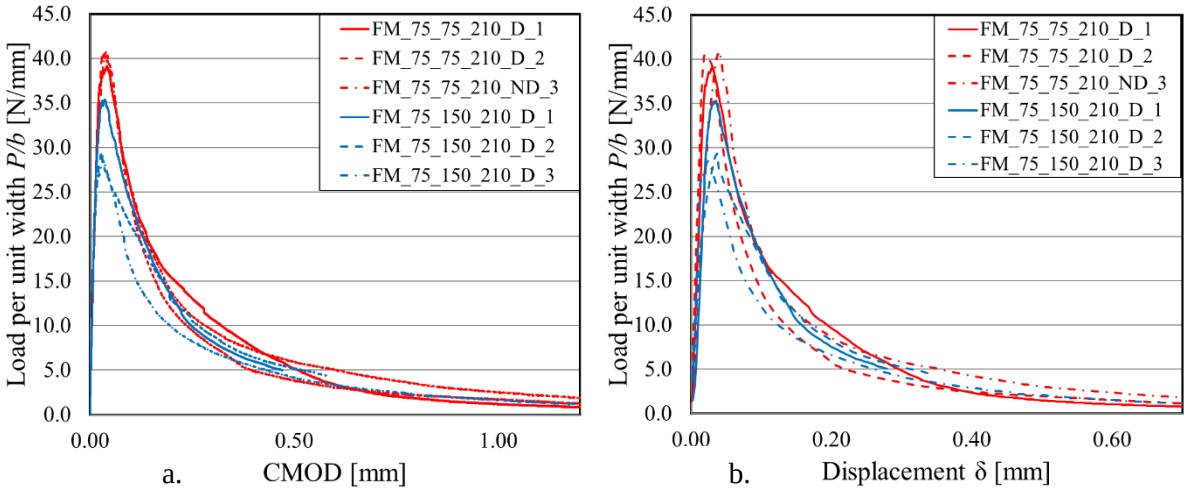

Figure 21. Load per unit width vs. CMOD (a) and load per unit width vs. displacement (b) for 75 mm depth specimens.

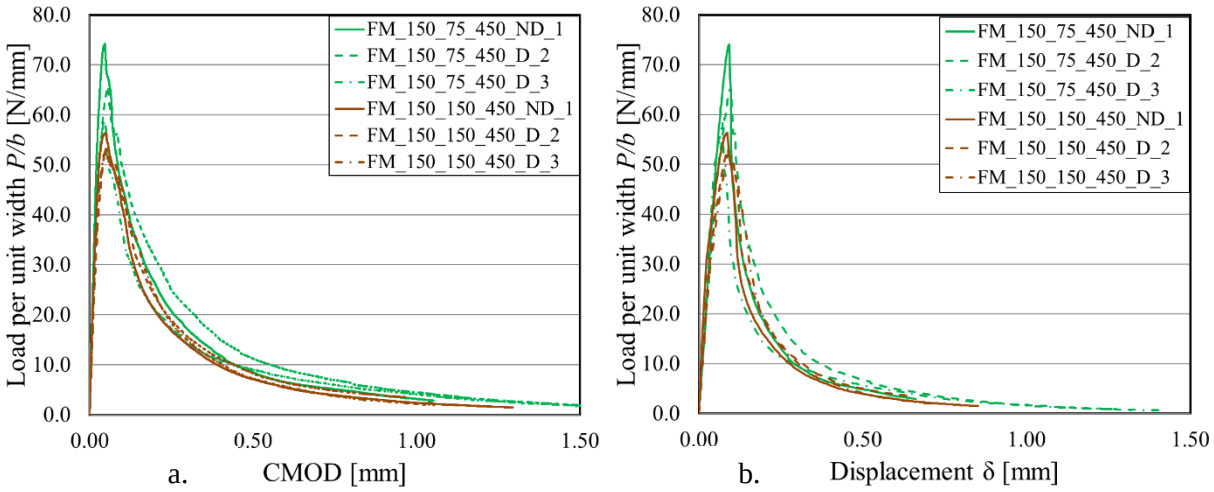

Figure 22. Load per unit width vs. CMOD (a) and load per unit width vs. displacement (b) for 150 mm depth specimens.

The fracture energy, G_F, of concrete was evaluated from the area under the load-deflection response as proposed by Hillerborg (1985) [40], Elices et al. (1992) [41], and Hoover et al. (2013) [42]. The value of G_F was adjusted to include the work done by the self-weight, P_0, of the specimen, as showed in Figure 24a. The value of G_F for each specimen is reported in Table 3. It can be observed that the values of the fracture energy, independently of the width or the depth of the specimen, are similar. These results would suggest that the fracture energy, G_F, is almost size and width-independent, therefore it can be considered a material property. In order to verify the accuracy in the evaluation of P_0, it is possible to compare the analytical and experimental values of the vertical displacement due to the self-weight at midspan.

Table 2. Dimensions of fracture mechanics specimens.

Specimen	Depth (*mm*)	Width (*mm*)	Length (*mm*)	Span (*mm*)	Weight (*N*)	Notch (*mm*)
FM_75_75_210_D_1	75.7	72.7	296.8	210	35.1	25.0
FM_75_75_210_D_2	75.5	76.0	296.3	210	36.5	23.0
FM_75_75_210_ND_3	75.2	76.8	297.0	210	36.8	23.0
FM_75_150_210_D_1	74.8	153.6	299.9	210	76.6	25.0
FM_75_150_210_D_2	76.0	152.7	296.3	210	76.0	26.0
FM_75_150_210_D_3	75.3	153.6	297.0	210	74.9	24.0
FM_150_75_450_ND_1	152.8	75.0	599.3	450	153.6	50.0
FM_150_75_450_D_2	152.8	75.7	599.0	450	151.0	51.5
FM_150_75_450_D_3	153.2	77.2	599.5	450	156.4	51.0
FM_150_150_450_ND_1	149.8	152.7	599.3	450	306.3	53.5
FM_150_150_450_D_2	149.7	152.8	598.8	450	301.9	55.0
FM_150_150_450_D_3	149.7	152.8	599.3	450	303.9	50.5

Figure 23. Specimen FM_75_150_210_D_2 at failure: side view (a) and surfaces of the fracture (b).

The self-weight, P_0, is considered as a concentrated load (Gerstle, 2010) [43], and is obtained comparing the bending moment due to a distributed load with the one due to a concentrated load:

$$\frac{mgLS}{4}-\frac{mgL^2}{8}=\frac{P_0 S}{4}\rightarrow P_0=Mg\left(1-\frac{L}{2S}\right) \tag{10}$$

Where m is the mass per unit length of the specimen, M is the mass of the specimen, and g is the acceleration of gravity.

The analytical displacement due to the self-weight can be evaluated through the following fracture mechanics formulas:

$$u=\frac{P_0}{bE}\hat{v}(\alpha) \qquad \hat{v}(\alpha)=\hat{v}_0+\hat{v}^c(\alpha) \qquad v_0=u_0\frac{bE}{P_0} \qquad \hat{v}^c(\alpha)=2\int_0^{\alpha}k^2(\alpha')d\alpha' \tag{11, a-b-c-d}$$

in which E is the elastic modulus of concrete evaluated according to Eurocode 2 (2004) [38], u_0 is the elastic displacement of the structure in the absence of a crack, k is the stress intensity factor, and α is

equal to a_0/d. The displacement due to the self-weight of the specimen can be obtained from the experimental response. If the initial pseudo linear response is extended toward the quadrant of negative values of the displacement, the intersection of the linear response with the horizontal line corresponding to $-P_0$ would provide an estimate of the deflection due to the selfweight. The values of the initial displacement due to the self-weight were reported in Table 3 for both the analytical and experimental procedures. No significant difference is observed between the theoretical and the experimental values of the displacement, which suggests that LEFM formulas could be employed for this calculation.

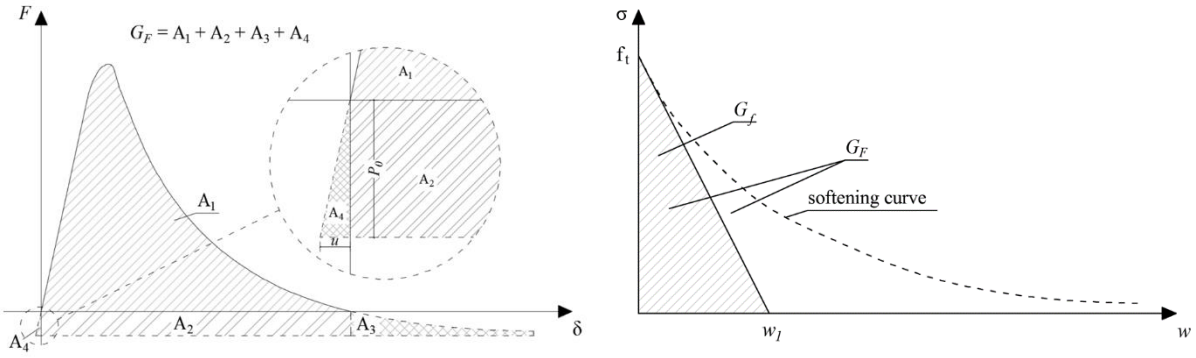

a. b.

Figure 24. Evaluation of the fracture energy G_F (a) and G_f (b).

Table 3. Fracture mechanics results.

Specimen	G_F (*N/mm*)		G_f (*N/mm*)		u_{theor} (μm)	u_{exp} (μm)	u_{theor}/u_{exp} (%)	σ_N (MPa)
FM_75_75_210_D_1	0.112	0.109 (CoV 0.12)	0.081	0.074 (CoV 0.10)	0.088	0.067	130%	2.15
FM_75_75_210_D_2	0.095		0.067		0.074	0.060	123%	2.24
FM_75_75_210_ND_3	0.121		0.075		0.074	0.098	76%	2.27
FM_75_150_210_D_1	0.109	0.102 (CoV 0.10)	0.056	0.032 (CoV 0.66)	0.092	0.081	114%	1.99
FM_75_150_210_D_2	0.107		0.023		0.098	0.097	102%	1.60
FM_75_150_210_D_3	0.090		0.017		0.082	0.081	102%	1.59
FM_150_75_450_ND_1	0.125	0.127 (CoV 0.12)	/	0.072 (CoV 0.38)	0.455	0.693	66%	2.14
FM_150_75_450_D_2	0.143		0.092		0.476	0.752	63%	1.88
FM_150_75_450_D_3	0.112		0.053		0.467	0.640	73%	1.69
FM_150_150_450_ND_1	0.099	0.104 (CoV 0.05)	0.072	0.059 (CoV 0.26)	0.569	0.603	94%	1.69
FM_150_150_450_D_2	0.109		0.064		0.605	0.750	81%	1.60
FM_150_150_450_D_3	0.102		0.042		0.490	0.779	63%	1.59

Another fracture energy, G_f, corresponding to the area under the initial tangent of the softening curve σ-*w* (Figure 24b), can be evaluated using the tensile strength of concrete and the peak load, as described by Gerstle [43]. As noticed by Planas et al. (1992) [44], it is solely G_f that controls the maximum loads of structures and thus the size effect. The values of G_f are reported in Table 3. If specimens with the same

depth are considered, it can be noted that the value of G_f is affected by the width of the specimen. For a depth of 75 mm, the average value of G_f is equal to 0.032 N/mm or to 0.074 N/mm, for 150 mm width specimens and 75 mm width specimens, respectively. A similar trend was obtained for 150 mm depth specimens. The width effect is confirmed by comparing the load per unit width responses of Figure 21 and Figure 22, where the peak load appears usually higher for specimens with a smaller width. Results in Table 3 highlight also a size-effect. Squared cross-section specimens 75 mm x 75 mm and 150 mm x 150 mm have G_f equal to 0.074 N/mm and 0.059 N/mm, respectively. At the same time, for specimens with the same width but different depth, it can be observed that an increase in the depth causes a decrease in the nominal stress, σ_N, (Bažant, 1997) [45] at peak. The width effect has several causes that can be summarized as follows:

- Changes in the width of the specimens can be associated with a shifting from a plane stress condition (thin specimen) to a plane strain state (thick specimen) affecting therefore the peak load;
- Wall effect: during casting, large aggregates tend to distribute in the central portion of the mold, with a lower concentration near the edges. The concrete near the edges is usually rich of mortar and it has slightly different properties with respect to the concrete in the core of the prism. This aspect is emphasized for thin specimens;
- For thick specimens, the cure of the concrete take usually long time, especially in the core of the specimen. This aspect can lead to erroneous result if the specimens are tested too early with respect to the casting date. Specimens were tested at 300 days of age so curing of specimens should not be an issue in the experimental results herein presented. This is should have not influenced the results of the current study;
- Since concrete is a heterogeneous material, for larger specimens is easier to find a weak portion of concrete with respect to a thin specimen.

Digital image correlation (DIC) was used to evaluate the strain field near the crack tip. Displacements and strains were obtained for different square areas (subsets) for a 5 pixel step size, which provided points spaced at approximately 0.75 mm. A subset size of 41 pixels (approximately 6.30 mm) edge was employed. The DIC analysis reported in this section refers to the Cartesian system shown in Figure 20a. Figure 25 shows the strain component ε_{xx} in the central portion of the prism for specimen FM_75_150_210_D_2. The strain profile along the crack ligament for different values of the load is reported in Figure 25a. It can be observed that at peak load (point C) part of the FPZ has formed, and near the crack tip strains have exceeded the ultimate tensile strain of concrete, ε_t, equal to 0.00009, which was obtained by dividing the tensile strength by the elastic modulus of concrete. Values plotted in Figure 25a

were obtained by averaging the strain over a 8 mm wide strip of concrete centered with respect to the crack tip. The width of the strip was chosen considering the width of the FPZ in Figure 25b that shows the ε_{xx} at peak load for different values of *y*. It can be observed that the width of the FPZ can be roughly estimated to be in the range of 8-10 mm. From Figure 25a, it is also possible to estimate the length, *c*, of the FPZ, i.e. the portion of the section where softening occurs. In most of the specimens, the value of *c* is comprised in the range 20-30 mm. From the experimental results, the value of *c* seems to vary with the specimen dimensions.

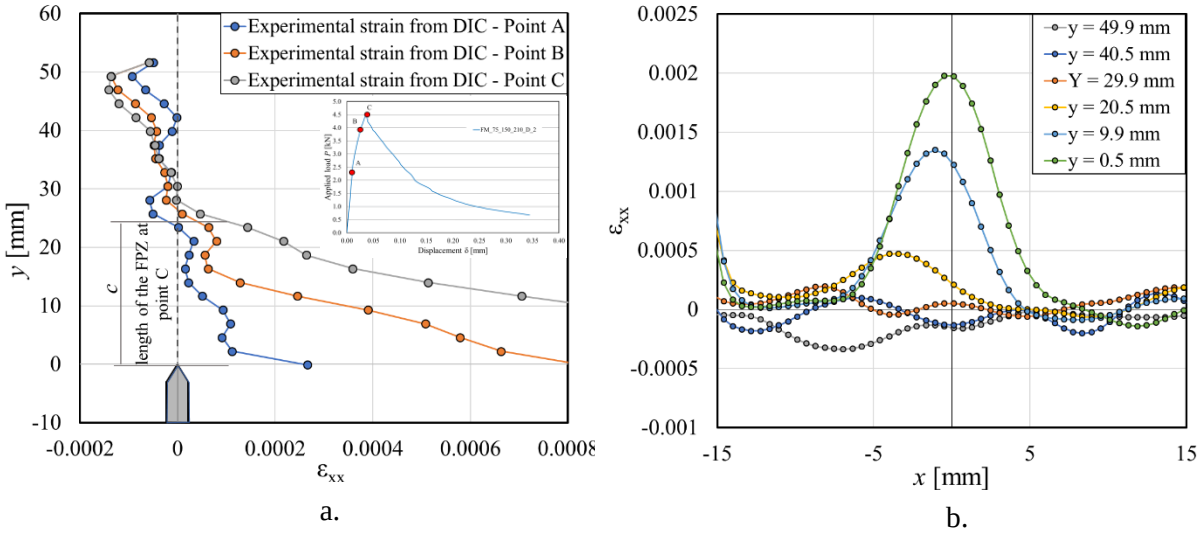

Figure 25. *y*- ε_{xx} plot (a) and ε_{xx}-*x* plot at peak load (b) for specimen FM_75_150_210_D_2.

3.1.2. Concrete – Type B

"Concrete – Type B" prisms were cast from 8 different batches of concrete, characterized by the same type of cement and same admixture of aggregates. The mixture proportions by weight of the constituents used in the eight batches of concrete were: cement (1.00): water (0.55): coarse aggregate (2.50): fine aggregate (3.00). Coarse aggregate comprised of river gravel with a maximum size of 10 mm was employed. A series of 24 compressive tests (three for each batch) on 150 mm-side cubes were performed at 28 days according to EN 12390-3 (2009) [36]. The compressive strength of "Concrete – Type B" at 28 days was equal to 23.69 MPa (CoV = 0.073).

3.1.3. Concrete – Type C

"Concrete – Type C" prisms were cast from the same batch of concrete. Concrete was made up of Portland cement with a water-cement ratio equal to 0.43 and limestone and sandstone aggregates with a maximum

diameter size of 15 mm. Some pictures of the concrete casting are showed in Figure 26. “Concrete – Type C” prisms were cured for 28 days by frequent application of water and use of plastic bags for covering the concrete samples to minimize water loss from concrete and to keep the concrete moist as recommended by ACI 308R-16 [46]. Compressive tests were performed at different ages on 150 mm cubic specimens according to EN 12390-3 [36]. Tests were performed at 7, 14, 21, 28, 56, 84, 112, 119 and 149 days after the date of casting. In addition, three 150 mm × 300 mm concrete cylinders based on EN 12390-6 [37] were tested every 7 days up to 28 days to measure the tensile strength of concrete. Three cylinders were also tested in compression at 28 days according to EN 12390-3 [36]. The average compressive strength of cubes and cylinders at 28 days were equal to 21.94 MPa (CoV 0.05) and 19.83 MPa (CoV 0.00), respectively. The average tensile strength of concrete at 28 days resulted equal to 1.91 MPa (CoV 0.14). The average values of the compressive and tensile strength at different ages are plotted in Figure 27.

Figure 26. “Concrete – Type C” casting: concrete colums (a)(b), concrete cubes (c), concrete cylinders (d), and concrete prisms (e).

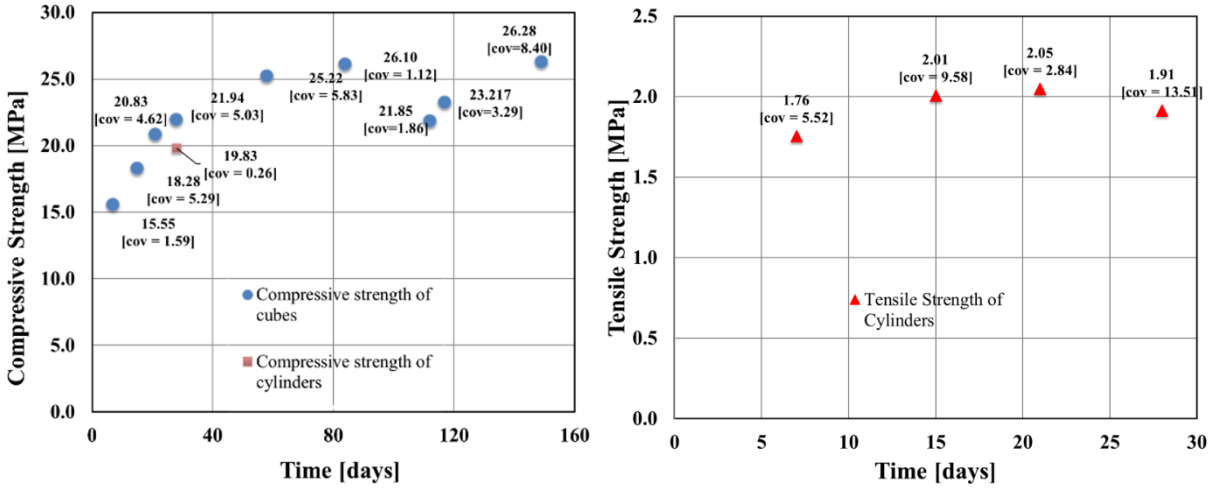

a. b.

Figure 27. Compressive (a) and tensile strength (b) of concrete as a function of time.

3.2. Masonry

All the masonry blocks described in this dissertation were constructed with solid clay bricks and a low strength mortar, except for the masonry arches described in section 6.3 that had different mechanical properties, reported in section 3.2.1.

Twenty cylinders were cored from five half-bricks extracted from the masonry blocks after the direct shear tests were performed. The nominal dimensions of the cylinders were equal to 50 mm (*diameter*) × 50 mm (*length*). Out of twenty cylinders, seven were used to determine the tensile strength of bricks, f_{bt}, through splitting tests (Figure 28b), while thirteen were used to define the compressive strength of bricks (Figure 28a), f_{bc}, according to [47]. The tensile strength of bricks, f_{bt}, resulted equal to 3.16 MPa (CoV 0.12), while the compressive strength of bricks, f_{bc}, resulted equal to 20.3 MPa (CoV 0.17). Out of the thirteen cylinders tested in compression, five were instrumented with two strain gages applied on opposite sides along the length of the specimens. The average strain calculated from the measurements of the two strain gages was used to define the elastic modulus of the bricks, E_b, evaluated as the slope of stress-strain response between the 5% and the 30% of the peak stress. The elastic modulus of the bricks, E_b, resulted equal to 7.3 GPa (CoV 0.29). In addition, fracture mechanics tests (Figure 28d-e-f) were performed using a three-point bending set-up (see section 3.1.1.1) [48] on three 250 mm length (L) × 55 mm width (b) × 120 mm depth (d) notched bricks, selected from the group of bricks employed to construct the masonry blocks. The fracture energy of each brick was evaluated as the area under the load-deflection response divided by the area of the ligament [40] [41] [42] and the average value of the fracture energy resulted equal to 34 N/m (CoV 0.16). Double punch tests (Figure 28c) were performed according to [49] on

fourteen mortar joint samples extracted from the masonry blocks after single-lap shear tests were performed. The compressive strength of mortar joints obtained from double punch tests, f_{mdp}, resulted equal to 23.1 MPa (CoV = 0.25). The compressive strength of the mortar joint, f_m^{**} can be evaluated from the value obtained from double punch tests using the following formula:

$$f_m^{**} = 0.555\, f_{mdp} + 3.068 \tag{12}$$

The compressive strength f_m^{**} of the mortar joints resulted equal to 15.9 MPa.

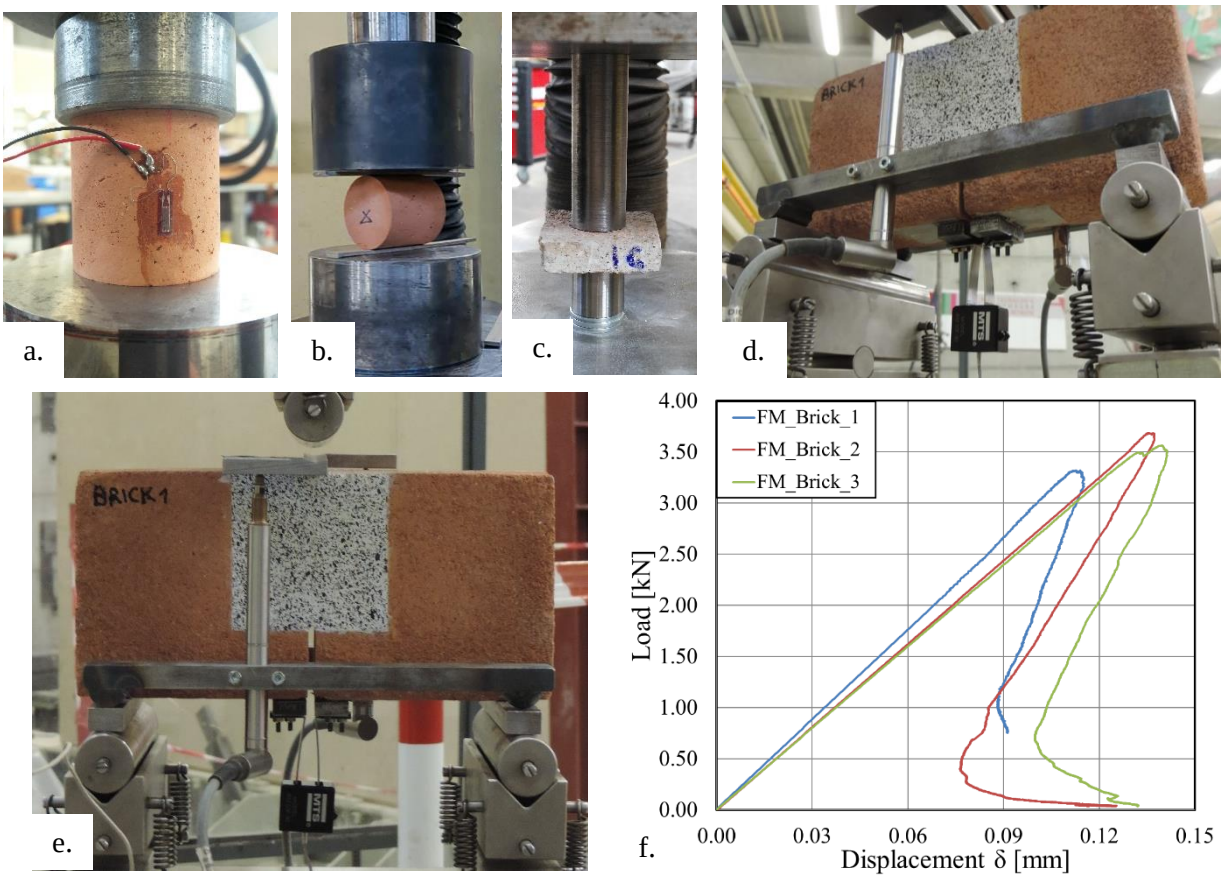

Figure 28. Material characterization: a) compression test on a cylinder cored from a half brick; b) Splitting test on a cylinder cored from a half brick; c) Double punch test on a mortar joint; d) and e) Fracture mechanics test on a notched brick; f) Load-displacement response obtained from fracture mechanics tests performed on notched bricks.

3.2.1. Material characterization of masonry arches

This section reports briefly the material characterization performed on the masonry arches described in section 6.3. Twenty-nine brick cylinders, cored from bricks extracted from the masonry arches after tests

were performed, were tested in compression (Figure 29a). The average compressive strength of bricks, f_{bc}, evaluated according to [47], resulted equal to 44.7 MPa. Double punch tests [49] (Figure 29b) were performed on thirteen mortar joint samples obtained from the masonry arches. The compressive strength f_m^{**} of the mortar joints resulted equal to 5.8 MPa.

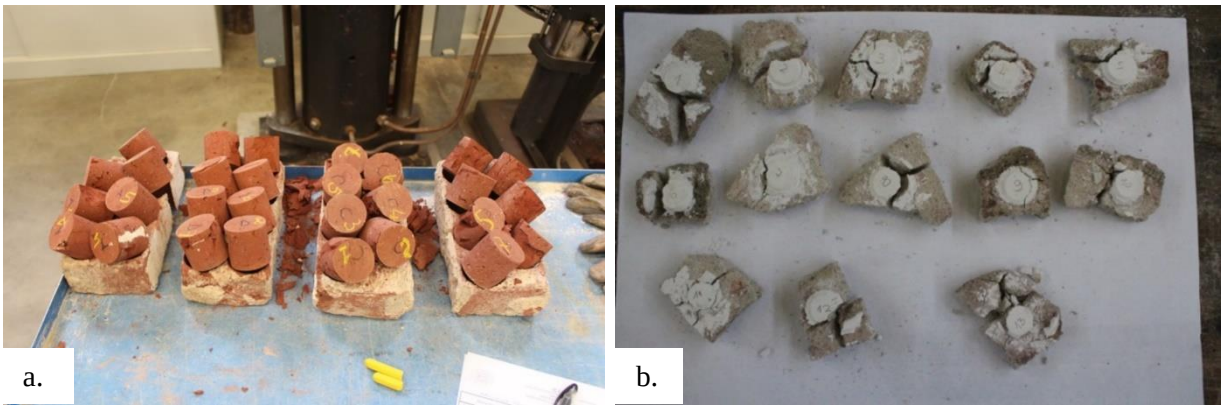

Figure 29. Material characterization of masonry arches: a) Cylinders cored from the bricks of the arches tested in compression; b) Mortar joints after double punch test.

3.3. Composite material

This section will describe the main mechanical properties of the composite materials used in the experimental investigations described in the present dissertation. First, the material properties of the composites constituents (fiber and matrix) will be described, then for SRP and SRG composite materials, the results obtained from tensile tests will be presented.

3.3.1. Steel fibers

Steel fibers (cords) were in the form of a unidirectional sheet made of ultra-high strength galvanized steel micro-cords fixed to a fiberglass micromesh to facilitate installation (Figure 30). Each micro-cord consists of five filaments. Three of the five filaments are straight, and the remaining two filaments are wrapped around the other three with a high torque angle. The cross-sectional area of the cord A_{cord} was 0.538 mm^2. Fiber sheets with five different densities are investigated in the present dissertation and are referred to as low density (LD), medium-low density (MLD), medium density (MD), high density (HD), and ultra-high density (UHD). The LD steel fiber sheets had 0.156 cords/mm, the MLD steel fiber sheets had 0.234 cords/mm, the MD steel fiber sheets had 0.314 cords/mm, the HD steel fiber sheets had 0.472 cords/mm, while the UHD steel fiber sheets had 0.709 cords/mm. Mechanical properties of the fibers reported by the manufacturer [6] are provided in Table 4.

Table 4. Properties of the steel fibers (textile) provided by manufacturer [6].

Property	LD steel fibers	MLD steel fibers	MD steel fibers	HD steel fibers	UHD steel fibers
Number of Cords/mm	0.156	0.234	0.314	0.472	0.709
Tensile Strength, $f_{f,u}^{A}$ [MPa]	> 3000	> 3000	>3000	> 3000	> 3000
Elastic Modulus, E_f [GPa]	>190	>190	>190	> 190	> 190
Break Deformation, $\varepsilon_{f,u}$ [%]	>2	>2	>2	> 2	> 2
Equivalent Thickness, $t_{f,A}^{*}$ [mm]	$t_{f,LD}^{*}$ 0.084	$t_{f,MLD}^{*}$ 0.126	$t_{f,MD}^{*}$ 0.169	$t_{f,HD}^{*}$ 0.254	$t_{f,UHD}^{*}$ 0.381

Note: $f_{f,u}^{A}$ is the tensile strength of the fibers. $t_{f,A}^{*}$ is the equivalent thickness of the fibers. Superscript A represents the steel fiber density (LD = low density, MLD = medium-low density, MD = medium density, HD = high density, UHD = ultra-high density).

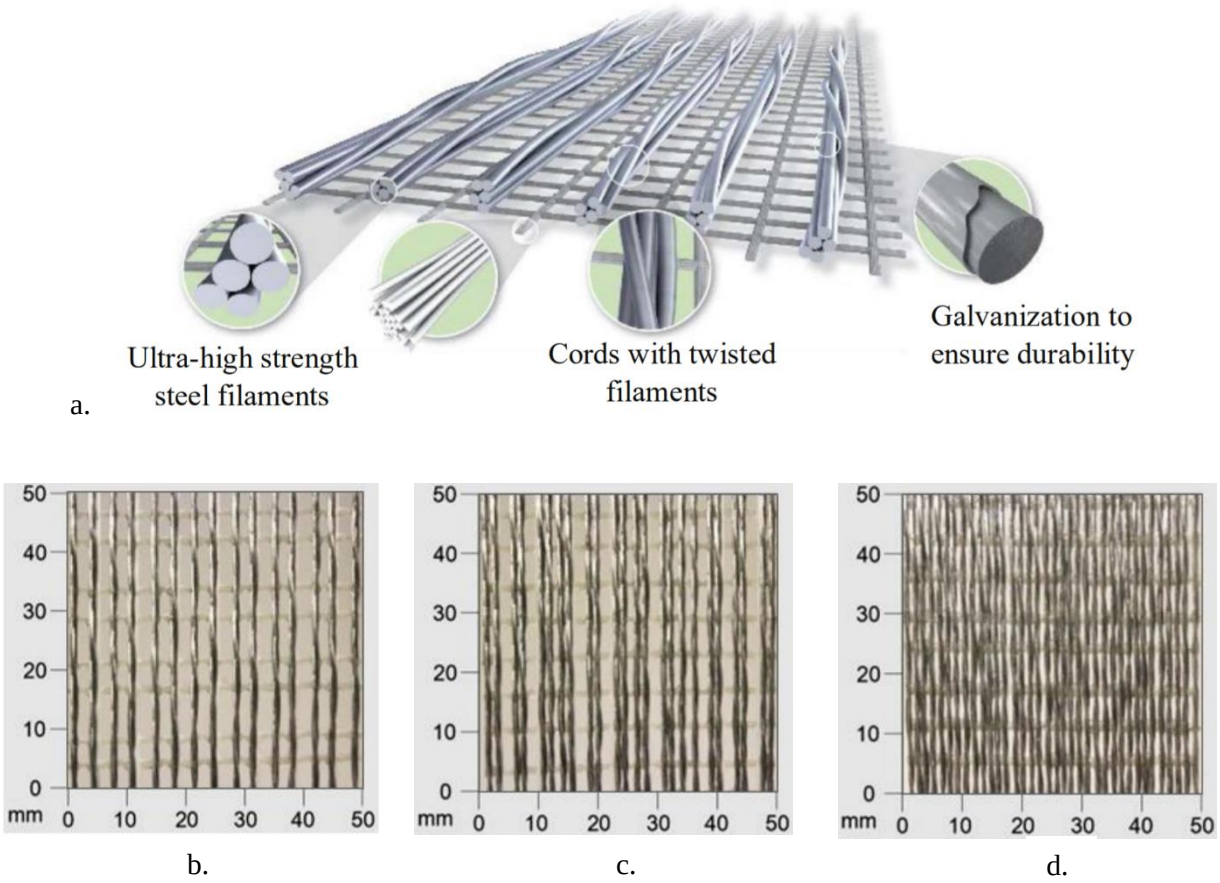

Figure 30. Steel fibers: sketch of the fiber sheet (a), medium density (MD) steel fibers (b), high density (HD) steel fibers (c), ultra-high density (UHD) steel fibers (d).

3.3.2. Basalt fibers

Basalt fibers were in the form of a balanced bi-axial mesh. Two different density of basalt fibers were employed, i.e. low-density basalt (LDB) fibers and high-density basalt (HDB) fibers. LDB fibers were spaced at 17 mm on center in both directions, while HDB fibers were spaced at 8 mm on center in both directions. The property of the basalt fibers, as reported by the manufacturer [6], are showed in Table 5.

Table 5. Properties of the basalt fibers provided by manufacturer [6].

Property	LDB fibers	HDB fibers
Sheet characteristic tensile stress [MPa]	> 1700	> 1700
Sheet elastic modulus [GPa]	> 70	> 70
Sheet break deformation [%]	> 1.90	> 1.90
Number of cords/cm	0.59	1.18
Mass (including heat-sealing) [g/m^2]	≈ 200	≈ 400

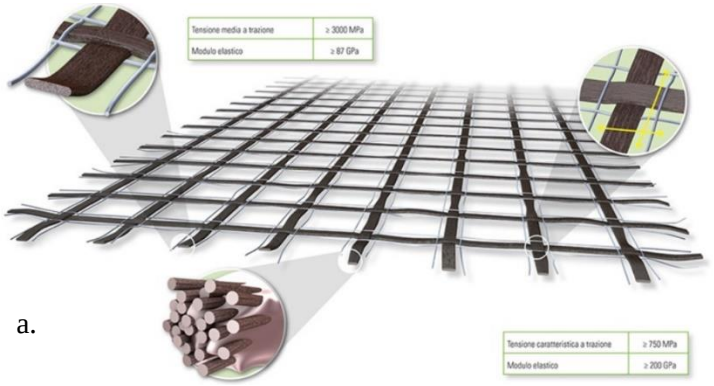

a.

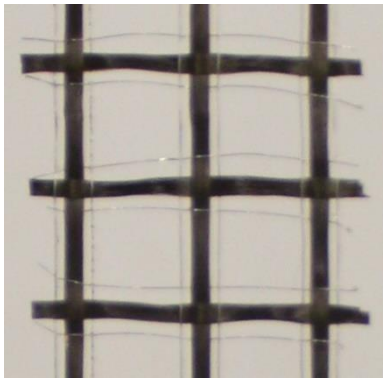

b.

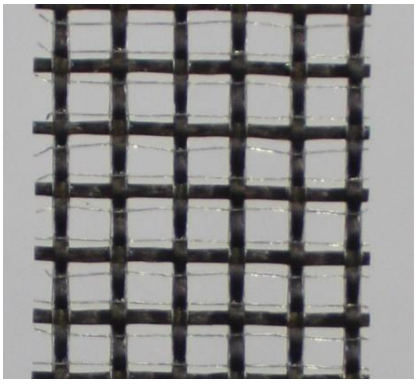

c.

Figure 31. Basalt fibers: sketch of the fiber sheet (a), low density basalt (LDB) fibers (b), high density basalt (HDB) fibers (c).

3.3.3. Epoxy matrix

The epoxy matrix is a two-component epoxy thixotropic gel system. The mechanical properties of the epoxy reported by the manufacturer [6] are provided in Table 6.

Table 6. Mechanical properties of the epoxy provided by manufacturer [6].

Property	
Tensile Strength, f_m [MPa]	> 14
Flexural Elastic Modulus, $E_{m,f}$ [GPa]	> 2.50
Elastic Modulus Under Compression, $E_{m,c}$ [GPa]	> 5.30

3.3.4. Mortar matrix

Two types of mortar matrices were employed in the experimental works described in the present dissertation, i.e. a lime-based mortar matrix and a cement-based mortar matrix. The lime-based mortar matrix was used for SRG or B-FRCM systems bonded to a masonry substrate, while the cement-based mortar matrix was used for SRG systems bonded to a masonry or a concrete substrate.

3.3.4.1. Lime-based mortar matrix

The lime-based mortar matrix was a hydraulic mortar made of lime and mineral binder with fine particle size developed for concrete and masonry applications and intended for highly breathable historical masonry restoration. Different batches of the lime-based mortar matrix were used to strengthen the masonry blocks and the concrete prisms. The mortar matrix of seven batches was characterized by performing fracture mechanics tests or flexural and compressive tests on mortar specimens casted with the same mortar used to strengthen the masonry blocks (Figure 32). The seven different batches are referred to as B1, B2, B3, and B4 in this dissertation and are reported in the name of the specimen. If the type of mortar batch is not present in the specimen name, the characterization of the mortar batch was not performed for that specimen, and the values provided by the manufacturer were considered. Fracture mechanics tests were performed on 300 mm length (L) × 70 mm width (b) × 70 mm depth (d) notched mortar prisms using the same test set-up adopted for concrete (see section 3.1.1.1). Flexural and compressive tests were performed on 40 mm × 40 mm × 160 mm mortar prisms according to [50]. The average value of the Mode-I fracture energy of the lime-based mortar matrix, $G_{F,I,lm}$, the flexural strength, f_{lmt}, and the compressive strength, f_{lmc}, are reported in Table 7 for the seven mortar batches considered.

The flexural strength, f_{lmt}, and the compressive strength, f_{lmc}, as reported by manufacturer [6] resulted equal to 5 MPa and 15 MPa, respectively.

Table 7. Mechanical properties of the lime-based mortar matrix.

Batch of mortar	Fracture energy [N/m]	Compressive strength, f_{lmc} [MPa]	Flexural strength, f_{lmt} [MPa]
B1	39 (0.21)	/*	/*
B2	/	10.70 (0.03)	3.02 (0.08)
B3	30	15.7 (0.04)	5.87 (0.13)
B4	29	11.3 (0.07)	5.18 (0.08)
B5	23	10.2 (0.05)	5.97 (0.06)
B6	/	13.2 (0.01)	5.40 (0.05)
B7	/	12.4 (0.01)	4.67 (0.04)

* If the value of the compressive strength, f_{lmc}, and flexural strength, f_{lmt}, of the mortar matrix are not specified, the value provided by the manufacturer [6] was considered.

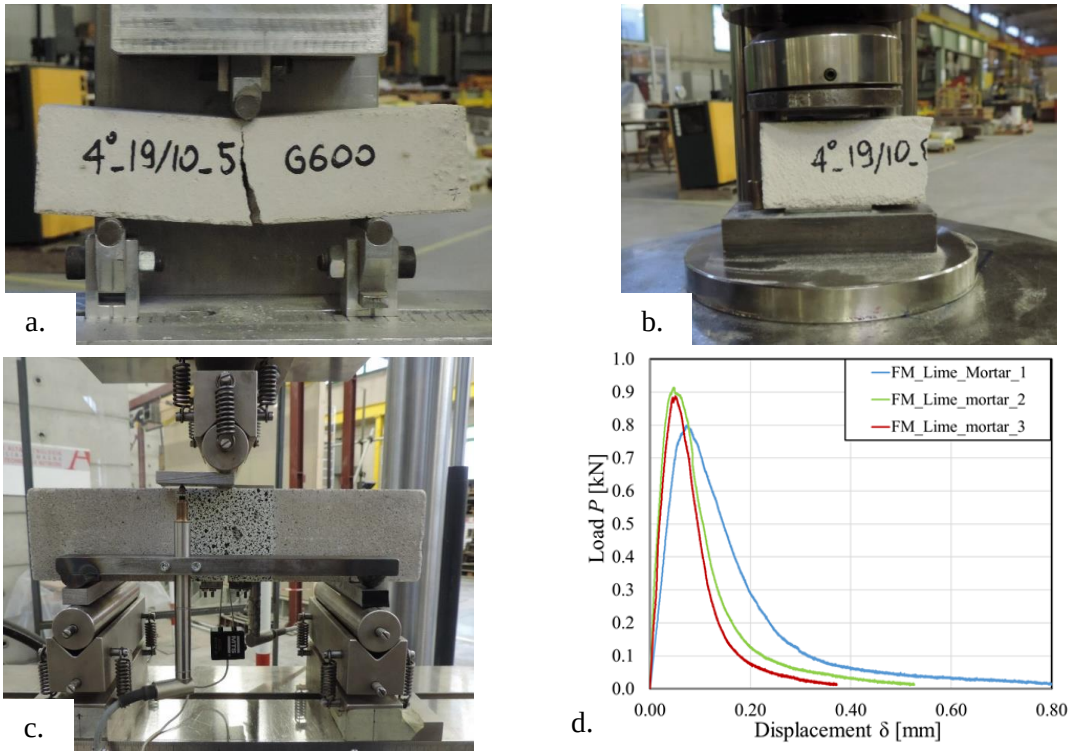

Figure 32. Lime-based mortar characterization: a) Three-point bending (TPB) test on a lime-based mortar prism; b) Compression test on a lime-based mortare cube; c) Fracture mechanics test on a notched lime-based mortar prism; d) Load-displacement responses obtained from fracture mechanics tests performed on notched mortar prisms.

3.3.4.2. Cement-based mortar matrix

The cement-based mortar matrix was a cementitious grout developed for concrete and masonry substrates. Different batches of the cement-based mortar matrix were used to strengthen the masonry blocks and the concrete prisms. The mortar matrix of one batch was characterized by performing fracture mechanics tests and flexural and compressive tests on mortar specimens casted with the same mortar used to strengthen the masonry blocks (Figure 33). The batch is referred to as C1 in this dissertation and is reported in the name of the specimen. If the type of mortar batch is not present in the specimen name, the characterization of the mortar batch was not performed for that specimen, and the values provided by the manufacturer were considered. Fracture mechanics tests were performed on three 300 mm length (L) × 70 mm width (b) × 70 mm depth (d) notched mortar prisms using the same test set-up adopted for concrete (see section 3.1.1.1). Flexural and compressive tests were performed on 40 mm × 40 mm × 160 mm mortar prisms according to [50]. The average value of the Mode-I fracture energy of the mortar matrix, $G_{F,I,cm}$, the flexural strength, f_{cmt}, and the compressive strength, f_{cmc}, of the mortar batch C1 are equal to 101 N/m (CoV 0.22), 7.61 MPa (CoV 0.09), and 46.40 MPa (CoV 0.03), respectively. The flexural strength, f_{cmt}, and the compressive strength, f_{cmc}, as reported by manufacturer [6] resulted equal to 50 MPa and 9 MPa, respectively.

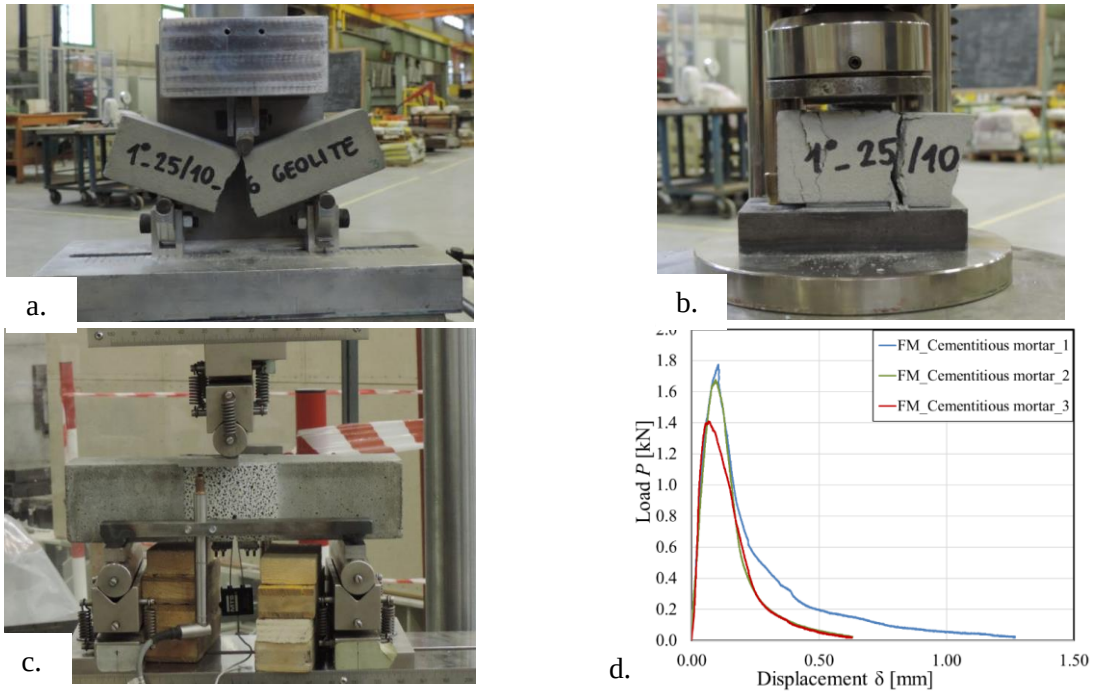

Figure 33. Cement-based mortar characterization: a) Three-point bending (TPB) test on a cement-based mortar prism; b) Compression test on a cement-based mortare cube; c) Fracture mechanics test on a notched cement-based mortar prism; d) Load-displacement responses obtained from fracture mechanics tests performed on notched mortar prisms.

3.3.5. Geopolymer matrix

Coal fly ash (FA), from the coal fired power station of Torrevaldaliga Nord (Rome, Italy), was used as precursor for geopolymerization. The FA is mainly constituted of silica and alumina (78.6 wt.% as reported in Table 8) and contains quartz, mullite, and maghemite as crystalline phase [51]. The amorphous content of FA is 65.32 ± 0.75 wt.% [52]. Aqueous solutions of sodium silicate (SiO_2/Na_2O ratio = 2.07, ρ = 1.53 g/cm^3) and sodium hydroxide (NaOH) were used as alkaline activators. Three different sodium hydroxide solutions with different molar concentrations (8M, 6M, and 4M) were prepared by dissolving solid sodium hydroxide pellets in deionized water. As fine aggregate, silica sand with maximum diameter d_{max} equal to 1 mm was used. To obtain the geopolymer matrix, fly ash (28.1 wt.%), sodium silicate solution (10.6 wt.%), and NaOH solution (2.1 wt.%) were introduced into a mixer. An extra amount of water (3.0 wt.%) was added to obtain a workable mixture. As a result, the liquid/fly ash ratio for all the three mixtures was equal to 0.56. The compound was mixed for 5 minutes after which sand (56.2 wt.%) was gradually added for the next 30 s. Afterward, mixing was performed for 30 s, then paused for 90 s, and resumed for additional 60 s in accordance with the procedure used in [53].

The geopolymer matrices were named GEO4, GEO6, and GEO8. These names refer to the three molar concentrations of NaOH solution used (i.e. molar concentration equal to 4M, 6M, and 8M).

One single batch of each geopolymer matrix was mixed and used to cast prisms and cylinders for the characterization of the geopolymer matrix as well as to construct FRGM composite strips for single-lap direct shear tests.

Table 8. Main oxide composition of fly ash.

	SiO_2	Al_2O_3	Fe_2O_3	CaO	MgO	SO_3	Na_2O	K_2O	LOI
Content (wt.%)	49.37	29.23	2.71	6.63	1.05	0.33	0.05	0.60	3.28

The workability of the geopolymer matrices was determined immediately after the compound was mixed according to EN 1015-3 [54]. Afterward, the slurry was poured into cylindrical and prismatic molds that were vibrated on a shaker. Cylinders had radius and height equal to 50 mm and 20 mm, respectively. The dimensions of the prisms were 40 mm × 40 mm × 160 mm. Molds were sealed in plastic bags and cured at T = 21 ± 2°C for 24 h after which the hardened cylinders and prisms were de-molded and cured in the same laboratory conditions until were used to determine the mechanical and physical properties of the matrices.

A slight improvement of workability of the mixtures was found as the molarity of the NaOH solution used decreases. Such a behavior can be ascribed to an increase of the content of water related to the

dilution of the NaOH solution when the molarity decreases. For the three matrices, the workability, which is expressed as consistency %, was determined to be between 55 and 65%, which was proved to be sufficient to cast FRGM composite strips. The effect of NaOH concentration on workability loss agrees with what reported by Singh et al. [55], who found a correlation between activator concentration and the time required for the formation of alkali aluminosilicate gels, i.e. the higher is the concentration, the faster is the workability loss.

Bulk density (ρ_{bulk}) and water absorption of the matrices were determined from the half prisms obtained from flexural tests at the age of 7 and 28 days; the former was determined by dividing the dry mass by the geometrical volume, the latter was obtained by soaking the dried prisms in water for 24h and was calculated as the difference of wet mass and dry mas divided by the dry mass. Cylinders were used to perform capillary water absorption tests according to EN 13057 [56] at the age of 7 and 28 days. The pore size distribution of samples (Figure 35b) extracted from the prisms at 28 days was investigated by means of mercury intrusion porosimetry (MIP, Carlo Erba 2000 instrument equipped with a macropore unit Model 120, Fison Instruments). Samples, which had a volume approximately equal to 1 cm^3, were cut by a diamond saw, dried under vacuum, and kept under a P_2O_5 dried atmosphere in a vacuum dry box until MIP was performed.

Regardless of NaOH molarity used, prisms cured for 7 days showed water absorption and bulk density values between 8.2 and 8.4% and 1.84 - 1.87 g/cm^3, respectively. At 28 days, the bulk density and water absorption increased and decreased, respectively, with increasing NaOH molarity (Figure 34). The GEO8 matrix showed the highest value of bulk density and the lowest water absorption among the three matrices. The influence of curing time on the development of the pore structure of the material is evident from capillary water absorption results. For the three matrices, cylinders cured for 7 days saturated after 10 minutes, whereas after 28 days, cylinders reached the saturation after approximately 185 minutes. The rate of saturation is similar among the three different matrices, both at 7 and 28 days. However, for cylinders that were cured for 28 days, the amount of water absorbed per unit area decreased when the molar concentration of NaOH increased, which confirms that the GEO8 matrix has a more compact and less porous structure than the GEO6 and GEO4 matrices. These results are in agreement with the results of bulk density and water absorption reported in Figure 34.

Those results were also confirmed by the MIP analysis performed on geopolymers at 28 days. The pore size distributions of samples are reported as a function of the specific volume of mercury intruded in the sample. For the three matrices, 40% of the total porosity corresponded to pores with a diameter in the range 0.1 – 1 μm, which are classified as capillary pores [57]. Among the three geopolymers, GEO8 exhibited the least porous microstructure. Similar pore size distributions were observed for GEO6 and

GEO4. The total open porosity (Pt [%]) and the average pore radius (r_m [µm]) decreased for the three geopolymers as follows: GEO4 (20.9%, 0.36 µm) > GEO6 (17.9%, 0.28 µm) > GEO8 (17.2%, 0.21 µm).

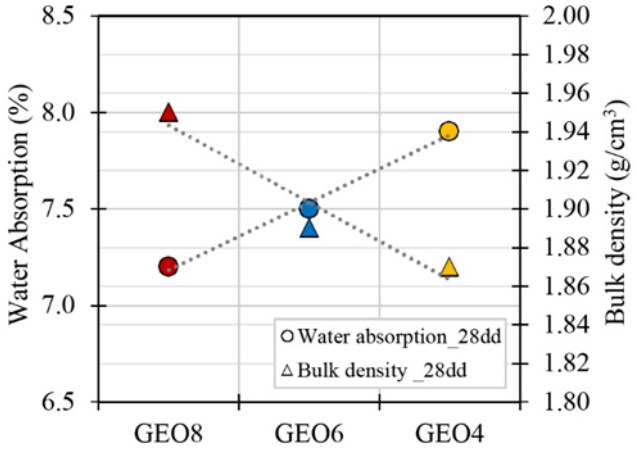

Figure 34. Water adsorption and bulk density of geopolymer matrices at 28 days.

Three-point flexural strength (R_f) and compressive strength (R_c) were determined according to EN 196-1 [58] by means of a 100 kN Amsler Wolpert testing machine after 7 and 28 days. 40 mm × 40 mm × 160 mm prisms were used. R_f and R_c are the average of three and five measurements, respectively. Prior to determining the mechanical properties, an evaluation of the dynamic modulus of elasticity was performed using a commercial ultrasonic testing instrument comprised of a pulse generator and two transducers (55 kHz) that were positioned at the two ends of 160 mm long prisms. Dynamic modulus of elasticity is reported as the average of three measurements.

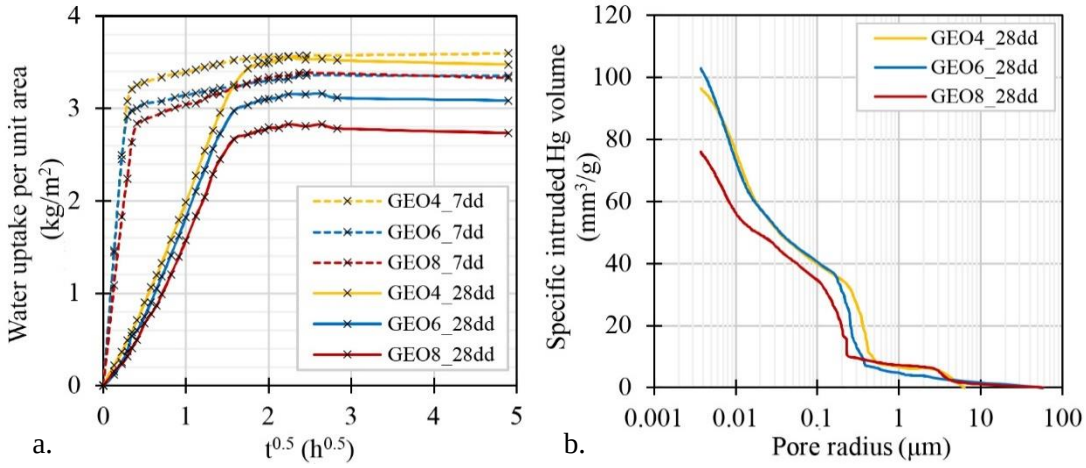

Figure 35. a) Capillary water absorption test results at 7 and 28 days; b) Pore size distributions of geopolymer matrices at 28 days.

The influence of both curing time and NaOH molar concentration on the mechanical properties of geopolymer can be observed in Figure 36. An increase of the strength was observed as a function of the curing time for all specimens tested. Figure 36 reports only the mechanical data at 7 and 28 days as these ages are the ones usually considered for mechanical characterization of cement based materials. At the age of 28 days, GEO8 achieved the highest values of both flexural (5.6 MPa) and compressive (33.6 MPa) strength among the three matrices; compressive strength decreased linearly with decreasing NaOH molar concentration. The same trend was obtained when the dynamic modulus of elasticity (E_d) was evaluated, which confirms a more compact and stiff structure of GEO8 compared to the GEO6 and GEO4. These results were somehow expected since previous studies on fly ash based geopolymers already assessed the importance of the NaOH concentration on the strength development [55] [59]. The NaOH activates the leaching of Si and Al of the fly ash; the higher is the NaOH concentration, the higher results the amount of leaching and the subsequent geopolymerization degree and mechanical properties of the geopolymer [59]. It is important to highlight that even if the physical and mechanical properties indicate that GEO8 is the best matrix among the three formulations investigated, the mechanical properties of both the GEO6 and GEO4 matrices are comparable to the properties of commercially available hydraulic binders used for strengthening applications of RC [60].

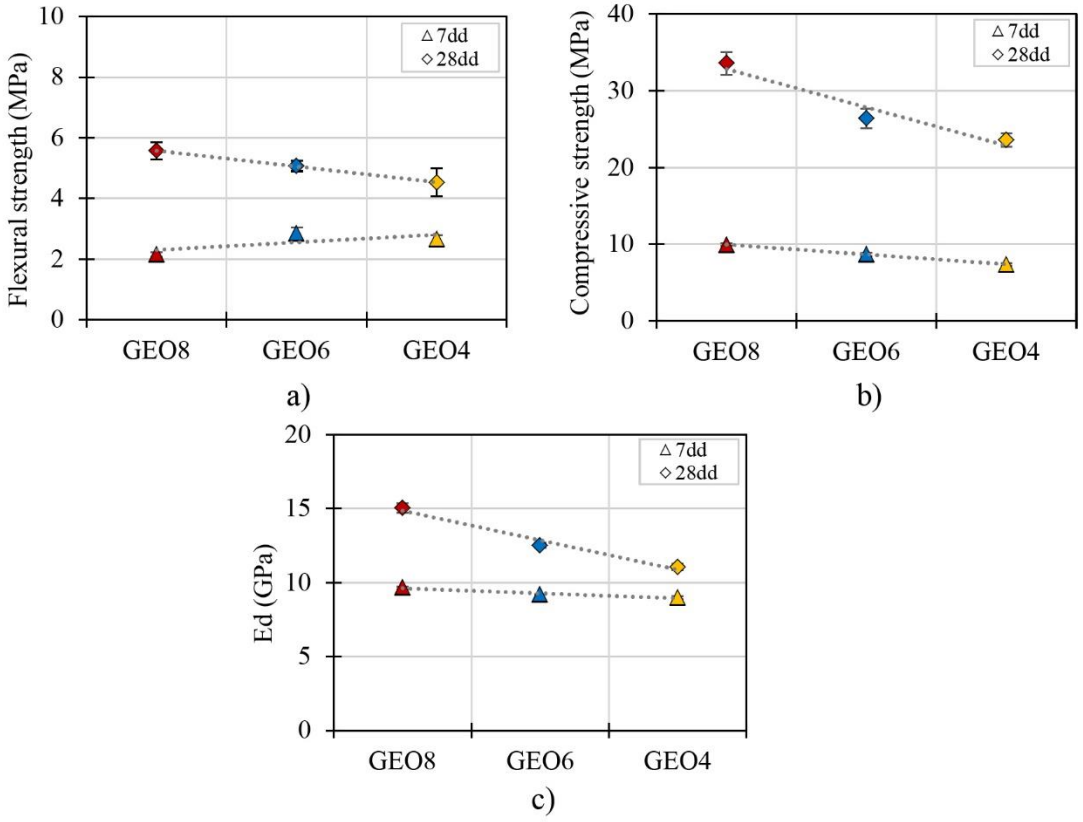

Figure 36. Flexural (a) and compressive (b) strength, and dynamic modulus of elasticity (c) of geopolymer matrices at 7 and 28 days.

Drying shrinkage of the three geopolymer matrices was investigated according to EN 12617-4 [61] using 40 × 40 × 160 mm prisms. The length of the prisms was measured at the age of 1, 3, 7, 14, 21, 28 and 56 days. Shrinkage was determined as the specific length variation, i.e. the change in length over the initial specimen length. The average of the specific length of three prisms for each age was used to study shrinkage for each matrix type.

Shrinkage behavior of the three geopolymer matrices is reported in Figure 37. GEO4 and GEO6 exhibit higher shrinkage than GEO8, however the values are in good agreement with data recently reported in the literature for geopolymers [62]. Moreover, when the FGRM strip was applied to concrete, no visual evidence of microcracks/crevices was observed on the hardened matrix (Figure 38), which indicates that shrinkage does not promote superficial damage.

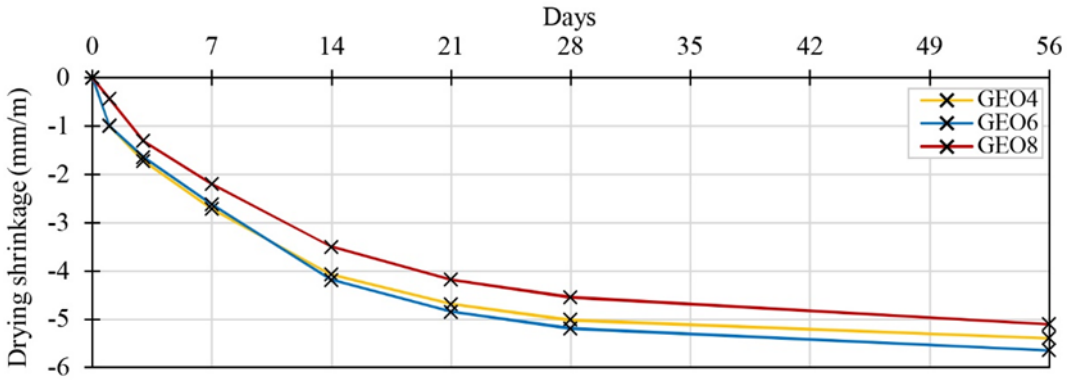

Figure 37. Drying shrinkage of geopolymer matrices.

Figure 38. Top portion of the bonded region of the composite strip applied to a concrete surface.

3.3.6. SRP composite

SRP composite strips consisting in HD steel fibers or UHD steel fibers embedded in the thermosetting epoxy resin described in section 3.3.3 were tested in tension. Three HD composite strips and three UHD composite strips were tested according to [63] (Figure 39). The composite strips were the same strips used to strengthen the concrete prisms, which were tested in tension after single-lap shear tests were performed. The tensile test results are reported in Table 9. The name of the composite strip reflects the name of the corresponding single-lap specimen (see Section 4.1.1.2 for the explanation of the nomenclature adopted) except for the suffix DS that has been substituted by T.

Table 9. Tensile test results of HD and UHD composite strips.

Composite strip	SRP Elastic Modulus referred to the area of the fibers $E_{f,SRP}^{HD}$ or $E_{f,SRP}^{UHD}$ [GPa]	Tensile strength of the composite referred to the area of the fibers $f_{f,u}^{A}$ [MPa]
T_300_50_HD_D_S_1	274	2983
T_300_50_HD_D_S_3	245	3110
T_300_50_HD_D_S_4	254	3088
T_300_50_UHD_D_B_3	255	2978
T_300_50_UHD_D_B_4	230	2673
T_300_50_UHD_D_B_5	225	2694

Note: $f_{f,u}^{A}$ is the tensile strength of the fibers. $E_{f,SRP}^{A}$ is the elastic modulus of the SRP strip referred to the area of fibers.

Superscript A represents the steel fiber density (LD = low density, MLD = medium low density, MD = medium density, HD = high density, UHD = ultra-high density).

The average elastic modulus for the HD $\left(\overline{E_{f,SRP}^{HD}}\right)$ and UHD $\left(\overline{E_{f,SRP}^{UHD}}\right)$ SRP composites referred to the area of fibers is equal to 258 GPa (CoV = 0.06) and 237 GPa (CoV = 0.07), respectively, while the average tensile strength (referred to the area of the fibers) for the HD fiber $\left(\overline{f_{f,u}^{HD}}\right)$ and the UHD $\left(\overline{f_{f,u}^{UHD}}\right)$ fiber composite is equal to 3060 MPa (CoV = 0.02) and 2782 MPa (CoV = 0.06), respectively. Digital image correlation was employed to determine the elastic modulus [64]. DIC images were taken only up to half of the ultimate tensile strength of the fibers in order to protect the DIC equipment, since the aim of the tensile test was to determine the elastic modulus in the initial branch of the stress-strain response. The elastic modulus was computed as the slope of the stress-strain response, between two fixed percentages

of the ultimate tensile strength of the fibers, i.e. 20% and 40%. The stress was calculated as load divided by the area of the steel fibers.

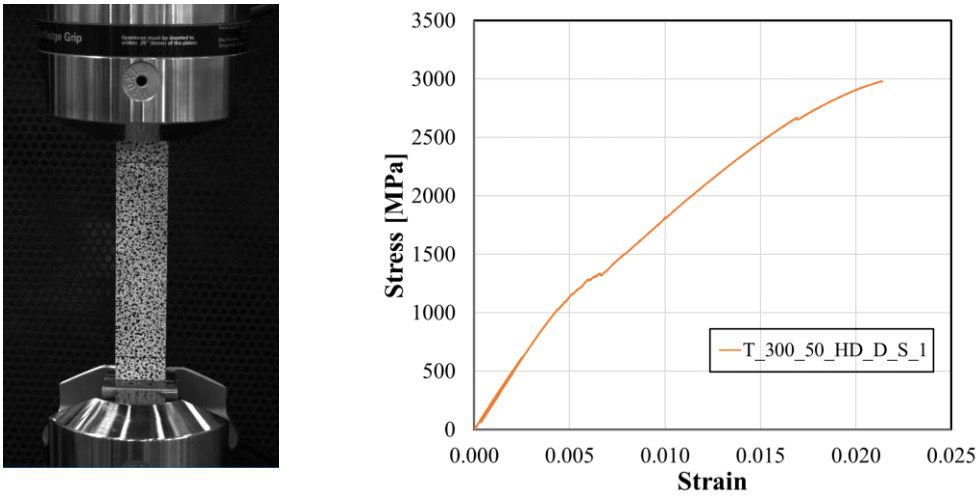

a. b.

Figure 39. a) Photo of the tensile test; b) Stress-strain response of composite strip T_300_50_HD_D_S_1 (Strain was obtained from the machine stroke).

3.3.7. SRG composite

Direct tensile tests were carried out to characterize SRG composites. Two types of SRG composites were characterized and consisted in LD steel fibers embedded in a lime-based mortar matrix and LD steel fibers embedded in a cement-based mortar matrix. Prismatic specimens were manufactured with aluminum molds and had a 10 mm-constant thickness and 600 mm length. The width of the mortar matrix was equal to 40 mm. Specimens were comprised of five fibers (cords), corresponding to a total area of the textile equal to 2.67 mm^2. The textiles were placed in the middle of the thickness taking care of ensuring their linearity. Each coupon was made individually, i.e. it was not cut from a larger plate. Specimens were demolded after 2-3 days and kept wet until 28 days had passed from manufacturing [65]. Specimens were stored in laboratory conditions for at least 7 days before testing. Five monotonic displacement controlled tests were carried out for each type of SRG composite. The displacement rate was 0.01 mm/s.

The coupons were gripped on the mortar, i.e. the entire composite width was clamped and the load was transferred to the textile through the matrix. In order to ensure a uniform load distribution and avoid mortar crushing in (or close to) the gripping regions, the ends of each specimen were reinforced by applying carbon textile bonded with epoxy resin (Figure 40). Specimens were gripped by the wedges of the testing machine, which apply a lateral pressure by a hydraulic clamping. The load was measured by the load cell integrated in the testing machine and divided by the cross-section area of the textile to

calculate the stress. Such conventional method to define stresses prevents the results from being affected by the variations of the mortar thickness, which are hardly controllable, especially in field applications. Displacements were recorded by an extensometer placed on the mortar matrix, with a measurement base equal to 200 mm excluding the gripping areas (Figure 42 and Figure 43). Average strains were then evaluated as the recorded displacement field divided by the base length of the device.

The stress-strain tensile behavior of the SRG systems (Figure 41), is characterized by three response stages: (I) un-cracked, in which the mortar matrix contributes to both load bearing capacity and stiffness; (II) crack development, during which crack pattern develops progressively; and (III) cracked, in which the crack pattern has completely developed. The same behavior can be observed in different types of mortar-based composites. The relevance of these three stages on the whole tensile behavior depends on a number of factors, including the tensile strength and the Young's modulus of the matrix, the layout of the fabric, and the fiber-to-mortar bond properties [66] [67] [68].

The results of direct tensile tests on SRG composites are the stress and strain of the transition points between stages I and II (σ_I, ε_I) and between stages II and III (σ_{II}, ε_{II}), the peak stress (f_t) and the corresponding load per unit width (F_t) and strain (ε_t), the Young's modulus in the three stages (E_I, E_{II}, E_{III}), the saturation crack spacing (d_s) and, finally, the failure mode (FM). Two failure modes were identified, such as rupture of the fibers (A) and sliding of the textile in the gripping area without tensile rupture (B). The transition point between stages I and II corresponds to the development of the first crack, identifiable in the response curve by the first stress drop, while the transition point between stages II and III correspond to the beginning of the branch with constant slope that continued until the rupture of the fibers. After the transition between stages II and III no load drops occur, except for the ones that correspond to the rupture of single fibers (observed for two lime-based SRG composites). E_I and E_{III} are easily calculable as the slope of the first and last portions of the response curve, respectively, while EII is computed through a linear regression of the irregular portion of the curve corresponding to stage II. The saturation crack spacing, defined as the mean distance between cracks in the last stage, provides information on the textile-to-matrix load transfer capacity and affects both the structural performance under shear loads and the durability of the system, as crack development exposes the textile to the aggression of the external environment.

Table 10. Results of tensile tests performed on SRG composites.

	σ_I [N/mm^2]	ε_I [%]	E_I [N/mm^2]	σ_{II} [N/mm^2]	ε_{II} [%]	E_{II} [N/mm^2]	f_t [N/mm^2]	F_t [kN/m]	ε_t [%]	E_{III} [N/mm^2]	d_s [mm]	FM
TT_Lime mortar_Steel_1	299	0.020	1495	248	0.081	\	2421	203	1.17	199	29	A
TT_Lime mortar_Steel_2	199	0.012	1692	376	0.198	95	\	\	\	\	55	B
TT_Lime mortar_Steel_3	294	0.014	2082	288	0.219	\	\	\	\	\	22	B
TT_Lime mortar_Steel_4	212	0.026	911	214	0.175	\	2620	220	1.38	200	25	B
TT_Lime mortar_Steel_5	394	0.017	2355	378	0.164	\	2733	230	1.35	199	23	A
TT_Cem. mortar_Steel_1	522	0.017	3122	489	0.286	\	2182	183	1.09	162	26	A
TT_Cem. mortar_Steel_2	506	0.017	2979	511	0.238	\	2744	230	1.31	173	27	A
TT_Cem. mortar_Steel_3	723	0.022	3287	469	0.187	\	2576	216	1.07	201	36	A
TT_Cem. mortar_Steel_4	520	0.023	2262	446	0.212	\	2813	236	1.57	174	34	A
TT_Cem. mortar_Steel_5	661	0.026	2544	575	0.202	\	2364	199	1.05	178	35	A

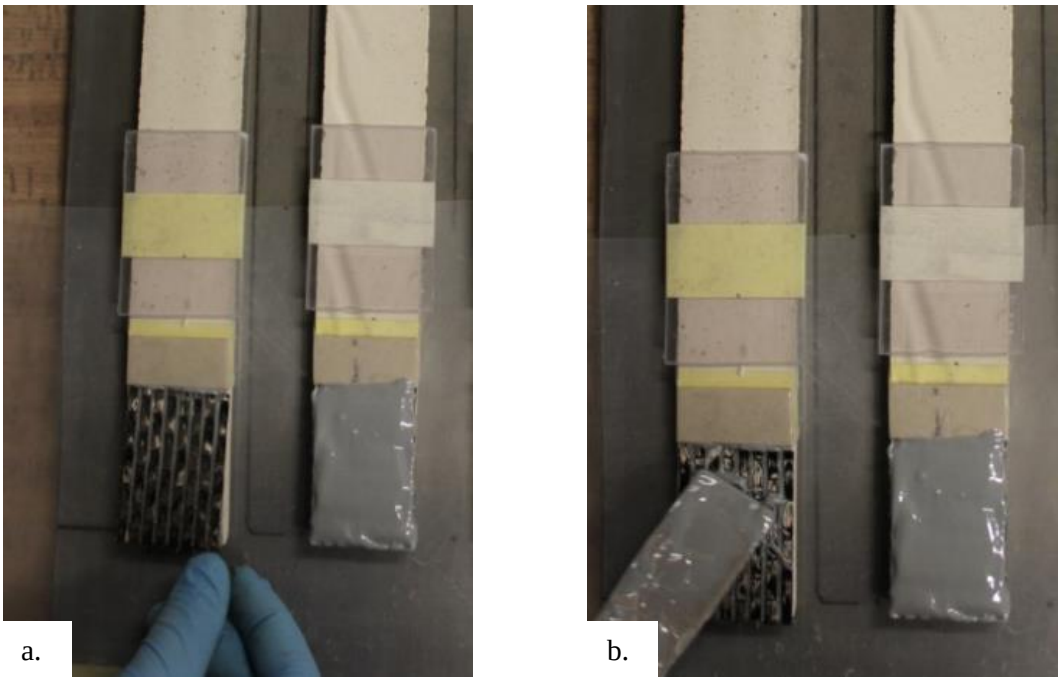

Figure 40. Application of carbon tabs to the ends of the SRG strip (a,b).

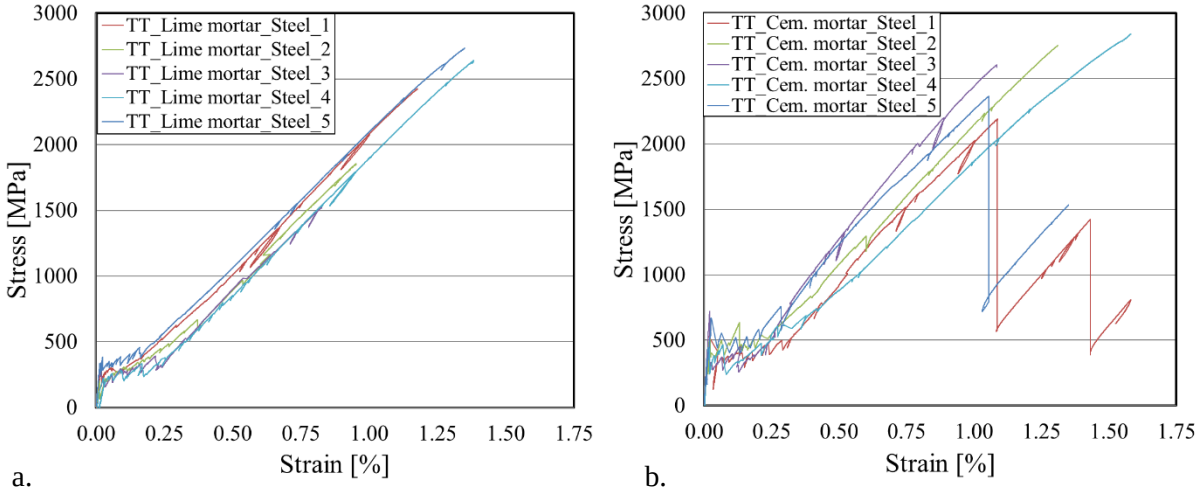

Figure 41. Stress strain responses of SRG strips tested in tension. The SRG composite consisted in LD steel fibers embedded in a lime-based (a) or cement-based (b) mortar matrix.

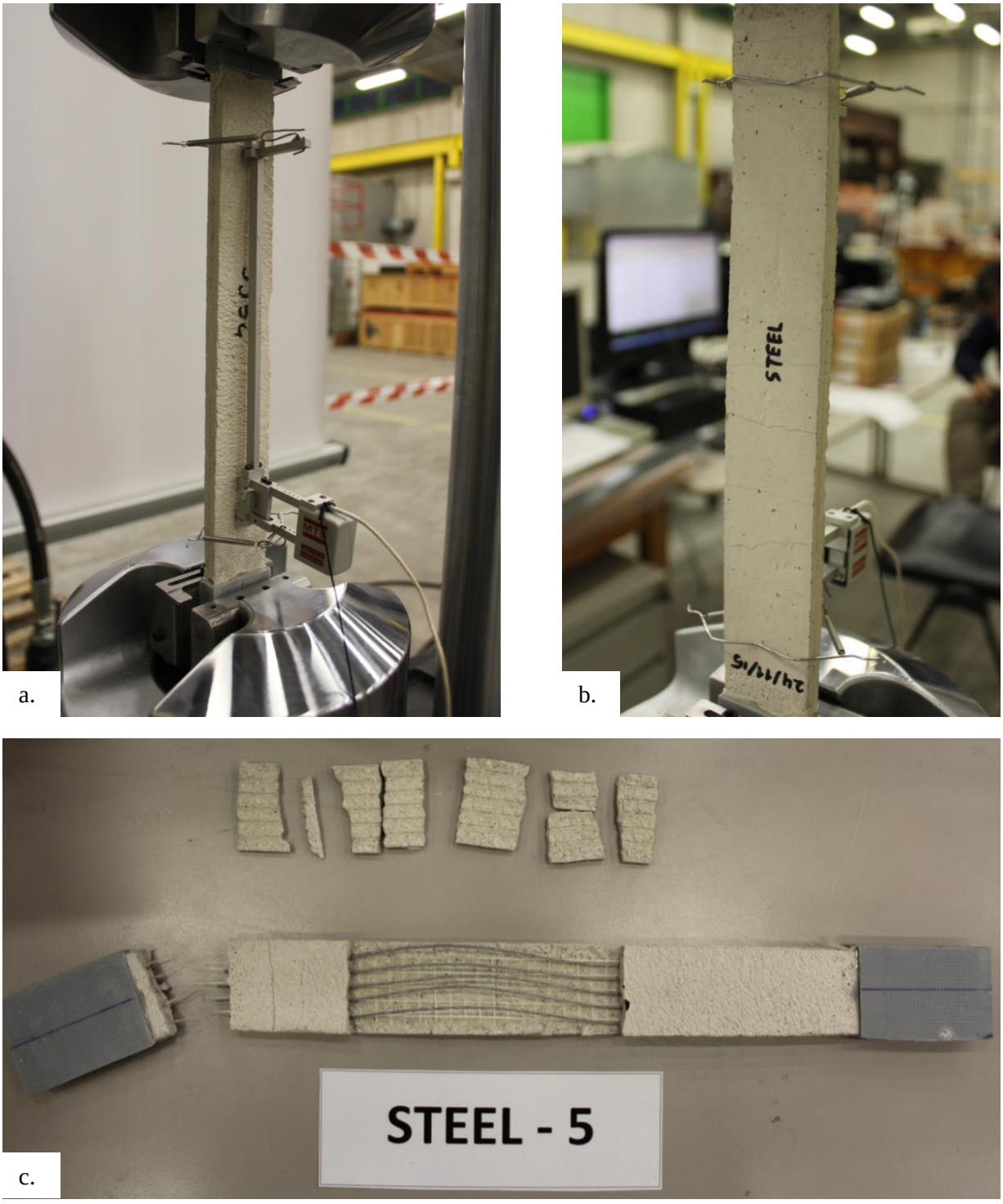

Figure 42. Tensile test on a SRG strip consisting in LD steel fibers embedded in a lime-based mortar matrix: a) Test set-up; b) Crack pattern in the mortar matrix during the test; c) Failure mode.

Figure 43. Tensile test on a SRG strip consisting in LD steel fibers embedded in a cement-based mortar matrix: a) Test set-up; b) Crack pattern in the mortar matrix during the test; c) Failure mode.

4. Bond between steel fiber reinforced composite materials and quasi-brittle interfaces

This chapter presents an investigation of the bond between steel fiber reinforced composite material and quasi-brittle substrates. The first section is focused on the study of the debonding phenomenon between composite materials and concrete substrates. SRP, SRG, and FRGM composites were bonded to a concrete surface and tested using a single-lap shear test set-up. The second section is focused on the study of the debonding mechanism in SRG-masonry joints. Masonry blocks with different bonded lengths and widths were tested in direct shear. Masonry blocks were also subjected to salt degradation in order to investigate the effect of the salt attack on the bond performances.

4.1 Bond between steel fiber reinforced composite materials and a concrete substrate

In this section the bond performances of several composite materials bonded to a concrete surface will be investigated. SRP composites were bonded to a concrete substrate and tested in direct-shear varying several parameters, i.e. the density of steel fibers, the bonded width, and the face to which the composite strip was applied. Bond tests on SRP systems were also performed using a three-point bending set-up. A numerical analysis is implemented to simulate the debonding phenomenon in SRP-concrete joints. SRG composites were applied to a concrete surface in order to investigate the effect of the different fiber densities on the load responses and failure modes. Finally, an experimental investigation on FRGM systems bonded to concrete substrates is presented in order to show the suitably of a newly developed geopolymer matrix for bond applications.

4.1.1 SRP-concrete joints

4.1.1.1 Background

In the field of structural rehabilitation of existing buildings, composite materials stood out as one of the most employed strengthening technique of the last decades. In particular, the large use of fiber reinforced polymer (FRP) composites used to increase the strength of an existing structural member, is mainly due to the several advantages associate with FRPs when compared with traditional strengthening systems. Some of the key features that has determined the large spread of FRP systems are the high strength-to-weight ratio, the ease of installation, and the possibility to design the arrangement of the fibers to fit the

design needs of a specific application. Recently, a new type of composite material has been developed for strengthening applications, which employs high-strength steel fibers embedded in a thermosetting epoxy resin. Steel reinforced polymer (SRP) composites, also known as steel fiber reinforced polymer (SFRP) composites, are a promising strengthening technique that owes its success to the low cost of the steel fibers with respect to the most common fibers employed in traditional FRP systems (carbon, glass, or aramid) and the possibility of bending the fibers without the need of chamfering the edges of columns [69] and beams [70]. SRP composites have been successfully applied to reinforced concrete beams [71] [72] [73] [74] [75] [76] [77] [78] [79] and slabs [80], and plain and reinforced concrete columns [81] [82] [69], showing that they can increase the capacity of the structural member and its ductility.

In this section the bond behavior of SRP-concrete joints is studied. Single-lap shear tests are performed to determine the interfacial cohesive material law (CML), which is the relationship between the interfacial shear stress and the slip between the composite and the substrate when a fracture mechanics mode-II loading condition at the interface is assumed. SRP strips are bonded to one face of concrete prisms. Digital image correlation (DIC) is employed to obtain the longitudinal strain profile along the SRP strip, which is then used to determine directly the CML. Three different functions are used to fit the strain profile, which allow for obtaining three different CMLs. Parameters that are considered in this study are the density of the steel fibers (cords), the face of the concrete prism to which the composite is applied (i.e., the face opposite or the face adjacent to the face used to cast the prism), and the width of the composite strip. Results of single-lap shear tests are compared with results of six notched beam tests [83] in terms of bond capacity. The influence of the bonded width, the face to which the composite strip is applied, and the fiber density are analyzed. In addition, an alternative method to determine the interfacial fracture energy, i.e. the area under the CML function, is proposed. Finally, a numerical analysis is performed in order to simulate the bond between SRP systems and concrete substrates.

4.1.1.2 Experimental program

All concrete prisms of this experimental program were cast from the same batch of concrete, i.e. "Concrete – Type A" (see section 3.1.1). The SRP composite consisted in steel fibers (described in section 3.3.1) embedded in a thermosetting epoxy resin (described in section 3.3.3). The property of the composite strip are described in section 3.3.6.

Fifty-seven specimens were tested using a single-lap shear test set-up in order to evaluate the stress-transfer mechanism in SRP-concrete joints. All concrete prisms have the same nominal dimensions equal to 150 mm (*width*) × 150 mm (*depth*) × 600 mm (*length*). In this paper the width of the concrete prism is named *b*, as shown in Figure 44. Prior to applying the composite material, all specimens were sandblasted with silica sand. The SRP composite strips were applied using a wet lay-up process, following the

manufacturer's recommendations [6]. After casting, the composite strips were left to cure for seven days at room temperature and humidity. SRP strips were applied approximately between 300 and 350 days after the concrete prisms were cast.

Three main parameters were investigated in this study: the side to which the composite strip is applied, the width b_f of the composite strip, and the density of the steel fibers. The side to which the SRP strip was applied was varied in order to fully understand the width effect and interpret the results published in the literature. Six different bonded widths of the SRP strips were used to strengthen the concrete specimens, i.e. nominally 15 mm, 30 mm, 40 mm, 50 mm, 75 mm, and 90 mm. Out of 57 specimens, 51 specimens had a nominal bonded length equal to 300 mm, while 6 specimens had a nominal bonded length equal to 200 mm. The nominal thickness of the SRP strip was equal to 4 mm. Fiber sheets with three different densities were investigated in this section: medium density (MD), high density (HD), and ultra-high density (UHD) steel fibers. The steel fibers were arranged across the width of the SRP strip in order to have a distance between the external fibers and the edges of the matrix equal to half of the fiber spacing. Since the actual dimensions of the SRP strips slightly differed from the nominal ones, the actual bonded width, $b_{f,actual}$, and the actual thickness, t_{SRP}, are reported in Table 11 for each specimen. The value of $b_{f,actual}$ and t_{SRP} for each specimen were obtained as the average of three measurements made in the unbonded region of the SRP strip, after single-lap shear tests were performed. The bonded region started 70 mm from the top edge of the concrete prism, in order to provide an initial notch. Fibers were embedded in the matrix for the entire length of the strip, including the portion outside from the bonded area. In this work, the portion of the SRP strip clamped by the grips of the testing machine is referred as loaded end, while the opposite edge of the composite strip is referred as free end.

The faces of the concrete prisms were classified in two different types. The side (S) face was one of the two rectangular formed faces adjacent to the screeded (or casting) face, while the bottom (B) face was the formed face opposite to the screeded face Figure 44c. SRP strips were applied on both S and B faces. All specimens were tested using a direct single-lap shear test set-up using a servohydraulic universal machine. The classical push pull configuration was adopted where the concrete prism was restrained against two steel plates and the SRP strip was pulled Figure 44a-b. Two linear variable differential transformers (LVDTs) were mounted on the concrete surface close to the beginning of the bonded area. The LVDTs (LVDT a and LVDT b in Figure 44a) reacted off of a thin aluminum Ω-shaped plate that was glued directly to the SRP strip at the beginning of the bonded area. The average value of the LVDTs is referred to as global slip, g, in this paper, and was used to control the test at a constant rate. Out of 57 specimens, 54 were tested at a rate equal to 0.00084 mm/s (which is considered as the standard rate in this study), while 3 specimens were tested at a rate equal to 0.0084 mm/s. Two additional LVDTs, named LVDT c and LVDT d, were placed in the back of the prism and were mounted horizontally in order to

measure the out of plane displacements, w_c and w_d, respectively (Figure 44d). LVDT c and LVDT d reacted off of the face of the concrete prism opposite to the one where the SRP strip was applied and were fixed to the bottom plate of the test set-up using two magnets (Figure 44d). A pre-compression load was applied to the concrete prism before single-lap shear tests were performed. Three strain gages were mounted along the longitudinal direction of each bar at 120° apart one another. The average measurement of the three strain gages was used to determine the tensile stress on each bar at the beginning of the test and for the entire duration of the test.

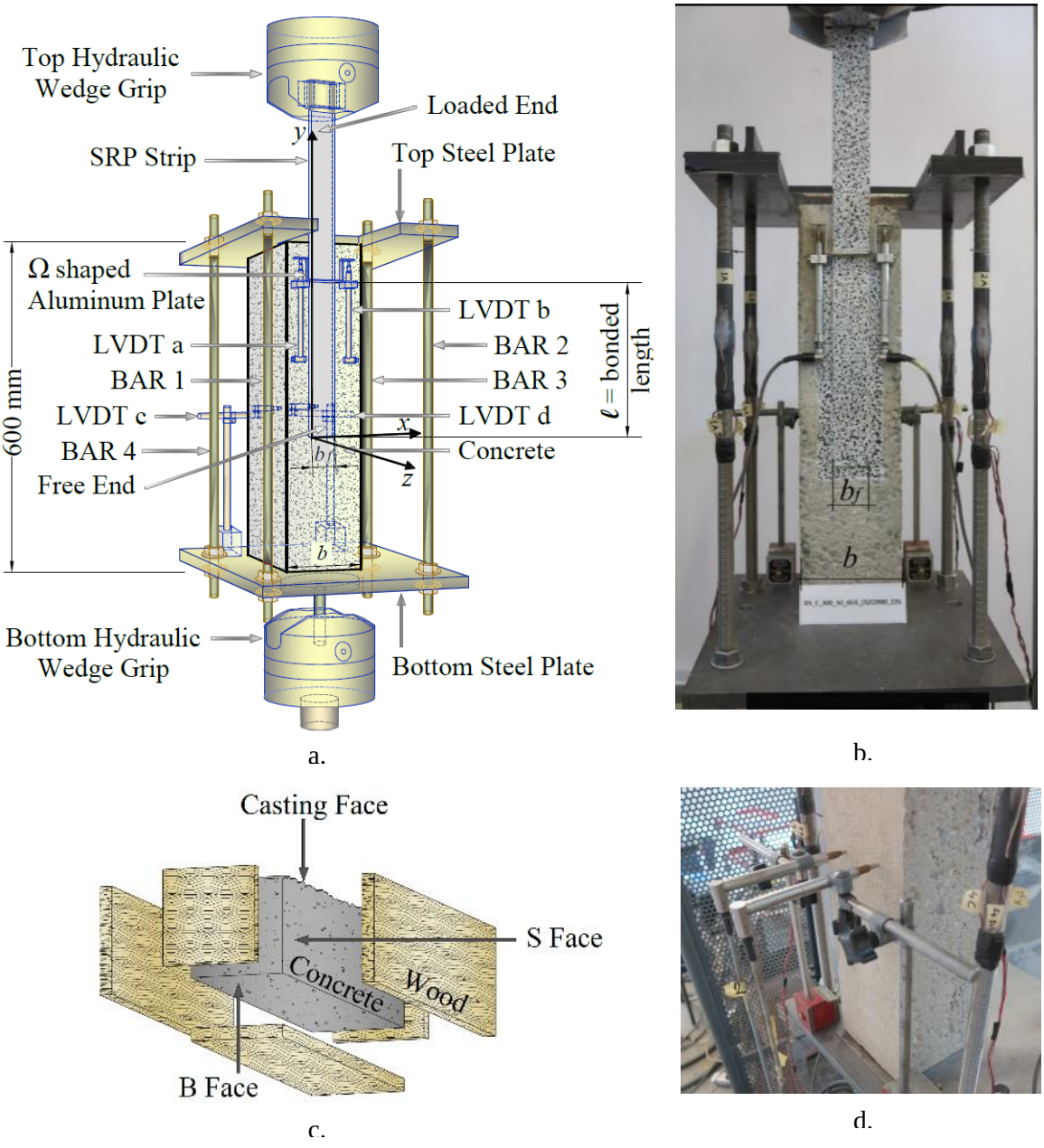

Figure 44. a) Single-lap shear test set-up; b) Photo of specimen DS_300_50_HD_D_B_2; c) Sketch of the casting procedure and definition of the faces of the prism; d) Photo of LVDT c and d.

Based on the tensile stress measured from strain gages, the same pre-compression (1 MPa) was applied to each specimen at the beginning of the test. For 42 specimens, digital image correlation (DIC) was used to measure the displacement field and, consequently, determine the strain field on the SRP strip and adjacent concrete surface. In order to perform the DIC measurements, the surface of the SRP strip and of the concrete region close to the edges of the composite strip were painted with a white paint and hatched with black points.

Specimens were named following the notation DS-X-Y-A-B-C-E-Z, where X = bonded length (ℓ) in mm; Y = bonded width (b_f) in mm; A represents the steel fiber density (MD = medium density, HD = high density, UHD = ultra-high density); B indicates the use of DIC in the test (D = DIC, ND = no DIC); C denotes the face of the prism to which the SRP strip was applied (B = bottom, S = side); E (if present) indicates that the loading rate was different from the standard rate (0.00084 mm/s) used for the majority of the specimens (10R = ten times the standard rate); and Z = specimen number (Table 11).

Table 11. Characteristics of the single-lap shear test specimens.

Specimen Name	Concrete face	SRP strip			Fibers	DIC
		Actual Bonded width $b_{f,actual}$ [mm]	Actual Thickness t_{SRP} [mm]	Density	Number of cords	
DS_300_15_HD_D_S_1	S	18	4.4	HD	8	✓
DS_300_15_HD_D_S_2	S	17.5	4.6	HD	8	✓
DS_300_15_HD_D_S_3	S	18	4.4	HD	8	✓
DS_300_15_HD_D_S_4	S	18	5.4	HD	8	✓
DS_300_15_HD_D_S_5	S	18	4.3	HD	8	✓
DS_300_15_HD_D_B_1	B	18	4.2	HD	8	✓
DS_300_15_HD_D_B_2	B	18	4.3	HD	8	✓
DS_300_30_HD_D_S_1	S	30	4.5	HD	14	✓
DS_300_30_HD_D_S_2	S	29	4.4	HD	14	✓
DS_300_30_HD_D_S_3	S	32	4.5	HD	14	✓
DS_300_30_HD_D_S_4	S	32	4.5	HD	14	✓
DS_300_30_HD_D_S_5	S	31	4.5	HD	14	✓
DS_300_30_HD_ND_B_1	B	32	4.3	HD	14	×
DS_300_30_HD_D_B_2	B	31.5	4.9	HD	14	✓
DS_300_30_HD_D_B_3	B	31.5	4.6	HD	14	✓
DS_300_40_HD_D_S_1	S	43	4.8	HD	19	✓
DS_200_40_HD_D_S_2	S	40	4.2	HD	19	✓
DS_200_40_HD_D_S_3	S	40	4.1	HD	19	✓
DS_200_40_HD_D_S_4	S	40	4.3	HD	19	✓
DS_300_40_HD_ND_B_1	B	42	4.8	HD	19	×
DS_300_40_HD_D_B_2	B	42	4.6	HD	19	✓

DS_300_40_HD_D_B_3	B	41.5	4.6	HD	19	✓
DS_300_50_HD_D_S_1	S	51.0	4.3	HD	24	✓
DS_300_50_HD_D_S_2	S	52.0	4.6	HD	24	✓
DS_300_50_HD_D_S_3	S	50.0	4.2	HD	24	✓
DS_300_50_HD_D_S_4	S	52.0	4.2	HD	24	✓
DS_300_50_HD_D_S_5	S	52.0	4.7	HD	24	✓
DS_200_50_HD_ND_S_6	S	52.5	4.5	HD	24	×
DS_200_50_HD_D_S_7	S	53.5	4.5	HD	24	✓
DS_300_50_HD_ND_S_10R_1	S	53.0	3.9	HD	24	×
DS_300_50_HD_D_S_10R_2	S	53.0	4.3	HD	24	✓
DS_300_50_HD_D_S_10R_3	S	53.0	4.2	HD	24	✓
DS_300_50_HD_ND_B_1	B	52.0	4.3	HD	24	×
DS_300_50_HD_D_B_2	B	52.0	4.6	HD	24	✓
DS_300_50_HD_D_B_3	B	52.5	4.5	HD	24	✓
DS_200_50_HD_D_B_4	B	52.5	4.2	HD	24	✓
DS_300_75_HD_D_S_1	S	75	4.2	HD	36	✓
DS_300_75_HD_D_S_2	S	76.5	4.0	HD	36	✓
DS_300_75_HD_D_S_3	S	74.5	4.4	HD	36	✓
DS_300_75_HD_D_S_4	S	75	4.0	HD	36	✓
DS_300_75_HD_ND_B_1	B	74.5	4.7	HD	36	×
DS_300_75_HD_D_B_2	B	76	4.4	HD	36	✓
DS_300_75_HD_D_B_3	B	76	4.3	HD	36	✓
DS_300_90_HD_D_B_1	B	94	4.0	HD	44	✓
DS_300_90_HD_ND_B_2	B	93	4.2	HD	44	×
DS_300_90_HD_D_B_3	B	92	4.4	HD	44	✓
DS_300_50_MD_ND_B_1	B	49.0	4.4	MD	15	×
DS_300_50_MD_ND_B_2	B	48.0	4.3	MD	15	×
DS_300_50_MD_ND_B_3	B	48.5	4.6	MD	15	×
DS_300_50_UHD_ND_S_1	S	51.0	4.4	UHD	35	×
DS_300_50_UHD_ND_S_2	S	51.5	4.5	UHD	35	×
DS_300_50_UHD_ND_S_3	S	51.0	4.5	UHD	35	×
DS_300_50_UHD_ND_B_1	B	50.5	4.5	UHD	35	×
DS_300_50_UHD_ND_B_2	B	52.0	4.5	UHD	35	×
DS_300_50_UHD_D_B_3	B	50.0	4.3	UHD	35	✓
DS_300_50_UHD_D_B_4	B	52.5	4.2	UHD	35	✓
DS_300_50_UHD_D_B_5	B	50.0	4.2	UHD	35	✓

Note: Specimens for which DIC was employed were marked with a tick (✓) in the DIC column.

Six concrete prisms 600 mm length (L) × 150 mm width (b) × 150 mm depth (d) were tested using a TPB set-up. All specimens had a central notch with a U-shaped tip. The notch length a_0 was equal to half of the depth d. The net span S was equal to three times the depth of the specimen. The SRP strip was applied to the bottom face (B face) of the prism, which was the face where the prism was notched. The SRP strip

was centered with respect to the bottom face of the prism. The bonded width (b_f) was equal to 50 mm, while the bonded length was equal to 180 mm on each half of the block across the notch. An unbonded length of 10 mm on each side of the notch was used to avoid spalling of the edge of the notch. The nominal thickness of each layer of matrix was 2 mm, thus, the total nominal thickness of the composite strip was equal to 4 mm. Three beams were strengthened with MD steel fibers, while three specimens were strengthened with HD steel fibers. The test set-up was similar to the one used for fracture mechanics tests except for the clip-on gage that was omitted because of the presence of the SRP strip (see section 3.1.1.1). The average of LVDT a and b (shown in Figure 45) measurements represents the vertical deflection δ of the point load and was used to control the test. The test rate was equal to 0.0005 mm/s. Specimens were named following the notation TPB-X-Y-A-C-Z (Table 12), where symbols were used according to the notation of single-lap shear tests. Figure 45a shows a sketch of the set-up; a photo of specimen TPB_360_50_MD_B_1 is shown in Figure 45b. Table 12 provides the details of each specimen.

Table 12. Characteristics of notched beam test specimens.

Specimen Name	Face of the prism	SRP strip			Fibers
		Actual bonded width $b_{f,\text{actual}}$ [mm]	Actual thickness t_{SRP} [mm]	Density	Number of cords
TPB_360_50_MD_B_1	B	52	4.6	MD	15
TPB_360_50_MD_B_2	B	52.5	4.4	MD	15
TPB_360_50_MD_B_3	B	51.5	4.4	MD	15
TPB_360_50_HD_B_1	B	52.5	4.6	HD	35
TPB_360_50_HD_B_2	B	51	4.3	HD	35
TPB_360_50_HD_B_3	B	51.5	4.5	HD	35

Note: All specimens were tested at a rate equal to 0.0005 mm/s.

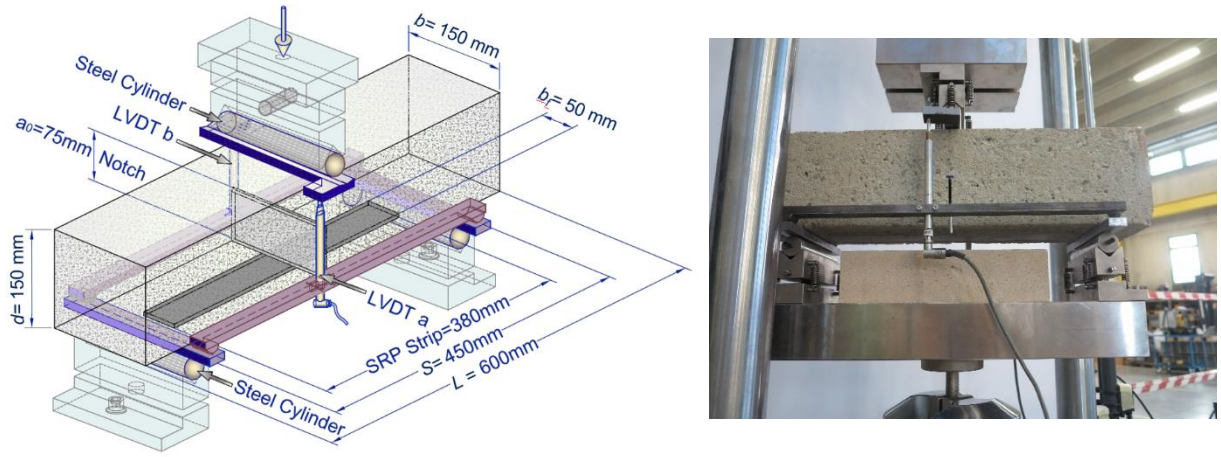

a. b.

Figure 45. Three-point bending test of notched beams: a) Test set-up; b) Photo of specimen TPB_400_50_MD_B_1.

4.1.1.3 Load responses

The load responses of single-lap shear tests are plotted in Figure 46 for representative specimens, characterized by different fiber densities and different faces of the concrete prism to which the SRP strip was applied. In addition, the load per unit width-global slip responses of representative specimens cast with different bonded widths of the SRP strip are reported in Figure 47, both for S-face and B-face specimens. An idealized load response is sketched in Figure 46a.

The initial linear response is followed by a non-linear branch until the peak load, P^*, is reached. A drop in the load after the peak marks the onset of the interfacial crack propagation. As the crack propagates, the load remains nominally constant and the average value, P_{crit}, is determined as the mean value of the load corresponding to the range of the global slip [g_1-g_2]. The peak load P^* is generally greater than P_{crit} because the interfacial crack requires additional energy to be created rather than to self-similarly propagate. The global slip range [g_1-g_2] varies slightly for each test. The range is determined on the basis of the strain analysis results (presented in section 4.1.1.6) for specimens in which DIC was employed, while it is identified directly on the load-global slip response for the remaining specimens. For specimens without DIC, the slip g_1 was evaluated by considering the point in the load response where a substantial drop of the load was observed after the peak load was reached. For the same specimens, the slip g_2 was determined as the point in the load response at the beginning of the last ascending branch of the response, which is associated with the presence of Mode-I (see section 4.1.1.4). For all specimens strengthened with a 15 mm width SRP strip, the global slip range [g_1,g_2] was determined directly on the load-global slip response, because for these specimens it was not possible to analyze properly the strain behavior along the SRP strip due to the limited width of the SRP strip (see section 4.1.1.5).

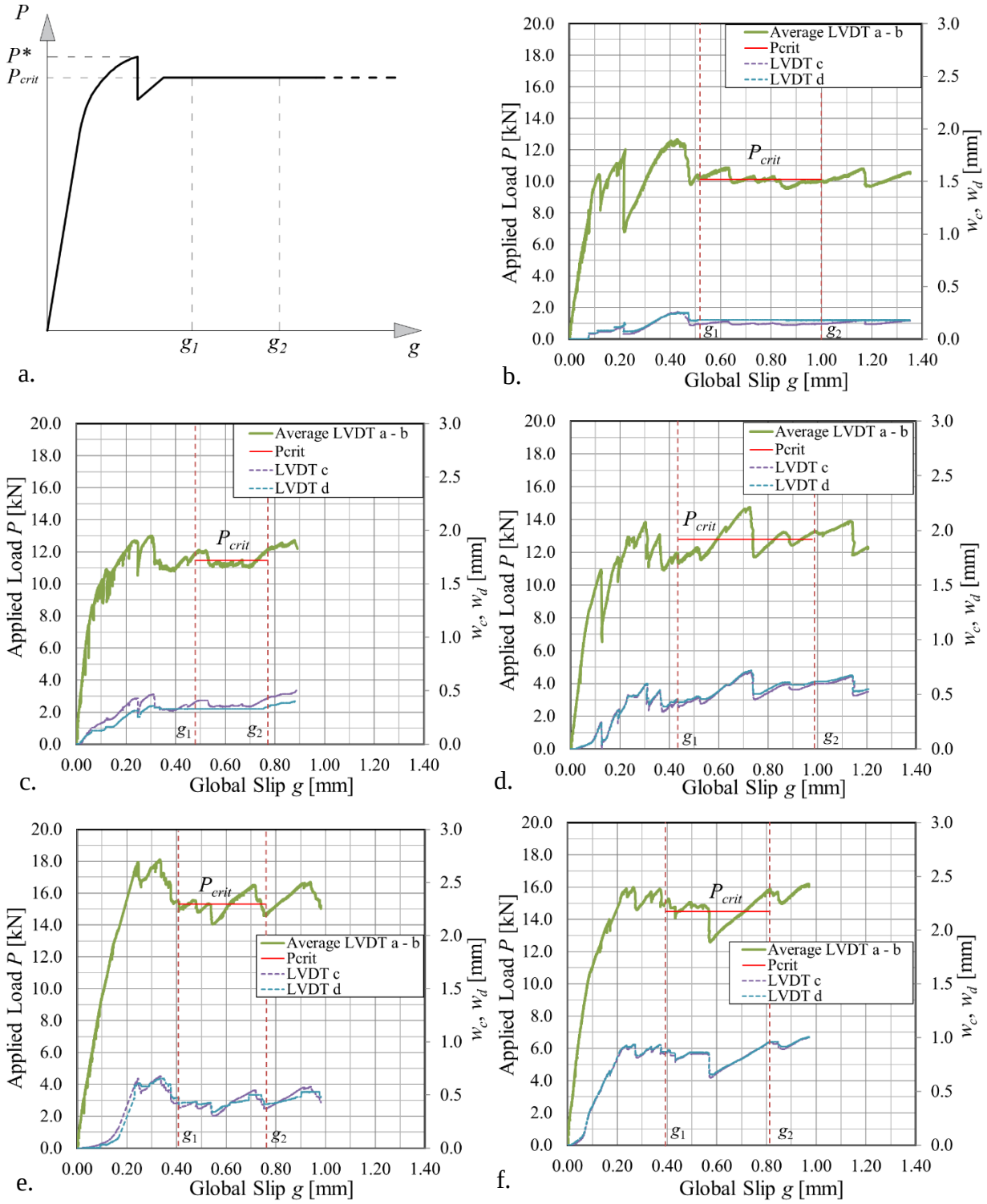

Figure 46 a) Idealized applied load *P*-global *g* slip response for SRP-concrete joints; b) Load response of specimen: b) DS_300_50_MD_ND_B_2; c) DS_300_50_HD_D_S_5; d) DS_300_50_HD_ND_B_1; e) DS_300_50_UHD_ND_S_3; and f) DS_300_50_UHD_D_B_5.

Specimens DS_300_15_HD_D_B_1 and DS_300_15_HD_D_B_2 showed a different failure mode with respect to all the other specimen (see section 4.1.1.4). For these specimens, the crack started to develop in the concrete substrate. As the residual bonded length was approximately 100 mm, crack propagation shifted from the substrate to the matrix-fibers interface. The initial crack in the concrete substrate was associated with a first part of the load response similar to other specimens, characterized by a drop that corresponded to the start of the crack propagation at the concrete surface Figure 47b. After the drop, the load remained constant within a limited range of the global slip, and then continued to increase until failure. The second portion of the load response, characterized by an increasing branch, corresponded to the propagation of the crack at the matrix-fiber interface. The value of P_{crit} for specimens DS_300_15_HD_D_B_1 and DS_300_15_HD_D_B_2 was evaluated within the range of the global slip where the load remained approximatively constant. The load P_{crit} is often termed load-carrying capacity. Figure 46b-f provide a representative load response for each fiber density bonded to B face or S face of the prism. Test results are summarized in Table 13. The average value of P_{crit} for specimens characterized by the same width of the SRP strip, the same fiber density, and the same side to which the composite strip is applied was referred as $\overline{P}_{crit}^{Y,A,C,E}$. Superscripts Y, A, C, and E (if present) are defined in section 4.1.1.2. The displacements measured by LVDT c and LVDT d are named w_c and w_d, respectively. The average values of w_c and w_d between g_1 and g_2 are named $\overline{w_c}$ and $\overline{w_d}$ and reported in Table 13.

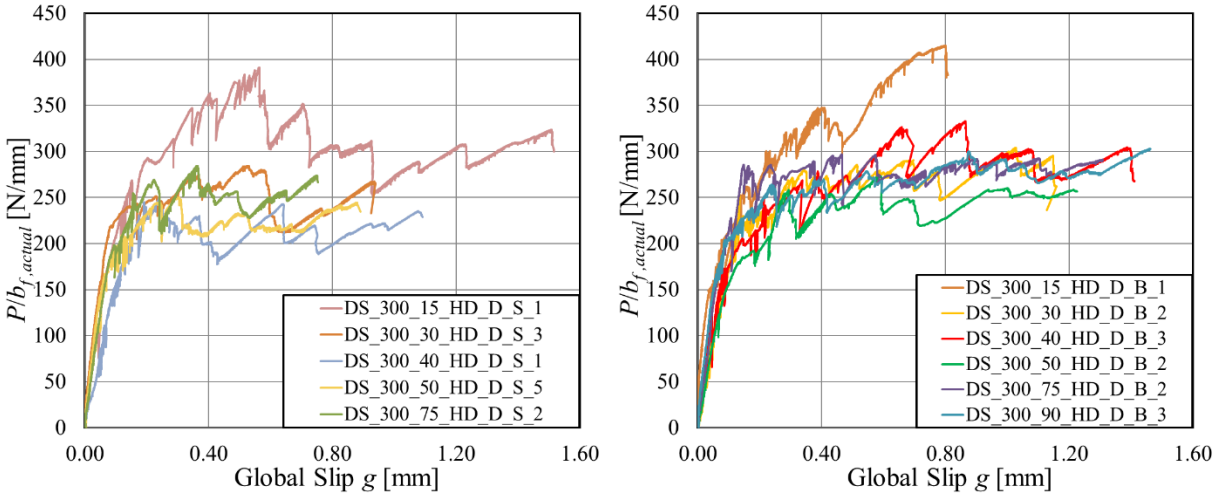

Figure 47. Load response of representative specimens: a) S-face specimens; b) B-face specimens.

Table 13. Test results of single-lap direct shear tests

Specimen Name	g_1 [mm]	g_2 [mm]	P^* [kN]	P_{crit} [kN]	$\overline{P}_{crit}^{Y,A,C}$ [kN]	$\overline{w}_c$ [mm]	$\overline{w}_d$ [mm]
DS_300_15_HD_D_S_1	0.60	1.23	7.04	5.37		0.05	0.03
DS_300_15_HD_D_S_2	0.46	0.72	5.26	4.40	$\overline{P}_{crit}^{15,HD,S}$	0.00	0.01
DS_300_15_HD_D_S_3	0.65	1.21	6.23	5.37	4.82	0.07	0.02
DS_300_15_HD_D_S_4	0.38	0.65	5.12	4.45		0.00	0.00
DS_300_15_HD_D_S_5	0.62	1.19	5.16	4.51		0.00	0.00
DS_300_15_HD_D_B_1	0.42	0.52	7.47	5.78	$\overline{P}_{crit}^{15,HD,B}$	0.05	0.06
DS_300_15_HD_D_B_2	0.47	0.52	7.28	5.73	5.76	0.03	0.07
DS_300_30_HD_D_S_1	0.41	0.92	8.44	7.50		0.00	0.02
DS_300_30_HD_D_S_2	0.42	0.84	8.05	7.20	$\overline{P}_{crit}^{30,HD,S}$	0.00	0.00
DS_300_30_HD_D_S_3	0.62	0.91	9.11	7.50	7.06	0.04	0.00
DS_300_30_HD_D_S_4	0.40	1.02	7.64	6.71		0.02	0.00
DS_300_30_HD_D_S_5	0.41	0.91	8.50	6.39		0.01	0.04
DS_300_30_HD_ND_B_1	0.27	0.75	10.60	8.76	$\overline{P}_{crit}^{30,HD,B}$	0.14	0.20
DS_300_30_HD_D_B_2	0.70	1.01	9.57	8.58	8.83	0.08	0.05
DS_300_30_HD_D_B_3	0.78	1.16	11.44	9.16		0.19	0.12
DS_300_40_HD_D_S_1	0.66	0.98	11.09	9.01		0.10	0.15
DS_200_40_HD_D_S_2	0.21	0.46	11.32	9.01	$\overline{P}_{crit}^{40,HD,S}$	0.09	0.06
DS_200_40_HD_D_S_3	0.21	0.42	10.04	8.50	8.89	0.07	0.06
DS_200_40_HD_D_S_4	0.25	0.46	9.82	9.05		0.14	0.12
DS_300_40_HD_ND_B_1	0.42	0.94	14.17	11.63	$\overline{P}_{crit}^{40,HD,B}$	0.16	0.17
DS_300_40_HD_D_B_2	0.50	0.92	12.60	10.99	11.57	0.16	0.20
DS_300_40_HD_D_B_3	0.68	1.38	13.81	12.09		0.38	0.42
DS_300_50_HD_D_S_1	0.39	0.78	14.45	12.25		0.29	0.41
DS_300_50_HD_D_S_2	0.64	1.02	13.82	12.27		0.13	0.07
DS_300_50_HD_D_S_3	0.48	0.80	13.15	11.92	$\overline{P}_{crit}^{50,HD,S}$	0.06	0.13
DS_300_50_HD_D_S_4	0.49	0.81	12.33	10.44	11.98	0.25	0.29
DS_300_50_HD_D_S_5	0.48	0.77	13.01	11.47		0.49	0.40
DS_200_50_HD_ND_S_6	0.36	0.60	15.70	13.07		0.44	0.58
DS_200_50_HD_D_S_7	0.33	0.80	14.10	12.45		0.78	0.68
DS_300_50_HD_ND_S_10R_1	0.60	1.10	15.70	13.87	$\overline{P}_{crit}^{50,HD,S,10R}$	0.52	0.40
DS_300_50_HD_D_S_10R_2	0.65	1.20	19.34	15.48	14.57	0.68	0.70
DS_300_50_HD_D_S_10R_3	0.44	1.20	17.50	14.37		0.75	0.70
DS_300_50_HD_ND_B_1	0.44	0.98	14.76	12.78		0.70	0.72
DS_300_50_HD_D_B_2	0.47	0.96	14.22	12.64	$\overline{P}_{crit}^{50,HD,B}$	0.54	0.48
DS_300_50_HD_D_B_3	0.43	0.85	13.89	12.28	13.02	0.34	0.47
DS_200_50_HD_D_B_4	0.39	0.81	15.71	14.39		0.40	0.54
DS_300_75_HD_D_S_1	0.35	0.92	19.71	17.23	$\overline{P}_{crit}^{75,HD,S}$	0.87	0.88
DS_300_75_HD_D_S_2	0.58	0.96	17.34	15.10	16.94	0.52	0.50

DS_300_75_HD_D_S_3	1.10	2.38	22.06	18.69		1.07	1.15
DS_300_75_HD_D_S_4	0.74	0.93	19.88	16.76		0.87	0.87
DS_300_75_HD_ND_B_1	0.70	1.48	21.79	20.25	$\overline{P}_{crit}^{75,HD,B}$ 20.57	0.69	1.21
DS_300_75_HD_D_B_2	0.97	1.45	22.56	21.68		1.63	1.54
DS_300_75_HD_D_B_3	0.55	1.05	22.08	19.79		1.47	1.34
DS_300_90_HD_D_B_1	0.56	1.21	28.44	25.77	$\overline{P}_{crit}^{90,HD,B}$ 24.83	2.08	2.18
DS_300_90_HD_ND_B_2	0.42	0.90	25.37	23.37		1.45	1.43
DS_300_90_HD_D_B_3	0.47	1.10	27.88	25.37		1.68	1.63
DS_300_50_MD_ND_B_1	0.42	0.83	13.09	11.48	$\overline{P}_{crit}^{50,MD,B}$ 10.81	0.36	0.31
DS_300_50_MD_ND_B_2	0.52	1.00	12.69	10.14		0.15	0.18
DS_300_50_MD_ND_B_3**	0.68	1.12	16.14	12.41		0.58	0.60
DS_300_50_UHD_ND_S_1	0.41	0.79	15.17	13.73	$\overline{P}_{crit}^{50,UHD,S}$ 14.52	0.29	0.40
DS_300_50_UHD_ND_S_2**	0.63	1.04	20.74	17.63		0.66	0.70
DS_300_50_UHD_ND_S_3	0.41	0.76	19.29	15.31		0.42	0.43
DS_300_50_UHD_ND_B_1	0.45	0.87	18.11	16.29	$\overline{P}_{crit}^{50,UHD,B}$ 15.64	0.61	1.09
DS_300_50_UHD_ND_B_2	0.46	0.75	19.55	16.13		0.76	0.92
DS_300_50_UHD_D_B_3	0.46	0.80	17	16.07		0.88	0.86
DS_300_50_UHD_D_B_4	0.32	0.74	17.32	15.24		0.99	1.19
DS_300_50_UHD_D_B_5	0.39	0.81	16.21	14.49		0.81	0.82

**Test was not used to determine the average value of the load-carrying capacity because of the failure mode.

The load responses of TPB tests performed on notched concrete prisms strengthened with MD steel fibers and HD steel fibers are represented in Figure 48a and Figure 48b, respectively. The load responses of TPB tests feature a trend similar to the response of single-lap shear tests, although the constant load branch (or plateau) appears to be shorter in notched beam test responses with respect to single-lap shear test responses because the bonded length is shorter.

It should be noted that the evaluation of the debonding force in notched beams depends on whether fracture of concrete occurs prior to debonding of the SRP strip or simultaneously. DIC analysis (not reported in this paper for sake of brevity) performed on specimen TPB_360_50_HD_B_3 suggests that the crack in concrete propagated from the initial notch to the extrados of the prism before the SRP strip completely detached from the concrete substrate. Because of compatibility, when the notch opens by a certain amount the slip at the beginning of the bonded area should be equal to half of the opening of the notch (if the strip on both sides debonds symmetrically). The magnitude of the opening of the notch when the concrete crack reaches the extrados can be obtained from fracture tests performed on concrete prisms from the same batch of concrete (see section 3.1.1.2). The crack mouth opening displacement (CMOD) values obtained at failure for notched concrete beams tested in section 3.1.1.2 is approximately double the slip of the steel fibers when debonding initiated in a single-lap shear test, which correspond to the last point of the CML that will be presented and discussed in the next sections. Based on this observation,

which confirms that the crack in concrete reached the extrados prior to the debonding of the strip, the force P_d in the SRP needed to detach the strip from concrete was evaluated as:

$$P_d = \frac{P_{max} S}{4d} \tag{13}$$

Where S and d represent the net span and the depth of the concrete prism, respectively. It should be noted that for notched beam tests, the difference between the plateau and maximum load (P_{max}) was small (except for specimen TPB_360_50_MD_B_3). Thus, the maximum load (P_{max}) was used in Equation (13).

Table 14 summarizes the results of the tests on notched beams strengthened with SRP strips.

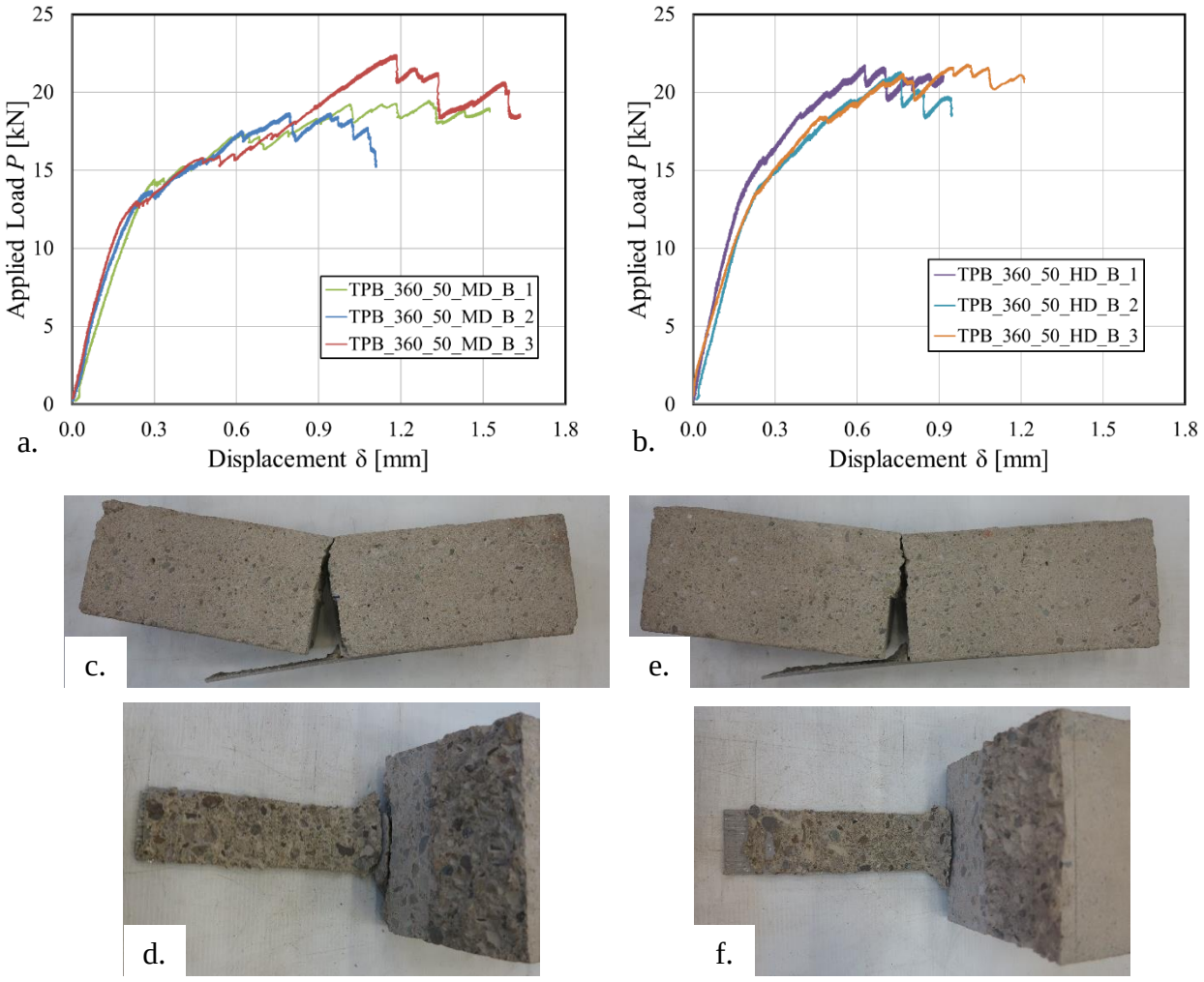

Figure 48. a) Load responses for notched beam specimens with MD fibers tested in TPB; b) Load response for notched beam specimens with HD fibers tested in TPB. Failure mode of specimen TPB_360_50_MD_B_1 (c and d). Failure mode of specimen TPB_360_50_HD_B_1 (e and f).

Table 14. Test results of TPB tests on notched beams strengthened with SRP strips.

Specimen Name	P_{max} [kN]	P_d [kN]	$\overline{P_d}$ [kN]
TPB_360_50_MD_B_1	19.48	14.55	14.28
TPB_360_50_MD_B_2	18.68	14.01	
TPB_360_50_MD_B_3**	22.41	16.70	
TPB_360_50_HD_B_1	21.76	16.25	16.15
TPB_360_50_HD_B_2	21.33	15.96	
TPB_360_50_HD_B_3	21.79	16.23	

**The test was not used to compute the average because of the failure mode.

4.1.1.4 Failure modes

The failure mode of all single-lap shear test specimens was debonding of the SRP strip from concrete, which always occurred in a thin mortar-rich layer of concrete, where the epoxy impregnates the substrate Figure 49. The thickness of the layer of concrete attached to the composite strip was between 1 mm and 2 mm. At the free end (i.e., the end of the strip opposite to where the load was applied), a bulb of concrete remained attached to the composite strip due to the presence of Mode-I. The detachment of the concrete bulb from the substrate determines an increase in the amount of energy needed to fully detach the strip, which causes an ascending branch in the last portion of almost all the load-responses. The presence of an ascending branch in the last part of the response was used to define g_2 for those specimens without DIC analysis.

Specimens DS_300_50_MD_ND_B_3 and DS_300_50_UHD_ND_S_2 showed a slightly different type of failure, characterized by the propagation of the crack at the fiber-matrix interface in limited regions of the bonded area. This type of failure was probably due to a wrong impregnation of the steel fibers within the epoxy matrix during the application of the strips and affected both the values of global slip and the transferable force at the SRP-concrete interface. The aforementioned specimens will not be considered in the remainder of the paper. Therefore, they will not be used to compute the average of the load-carrying capacity.

Specimens DS_300_15_HD_D_B_1 and DS_300_15_HD_D_B_2 showed a mixed failure mode, characterized by the detachment of the SRP strip from the concrete substrate in the first 100 mm of bonded length and by the crack propagation at the matrix-fiber interface for the remaining part of the bonded area (Figure 50). The propagation of the crack at the matrix-fiber interface can be due to the presence of Mode-

I. The Mode I fracture process entailed for a different crack path in the concrete substrate when the crack propagation is close to the free end, i.e. the crack propagated deeper in the concrete substrate in the last portion of the bonded region. Since, as observed above, the presence of Mode I determined a greater load in the last portion of the load-response, it is possible that for specimens with a narrow strip the fracture propagated at the fiber-matrix interface because it required a lower load than the one needed to continue to fracture the concrete substrate through the detachment of a large bulb of concrete.

a.

b.

c.

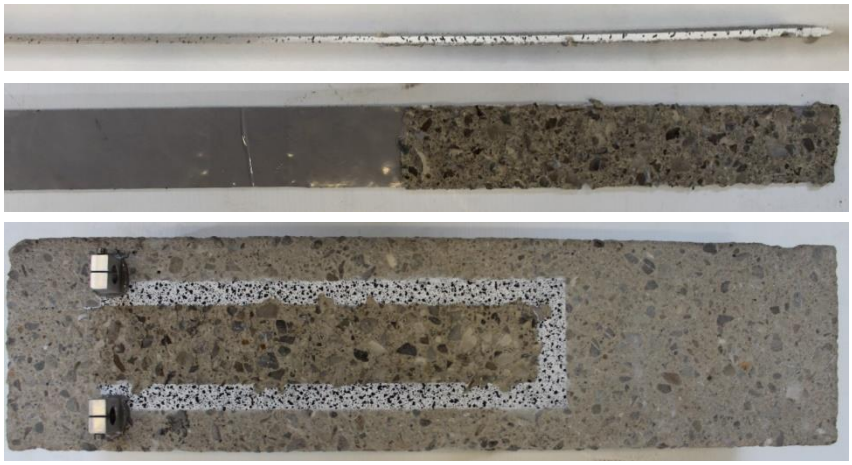

Figure 49. Failure mode for specimen DS_300_50_UHD_D_B_4: a) Side view of the SRP strip; b) Fracture surface on the SRP strip; c) Concrete substrate.

a.

b.

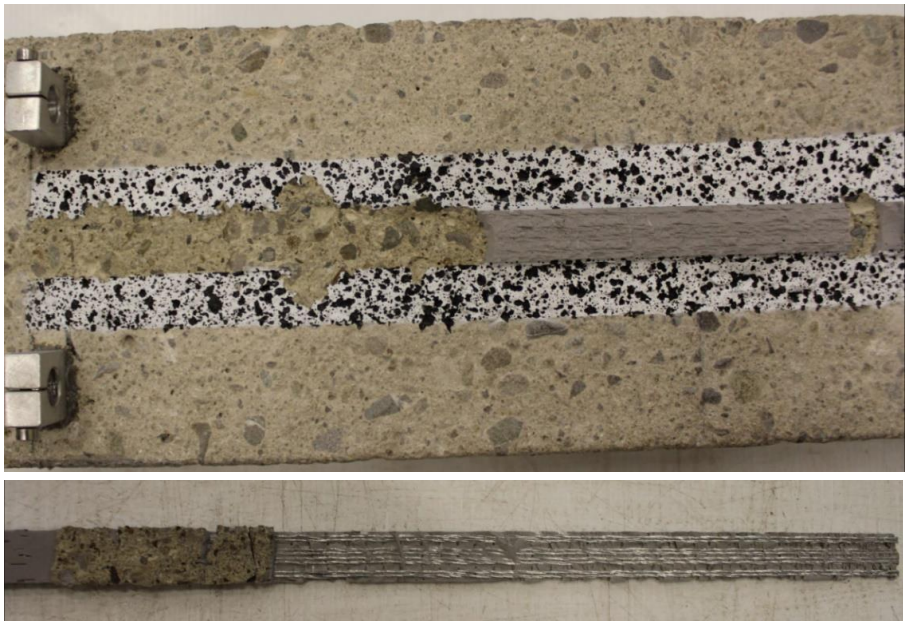

Figure 50. Failure mode for specimen DS_300_15_HD_D_B_1: a) Concrete substrate; b) Fracture surface on the SRP strip.

It can be observed that for B-face specimens, the amount of large aggregates that remains attached to the SRP strips is larger than the one for S-face specimens, for which the concrete that remains attached to the composite is rich in small aggregates. Figure 51 compares the distribution of the aggregates in the layer of concrete attached to the SRP strips after tests were performed for specimen DS_300_75_HD_D_S_2 and specimen DS_300_75_HD_ND_B_1. From this comparison, it appears that during casting a large amount of aggregates concentrated near the B-face of the prism with respect to the S-face. The influence of the face to which the composite strip is applied on the load responses will be discussed in sections 4.1.1.11 and 4.1.1.12.

a.

b.

Figure 51. Fracture surface of specimen DS_300_75_HD_D_S_2 (a) and specimen DS_300_75_HD_ND_B_1 (b).

The failure mode of all notched beams tested using a TPB set-up was the debonding of the composite strip from one side of the notch. It is worth noting that debonding of the SRP strip from the concrete substrate initiated on each side of the notch, although full propagation occurred only on one side. A thin layer of concrete was attached to the debonded portion of the composite strip at failure. Near the notch, a concrete wedge formed due to the limited extension of the unbonded length. The wedge extended for approximately 10-20 mm along the bonded length and then crack propagation continued at the SRP-concrete interface Figure 48c-f. Even though debonding occured mainly on one side, the wedge formed on both sides of the notch. Notwithstanding specimen TPB_360_50_MD_B_3 showed the same type of failure, the concrete wedge that detached from the side of the notch where debonding occurred was larger with respect to other tests. A larger wedge entails for a higher amount of energy needed to fracture

concrete close to the notch and leads to a higher value of the maximum load P_{max} as shown in Figure 48a and Table 14. Figure 52 shows in red the large concrete wedge detached from the right side of specimen TPB_360_50_MD_B_3 with respect to the concrete wedge (in green) detached from the left side. Specimen TPB_360_50_MD_B_3 will not be considered in the remainder of the paper.

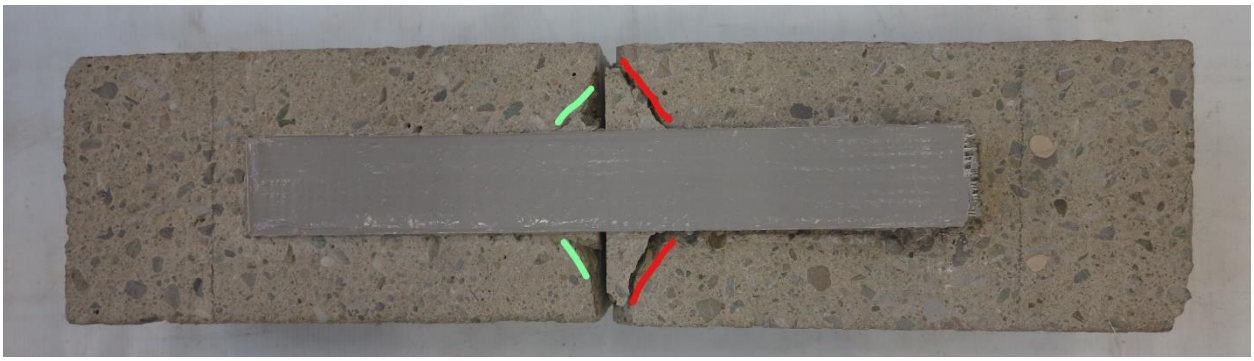

Figure 52. Failure mode for specimen TPB_360_50_MD_B_3

4.1.1.5 Longitudinal strain across the composite width

Digital image correlation (DIC) was employed to determine the displacement and consequently obtain the strain fields on the composite surface and on the portion of concrete surface close to the composite edges. The displacement field was determined using a 5-pixel step size, which implies a spacing between two consecutive points equal to 1.67 mm. DIC analysis was performed using three different subsets (i.e. 21, 31, and 41 pixels), in order to investigate the influence of the subset dimension on the displacement field. Results obtained using different subsets were similar The 21 pixel subset, which corresponds to 7 mm square areas, was chosen to evaluate the strain profile in the remainder of the work [64]. The strain field evaluated from the DIC analysis and reported in this experimental work refers to the Cartesian system of Figure 44a. The variation of the longitudinal strain component, ε_{yy} , across the width of the specimen is shown in Figure 53 for all the widths investigated in this study. The strain plots of Figure 53a-b-c-d-e-f refer to the representative B-face specimens represented in Figure 47b. The longitudinal strains ε_{yy} were evaluated at different locations along the SRP strip, corresponding to different values of the y coordinate. The plots of Figure 53 correspond to a DIC image taken at a value of the global slip, g, within the range $[g_1,g_2]$, in order to assure that the debonding mechanism was fully established. For all specimens, the values of y, for which the longitudinal strain has been plotted, are comprised within the stress transfer zone (STZ), i.e. the portion of the SRP strip where shear stresses are transferred to the concrete substrate. More details about the STZ can be found in [10] and will also be provided in section

4.1.1.6. If the width of the composite strip is between 30 mm and 90 mm, the trend of ε_{yy} across the width of the composite is characterized by a central region in which ε_{yy} is nominally constant. Close to the edges of the composite strip, ε_{yy} starts to decrease until it becomes null on the concrete surface at a distance from the composite edge approximately equal to 10 mm. The central region of the SRP strip, characterized by a constant value of ε_{yy}, becomes larger as the width of the composite strip increases. The lateral regions, characterized by a gradient of ε_{yy}, have approximately the same width equal to 20 mm on both sides of the composite strip, regardless of the width of the strip. The 15 mm wide strips do not exhibit a central region within the composite width with nominally constant strains (Figure 53a), which could be associated with the different failure mode observed earlier. Figure 54 shows the variation of the shear strain, ε_{xy}, across the width of the composite strip for specimen DS_300_15_HD_D_B_1 and specimen DS_300_50_HD_D_B_2. The shear strain, for specimen DS_300_15_HD_D_B_1, continuously changes across the width of the SRP strip, determining a fracture mixed Mode II and Mode III [84] condition. Conversely, for specimen DS_300_50_HD_D_B_2, the central region of the composite strip does not experience any shear strain, which implies that a Mode II loading condition exists. For this specimen, the mixed Mode II and Mode III fracture condition occurs in the edge regions of the composite strip, characterized by high shear strains (Figure 54b), and extends in the concrete surface adjacent to the composite strip. It can be assumed that as the width of the composite strip increases, the central portion characterized by a pure Mode II condition tends to become larger. This behavior is confirmed for S-face specimens. It can be observed that in the central region of the composite strip, for specimens with a width of the SRP strip larger or equal to 30 mm, ε_{yy} exhibits some fluctuation within the nominally constant strain region. These fluctuations of ε_{yy}, in the central region, are due to the non-uniform distribution of the aggregates across the width of the specimen and to the different size of the aggregates themselves [27].

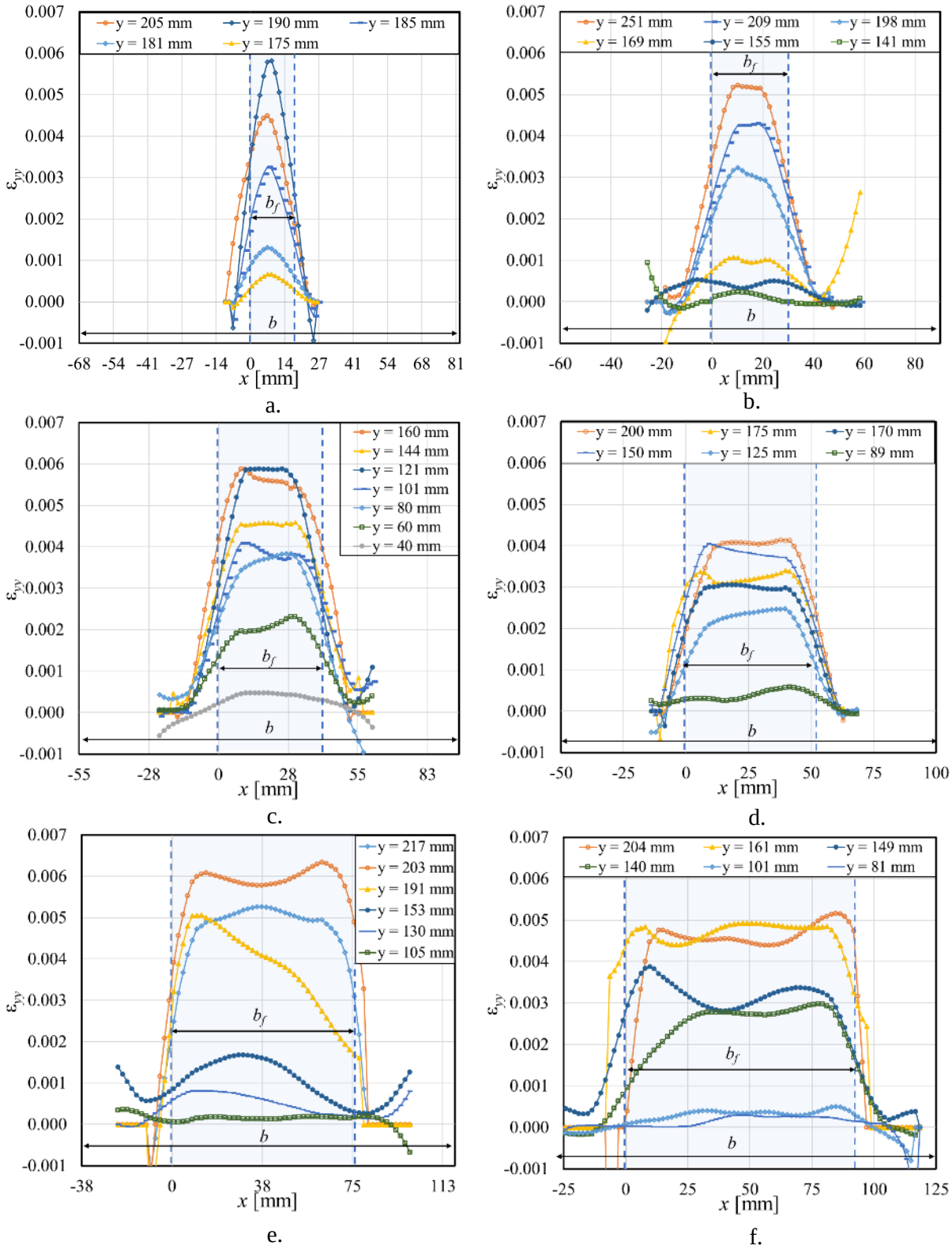

Figure 53. Longitudinal strains across the width of the SRP strip at different locations along the composite strip for specimens DS_300_15_HD_D_B_1 (a), DS_300_30_HD_D_B_2 (b), DS_300_40_HD_D_B_3 (c), DS_300_50_HD_D_B_2 (d), DS_300_75_HD_D_B_2 (e), and DS_300_90_HD_D_B_3 (f).

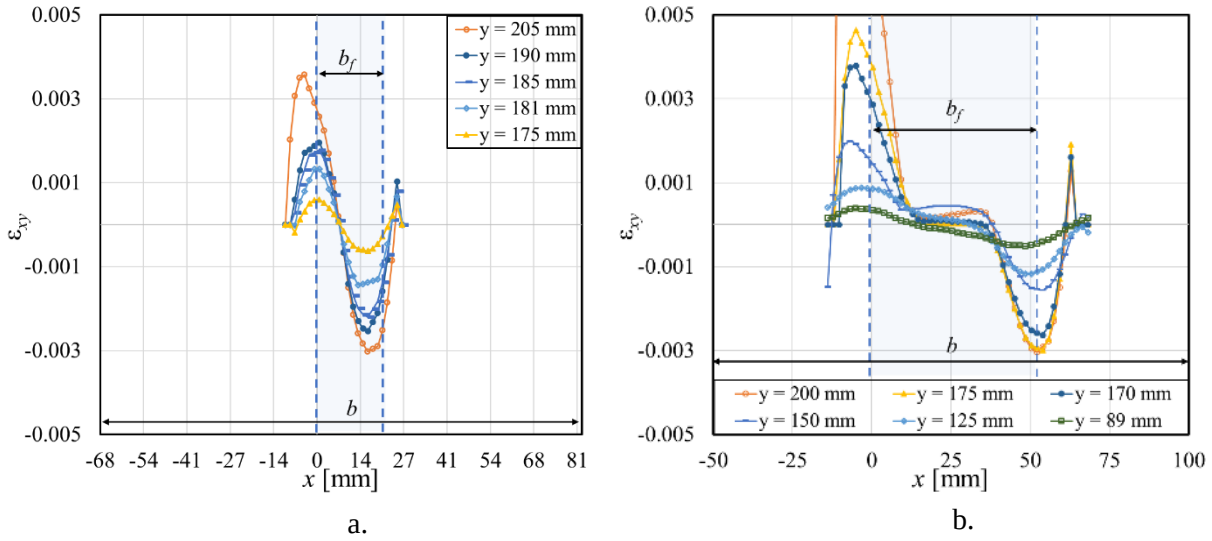

Figure 54. Shear strains across the width of the SRP strip at different locations along the composite strip for specimen DS_300_15_HD_D_B_1 (a) and specimen DS_300_50_HD_D_B_2 (b).

4.1.1.6 Best-fit of strain profile

The digital image correlation (DIC) introduced in section 4.1.1.5 was used for forty-two single-lap test specimens to obtain the strain field on the surface of the SRP strip and adjacent concrete surface. In order to determine the interfacial CML of the SRP-concrete interface, the longitudinal strain ε_{yy} was plotted along the center line of the SRP strip. The profile of ε_{yy} corresponds to the average of the strain component across a 15mm-wide centered strip computed for each value of the *y* coordinate. Averaging the strain across a 15 mm width allows for taking into account the variation of the strain due to the presence of a non-homogeneous substrate and local material variations in the SRP [85]. A 15-mm strip was chosen to average the strain based on the aggregate size.

The experimental nonlinear strain distribution along the bonded length was approximated using three different functions described below.

Function (14) was introduced by Dai et al. [35]:

$$\varepsilon_{yy}(y) = \frac{Ae^{B(Ay+C)}}{e^{B(Ay+C)}+1} \tag{14}$$

Function (15) is proposed by the author in this dissertation and represents a sinusoidal trend of the strain profile:

$$\varepsilon_{yy}(y)=\begin{cases}0, & if \quad \varepsilon_1'(y)<0 \quad \& \quad \varepsilon_1''(y)>0\\ \varepsilon_1(y), & if \quad \varepsilon_1'(y)\geq 0\\ 2D, & if \quad \varepsilon_1'(y)<0 \quad \& \quad \varepsilon_1''(y)<0\end{cases} \tag{15}$$

where:

$$\varepsilon_1(y)=-D\cos\left(\left(\frac{y-P}{E}\right)^F\pi\right)+D \tag{16}$$

Function (15) consists of three branches: 1) an initial constant branch equal to zero; 2) a second branch characterized by a sinusoidal S-shaped trend; and 3) a third constant portion equal to 2*D* (Figure 55a). Figure 55a shows the coordinates y_A and y_B that represent, respectively, the coordinates of the beginning and end of the second branch of function (15).

Continuity of the function and its first derivative are enforced among the three branches. At the locations along the composite strip identified by coordinates y_A and y_B, function $\varepsilon_1(y)$ must satisfy the following conditions:

$$\varepsilon_1'(y_A)=0 \quad \varepsilon_1''(y_A)>0 \quad \varepsilon_1(y_A)=0 \tag{17}$$

$$\varepsilon_1'(y_B)=0 \quad \varepsilon_1''(y_B)<0 \quad \varepsilon_1(y_B)=2D \tag{18}$$

$(\ )'$ and $(\ )''$ indicate the first and second derivative with respect to *y*, respectively.

Function (19) is proposed by the author in this dissertation and represents a polynomial trend of the strain profile.

$$\varepsilon_{yy}(y)=\begin{cases}0, & if \quad \varepsilon_2'(y)<0 \quad \& \quad \varepsilon_2''(y)>0\\ \varepsilon_2(y), & if \quad \varepsilon_2'(y)\geq 0\\ \varepsilon_2(y=y_D), & if \quad \varepsilon_2'(y)<0 \quad \& \quad \varepsilon_2''(y)<0\end{cases} \tag{19}$$

where:

$$\varepsilon_2(y) = H(y - y_C)^3 + I(y - y_C)^2 + L(y - y_C) \tag{20}$$

Similarly to function (15), function (19) consists of three branches: 1) an initial constant branch equal to zero; 2) a second branch characterized by a polynomial S-shaped trend; and 3) a third constant function with its value equal to the last value of the second branch (Figure 55b). Figure 55b shows the coordinates y_C and y_D that correspond to, respectively, the beginning and the end of the second branch of function (19). Continuity of the function and its first derivative are enforced among the three branches. At the locations along the composite strip identified by coordinates y_C and y_D, function $\varepsilon_2(y)$ must satisfy the following conditions:

$$\varepsilon_2'(y_C) = 0 \quad \varepsilon_2''(y_C) > 0 \quad \varepsilon_2(y_C) = 0 \tag{21}$$

$$\varepsilon_2'(y_D) = 0 \quad \varepsilon_2''(y_D) < 0 \quad \varepsilon_{yy}(y = y_D) = \varepsilon_2(y = y_D) \tag{22}$$

$( )'$ and $( )''$ indicate the first and second derivative with respect to y, respectively.

Parameters A, B and C of function (2), D, E, P, F, y_A, and y_B of function (15), and H, I, L, y_C, and y_D of function (19) are determined from a best fit procedure of the experimental strain profile. It should be observed that the number of DIC images that can be used is arbitrarily chosen and each image corresponds to a strain profile that can be fitted with the functions presented above or any other similar function.

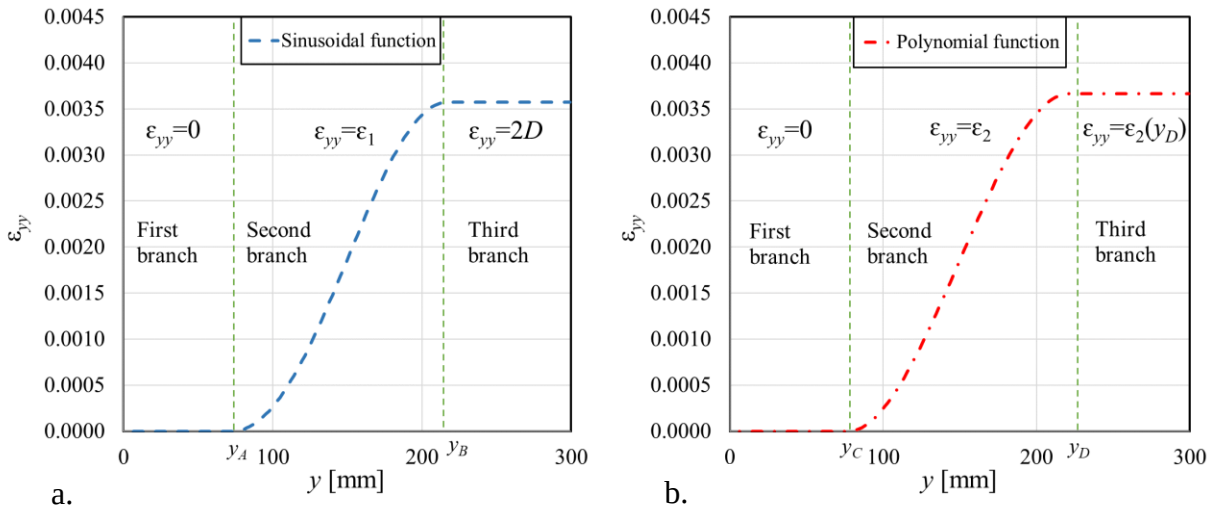

Figure 55 Characteristic trend of function (15) (a) and function (19) (b).

Figure 56b shows the experimental strain profile of specimen DS_300_50_UHD_D_B_5 corresponding to the DIC image taken at point B of the load response (Figure 56a). The three fitting functions for the experimental strain profile are plotted in Figure 56b. The strain distribution during the debonding process can be divided into three main regions: (A) the stress-free zone (SFZ); (B) the stress-transfer zone (STZ); and (C) the fully-debonded zone (FDZ) [10]. Stress transfer occurs in the STZ, usually characterized by an "S-shaped" strain profile. In the FDZ, the composite strip is completely debonded from the concrete substrate, i.e. no interfacial shear transfer takes place and the strain is nominally constant and equal to ε_{max} (Figure 56b). As the global slip increases during the test, the STZ moves gradually from the loaded end to the free end of the composite strip, and the length of the FDZ increases while the strain in this zone remains constant. This fact is consistent with the observation that the load remains constant (P_{crit}) after the debonding process initiates. Similarly to Figure 56, Figure 57b shows the experimental strain profile of specimen DS_300_90_HD_D_B_3, together with the three fitting functions, corresponding to the DIC image taken at point C of the load response Figure 57a.

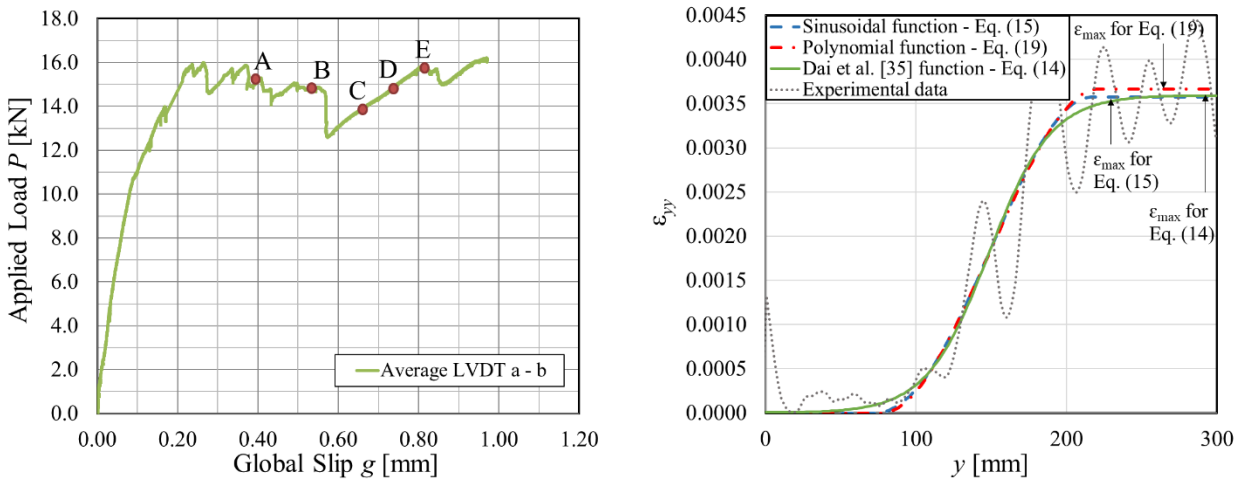

Figure 56 a) Load response of specimen DS_300_50_UHD_D_B_5. b) Experimental ε_{yy} profile for point B of the load response of specimen DS_300_50_UHD_D_B_5 and fitting functions (14), (15) and (19).

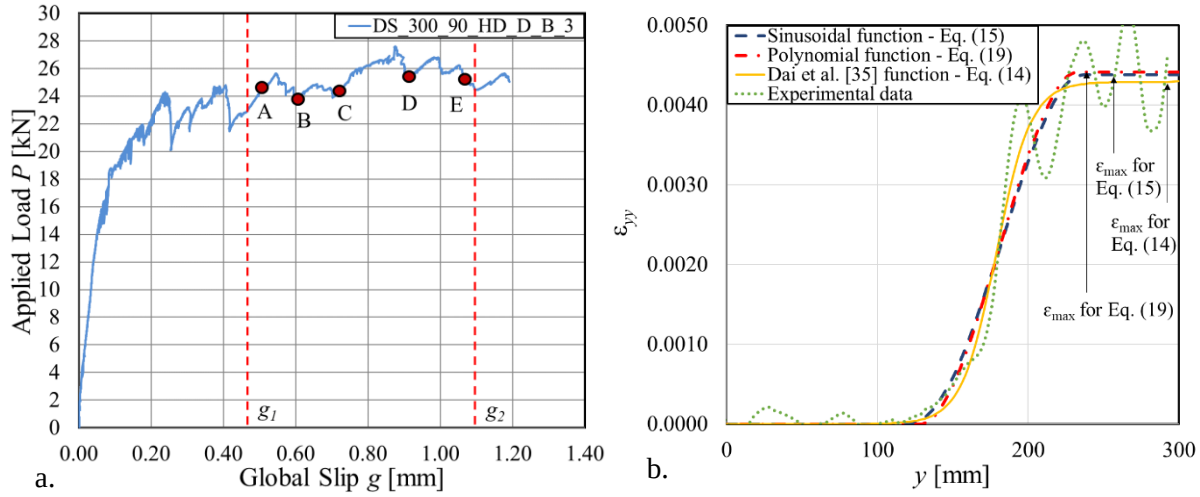

Figure 57. Specimen DS_300_90_HD_D_B_3: a) Load response; b) experimental ε_{yy} profile for point C and fitting functions; d) cohesive material law $\tau_{zy}(s)$ obtained using functions (14), (15), and (19) to fit the experimental strain profile of point C.

Figure 58a shows the experimental strain profile corresponding to point B of Figure 56a and the fitted strain profiles, using function (14), for five points of the load response (Figure 56a) of specimen DS_300_50_UHD_D_B_5. Figure 58b shows the experimental strain profile corresponding to point C of Figure 57a and the fitted strain profiles, using function (14), for five points of the load response (Figure 57a) of specimen DS_300_90_HD_D_B_3.

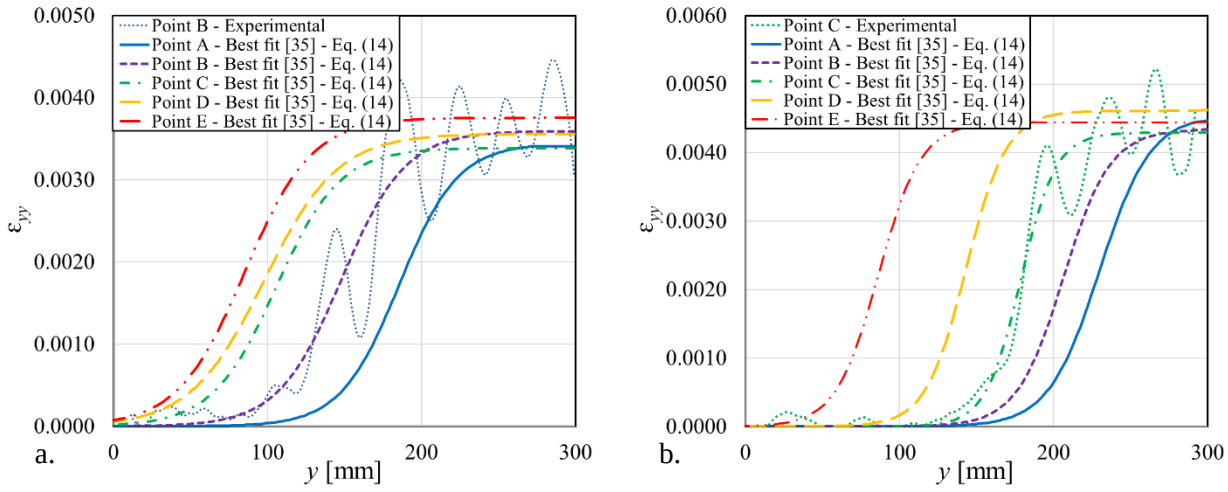

Figure 58. a) Experimental ε_{yy} profile for point B (Figure 56a) of specimen DS_300_50_UHD_D_B_5, and fitted strain profiles, using function (14) [35], that correspond to points A, B, C, D, and E of the load response of Figure 56a; b) Experimental ε_{yy} profile for point C (Figure 57b) of specimen DS_300_90_HD_D_B_3, and fitted strain profiles, using function (14) [35], that correspond to points A, B, C, D, and E of the load response of Figure 57a.

The global slip range [g_1-g_2] was determined as the range of slips where the "S-shaped" strain profile was completely developed, for specimens in which DIC was employed. For specimen DS_300_50_UHD_D_B_5 this range was comprised between point A and point E (Figure 56a), while for specimen DS_300_90_HD_D_B_3 this range is showed in Figure 57a. It can be observed that a translation of the STZ along the length of the SRP strip occurred as the global slip increased while its shape remained constant.

At the end of this section, it is important to discuss the choice of three different functions to fit the experimental strain profile. The reason behind proposing the new functions (15) and (19) to fit the strain profile is because function (14) does not correspond to a finite effective bond length, i.e. the length over which the shear stresses are transferred when the load sharing is fully established. In fact, the effective bond length, L_{eff}, which corresponds to the length of the STZ, can be evaluated for each function used to fit the experimental strain profile as:

$$L_{eff} = \frac{\sqrt{2E_f t^*_{f,A}}}{B\sqrt{G_F}} \ln\left(\frac{1+\alpha}{1-\alpha}\right) \tag{23}$$

where α is assumed equal to 0.96 and G_F [10] is the fracture energy of the interface, which will be introduced in section 4.1.1.8.

$$L_{eff} = y_B - y_A \tag{24}$$

$$L_{eff} = y_D - y_C \tag{25}$$

Equation (23) corresponds to the effective bond length when function (14) is used and was proposed by Dai et al. [35], while equations (24) and (25) can be used to evaluate L_{eff} when sinusoidal and polynomial functions are employed, respectively. Equation (23) requires that an assumption is made on the percentage of the load transferred through the effective bond length; whereas, equations (24) and (25) provide the actual length of the STZ, i.e. the distance between the two points where the derivative of the strain function is zero. Further discussion on the choice of the three function is provided in section 4.1.1.8 as the cohesive material law is introduced.

4.1.1.7 Best-fit of displacement profiles

It is worth noting that DIC is a full field optical technique that measures directly the displacements of the analyzed area. Strains are obtained after interpolating the displacement field as the derivative of displacements, thus the plot of the experimental strain profile could be affected by the subset and step used to perform the DIC analysis. If on one side, fitting of the experimental displacements provides less scattered experimental results, on the other side fitting of the strains has some advantages: 1) fitting of the experimental strains is an overall procedure that can be performed also for tests in which strain gages are adopted instead of DIC. 2) It is easier to define the STZ, characterized by an S-shaped profile, from the strain profile rather than from the displacement profile. 3) It is easier to define the point along the composite strip where the STZ begins from the strain profile, as it shifts along the bonded length. 4) The slip should be measured in the centerline of the composite to avoid the width effect [10]; however, the displacement of concrete can be obtained only from the side of the strip as reported in Czaderski et al. [86].

The experimental slips at any location of the SRP strip were evaluated from DIC measurements by subtracting the displacements of the concrete near the edge of the SRP strip (following the procedure proposed in [86]) from the displacements of the SRP strip, evaluated as the average values of a 15 mm wide strip centered with respect to the SRP strip. The fitting of the experimental slip in the center of the SRP strip was performed in order to define the corresponding strain profile and compare it with the one obtained from the fitting of the experimental strains. The function proposed by [86] was employed to fit the experimental slips (Figure 59a) corresponding to point B of Figure 56a. An additional function, proposed by the authors and representing a polynomial trend, was used to fit the experimental slips (Figure 59a):

$$s(y)=\begin{cases} R, & if \quad y<y_E \\ s_1(y), & if \quad y_E \le y \le y_F \\ s_2(y), & if \quad y>y_F \end{cases} \tag{26}$$

where:

$$s_1(y)=M\left(y-y_E\right)^4+N\left(y-y_E\right)^3+O\left(y-y_E\right)^2+R \tag{27}$$

$$s_2(y)=s_1\left(y_F\right)+s_1'\left(y_F\right)\left(y-y_F\right) \tag{28}$$

The slip profile (26) is comprised of three branches. The first branch when $y<y_E$ represents a constant branch with the slip equal to *R*. The second branch is a polynomial function up to $y=y_F$. Finally, the

third branch is a linear function. Continuity of the slip and its first derivative among the three branches is enforced. Parameters M, N, O, R, y_E and y_F are determined from a best fit procedure of the experimental slip profile. y_E and y_F are the coordinates along the SRP strip that identify, respectively, the beginning and the end of the STZ.

It should be noted that the slip in the STZ is a fourth order polynomial function, which would provide a third order strain function in agreement with, and therefore fully comparable with, function (19) proposed by the authors.

Figure 59b compares the strain profile obtained by fitting the experimental strain with the polynomial function (19) (dashed and dotted line) and the strain profile obtained by fitting the experimental slip profile by means of function (26) (dashed line) and the function proposed in [86] (dotted line). The strain profiles are in good agreement. A similar trend was observed for the other points of the load response of Figure 56a and for the other specimens.

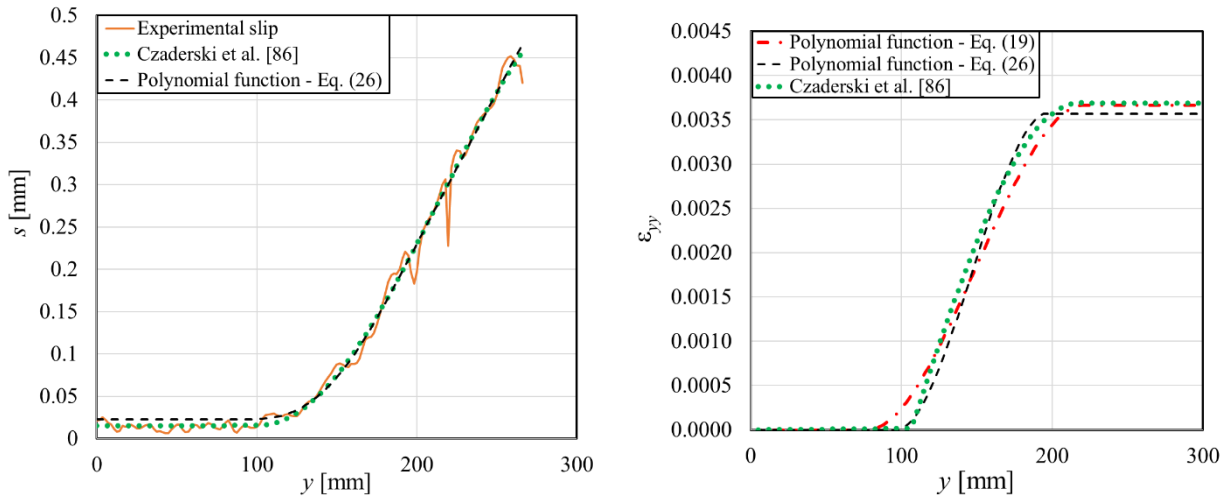

a. b.

Figure 59 a) Experimental slip profile for point B (Figure 56a) of specimen DS_300_50_UHD_D_B_5, and fitted slip profiles, using function (26) and the function proposed by Czaderski et al. [86]. b) Fitted strain profiles referred to point B (Figure 56a) of specimen DS_300_50_UHD_D_B_5, using function (19), and strain profile obtained from function (26) and slip function proposed by Czaderski et al. [86].

4.1.1.8 Interfacial cohesive material law (CML) obtained from the strain profiles of section 4.1.1.6

The strain profiles presented in section 4.1.1.6 are analyzed herein to obtain the interfacial cohesive material law. From the analytical expression of the strain profile it is possible to determine the value of the interfacial shear stress at any location of the composite strip [35]:

$$\tau_{zy}(y) = E_f t^*_{f,\mathrm{A}} \frac{\mathrm{d}\varepsilon_{yy}}{\mathrm{d}y} \tag{29}$$

where E_f is the elastic modulus of the fibers and $t^*_{f,\mathrm{A}}$ is the equivalent thickness of the fibers, obtained by dividing the total cross-sectional area of the steel fibers by the width of the SRP strip. Subscript A is used, according to the notation of section 4.1.1.2, to indicate the density of the fibers. For example, $t^*_{f,HD} = 0.254$ mm is the equivalent thickness of the high-density fibers. E_f and $t^*_{f,\mathrm{A}}$ are provided by the manufacturer [6] (see Table 4 in section 3.3.1).

It should be observed that the same calculation can be carried out with the elastic modulus of the composite referred to the bare fibers, $E^{\mathrm{A}}_{f,SRP}$, and the equivalent thickness, $t^*_{f,\mathrm{A}}$. The superscript A is used, according to the notation of section 4.1.1.2, to indicate the density of the fibers. With FRP composites, using the elastic modulus of the fibers and their equivalent thickness is customary. However, the rigorous computation of the fracture parameters requires the use of the elastic modulus of the composite referred to either the bare fibers or the entire area of the composite and the corresponding thickness. In other words, if the elastic modulus of the composite referred to the bare fibers is used, the evaluation of the fracture parameters will be performed considering the equivalent thickness of the fibers (textile). Alternatively, if the elastic modulus of the composite refers to the entire cross section area of the strip, the (nominal or actual) thickness of the SRP strip has to be considered for the evaluation of the fracture mechanics parameters.

The slip between the SRP strip and the concrete substrate at any location of the composite strip can be evaluated from the strain profile (provided that concrete is considered rigid):

$$s(y) = \int_0^y \varepsilon_{yy}\mathrm{d}y \tag{30}$$

Combining relationships (29) and (30), the fundamental differential equation that describes the Mode-II debonding phenomenon at the macro-scale is:

$$E_f t^*_{f,\mathrm{A}} \frac{\mathrm{d}^2 s}{\mathrm{d}y^2} - \tau_{zy}(s) = 0 \tag{31}$$

Function (14) is derived in [35] by integrating the fundamental equation (31) and using the following CML:

$$\tau_{zy} = A^2 B E_f t^*_{f,A} e^{(-Bs)} \left(1 - e^{(-Bs)}\right) \tag{32}$$

The interfacial $\tau_{zy}(s)$ relationship, or cohesive material law (CML), can be expressed in closed form also using the polynomial expression (19) of the strain, adopting the solution proposed by Cardano in 1545 [87]. A closed form solution of the $\tau_{zy}(s)$ relationship cannot be obtained if the sinusoidal function (15) is used to fit the strain profile. Therefore, in this case the $\tau_{zy}(s)$ relationship can be obtained by combining directly the shear stress and the slip at the same coordinate *y* along the composite strip using Equations (29) and (30), respectively.

As pointed out in section 4.1.1.6, the choice of different functions to fit the strain profile is related to the fact that only certain functions entail for a finite effective bond length. A different point of view of the same issue can be found as pointed out in [88]. In fact, only certain shapes of the CML allow to integrate the fundamental equation (31) and obtain a finite length of the strain distribution. Even the solution obtained by Dai et al. [35] required some mathematical compromise. Some researchers [89] [90] would prefer, for example, to use a simple bi-linear function for the CML. Nevertheless, Focacci and Carloni [91] proved that even the simple bi-linear function does not allow to integrate equation (31) unless an infinite effective bond length is accepted together with a mathematical compromise or the bi-linear function itself presents specific characteristics.

The CMLs for specimen DS_300_50_UHD_D_B_5 are represented in Figure 60a for the strain profile corresponding to point B of the load response (Figure 56a).

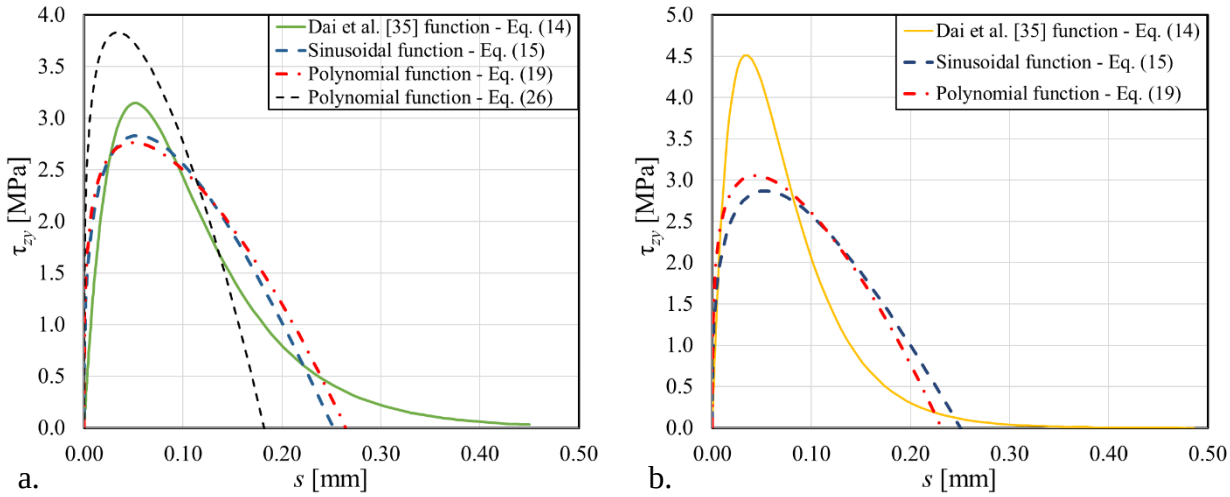

Figure 60. a) Cohesive material law $\tau_{zy}(s)$ for specimen DS_300_50_UHD_D_B_5 obtained using functions (14), (15), (19), and (26) to fit the experimental strain and slip profiles of point B (Figure 56a); b) Cohesive material law $\tau_{zy}(s)$ for specimen DS_300_90_HD_D_B_3 obtained using functions (14), (15), and (19) to fit the experimental strain and slip profiles of point C (Figure 57a).

The CMLs plotted in Figure 60a correspond to functions (14), (15), (19), and (26) used to fit the strain and slip profiles. The CMLs for specimen DS_300_90_HD_D_B_3 are presented in Figure 60b for the strain profile corresponding to point C of the load response (Figure 57a). The CMLs plotted in Figure 60b correspond to functions (14), (15), and (19), used to fit the strain and slip profiles.

The interfacial fracture energy G_F, i.e. the energy required to fully break the unit area of the cohesive crack, corresponds to the area under the entire $\tau_{zy}(s)$ curve:

$$G_F = \int_0^{\infty} \tau_{zy}(s)\, ds \tag{33}$$

Table 15 summarizes the average value of the maximum strain corresponding to the debonding of the SRP strip, $\overline{\varepsilon_{\max}}$, the maximum shear stress, $\overline{\tau_{\max}}$, the slip corresponding to the maximum shear stress, $\overline{s_{\mathrm{m}}}$, the effective bond length, $\overline{L_{eff}}$, and the fracture energy, $\overline{G_F}$, for each specimen tested employing DIC. The value of each parameter, for each test, is obtained as the average calculated from ten points of the load response within $[g_1,g_2]$, which correspond to ten images of DIC. Functions (14), (15), and (19) were used to fit the strain profiles and obtain the average parameters of Table 15.

Table 15. Fracture mechanics parameters

Specimen Name	Strain Function	$\overline{\varepsilon_{\max}}$ (CoV)	$\overline{\tau_{\max}}$ [MPa] (CoV)	$\overline{s_{\mathrm{m}}}$ [mm] (CoV)	$\overline{L_{eff}}$ [mm] (CoV)	$\overline{G_F}$ [N/mm] (CoV)	P_{crit} [kN]	$\overline{P_{theor}^{\varepsilon_{\max}}}$ [kN]	$\overline{P_{theor}}$ [kN]	$\overline{P_{theor}}/P_{crit}$ [%]
DS_300_30_HD_D_S_1	Dai et al. [35] Eq. (14)	0.0043 (0.04)	3.61 0.13)	0.043 (0.15)	114.5 (0.13)	0.45 (0.08)	7.50	6.27	6.28	83.7
	Sinusoidal Eq. (15)	0.0044 (0.05)	2.23 (0.09)	0.069 (0.10)	151.2 (0.09)	0.48 (0.09)	7.50	6.40	6.45	86.1
	Polynomial Eq. (19)	0.0043 (0.06)	3.11 (0.10)	0.040 (0.17)	100.3 (0.11)	0.44 (0.12)	7.50	6.17	6.18	82.4
DS_300_30_HD_D_S_2	Dai et al. [35] Eq. (14)	0.0039 (0.08)	3.85 (0.20)	0.033 (0.30)	101.0 (0.27)	0.38 (0.16)	7.20	5.52	5.54	76.9
	Sinusoidal Eq. (15)	0.0040 (0.08)	2.07 (0.12)	0.060 (0.15)	148.6 (0.12)	0.39 (0.16)	7.20	5.58	5.64	78.4
	Polynomial Eq. (19)	0.0039 (0.08)	3.10 (0.25)	0.035 (0.29)	96.7 (0.29)	0.37 (0.16)	7.20	5.45	5.47	75.9
DS_300_30_HD_D_S_3	Dai et al. [35] Eq. (14)	0.0045 (0.07)	5.07 (0.20)	0.033 (0.25)	86.0 (0.20)	0.49 (015)	7.50	6.91	6.93	92.4
	Sinusoidal Eq. (15)	0.0044 (0.08)	2.49 (0.06)	0.061 (0.10)	133.4 (0.04)	0.47 (0.16)	7.50	6.74	6.81	90.8
	Polynomial Eq. (19)	0.0043 (0.07)	4.54 (0.19)	0.028 (0.18)	69.8 (0.17)	0.45 (0.14)	7.50	6.63	6.64	88.5

DS_300_30_HD_D_S_4	Dai et al. [35] Eq. (14)	0.0036 (0.07)	4.55 (0.23)	0.024 (0.20)	76.0 (0.19)	0.31 (0.14)	6.71	5.53	5.54	82.6
	Sinusoidal Eq. (15)	0.0036 (0.07)	2.91 (0.31)	0.038 (0.24)	101.6 (0.24)	0.33 (0.14)	6.71	5.61	5.68	84.7
	Polynomial Eq. (19)	0.0036 (0.07)	3.68 (0.19)	0.024 (0.21)	71.3 (0.18)	0.31 (0.14)	6.71	5.49	5.50	82.0
DS_300_30_HD_D_S_5	Dai et al. [35] Eq. (14)	0.0033 (0.09)	3.75 (0.16)	0.024 (0.19)	85.0 (0.16)	0.27 (0.18)	6.39	4.97	4.99	78.2
	Sinusoidal Eq. (15)	0.0034 (0.08)	1.76 (0.10)	0.052 (0.13)	149.6 (0.11)	0.29 (0.16)	6.39	5.13	5.18	81.1
	Polynomial Eq. (19)	0.0033 (0.08)	3.09 (0.16)	0.025 (0.21)	79.3 (0.17)	0.27 (0.17)	6.39	4.95	4.97	77.7
DS_300_30_HD_D_B_2	Dai et al. [35] Eq. (14)	0.0053 (0.08)	4.41 (0.08)	0.052 (0.20)	113.0 (0.12)	0.67 (0.16)	8.58	8.01	8.03	93.6
	Sinusoidal Eq. (15)	0.0052 (0.08)	3.16 (0.05)	0.073 (0.13)	126.3 (0.05)	0.67 (0.17)	8.58	7.93	8.02	93.5
	Polynomial Eq. (19)	0.0051 (0.08)	3.87 (0.12)	0.048 (0.22)	97.5 (0.15)	0.64 (0.17)	8.58	7.81	7.83	91.3
DS_300_30_HD_D_B_3	Dai et al. [35] Eq. (14)	0.0055 (0.05)	4.51 (0.17)	0.058 (0.13)	116.0 (0.13)	0.72 (0.11)	9.16	8.30	8.31	90.7
	Sinusoidal Eq. (15)	0.0056 (0.05)	2.91 (0.05)	0.071 (0.27)	146.5 (0.05)	0.76 (0.11)	9.16	8.48	8.55	93.4
	Polynomial Eq. (19)	0.0054 (0.05)	4.01 (0.23)	0.051 (0.25)	103.5 (0.28)	0.71 (0.10)	9.16	8.22	8.22	89.8
DS_300_40_HD_D_S_1	Dai et al. [35] Eq. (14)	0.0038 (0.05)	2.89 (0.15)	0.041 (0.18)	125.3 (0.16)	0.35 (0.10)	9.01	7.84	7.85	87.2
	Sinusoidal Eq. (15)	0.0038 (0.06)	2.00 (0.10)	0.054 (0.11)	145.3 (0.12)	0.35 (0.11)	9.01	7.87	7.94	88.1
	Polynomial Eq. (19)	0.0037 (0.06)	2.69 (0.21)	0.036 (0.31)	105.4 (0.25)	0.33 (0.12)	9.01	7.70	7.71	85.6
DS_200_40_HD_D_S_2	Dai et al. [35] Eq. (14)	0.0036 (0.13)	3.70 (0.18)	0.031 (0.22)	93.9 (0.15)	0.32 (0.27)	9.01	7.03	7.08	78.6
	Sinusoidal Eq. (15)	0.0037 (0.10)	2.94 (0.20)	0.038 (0.17)	97.8 (0.15)	0.34 (0.19)	9.01	7.10	7.22	80.1
	Polynomial Eq. (19)	0.0036 (0.10)	3.38 (0.22)	0.028 (0.17)	79.2 (0.16)	0.32 (0.19)	9.01	7.02	7.04	78.2
DS_200_40_HD_D_S_3	Dai et al. [35] Eq. (14)	0.0036 (0.05)	3.86 (0.14)	0.029 (0.19)	89.7 (0.17)	0.32 (0.09)	8.50	6.97	6.98	82.1
	Sinusoidal Eq. (15)	0.0036 (0.05)	2.79 (0.13)	0.036 (0.15)	98.4 (0.11)	0.31 (0.10)	8.50	6.88	6.97	82.0
	Polynomial Eq. (19)	0.0036 (0.03)	3.33 (0.14)	0.027 (0.18)	79.4 (0.16)	0.31 (0.05)	8.50	6.96	6.96	82.0

DS_200_40_HD_D_S_4	Dai et al. [35] Eq. (14)	0.0040 (0.05)	3.03 (0.09)	0.043 (0.22)	124.5 (0.15)	0.38 (0.10)	9.05	7.65	7.66	84.6
	Sinusoidal Eq. (15)	0.0038 (0.05)	2.69 (0.08)	0.048 (0.18)	110.9 (0.14)	0.37 (0.10)	9.05	7.43	7.51	83.0
	Polynomial Eq. (19)	0.0038 (0.06)	2.79 (0.14)	0.037 (0.26)	101.0 (0.19)	0.35 (0.12)	9.05	7.37	7.38	81.6
DS_300_40_HD_D_B_2	Dai et al. [35] Eq. (14)	0.0047 (0.10)	5.17 (0.12)	0.035 (0.11)	84.7 (0.04)	0.53 (0.21)	10.99	9.43	9.47	86.2
	Sinusoidal Eq. (15)	0.0048 (0.07)	2.84 (0.21)	0.068 (0.06)	133.4 (0.15)	0.58 (0.14)	10.99	9.80	9.90	90.1
	Polynomial Eq. (19)	0.0046 (0.09)	4.36 (0.14)	0.032 (0.12)	77.0 (0.10)	0.51 (0.18)	10.99	9.25	9.28	84.4
DS_300_40_HD_D_B_3	Dai et al. [35] Eq. (14)	0.0056 (0.05)	5.19 (0.34)	0.053 (0.27)	110.1 (0.27)	0.75 (0.10)	12.09	11.18	11.20	92.6
	Sinusoidal Eq. (15)	0.0056 (0.04)	3.53 (0.25)	0.071 (0.21)	126.9 (0.21)	0.77 (0.08)	12.09	11.22	11.33	93.8
	Polynomial Eq. (19)	0.0056 (0.05)	4.44 (0.31)	0.051 (0.25)	98.7 (0.28)	0.76 (0.09)	12.09	11.20	11.21	92.8
DS_300_50_HD_D_S_1	Dai et al. [35] Eq. (14)	0.0044 (0.06)	2.86 (0.17)	0.056 (0.19)	147.5 (0.16)	0.47 (0.11)	12.25	10.76	10.81	88.3
	Sinusoidal Eq. (15)	0.0043 (0.04)	2.27 (0.12)	0.06 (0.15)	147.7 (0.12)	0.46 (0.08)	12.25	10.66	10.78	88.0
	Polynomial Eq. (19)	0.0042 (0.04)	2.69 (0.20)	0.048 (0.23)	119.5 (0.21)	0.44 (0.07)	12.25	10.42	10.46	85.4
DS_300_50_HD_D_S_2	Dai et al. [35] Eq. (14)	0.0042 (0.06)	3.17 (0.13)	0.046 (0.17)	125.4 (0.14)	0.42 (0.11)	12.27	10.22	10.47	85.3
	Sinusoidal Eq. (15)	0.0041 (0.04)	2.25 (0.13)	0.06 (0.11)	141.5 (0.12)	0.42 (0.08)	12.27	10.15	10.47	85.3
	Polynomial Eq. (19)	0.0041 (0.04)	2.73 (0.11)	0.042 (0.12)	109.6 (0.12)	0.40 (0.07)	12.27	10.02	10.26	83.6
DS_300_50_HD_D_S_3	Dai et al. [35] Eq. (14)	0.0042 (0.08)	2.43 (0.19)	0.061 (0.07)	165.1 (0.11)	0.43 (0.17)	11.92	10.29	10.16	85.2
	Sinusoidal Eq. (15)	0.0043 (0.11)	1.91 (0.18)	0.061 (0.34)	173.7 (0.1)	0.45 (0.23)	11.92	10.51	10.46	87.8
	Polynomial Eq. (19)	0.0042 (0.1)	2.48 (0.26)	0.051 (0.29)	133.0 (0.26)	0.44 (0.20)	11.92	10.40	10.27	86.2
DS_300_50_HD_D_S_4	Dai et al. [35] Eq. (14)	0.0035 (0.07)	2.29 (0.11)	0.045 (0.12)	144.9 (0.09)	0.30 (0.14)	10.44	8.61	8.83	84.6
	Sinusoidal Eq. (15)	0.0037 (0.1)	1.63 (0.11)	0.061 (0.19)	173.9 (0.06)	0.34 (0.2)	10.44	9.16	9.46	90.6
	Polynomial Eq. (19)	0.0036 (0.1)	2.09 (0.16)	0.043 (0.25)	128.7 (0.19)	0.32 (0.21)	10.44	8.83	9.07	86.9

DS_300_50_HD_D_S_5	Dai et al. [35] Eq. (14)	0.0038 (0.06)	3.25 (0.1)	0.038 (0.12)	111.6 (0.1)	0.36 (0.12)	11.47	9.41	9.64	84.0
	Sinusoidal Eq. (15)	0.0039 (0.05)	2.24 (0.12)	0.055 (0.07)	133.9 (0.09)	0.37 (0.1)	11.47	9.59	9.89	86.2
	Polynomial Eq. (19)	0.0038 (0.05)	2.84 (0.14)	0.034 (0.2)	99.6 (0.18)	0.35 (0.09)	11.47	9.33	9.55	83.3
DS_200_50_HD_D_S_7	Dai et al. [35] Eq. (14)	0.0041 (0.06)	4.36 (0.10)	0.032 (0.13)	88.0 (0.10)	0.40 (0.11)	12.45	10.47	10.48	84.2
	Sinusoidal Eq. (15)	0.0041 (0.06)	3.13 (0.14)	0.044 (0.10)	101.2 (0.12)	0.41 (0.11)	12.45	10.53	10.66	85.6
	Polynomial Eq. (19)	0.0040 (0.05)	3.80 (0.14)	0.030 (0.14)	78.0 (0.12)	0.40 (0.10)	12.45	10.44	10.45	83.9
DS_300_50_HD_D_S_10R_2	Dai et al. [35] Eq. (14)	0.0059 (0.07)	3.92 (0.50)	0.085 (0.26)	162.6 (0.29)	0.85 (0.15)	15.48	15.13	15.17	98.0
	Sinusoidal Eq. (15)	0.0059 (0.06)	3.51 (0.39)	0.067 (0.32)	146.7 (0.32)	0.86 (0.13)	15.48	15.12	15.27	98.7
	Polynomial Eq. (19)	0.0058 (0.06)	3.90 (0.47)	0.068 (0.37)	128.2 (0.39)	0.81 (0.11)	15.48	14.80	14.82	95.7
DS_300_50_HD_D_S_10R_3	Dai et al. [35] Eq. (14)	0.0049 (0.04)	4.32 (0.30)	0.051 (0.30)	115.6 (0.29)	0.59 (0.09)	14.37	12.61	12.62	87.8
	Sinusoidal Eq. (15)	0.0049 (0.04)	3.15 (0.21)	0.059 (0.16)	122.6 (0.19)	0.59 (0.08)	14.37	12.49	12.61	87.7
	Polynomial Eq. (19)	0.0049 (0.04)	3.66 (0.25)	0.046 (0.26)	100.9 (0.25)	0.57 (0.08)	14.37	12.42	12.42	86.5
DS_300_50_HD_D_B_2	Dai et al. [35] Eq. (14)	0.0041 (0.06)	3.37 (0.22)	0.043 (0.16)	120 (0.18)	0.42 (0.11)	12.64	10.18	10.43	82.5
	Sinusoidal Eq. (15)	0.0042 (0.06)	2.57 (0.25)	0.055 (0.26)	130.7 (0.20)	0.44 (0.12)	12.64	10.35	10.69	84.6
	Polynomial Eq. (19)	0.0042 (0.05)	3.04 (0.27)	0.042 (0.22)	106.1 (0.23)	0.43 (0.11)	12.64	10.29	10.54	83.3
DS_300_50_HD_D_B_3	Dai et al. [35] Eq. (14)	0.0042 (0.06)	2.89 (0.16)	0.05 (0.19)	138.4 (0.16)	0.42 (0.12)	12.28	10.21	10.46	85.2
	Sinusoidal Eq. (15)	0.0043 (0.09)	2.39 (0.11)	0.055 (0.15)	136.3 (0.15)	0.45 (0.17)	12.28	10.49	10.94	89.1
	Polynomial Eq. (19)	0.0043 (0.07)	2.60 (0.22)	0.049 (0.26)	124.7 (0.23)	0.44 (0.14)	12.28	10.48	10.85	88.4
DS_200_50_HD_D_B_4	Dai et al. [35] Eq. (14)	0.0055 (0.08)	4.33 (0.17)	0.059 (0.19)	121.5 (0.16)	0.73 (0.16)	14.39	13.91	13.95	97.0
	Sinusoidal Eq. (15)	0.0054 (0.05)	3.56 (0.18)	0.062 (0.21)	119.6 (0.14)	0.73 (0.11)	14.39	13.77	13.91	96.7
	Polynomial Eq. (19)	0.0052 (0.08)	4.50 (0.16)	0.041 (0.24)	85.1 (0.19)	0.65 (0.15)	14.39	13.07	13.10	91.07

DS_300_75_HD_D_S_1	Dai et al. [35] Eq. (14)	0.0039 (0.08)	3.10 (0.20)	0.043 (0.10)	122.6 (0.14)	0.38 (0.16)	17.23	14.27	14.31	83.1
	Sinusoidal Eq. (15)	0.0039 (0.11)	1.94 (0.11)	0.062 (0.11)	153.1 (0.06)	0.37 (0.22)	17.23	14.02	14.21	82.5
	Polynomial Eq. (19)	0.0038 (0.09)	2.48 (0.35)	0.042 (0.22)	118.9 (0.24)	0.35 (0.18)	17.23	13.68	13.73	79.7
DS_300_75_HD_D_S_2	Dai et al. [35] Eq. (14)	0.0035 (0.07)	3.02 (0.36)	0.038 (0.40)	121.3 (0.35)	0.29 (0.15)	15.10	12.88	12.91	85.5
	Sinusoidal Eq. (15)	0.0033 (0.05)	2.10 (0.30)	0.042 (0.24)	129.6 (0.29)	0.27 (0.11)	15.10	12.24	12.37	81.9
	Polynomial Eq. (19)	0.0034 (0.03)	2.82 (0.29)	0.030 (0.29)	94.8 (0.32)	0.28 (0.06)	15.10	12.51	12.51	82.9
DS_300_75_HD_D_S_3	Dai et al. [35] Eq. (14)	0.0044 (0.05)	3.87 (0.15)	0.042 (0.23)	110.2 (0.18)	0.47 (0.11)	18.69	15.91	15.93	85.2
	Sinusoidal Eq. (15)	0.0043 (0.06)	2.17 (0.10)	0.067 (0.14)	151.8 (0.08)	0.46 (0.13)	18.69	15.49	15.63	83.6
	Polynomial Eq. (19)	0.0043 (0.05)	3.58 (0.18)	0.037 (0.25)	90.5 (0.21)	0.46 (0.10)	18.69	15.64	15.65	83.8
DS_300_75_HD_D_S_4	Dai et al. [35] Eq. (14)	0.0039 (0.04)	2.42 (0.12)	0.052 (0.20)	153.4 (0.15)	0.37 (0.08)	16.76	14.12	14.12	84.3
	Sinusoidal Eq. (15)	0.0038 (0.06)	1.88 (0.10)	0.053 (0.17)	153.8 (0.12)	0.35 (0.12)	16.76	13.60	13.71	81.8
	Polynomial Eq. (19)	0.0038 (0.06)	2.52 (0.19)	0.039 (0.33)	114.5 (0.24)	0.35 (0.12)	16.76	13.67	13.69	81.7
DS_300_75_HD_D_B_2	Dai et al. [35] Eq. (14)	0.0060 (0.05)	4.21 (0.08)	0.071 (0.15)	135.0 (0.09)	0.88 (0.10)	21.68	22.06	22.09	101.9
	Sinusoidal Eq. (15)	0.0057 (0.03)	3.12 (0.07)	0.086 (0.08)	140.2 (0.07)	0.79 (0.05)	21.68	20.82	20.99	96.8
	Polynomial Eq. (19)	0.0056 (0.03)	3.86 (0.08)	0.055 (0.12)	105.9 (0.10)	0.76 (0.06)	21.68	20.58	20.58	94.9
DS_300_75_HD_D_B_3	Dai et al. [35] Eq. (14)	0.0049 (0.04)	4.42 (0.23)	0.044 (0.28)	108.0 (0.22)	0.57 (0.09)	19.79	17.84	17.86	90.2
	Sinusoidal Eq. (15)	0.0048 (0.05)	2.48 (0.07)	0.072 (0.07)	147.5 (0.08)	0.56 (0.11)	19.79	17.56	17.72	89.5
	Polynomial Eq. (19)	0.0047 (0.05)	3.74 (0.18)	0.042 (0.18)	92.7 (0.16)	0.53 (0.10)	19.79	17.22	17.24	87.1
DS_300_90_HD_D_B_1	Dai et al. [35] Eq. (14)	0.0046 (0.03)	3.30 (0.09)	0.054 (0.14)	133.0 (0.12)	0.52 (0.07)	25.77	20.99	21.00	81.5
	Sinusoidal Eq. (15)	0.0049 (0.05)	2.53 (0.12)	0.074 (0.14)	150.1 (0.11)	0.60 (0.10)	25.77	22.35	22.53	87.4
	Polynomial Eq. (19)	0.0049 (0.06)	3.14 (0.23)	0.053 (0.21)	118.4 (0.19)	0.58 (0.12)	25.77	22.18	22.22	86.2

DS_300_90_HD_D_B_3	Dai et al. [35] Eq. (14)	0.0046 (0.03)	3.95 (0.17)	0.044 (0.16)	111.2 (0.15)	0.50 (0.06)	25.37	20.28	20.29	80.0
	Sinusoidal Eq. (15)	0.0046 (0.06)	2.78 (0.10)	0.060 (0.14)	127.0 (0.11)	0.52 (0.11)	25.37	20.34	20.54	81.0
	Polynomial Eq. (19)	0.0045 (0.06)	3.44 (0.17)	0.041 (0.19)	96.2 (0.17)	0.49 (0.11)	25.37	19.89	19.91	78.5
DS_300_50_UHD_D_B_3	Dai et al. [35] Eq. (14)	0.0036 (0.05)	5.25 (0.29)	0.031 (0.35)	106.7 (0.32)	0.48 (0.10)	16.07	13.04	13.21	82.2
	Sinusoidal Eq. (15)	0.0042 (0.05)	2.56 (0.08)	0.056 (0.23)	186.9 (0.09)	0.63 (0.09)	16.07	14.85	15.11	94.0
	Polynomial Eq. (19)	0.0038 (0.06)	4.71 (0.29)	0.036 (0.46)	99.7 (0.42)	0.54 (0.11)	16.07	13.76	13.93	86.7
DS_300_50_UHD_D_B_4	Dai et al. [35] Eq. (14)	0.0041 (0.06)	3.50 (0.30)	0.059 (0.29)	178.1 (0.26)	0.62 (0.13)	15.24	14.73	15.68	102.9
	Sinusoidal Eq. (15)	0.0041 (0.05)	2.67 (0.12)	0.077 (0.18)	176.0 (0.13)	0.60 (0.1)	15.24	14.51	15.52	101.9
	Polynomial Eq. (19)	0.004 (0.07)	3.28 (0.28)	0.054 (0.35)	142.4 (0.30)	0.58 (0.14)	15.24	14.28	15.20	99.8
DS_300_50_UHD_D_B_5	Dai et al. [35] Eq. (14)	0.0035 (0.06)	3.25 (0.20)	0.045 (0.25)	156.1 (0.21)	0.43 (0.12)	14.49	12.37	12.54	86.5
	Sinusoidal Eq. (15)	0.0036 (0.06)	2.43 (0.15)	0.056 (0.12)	170.5 (0.12)	0.47 (0.11)	14.49	12.80	13.05	90.1
	Polynomial Eq. (19)	0.0035 (0.07)	3.12 (0.26)	0.043 (0.31)	130.1 (0.28)	0.44 (0.13)	14.49	12.47	12.64	87.2

4.1.1.9 Influence of the bond set-up

The influence of the bond set-up on the results can be analyzed by considering tests conducted on specimens with MD and HD steel fibers, applied to the B face of the concrete prims. Referring to Table 13 and Table 14, it is possible to evaluate the average value of P_{crit} or P_d for different densities, which allows to compare the results of two different test set-ups. For specimens tested using a single-lap shear test set-up, the value of $\bar{P}_{crit}^{MD,B}$ and $\bar{P}_{crit}^{HD,B}$ is equal to 10.81 kN and 13.02 kN, respectively. For strengthened notched beams tested using a TPB set-up, the average value of P_d is equal to 14.28 kN and 16.15 kN for specimens with MD and HD fibers, respectively. Results obtained from TPB set-up are 32.1 % greater than the one obtained from direct shear tests for MD steel fibers and 24.0 % greater for HD steel fibers. These results indicate that the test set-up has a great influence on bond results. In TPB set-up, the curvature of the notched beam during the test affects the debonding process between the composite strip and the concrete substrate, which in turn causes higher values of the load-carrying capacity with respect to single-lap shear tests. Results from different set-ups should not be compared. In addition, from

an energy balance point of view, it should be noted that the energy supply, i.e. the work of the external load, is used to fracture concrete along the notch and debond the SRP strip. Thus, it is reasonable to observe a different load-carrying capacity of the SRP strip when single-lap and notched beam tests are compared.

4.1.1.10 FRP-SRP analogy

The load response and failure mode, i.e. debonding in a thin layer of concrete underneath the SRP strip, suggests that SRP composites behave as FRP composites. The theoretical load-carrying capacity of the SRP-concrete interface, $\overline{P_{theor}}$, can be evaluated using the well-known formula obtained for FRP-concrete joints [26]:

$$\overline{P_{theor}} = b_f \sqrt{2E_f t^*_{f,\mathrm{A}} \overline{G_F}} \tag{34}$$

As the theoretical load-carrying capacity $\overline{P_{theor}}$ requires that the fracture energy is known, the average fracture energy of each test $\overline{G_F}$ obtained from the direct procedure (see section 4.1.1.8) associated with the fitting of the ε_{yy} profile with three different strain functions, was used. Thus, three values of the theoretical load-carrying capacity, named $\overline{P_{theor}}$ and associated with the three fitting functions, were computed for each test. Table 15 reports, for each specimen analyzed with DIC, the percentage ratio $\overline{P_{theor}} / P_{crit}$. For almost all the specimens, the percentage ratio $\overline{P_{theor}} / P_{crit}$ is comprised within the range 80% - 95%. The value of $\overline{P_{theor}}$ is always lower than P_{crit}. The value of $\overline{P_{theor}}$ depends on the values of the elastic modulus and thickness of the fibers. If the modulus of the composite and its actual thickness are used, the value of $\overline{P_{theor}}$ would be always greater than the experimental P_{crit}. Several factors should be considered to discuss the difference between $\overline{P_{theor}}$ and P_{crit}:

i) Eq. (34) is derived under the assumption of constant ε_{yy} across the entire width of the composite (Figure 61a). In section 4.1.1.5, it has been observed that ε_{yy} is constant only in the central region of the width of the SRP strip, while close to the edges there is a high gradient of ε_{yy} with the additional presence of shear strain.

ii) In addition to a constant strain across the width of the composite, as shown in Figure 61a, Eq. (34) implies that the interfacial fracture surface has the same width of the composite and is nominally plane.

iii) Furthermore, when the width of the SRP strip, b_f, is smaller than the width of the concrete prism, b, the debonding phenomen is a 3D phenomenon, that affects an area that is larger than the horizontal projection of the bonded region of the SRP strip. The fracture surface is not plane and therefore Eq. (34) should be modified.

It can be observed that if the strain on the surface is assumed to be representative of the strain throughout the thickness of the composite, then the strain across the width at the beginning of the STZ (at the loaded end) can be used to compute the load-carrying capacity:

$$P_{crit}^{\varepsilon_{yy}} = t_{f,\mathrm{HD}}^{*} E_{f,SRP}^{\mathrm{HD}} \int_{0}^{b_f} \varepsilon_{yy}\big|_{y=\ell} \, \mathrm{d}x \tag{35}$$

Eq. (35) does not take into account what observed in *iii*). In Eq. (35), the elastic modulus of the composite referred to the fibers, $E_{f,SRP}^{\mathrm{HD}}$, evaluated in Section 3.3.6, has been employed. As discussed in [92], the actual modulus of the composite should be always used for the evaluation of the load-carrying capacity of SRP-concrete joints. The actual elastic modulus of the composite varies for each strip since it depends on the percentage volume of fibers and matrix in the cross-section of the strip. To overcome this problem, the elastic modulus of the fibers, E_f, and the equivalent thickness of the fibers, $t_{f,\mathrm{A}}^{*}$ are generally used in literature (and also in this work) to evaluate the load-carrying capacity of both FRP and SRP strips bonded to a concrete substrate, even if this procedure entails a slight underestimation of the load-carrying capacity.

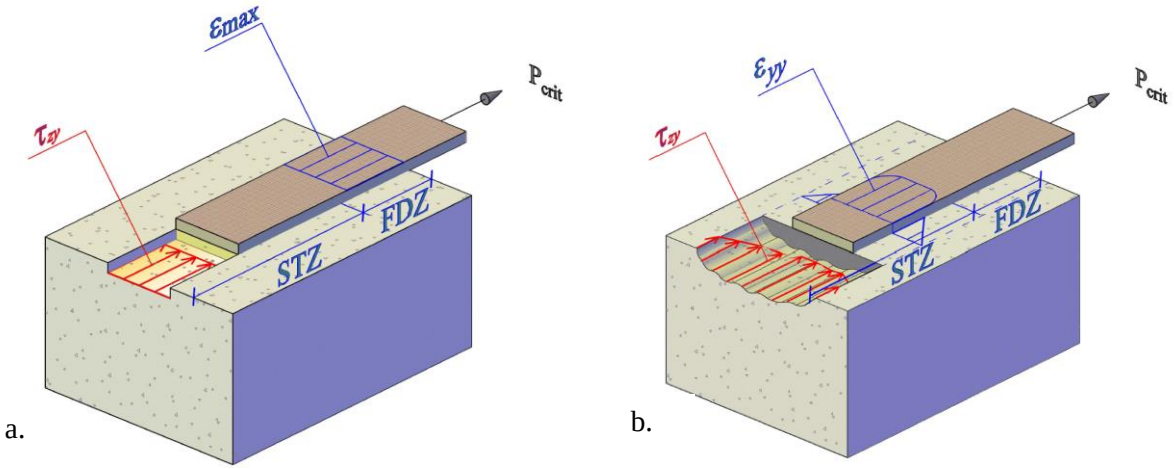

Figure 61: Fracture surface, longitudinal strain component in the SRP, and shear stress distribution: a) pure Mode-II condition and b) experimental evidence.

For specimen DS_300_90_HD_D_B_3 the value of $P_{crit}^{\varepsilon_{yy}}$ is evaluated for different values of the global slip, i.e. points A, B, C, D, and E in in the load response of Figure 57a. For each point, the value of $P_{crit}^{\varepsilon_{yy}}$ was evaluated averaging the values between the range $\left[y_D - D_{\max}/2; y_D + D_{\max}/2\right]$. Finally, averaging the value of $P_{crit}^{\varepsilon_{yy}}$ obtained for the five different points, the mean value of the load carrying capacity, $\overline{P_{crit}^{\varepsilon_{yy}}}$, was calculated (Table 16). It can be observed that for specimen DS_300_90_HD_D_B_3 the value of $\overline{P_{crit}^{\varepsilon_{yy}}}$ is equal to 25.25 kN, which is very similar to the experimental value of P_{crit} (25.37 kN).

Table 16. Evaluation of $\overline{P_{crit}^{\varepsilon_{yy}}}$ for specimen DS_300_90_HD_D_B_3

Point A										
y [mm]	282.9	281.1	279.3	277.5	275.7	273.9	272.1	270.4	268.6	
$P_{crit}^{\varepsilon_{yy}}$ [kN]	27.20	26.60	25.79	24.93	24.16	23.61	23.19	22.89	22.86	
Point B										
y [mm]	256.1	254.3	252.5	250.7	248.9	247.1	245.4	243.6	241.8	
$P_{crit}^{\varepsilon_{yy}}$ [kN]	30.60	30.71	30.60	30.07	29.21	28.00	26.55	25.08	23.85	
Point C										
y [mm]	240.0	238.2	236.4	234.6	232.9	231.1	229.3	227.5	225.7	$\overline{P_{crit}^{\varepsilon_{yy}}}$
$P_{crit}^{\varepsilon_{yy}}$ [kN]	27.31	27.53	27.43	27.06	26.55	26.03	25.52	24.99	24.25	25.25 kN
Point D										
y [mm]	197.1	195.4	193.6	191.8	190.0	188.2	186.4	184.6	182.9	
$P_{crit}^{\varepsilon_{yy}}$ [kN]	22.93	21.41	20.26	19.59	19.47	19.98	20.96	22.01	22.91	
Point E										
y [mm]	159.6	157.9	156.1	154.3	152.5	150.7	148.9	147.1	145.4	
$P_{crit}^{\varepsilon_{yy}}$ [kN]	23.36	22.79	23.15	24.03	25.71	27.16	28.47	29.54	30.20	

The load-carrying capacity can be obtained as:

$$\overline{P_{theor}^{\varepsilon_{\max}}} = E_f t_{f,\mathrm{A}}^{*} b_f \overline{\varepsilon_{\max}} \tag{36}$$

$\overline{P_{theor}^{\varepsilon_{\max}}}$ is obtained from the average maximum strain $\overline{\varepsilon_{\max}}$ in the FDZ, reported in Table 15 as the average of ten values from ten strain profiles fitted with the above mentioned functions (14), (15), and (19). The

values of $\overline{P_{theor}^{\varepsilon_{max}}}$ are reported in Table 15. The elastic modulus of the fibers and their equivalent thickness were used to compute $\overline{P_{theor}^{\varepsilon_{max}}}$. $\overline{P_{theor}^{\varepsilon_{max}}}$ matches the values of $\overline{P_{theor}}$ reported in Table 15. It should be noted that $\overline{P_{theor}^{\varepsilon_{max}}}$ could have been computed using the elastic modulus of the composite referred to the bare fibers, $E_{f,SRP}^{A}$, and the equivalent thickness, $t_{f,A}^{*}$.

The similarities between SRP and FRP composites can be further investigated by means of Equation (34). It is reasonable to assume that the interfacial fracture energy, G_F, for specimens with the strip applied to the same face (S or B) should be the same, independently of the stiffness of the composite strip. Using this assumption, and considering equation (34), the ratio between the theoretical load-carrying capacity evaluated for MD steel fibers and HD steel fibers, $r_{MD/HD}$, can be obtained as:

$$r_{MD/HD} = \frac{b_f \sqrt{2E_f t^*_{f,MD} G_F}}{b_f \sqrt{2E_f t^*_{f,HD} G_F}} = \sqrt{\frac{t^*_{f,MD}}{t^*_{f,HD}}} = \sqrt{\frac{0.169}{0.254}} = 0.816 \tag{37}$$

Similarly, the ratio between the theoretical load-carrying capacity evaluated for HD steel fibers and UHD steel fibers, $r_{HD/UHD}$, should be equal to:

$$r_{HD/UHD} = \frac{b_f \sqrt{2E_f t^*_{f,HD} G_F}}{b_f \sqrt{2E_f t^*_{f,UHD} G_F}} = \sqrt{\frac{t^*_{f,HD}}{t^*_{f,UHD}}} = \sqrt{\frac{0.254}{0.381}} = 0.816 \tag{38}$$

$t^*_{f,MD}$, $t^*_{f,HD}$, and $t^*_{f,UHD}$ are the equivalent thickness of MD steel fibers, HD steel fibers, and UHD steel fibers. As mentioned above, the fracture energy, G_F, was considered a constant value, and therefore the ratio of the load-carrying capacities depends only on the square root of the ratio between the equivalent thicknesses of the different densities.

The ratio $\bar{P}_{crit}^{MD,B} / \bar{P}_{crit}^{HD,B}$ between the average experimental critical load evaluated for B-face specimens with MD steel fibers ($\bar{P}_{crit}^{MD,B} = 10.81$ kN) and HD steel fibers ($\bar{P}_{crit}^{HD,B} = 13.02$ kN) is equal to 0.830. Similarly, the ratio $\bar{P}_{crit}^{HD,B} / \bar{P}_{crit}^{UHD,B}$ between the average experimental critical load evaluated for B-face specimens with HD steel fibers ($\bar{P}_{crit}^{HD,B} = 13.02$ kN) and UHD steel fibers ($\bar{P}_{crit}^{UHD,B} = 15.64$ kN) is equal to 0.832. In both cases, the experimental results are in good agreement with the theoretical prediction proposed for FRP composites. This observation confirms that FRP and SRP composite strips bonded to concrete surfaces have a similar behavior. It should be noted that the width effect does not affect the ratios of the load-carrying capacities.

4.1.1.11 Fracture parameters

In this section, the fracture mechanics parameters presented in Table 15 and obtained by fitting the experimental strain profiles with three different functions are discussed. Only specimens tested with DIC and reported in Table 15 will be considered in this section.

In general, the three functions, i.e. Dai et al. [35], sinusoidal and polynomial, provide similar results for $\overline{\varepsilon_{\max}}$ and $\overline{G_F}$, while a large scatter can be observed for $\overline{L_{eff}}$, $\overline{s_{\mathrm{m}}}$ and $\overline{\tau_{\max}}$. For example, considering S face specimens with HD steel fibers and a 50 mm-wide strip, the average value of L_{eff} obtained from the sinusoidal function is 30.5% and 11.4% higher than the values obtained from the polynomial and Dai et al. [35] functions, respectively.

Similarly, the value of $\overline{s_{\mathrm{m}}}$ and $\overline{\tau_{\max}}$ determined with the sinusoidal function appear to be different from the values defined with the polynomial and Dai et al. [35] functions.

The fracture energy and effective bond length, evaluated in section 4.1.1.8, are plotted in Figure 62 as a function of the ratio b_f/b for HD specimens. Figure 62a-b shows the average value of $\overline{G_F}$ together with the standard deviation obtained using the polynomial function, for S-face and B-face specimens, respectively. In the same graphs it is also reported the fracture energy, $G_F^{P_{crit}}$, which has been back-calculated from Eq. (34), substituting P_{theor} with P_{crit} for each specimen:

$$G_F^{P_{crit}} = \frac{P_{crit}^2}{2b_f^2 E_f t_{f,\mathrm{A}}^*} \tag{39}$$

Considering the polynomial strain function, the average value of $\overline{G_F}$ for S-face specimens (with HD steel fibers) is equal to 365 N/m, 330 N/m, 390 N/m, and 357 N/m for a ratio b_f/b equal to 0.2, 0.27, 0.33, and 0.5, respectively. It can be observed that the fracture energy is almost constant, regardless of the ratio b_f/b. Similar results were obtained using the fitting function proposed by Dai et al. [35] or the sinusoidal function (for HD specimens). Those results are not plotted for the sake of brevity. The fracture energy $G_F^{P_{crit}}$, for S-face specimens with HD steel fibers, is equal to 550 N/m, 495 N/m, 541 N/m, and 530 N/m for a ratio b_f/b equal to 0.2, 0.27, 0.33, and 0.5, respectively. The average value of $\overline{G_F}$ is lower than $G_F^{P_{crit}}$. The reason of this difference can be explained considering that $\overline{G_F}$ was evaluated considering a 15-mm wide strip within the central region of the SRP strip, while $G_F^{P_{crit}}$ is determined directly from the load-carrying capacity P_{crit}. $\overline{G_F}$ is a pure Mode-II fracture energy and does not take into account of the mixed Mode-II – Mode-III condition close to the edges of the strip.

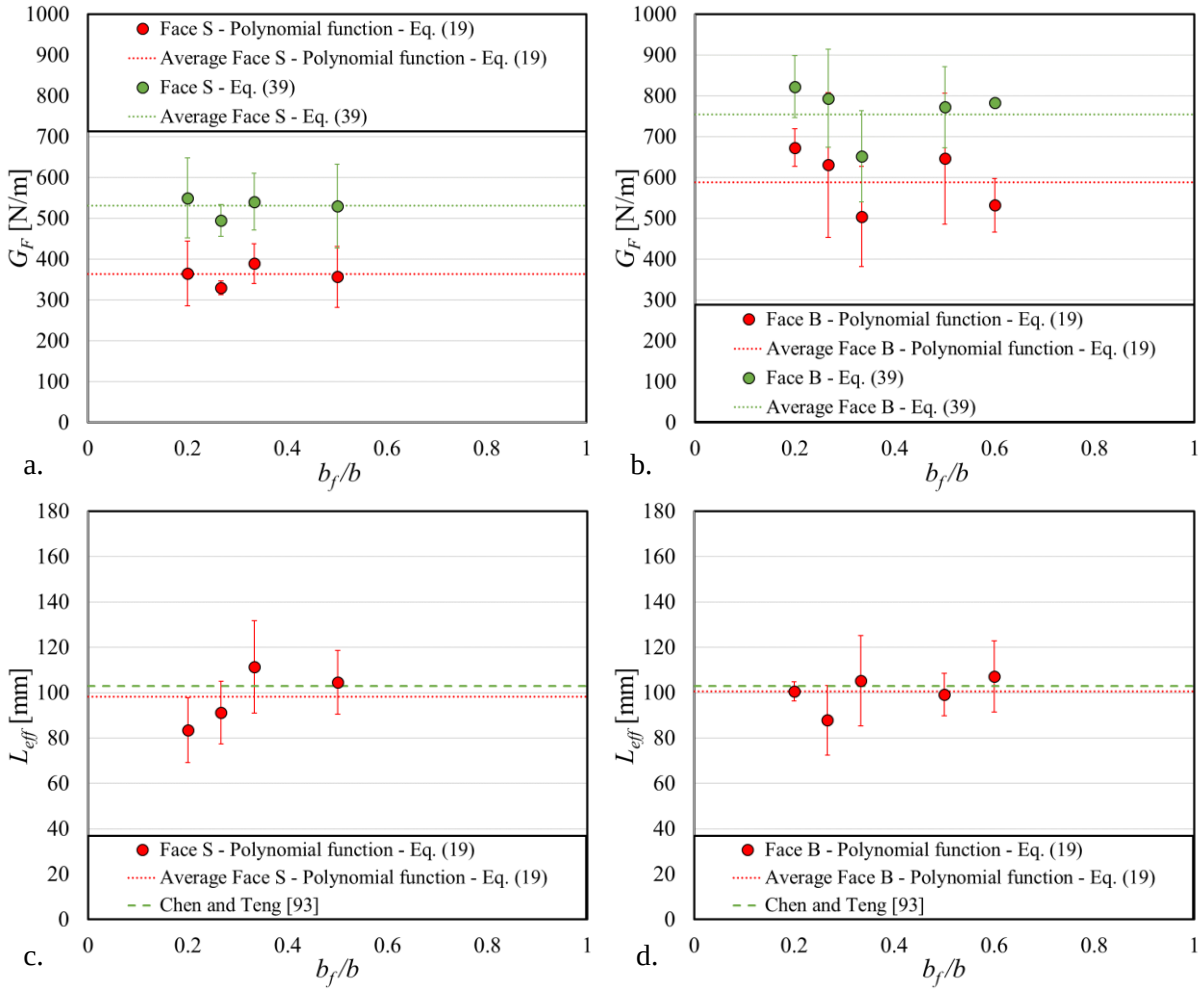

Figure 62. Comparison between the fracture energy evaluated through the strain fitting from Eq. (19) and the fracture energy evaluated using Eq. (39) for S-face specimens (a) and B-face specimens (b) and comparison between the value of Leff evaluated through the strain fitting from Eq. (19) and through Eq. (40) proposed by Chen and Teng [93] for S-face specimens (c) and B-face specimens (d).

On the other hand, $G_F^{P_{crit}}$ can be considered as a fictitious fracture energy influenced by the presence of different fracture modes across the width of the strip. Considering B-face specimens with HD steel fibers analyzed with the polynomial strain function, the average value of $\overline{G_F}$ resulted equal to 673 N/m, 631 N/m, 504 N/m, 647 N/m, and 532 N/m for a ratio b_f/b equal to 0.2, 0.27, 0.33, 0.5, and 0.6, respectively. Similar results, were obtained using Eq. (14) or Eq. (15) for fitting the experimental longitudinal strains. The fracture energy, $G_F^{P_{crit}}$, for B-face specimens with HD steel fibers, is equal to 822 N/m, 794 N/m, 652 N/m, 773 N/m, and 783 N/m for a ratio b_f/b equal to 0.2, 0.27, 0.33, 0.5, and 0.6, respectively. As observed for S-face specimens, $G_F^{P_{crit}}$ resulted always greater than $\overline{G_F}$ also for B-face specimens (if the elastic modulus of the fibers E_f is used). Results are more scattered than the ones obtained for the S-face

specimens. It is worth noting that, for HD steel fibers, the overall number of B-face specimens tested with DIC (11 specimens) is lower than the number of S-face specimens tested with DIC (19 specimens), and for each width no more than three B-face specimens were tested with DIC. The scatter in the results for B-face specimens can be attributed to the low number of specimens tested with DIC.

Comparing the average values of $\overline{G_F}$ obtained for each b_f/b ratio for B-face specimens (strengthened with HD steel fibers) with the equivalent values determined for S-face specimen, it can be noted that B-face specimens presents always a fracture energy that is greater than S-face specimens. Considering the polynomial strain function, the ratio of the average value of $\overline{G_F}$ for B-face specimens with HD steel fibers to the average value of $\overline{G_F}$ for S-face specimens with HD steel fibers is equal to 1.84, 1.90, 1.30, and 1.81 for a ratio b_f/b equal to 0.2, 0.27, 0.33, and 0.5, respectively. It can be observed that SRP strips applied to the B face of the specimen had a Mode-II fracture energy greater than strips applied on the S face of the specimen. Due to the geometry of the molds and the direction of casting (Figure 44c), a large amount of aggregates distributes near the B face of the specimen with respect to the S face. The large amount of aggregates influences the debonding phenomenon, which in turn might require a greater amount of energy to propagate the interfacial cohesive crack. The presence of more and larger aggregates near the B face could also explain the larger scatter of the results in terms of fracture energy when compared to the S-face results. It should be noted that the interfacial Mode-II fracture energy appears to be approximately four times greater than the Mode-I fracture energy of concrete. This result is in good agreement with some assumptions found in the literature [94].

Figure 62c-d showed the average value of $\overline{L_{eff}}$ together with the standard deviation obtained using the polynomial function for S-face and B-face specimens, respectively, strengthened with HD steel fibers. The average values of the effective bond length are quite scattered when plotted versus the ratio b_f/b. For S-face and B-face specimens with HD steel fibers, the average value of $\overline{L_{eff}}$ evaluated through the polynomial function is comprised within the range 83 mm – 111 mm, and 88 mm – 107 mm, respectively (Figure 62c-d). From the available results, it appears that the ratio b_f/b and the face to which the composite strip is applied don't affect the effective bond length. In Figure 62c-d it is also reported the value of L_{eff} determined using the formula proposed by Chen and Teng [93]:

$$L_{eff} = \sqrt{\frac{E_f t^*_{f,A}}{\sqrt{f_{cm}}}} \tag{40}$$

Where the cylindrical compressive strength at 28 days f_{cm} was evaluated from R_{cm} according to [38]:

$$f_{cm} = 0.83R_{cm} \tag{41}$$

From Figure 62c and Figure 62d, it can be observed that the value of L_{eff} obtained from Chen and Teng [93] formula is in good agreement with the average value of $\overline{L_{eff}}$ determined for S-face and B-face specimens (strengthened with HD steel fibers) for different values of the ratio b_f/b, using the polynomial fitting function. A good agreement is observed also using the Dai et al. [35] fitting function (Table 15), while using the sinusoidal function, the values of $\overline{L_{eff}}$ seemed to be slightly different with respect to the value of L_{eff} obtained from Chen and Teng [93] (Table 15).

Specimen reinforced with UHD steel fibers show an increase of $\overline{L_{eff}}$ with respect to specimens with HD fibers. The average $\overline{L_{eff}}$ is equal to 147 mm, 178 mm, and 124 mm for Dai et al. [35], sinusoidal, and polynomial function, respectively, when UHD fibers are applied to the B-face of specimens with a composite width equal to 50 mm. On the other hand, the average $\overline{L_{eff}}$ of B-face specimens with HD steel fibers and a composite width equal to 50 mm is equal to 127 mm, 129 mm, and 105 mm for Dai et al. [35], sinusoidal, and polynomial function, respectively. An increase of the stiffness of the composite strip leads to an increase of the effective bond length.

4.1.1.12 Width effect

In this section, a background on the width effect is presented and the influence of the width effect on the experimental results is analyzed considering specimens strengthened with HD steel fibers and tested in direct-shear.

Early studies on the width effect in FRP-concrete joints are dated back to the end of 1990s. Among the first researchers who observed that the load-carrying capacity of the FRP strip bonded to a concrete substrate varied with the ratio of the width of the composite bf to the width b of the concrete prism, Neubauer and Rostasy [20] [95] proposed the following formula for the maximum bond force $T_{u,\max}$ (i.e. the bond capacity, which in this dissertation is identified by the symbol P_{crit} for experimental values):

$$T_{u,\max} = 0.64 k_b b_f \sqrt{E_{FRP} t_{FRP} f_{ct}} \tag{42}$$

where b_f, E_{FRP}, and t_{FRP} are the width, elastic modulus, and thickness of the composite, while f_{ct} is the surface tensile strength of concrete. The width factor k_b is:

$$k_b = \sqrt{1.125\frac{2-\left(b_f/b\right)}{1+\left(b_f/400\right)}} \tag{43}$$

where b is the width of the concrete prism. It should be noted that k_b was firstly proposed by Holzenkampfer [96] based on the size effect formula by Bazant [45] [42]. Equation (42) was derived by assuming that the fracture energy of the interface was determined as:

$$G_F = k_b^2 C_F f_{ct} \tag{44}$$

The coefficient C_F was calibrated against 70 bond tests by the authors. Equation (44) implies that the fracture energy is not a true material property but depends on the width factor.
Brosens and Van Gemert [97] adjusted Equation (43) by changing the expression of k_b:

$$k_b = \sqrt{1.5\frac{2-\left(b_f/b\right)}{1+\left(b_f/100\right)}} \tag{45}$$

Later on, Brosens [98] modified the expression of the fracture energy reported in [97]:

$$G_F = k_c k_b^2 C_F f_{ct} \tag{46}$$

k_c depends on the concrete surface condition and varies between 0.65 and 1.00. The width factor is:

$$k_b = \sqrt{k\frac{2-\left(b_f/b\right)}{1+\left(b_f/b_0\right)}} \tag{47}$$

k is calibrated against the experiments (as well as CF) and $b_0 = t_{ref}/\left(k-1\right)$. t_{ref} (firstly introduced in [97]) is the thickness of the portion of concrete near the surface of concrete where the composite is applied and can be assumed equal 2.5-3 times the aggregate size.
Chen and Teng [93] collected a large database of experimental results to calibrate the width factor. The bond capacity P_u proposed by the authors is (when the bonded length is sufficiently long):

$$P_u = 0.427\beta_p b_f \sqrt{E_{FRP} t_{FRP} \sqrt{f_c^{'}}} \tag{48}$$

where $f_c^{'}$ is the specified compressive strength of concrete and the width factor β_p is:

$$\beta_p = \sqrt{\frac{2-\left(b_f/b\right)}{1+\left(b_f/b\right)}} \tag{49}$$

It should be noted that when data are collected from different studies, certain parameters, such as the rate of testing and the face of the concrete prism to which the composite is applied, are typically not reported although they strongly affect the results. Teng et al. [8] in 2003 slightly modified the expression of the bond capacity without changing the width factor.

Additional data were considered by Lu et al. [99], who proposed a slightly different expression of the width factor β_w:

$$\beta_w = \sqrt{\frac{2.25-\left(b_f/b\right)}{1.25+\left(b_f/b\right)}} \tag{50}$$

It should be noted that Lu et al. [99] applied the width factor to the fracture energy G_F.

Subramaniam et al. [84] [85] conducted two experimental campaigns to investigate the width effect and their results contradicted somehow the expressions of the width factor proposed in the literature. The results presented by the authors were all obtained from tests conducted at the same testing rate but the face of the prism to which the composite was applied was not reported.

Wu et al. [100] performed an analytical study based on a database of 628 shear tests. A closed-form solution was used to determine the bond parameters by matching the analytical solution with test results. The coefficients of the bond capacity model were derived by regression analyses. Wu et al. [100] proposed a new formulation of the width factor as a function of both the width ratio and concrete strength:

$$\kappa_w^{WU} = \lambda + \left(1-\lambda\right)\cdot b_f/b \tag{51}$$

$$\lambda = 1 + 0.222\cdot\left(f_c^{'}\right)^{0.304} \tag{52}$$

Wu et al. [100] proposed the following formula to evaluate the load-carrying capacity:

$$P_{theor,Wu} = Q\left(E_{FRP}t_{FRP}\right)^{-0.5}\left(f_c^{'}\right)^{J}\kappa_w^{WU} \tag{53}$$

Where Q and J are equal to 0.703 and 0.108, respectively.

Lin et al. [101] performed a numerical analysis on composite strips bonded to a concrete substrate, considering several bonded widths, and obtained the following formula for the width factor:

$$\kappa_w^{LIN} = 1 + f_c^{'R}\left[8\left(E_{FRP}t_{FRP}\right)^{-S} + 0.001\right]\left(1 - b_f/b\right)^{0.5} \Big/ \left(1 + 0.01b_f^T\right) \tag{54}$$

where R, S, and T are equal to 0.385, 0.438, and 1.7, respectively.

The width factor proposed by Lin et al. [101] shall be used in Eq. (53) proposed by Wu et al. [100] in order to evaluate the load-carrying capacity of composite strips bonded to a concrete surface.

Additional numerical work has been carried out to investigate the effect of the width [102] [103] [104] [105], which points out what observed by Subramaniam et al. [84] [85], i.e. the distribution of the longitudinal strain component is not constant across the width of the composite, which is the source of the width effect.

Figure 63a shows the plot of $\overline{P}_{crit}^{Y,C,E}$ for each width and face divided by the actual width of the composite $b_{f,actual}$ as a function of the ratio b_f/b. It can be observed that both for S-face and B-face specimens, high values of P_{crit} per unit width are reached when the SRP composite strip is narrow (15 mm). As the width of the strip increases, the value of P_{crit} per unit width tends to a plateau, i.e. no substantial variations of P_{crit} per unit width are observed when the ratio b_f/b is increased. This behavior can be explained considering the strain analysis performed in section 4.1.1.5. For specimens with a 15 mm-wide strip, the presence of a mixed Mode-II – Mode-III condition entailed for a high amount of energy needed to propagate the crack. When the ratio b_f/b increases, the area across the SRP width characterized by a pure Mode II condition becomes larger than the region with a mixed mode condition, causing a decrease of the value of P_{crit} per unit width that tends to an approximatively constant value when the ratio b_f/b becomes equal or higher than 0.33.

Results plotted in Figure 63a indicate that regardless of the width of the composite strip, specimens with the composite strip applied to the B face reached higher values of P_{crit} than specimens with the SRP strip applied to the S face. Figure 63a includes the results of three S-face specimens with a width equal to 50 mm (b_f/b=0.33) tested at a rate equal to 10 times the rate used for the other tests. The value of $\overline{P}_{crit}^{Y,C,E}$ for these three specimens was 21.6% higher than S-face specimens tested at standard rate. On the basis of these observations, it appears that an accurate predictive formula can be defined only if homogeneous

specimens tested with a standard procedure are considered. In Figure 63b, the value of $\overline{P}_{crit}^{Y,C,E}$ per unit width for S-face and B-face specimens is shown again together with the most important models proposed in literature [101] [20] [97] [93] [100] [99] (already described above) that define the load-carrying capacity of the FRP-concrete interface as a function of the ratio b_f/b. Results from literature were plotted using the elastic modulus of the fibers, E_f, and the equivalent thickness of the fibers, $t_{f,A}^*$, instead of the values referred to the composite, i.e. E_{FRP} and t_{FRP}, respectively. It can be observed that most of the models are not able to predict the experimental behavior of this campaign. It is worth noting that the majority of the models proposed in literature are based on experimental data in which the testing conditions are not homogeneous. For example, in Chen and Teng [93], the database used to calibrate the predictive model considered specimens with different test rates and specimens for which the face of application of the composite strip was not reported. Among the different predictive models showed in Figure 63b, only the model proposed by Lin et al. [101] is in good agreement with the experimental data of S-face specimens. It should be noted that Eq. (54) implies that the width factor is influenced by the product between the elastic modulus and the thickness of the composite. The influence of the stiffness of the composite strip on the width factor should entail for a different distribution of ε_{yy} across the width of the composite strip when different densities of the steel fiber sheet are employed.

Figure 64a-b provides a comparison between the profile of ε_{yy} across the composite width for specimen DS_300_50_HD_D_B_2 and DS_300_50_UHD_D_B_5, respectively. Figure 64 shows that, regardless of the stiffness of the composite strip, the region of the SRP strip characterized by a pure Mode-II condition (see section 4.1.1.5) has always the same width for a 50 mm-wide strip. A similar observation can be made if the face of application of the composite strip is considered. Figure 64c shows the longitudinal strains across the width for specimen DS_300_50_HD_D_S_1. For this specimen, the width of the region with constant longitudinal strains is equal to 30 mm, i.e. the same value observed for specimen DS_300_50_HD_D_B_2. It appears that both the stiffness of the composite strip and the face of application of the SRP strip do not affect the strain profile across the width of the strip, and therefore the width factor should not be influenced by these parameters. Based on this experimental evidence, the authors proposed a new formula for the width factor, which is obtained by fitting the experimental results reported in Figure 63. The load-carrying capacity per unit width was evaluated through Eq. (34) introducing the revised width factor k_w:

$$\frac{P_{theor}^{\Gamma_F}}{b_f} = k_w \sqrt{2\Gamma_F E_f t_{f,\mathrm{A}}^*} \tag{55}$$

$$k_w = 1 + \left(1 - b_f / b\right)^{0.5} \Big/ \left(1 + 0.01 b_f^U\right) \tag{56}$$

Γ_F is the value of the fracture energy evaluated as:

$$\Gamma_F = \alpha \sqrt{f_{cm} f_{ctm}} \tag{57}$$

U and α are parameters obtained from a best fit procedure of the experimental data (Figure 63c). The symbol Γ_F was used to indicate the fracture energy rather than G_F, since the value determined in Eq. (57) is obtained from an empirical formula and not from experimental tests. Similarly, the load-carrying capacity is indicated as $P_{theor}^{\Gamma_F}$ in Eq. (55) since it is evaluated from Γ_F . Eq. (55) is used to fit the experimental data of S-face specimens and B-face specimens separately, since they showed a different trend. The values of *U* and α for S-face specimens are equal to 2.16 and 0.0733, respectively, while for B-face specimens are equal to 2.08 and 0.103, respectively. The trend of S-face specimens has been then fitted again, keeping the parameter *U* equal to the value determined for B-face specimens (2.08). This choice is related to the observation that the main fracture parameter that differs between S-face specimens and B-face specimens was the fracture energy, G_F, while results of Figure 64 indicate that the width factor should be independent from the face to which the composite strip is applied. A value of α equal to 0.0712 is obtained from this new fitting for S-face specimens (*U* was kept equal to 2.08). Figure 63c shows the comparison between the two different fittings made for S-face specimens. It can be noted that the two fittings are almost identical, therefore the last one (*U* = 2.08 and α = 0.0712) is chosen to represent the behavior of S face specimens, in order to maintain the same width factor both for S-face and B-face specimens. Since the SRP shear reinforcements are usually applied to the side faces of a concrete structural element (e.g. beam), the predictive formula obtained for S face specimens (*U* = 2.08 and α = 0.0712) shall be used to design the load carrying capacity of SRP composites used for shear strengthening. On the other hand, since the SRP flexural reinforcements are usually applied on the bottom face of a structural element, the predictive formula obtained for B face specimens (*U* = 2.08 and α = 0.103) shall be used to design the load-carrying capacity of SRP composites used for flexural strengthening. The value of Γ_F for S-face and B-face specimens resulted equal to 491 N/m and 709 N/m. These values are slightly higher than the average values of $\overline{G_F}$, obtained through the polynomial strain function considering all the different widths (red dotted lines in Figure 62a-b), that resulted equal to 364 N/m and 589 N/m for S-face and B-face specimens, respectively.

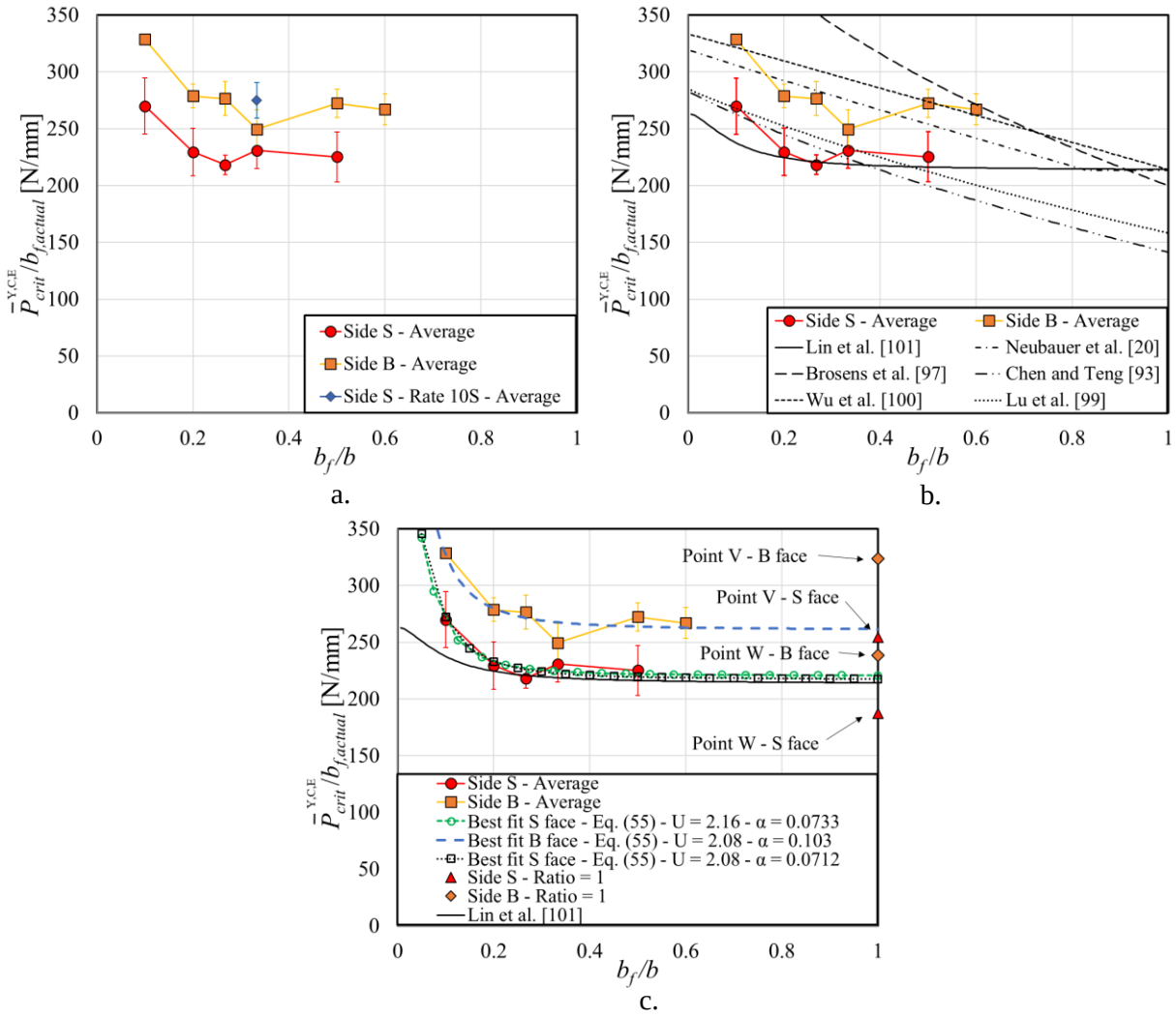

Figure 63. Average value of P_{crit} per unit width for different b_f/b ratios: a) Experimental results; b) Predictive behavior from literature; c) Best fitting using Eq. (55).

Eq. (55) is characterized by an asymptotic behavior that levels off when the ratio b_f/b is greater than 0.4. Using Eq. (34) it is possible to predict the value of the load carrying capacity per unit width when the ratio b_f/b is equal to 1 both for S-face and for B-face specimens (point W in Figure 63c). To this end, the value of G_F employed in Eq. (34) is set equal to the average of the values of $\overline{G_F}$ determined from the polynomial fitting (Table 15) for all S-face and B-face specimens, respectively.

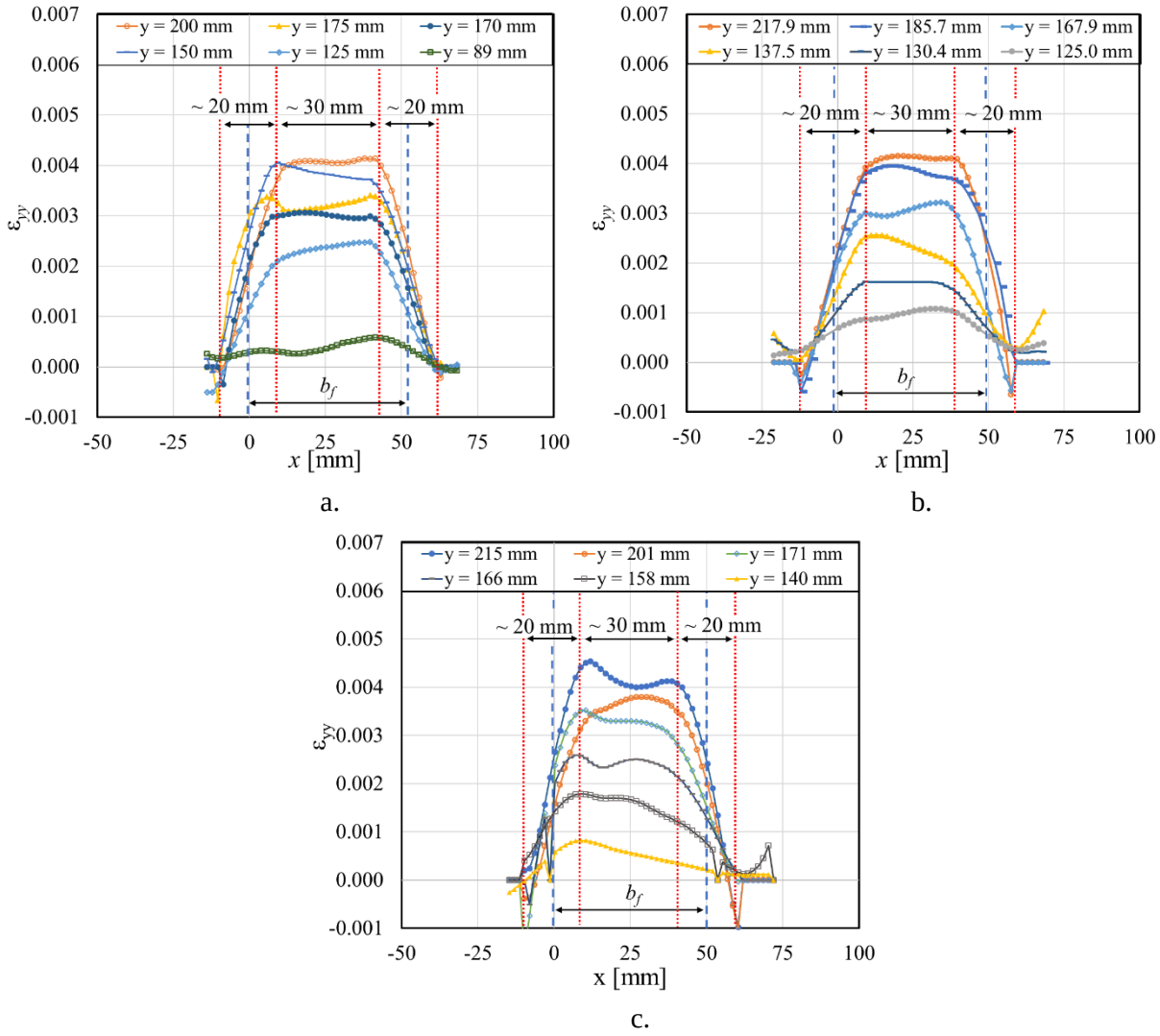

Figure 64. Longitudinal strains across the width of the composite strip for specimen DS_300_50_HD_D_B_2 (a), DS_300_50_UHD_D_B_5 (b), and DS_300_50_HD_D_S_1 (c).

For S-face specimens and B-face specimens the load-carrying capacity per unit width when b_f/b = 1 from Eq. (34) is lower than the value predicted by Eq. (55). It should be observed once again that both for the evaluation of P_{theor} and G_F the fracture mechanics formulation requires the use of the elastic modulus of the composite material instead of the elastic modulus of the fibers. However, if the elastic modulus of the composite referred to the bare fibers ($E_{f,SRP}^{HD}$ = 258 GPa) is employed to evaluate the load-carrying capacity per unit width when b_f/b = 1 via Eq. (34), a much higher value is obtained compared with the one predicted by Eq. (55) (point V in Figure 63c).This circumstance can be in part explained by referring to what previously observed, i.e. Eq. (34) doesn't take into account the high gradients of longitudinal strain component close to the edges of the composite strip. In addition, it should be noted that the

analytical evaluation via Eq. (34) of the load per unit width when b_f/b = 1 is valid only under the hypothesis that the fracture process occurs in a thin layer of concrete and only a small portion of the substrate beneath the strip is involved in the shear transfer. It is likely that when the width of the composite strip is equal or close to the width of the concrete prism, Eq. (34) needs to be modified or it is not applicable at all.

4.1.1.13 Alternative method to determine the interfacial fracture energy G_F from the load response of single-lap shear tests

At a generic point of the load response of a single-lap shear test defined by the value g^* of the global slip, after the debonding phenomenon has already started, the energy supply is represented by the area $W\left(g^*\right)$ under the applied load-global slip response up to that point of the response:

$$W\left(g^*\right) = \int_0^{g^*} P\mathrm{d}g \tag{58}$$

The already debonded area at that point of the load response has a length equal to L^*. The energy supply is partially used as stored elastic energy $U_e^{L^*}$ in the portion of the strip that has debonded:

$$U_e^{L^*} = \frac{1}{2}\frac{\left(P_{crit}\right)^2}{E_f b_f t_{f,\mathrm{A}}^*} L^* \tag{59}$$

In order to be consistent with the previous sections of this dissertation, the elastic modulus and equivalent thickness of the fibers will be used in this section unless otherwise specified.
Another portion of the energy supply is used to engage the portion of the bonded area, named STZ in section 4.1.1.6, through interfacial shear stresses:

$$W^{(\ell - L^*)} = \int_0^{s_f} P\mathrm{d}g \tag{60}$$

Where s_f is the maximum value of the slip beyond which complete separation of the SRP from concrete occurs. Finally, part of the energy supply is consumed in the fracture process that results in the debonding of the portion of the strip of length L^*. Thus, the energy balance yields:

$$W\left(g^*\right) - U_e^{L^*} - W^{\left(\ell - L^*\right)} = G_F b_f L^* \tag{61}$$

Dissipation phenomena as well as elastic energy stored in the bulk of the concrete prism are neglected. This energy balance can be used as an alternative method to determine the interfacial fracture energy G_F. In this paper, the authors selected arbitrarily $g^* = g_2$ and considered only those specimens with DIC in order to be able to determine the length L^*. As an example, $W\left(g^*\right)$ is shown in Figure 65a for specimen DS_300_50_UHD_D_B_5. Whereas, the elastic energy stored in the debonded portion of the strip is shown in Figure 65b for the same specimen. The strain profile fitted by function (14) and corresponding to point E, which also corresponds to the scenario $g^* = g_2$, is shown in Figure 58a and again in Figure 66. Figure 66 allows to determine the length L^*. The fracture energy obtained from Equation (61) is provided in Table 17.

Table 17. Alternative methods to determine the fracture energy.

Specimen Name	$G_F = \frac{W(g^*) - U_E^{L^*} - W^{(\ell - L^*)}}{b_f L^*}$ Eq. (61) [N/mm]	$G_F = \int_0^\infty \tau_{zy}(s)ds$ Eq. (33) Strain function polynomial [N/mm]	$G_F^{Pcrit} = \frac{P_{crit}^2}{2E_f t_{f,A}^* b_f^2}$ Eq. (39) [N/mm]	$G_F^{Pcrit} = \frac{P_{crit}^2}{2E_{f,SRP}^A t_{f,A}^* b_f^2}$ Eq. (62) [N/mm]	$G_F = k_b k_G \sqrt{f_{cm} f_{ctm}}$ Eq. (63) [N/mm]
DS_300_30_HD_D_S_1	0.73	0.44	0.65	0.48	0.29
DS_300_30_HD_D_S_2	0.78	0.37	0.64	0.47	0.29
DS_300_30_HD_D_S_3	0.80	0.45	0.57	0.42	0.29
DS_300_30_HD_D_S_4	0.44	0.31	0.46	0.34	0.29
DS_300_30_HD_D_S_5	0.50	0.27	0.44	0.32	0.29
DS_300_30_HD_D_B_2	1.37	0.64	0.77	0.57	0.29
DS_300_30_HD_D_B_3	0.87	0.71	0.88	0.65	0.29
DS_300_40_HD_D_S_1	0.51	0.33	0.45	0.33	0.29
DS_200_40_HD_D_S_2	0.21	0.32	0.53	0.39	0.29
DS_200_40_HD_D_S_3	0.19	0.31	0.47	0.34	0.29
DS_200_40_HD_D_S_4	0.81	0.35	0.53	0.39	0.29
DS_300_40_HD_D_B_2	0.55	0.51	0.71	0.52	0.29
DS_300_40_HD_D_B_3	0.93	0.76	0.88	0.65	0.29
DS_300_50_HD_D_S_1	0.58	0.44	0.60	0.44	0.29
DS_300_50_HD_D_S_2	0.55	0.40	0.58	0.42	0.29
DS_300_50_HD_D_S_3	0.98	0.44	0.59	0.43	0.29
DS_300_50_HD_D_S_4	0.50	0.32	0.42	0.31	0.29

DS_300_50_HD_D_S_5	0.49	0.35	0.50	0.37	0.29
DS_200_50_HD_D_S_7	0.68	0.40	0.56	0.41	0.29
DS_300_50_HD_D_S_10R_2	1.58	0.81	0.88	0.65	0.29
DS_300_50_HD_D_S_10R_3	0.62	0.57	0.76	0.56	0.29
DS_300_50_HD_D_B_2	0.46	0.43	0.61	0.45	0.29
DS_300_50_HD_D_B_3	0.53	0.44	0.57	0.42	0.29
DS_200_50_HD_D_B_4	0.81	0.65	0.78	0.57	0.29
DS_300_75_HD_D_S_1	0.52	0.35	0.55	0.40	0.29
DS_300_75_HD_D_S_2	0.59	0.28	0.40	0.30	0.29
DS_300_75_HD_D_S_3	2.65	0.46	0.65	0.48	0.29
DS_300_75_HD_D_S_4	0.52	0.35	0.52	0.38	0.29
DS_300_75_HD_D_B_2	3.36	0.76	0.84	0.62	0.29
DS_300_75_HD_D_B_3	0.75	0.53	0.70	0.52	0.29
DS_300_90_HD_D_B_1	0.74	0.58	0.78	0.57	0.29
DS_300_90_HD_D_B_3	0.65	0.49	0.79	0.58	0.29
DS_300_50_UHD_D_B_3	0.70	0.54	0.71	0.57	0.29
DS_300_50_UHD_D_B_4	0.63	0.58	0.58	0.47	0.29
DS_300_50_UHD_D_B_5	0.61	0.44	0.58	0.47	0.29

It is important to observe that the value obtained from equation (61), reported in Table 17, is not a pure fracture energy because it does not exclude the width effect. The values obtained from Eq. (61) are higher than the values of the fracture energy determined from the direct procedure presented in section 4.1.1.8, which consists of fitting the experimental strain profile and computing the fracture energy from Eq. (33). As a comparison, Table 17 provides the values of the fracture energy obtained from Eq. (33) and employing the fitting function (19) proposed by Dai et al. [35]. These values of the fracture energy were included in Table 15 and are reported in Table 17 for the sake of clarity.

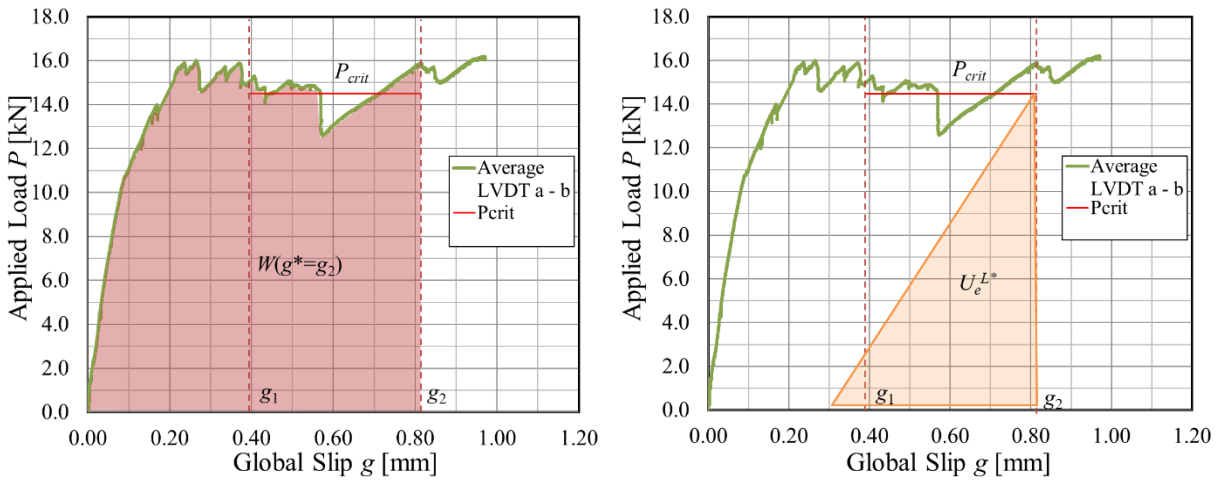

Figure 65. Load response of specimen DS_300_50_UHD_D_B_5: a) Energy supply, $W\left(g^{*}=g_{2}\right)$, represented by the area under the load-global slip response to reach the global slip g_2; b) Elastic energy, $U_e^{L^*}$, stored in the portion of the SRP strip that has debonded when $g=g_2$.

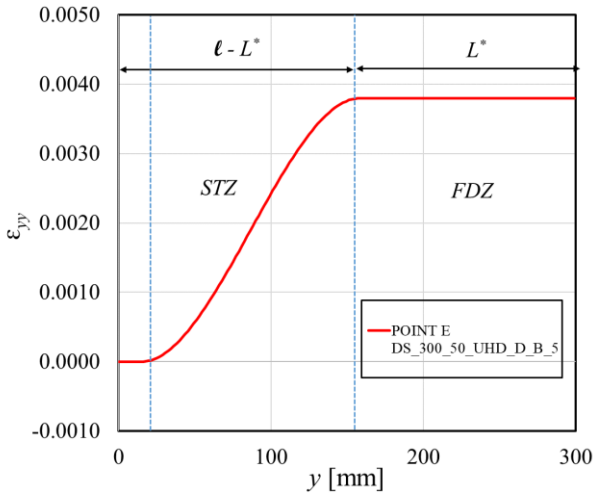

Figure 66 Strain profile fitted by function (14) corresponding to point E of the load response of Figure 56a.

The interfacial fracture energy can be obtained also from the load-carrying capacity P_{crit}, through Equation (39). The fracture energy determined from Eq. (39) should be higher than the one obtained from the direct procedure because of the width effect. Hence, the value of the fracture energy obtained from Eq. (39) is not a pure fracture energy as pointed out in [10]. The values of the fracture energy computed from Eq. (39) are provided in Table 17 for comparison.

In order to compare the fracture energy obtained experimentally with the formula proposed by the Italian Guidelines [2], Equation (39) will be re-written by using the elastic modulus $E^{\mathrm{A}}_{f,SRP}$ of the composite referred to the bare fibers (the notation was explained in section 3.3.6):

$$G_F^{Pcrit} = \frac{P_{crit}^2}{b_f^2 2E^{\mathrm{A}}_{f,SRP} t^*_{f,\mathrm{A}}} \tag{62}$$

Values of the fracture energy computed from Eq. (62) are reported in Table 17.
The Italian Guideline propose the following formula to compute the interfacial fracture energy, neglecting the confidence factor *FC* [2]:

$$G_F = k_b k_G \sqrt{f_{cm} f_{ctm}} \tag{63}$$

where:

$$k_b = \sqrt{\frac{2 - b_f/b}{1 + b_f/b}} \tag{64}$$

k_G is an empirical coefficient equal to 0.037 mm, while f_{cm} and f_{ctm} are the average compressive and tensile strength of concrete, respectively. The fracture energy computed from Eq. (63) is reported in Table 17. It should be observed that Eq. (63) includes factor k_b that takes into account the width effect. A comparison between the last two columns of Table 17 suggests that the value of coefficient k_G proposed in [2] can be safely applied to SRP composites bonded to concrete substrates.
It should be noted that if g^* is equal to g_u, which is the ultimate value of the global slip corresponding to the failure of the specimen, the energy balance could be written as:

$$W(g_u) - \frac{1}{2}\frac{(P_{crit})^2}{E_f b_f t^*_{f,\mathrm{A}}}\ell = G_F b_f \ell \tag{65}$$

Equation (65) corresponds to the scenario in which the SRP strip is about to fully debond and only an infinitesimal amount of the bonded area is still attached. $W(g_u)$ is shown in Figure 67a for specimen DS_300_50_UHD_D_B_5, and the elastic energy stored in the entire strip is shown in Figure 67b for the same specimen. The fracture energy obtained from Equation (65) is much lower than the values obtained

above from Equation (33). Unfortunately, even though the use of Equation (65) is appealing because it does not require the measurement of the strain along the SRP strip, it does not take into account that at the end of the test the fracture process is unstable and a snap-back phenomenon [106] should be expected if the test were controlled by the displacement at the free end. Thus, Equation (65) should not be used to compute the fracture energy.

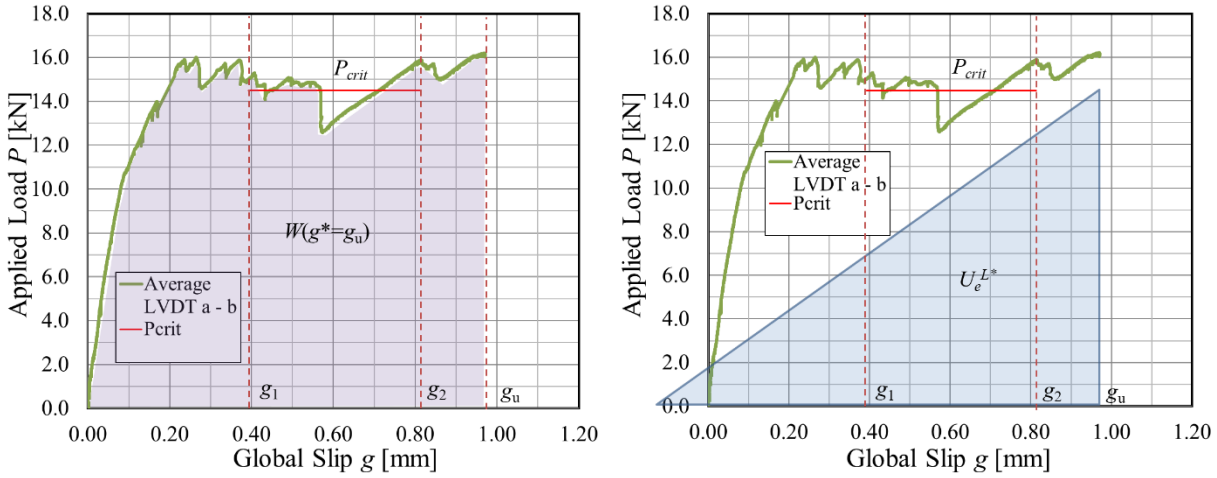

a. b.

Figure 67 Load response for specimen DS_300_50_UHD_D_B_5: a) Energy supply, $W\left(g^{*}=g_{u}\right)$, represented by the area under the load-global slip response to reach the global slip g_u. b) Elastic energy, $U_e^{L^*}$, stored in the portion of the SRP strip that has debonded when $g=g_u$.

4.1.1.14 Simulation of the bond behavior of SRP-concrete joints using lattice discrete particle model (LDPM)

In this section, the concrete behavior was simulated using the lattice discrete particle model (LDPM), developed by Cusatis et al. [107]. LDPM is a meso-scale model that simulates the failure behavior of concrete by modelling the coarse aggregates and the cementitious paste. In order to reproduce the concrete meso-structure, the coarse aggregate spheres (particles) are generated into the volume of the concrete prism by a try-and-reject random procedure. For the particle generation, a set of mix-design parameters are needed, i.e. the cement content, c, the water-to-cement ratio w/c, the aggregate to cement ratio a/c, the maximum aggregate size d_a, the minimum aggregate size, d_0, and the Fuller coefficient, η_f. A random number of coarse aggregate particles, ranging from d_0 to d_a, is thus generated according to the Fuller curve. Zero-radius aggregate pieces (nodes) are placed in the external surface. The particles are finally

placed throughout the volume of the prism one by one, using a procedure introduced by Bažant et al. [108], and also used by Cusatis et al. [109]. Once the particles are placed in the concrete volume, the lattice system that connect the aggregate particles is achieved through a Delaunay tetrahedralization of the particle centers. Following this procedure, a polyhedral cell, containing each particle, is obtained. The facets of these polyhedral cells are the surfaces along which forces are exchanged and where the damage can localize. The facets simulate the cementitious paste, and represent the locations in the concrete volume where fracture initiates and propagates. The governing equations of the model are based on the four-particle tetrahedron, that is the basic unit of the model. The four-particle tetrahedron is divided in four subdomains. In each subdomain, the displacement field is defined according to the rigid-body kinematics. Considering a displacement jump, $\mathbf{u}_{ck}$, at the centroid of each facet, the corresponding strain components can be defined as:

$$\varepsilon_{Nk} = \frac{\mathbf{n}_k^T \mathbf{u}_{ck}}{\ell_e}; \quad \varepsilon_{Mk} = \frac{\mathbf{m}_k^T \mathbf{u}_{ck}}{\ell_e}; \quad \varepsilon_{Lk} = \frac{\mathbf{l}_k^T \mathbf{u}_{ck}}{\ell_e}; \tag{66}$$

Where ℓ_e is the interparticle distance, and **n**, **m**, and **l** are unit vectors defining a local system for each facet. Meso-scale constitutive law are assigned to each facet and the equilibrium is imposed through the Principle of Virtual Work (PVV). The elastic behavior is formulated assuming that the normal and shear stresses are proportional to the corresponding strains:

$$\sigma_N = E_N \varepsilon_N; \quad \sigma_M = E_T \varepsilon_M; \quad \sigma_L = E_T \varepsilon_L; \tag{67}$$

Where $E_N = E_0$ (E_0, effective normal modulus), $E_T = \alpha E_0$ (α, shear-normal coupling parameter).
The LDPM formulation considers three different mesoscale phenomena beyond the elastic limit: (*i*) fracturing and cohesive behavior under tension and tension/shear; (*ii*) pore collapse and material compaction under high compressive stresses; and (*iii*) frictional behavior.

Fracturing behavior

The fracturing behavior, characterized by tensile normal strains ($\varepsilon_N > 0$), can be formulated through effective strain, $\varepsilon = \sqrt{\varepsilon_N^2 + \alpha\left(\varepsilon_M^2 + \varepsilon_L^2\right)}$, and effective stress, $\sigma = \sqrt{\sigma_N^2 + \left(\sigma_M^2 + \sigma_L^2\right)/\alpha}$, which allow to define the relationship between normal and shear stresses versus normal and shear strains using damage-type constitutive equations:

$$\sigma_N = \sigma\frac{\varepsilon_N}{\varepsilon};\quad \sigma_M = \sigma\frac{\alpha\varepsilon_M}{\varepsilon};\quad \sigma_L = \sigma\frac{\alpha\varepsilon_L}{\varepsilon};$$

(68)

The effective stress σ is incrementally elastic ($\dot{\sigma} = E_0\dot{\varepsilon}$) and can vary from 0 to the boundary limit $\sigma_{bt}(\varepsilon,\omega)$ expressed as:

$$\sigma_{bt}(\varepsilon,\omega) = \sigma_0(\omega)\exp\left[-H_0(\omega)\frac{\langle\varepsilon_{\max} - \varepsilon_0(\omega)\rangle}{\sigma_0(\omega)}\right] \tag{69}$$

Where the brackets $\langle\cdot\rangle$ are used in Macaulay sense: $\langle x\rangle = \max\{x,0\}$. The interaction between shear and normal loadings is represented by the coupling variable ω ($\tan\omega = \varepsilon_N \Big/ \left(\sqrt{\alpha}\varepsilon_T\right) = \sigma_N\sqrt{\alpha}\sigma_T$), where $\varepsilon_T = \sqrt{\varepsilon_M^2 + \varepsilon_L^2}$ is the total shear strain, and $\sigma_T = \sqrt{\sigma_M^2 + \sigma_L^2}$ is the total shear stress. The strength limit for the effective stress, $\sigma_0(\omega)$ is defined as:

$$\sigma_0(\omega) = \sigma_t\frac{-\sin(\omega) + \sqrt{\sin^2(\omega) + 4\alpha\cos^2(\omega)/r_{st}^2}}{2\alpha\cos^2(\omega)/r_{st}^2} \tag{70}$$

In which $r_{st} = \sigma_s/\sigma_t$ is the ratio between the shear strength, σ_s, and the tensile strength, σ_t. When the maximum effective strain reaches its elastic limit, the boundary σ_{bt} starts to decay with a post-peak slope, $H_0(\omega) = H_t(2\omega/\pi)^{n_t}$, that is assumed to be a power function of the variable ω. H_t is the softening modulus in pure tension (ω = π/2).

Pore collapse and material compaction

The LDPM formulation simulates the pore collapse and material compaction by introducing a strain-hardening normal boundary in compression σ_{bc} that limits the compressive normal stress component at the facet level. σ_{bc} is a function of the volumetric strain $\varepsilon_V = (V - V_0)/V_0$ (V and V_0 are the current and initial volume of the tetrahedron, respectively), and deviatoric strain $\varepsilon_D = \varepsilon_N - \varepsilon_V$. For a given deviatoric-to-volumetric strain ratio $r_{DV} = \varepsilon_D/\varepsilon_V$, the strain-hardening normal boundary can be defined as:

$$\sigma_{bc}\left(\varepsilon_D,\varepsilon_V\right)=$$
$$\begin{cases} \sigma_{c0} & for \quad -\varepsilon_{DV}\le 0 \\ \sigma_{c0}+\left\langle -\varepsilon_{DV}-\varepsilon_{c0}\right\rangle H_c\left(r_{DV}\right) & for \quad 0\le -\varepsilon_{DV}\le \varepsilon_{c1} \\ \sigma_{c1}\left(r_{DV}\right)\exp\left[\left(-\varepsilon_{DV}-\varepsilon_{c1}\right)H_c\left(r_{DV}\right)/\sigma_{c1}\left(r_{DV}\right)\right] & otherwise \end{cases} \tag{71}$$

Where $\varepsilon_{DV}=\varepsilon_V+\beta\varepsilon_D$ (β is a material parameter), $\varepsilon_{c0}=\sigma_{c0}/E_0$ is the compaction strain at the beginning of the pore collapse, $H_c(r_{DV})$ the initial hardening modulus, $\varepsilon_{c1}=\kappa_{c0}\varepsilon_{c0}$ the compaction strain at which hardening begins, κ_{c0} the material parameter governing the rehardening and $\sigma_{c1}(r_{DV})=\sigma_{c0}+\left(\varepsilon_{c1}-\varepsilon_{c0}\right)H_c\left(r_{DV}\right)$.

As explained in [107], the slope of the initial hardening modulus needs to tend to zero, and this condition is obtained imposing $H_c\left(r_{DV}\right)=H_{c0}\big/\left(1+\kappa_{c2}\left\langle r_{DV}-\kappa_{c1}\right\rangle\right)$, where H_{c0}, κ_{c1}, and κ_{c2} are assumed to be material parameters.

Frictional behavior

Due to frictional effects, the shear strength of concrete (in presence of compressive stresses) tends to increase. The frictional phenomenon is simulated using the incremental plasticity, evaluating the incremental stresses as $\dot{\sigma}_M=E_T\left(\dot{\varepsilon}_M-\dot{\varepsilon}_M^p\right)$ and $\dot{\sigma}_L=E_T\left(\dot{\varepsilon}_L-\dot{\varepsilon}_L^p\right)$. The plastic strain increments can be defined as $\dot{\varepsilon}_M^p=\dot{\lambda}\partial\varphi/\partial\sigma_M$ and $\dot{\varepsilon}_L^p=\dot{\lambda}\partial\varphi/\partial\sigma_L$. The plastic potential is defined as $\varphi=\sqrt{\sigma_M^2+\sigma_L^2}-\sigma_{bs}\left(\sigma_N\right)$ in which the formulation of the shear strength σ_{bs} is characterized by a nonlinear frictional law:

$$\sigma_{bs}\left(\sigma_N\right)=\sigma_s+\left(\mu_0-\mu_\infty\right)\sigma_{N0}-\mu_\infty\sigma_N-\left(\mu_0-\mu_\infty\right)\sigma_{N0}\exp\left(\sigma_N/\sigma_0\right) \tag{72}$$

Where σ_s is the cohesion, μ_0 and μ_∞ are the initial and final friction coefficients and σ_{N0} is the normal stress at which the friction coefficient transitions from μ_0 to μ_∞.

4.1.1.14.1 Modification of the fracturing behavior: shear softening

In this work the LDPM formulation proposed by Cusatis et al. [107] was modified in order to take into account the shear softening behavior when the total shear strain ε_T reached the elastic limit. In the original

formulation by Cusatis et al. [107], when the total shear strain was higher than the elastic strain limit, the normal stresses and the total shear stresses were not influenced and continued to assume a constant value equal to the one corresponding to the elastic limit, showing a perfect plastic behavior in shear. In the present work, a reduction factor, *RF*, is introduced in order to take into account the shear stress reduction when the total shear strain overcome the elastic limit. The reduction factor is needed to simulate single-lap shear tests since the debonding phenomenon is primary governed by shear stresses and shear strains. The inelastic shear strains can be defined as:

$$\varepsilon_{T,inel} = \varepsilon_T - \varepsilon_{el,lim} \tag{73}$$

Where $\varepsilon_{el,lim}$ indicates the elastic strain limit. Once the inelastic shear strain was evaluated, the reduction factor *RF* was calculated as a function of the facet interparticle distance, ℓ_e, (Figure 68c) and of the facet area, A_{fac}, obtaining:

$$RF = \min\left\{1;1-\left(\frac{RFS\cdot \ell_e \cdot \varepsilon_{T,inel}}{\sqrt{A_{fac}}}\right)^{RFE}\right\} \tag{74}$$

Where the reduction factor scale (*RFS*) and the reduction factor exponent (*RFE*) are two coefficients that can vary from 0 to infinity and should be calibrated based on the problem that is analyzed.

The *RFS* acted on the slope of the shear softening behavior, while the *RFE* acted on the shape of the softening branch (Figure 68a,b). Based on the simulations performed in this study, a RFS equal to 1.6 and a RFE equal to 0.6 were used. The influence of the RFS and RFE on the load responses obtained from numerical simulations was not investigated in this dissertation. The reduction factor was introduced only when the total shear strain overcame the elastic limit, therefore in Eq. (74) was assumed equal to 1 when the total shear strain was below the elastic limit.

The normal and shear stresses when the total strain is greater than the elastic limit can be evaluated introducing the reduction factor RF:

$$\begin{aligned}\sigma_N &= RF\cdot\sigma_{N,\lim}\\ \sigma_M &= RF\cdot\sigma_{M,\lim}\\ \sigma_L &= RF\cdot\sigma_{L,\lim}\end{aligned} \tag{75}$$

Where $\sigma_{N,lim}$, $\sigma_{M,lim}$, and $\sigma_{L,lim}$ are the normal and shear stresses when the total strain is equal to the elastic limit $\varepsilon_{el,lim}$.

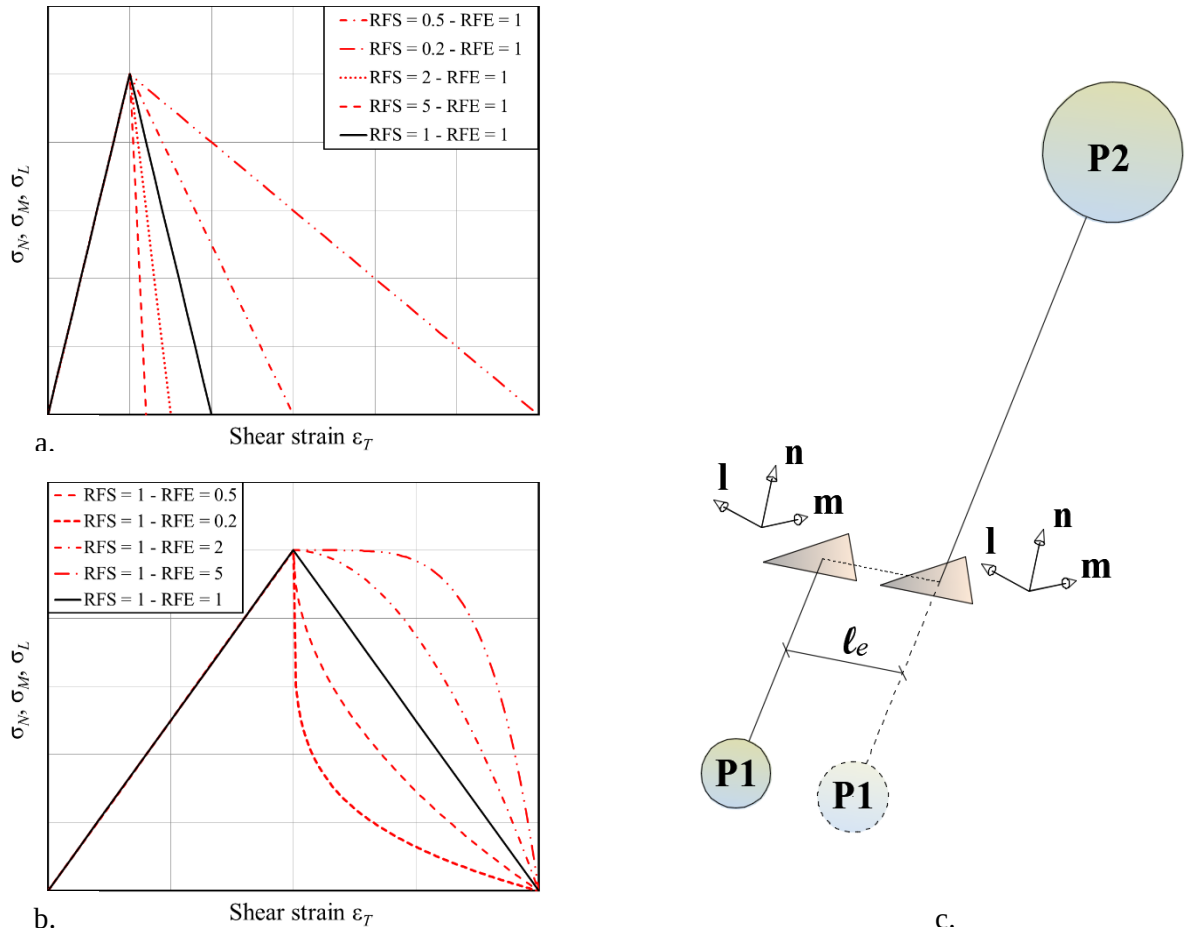

Figure 68. Variation of the shear softening behavior changing the RFS (a) and the RFE (b). Effect of meso-scale pure shear loading on LDPM facets (c).

4.1.1.14.2 Discretization

The concrete used in the experimental tests was calibrated with LDPM, based on the results obtained from the material characterization described in section 3.1.1. The first step of the concrete calibration consisted in the definition of the minimum aggregate size used in simulations, d_0. The choose of d_0 depended on the failure modes observed in single-lap shear tests. As described in section 4.1.1.4, for each specimen the failure mode consisted in the detachment of the SRP strip from the concrete substrate. A thin layer of concrete, with a thickness equal to approximately 1.6 mm, remained attached to the composite strip in the region corresponding to the bonded area. Since the interfacial fracture occurred in a thin layer of concrete close to the prism surface, the choose of the minimum aggregate size used in simulations was fundamental in order to obtain a correct prediction of the debonding load (or plateau load), P_{crit}. A preliminary study was conducted by the authors using LDPM to simulate single-lap shear tests, varying the size of d_0. Simulations conducted with three different minimum aggregate sizes (8 mm,

4 mm, and 2 mm), predicted high values of P_{crit}, which resulted larger than the average value obtained from experimental tests. In particular, an increase in the minimum aggregate size caused an increase in the plateau load. This fact can be explained considering that if a larger value of d_0 is employed, the interfacial crack needs more energy to initiate and propagate. Due to the high value of d_0 the crack has to propagate deeply in the concrete volume and has to fracture a larger area of concrete, determining high values of P_{crit}. In order to obtain a correct prediction of the plateau load, simulations were performed using a minimum aggregate size equal to 1.6 mm, in order to match the thickness of the concrete that remained attached to the SRP after single-lap shear tests were performed. A maximum aggregate size equal to 15 mm was chosen in simulations, in order to match the maximum size of the aggregates employed during the concrete casting.

4.1.1.14.3 Compression and three-point bending tests

Once the mix design parameters of the concrete were defined, the concrete was calibrated considering the results obtained from compression tests performed on 150 mm side cubes and fracture mechanics tests performed on notched concrete prisms. Since for the compressive tests no experimental tests were performed at the age of testing, the simulations were performed in order to match the cubic compressive strength at 300 days predicted by fitting the compressive strength versus time response (section 3.1.1). The simulations of three-point bending (TPB) tests were performed in order to match the entire load-displacement response of the 150 mm (width) × 150 mm (depth) × 600 mm (length) notched concrete specimens that were tested approximately at the same age of the single-lap shear tests. The simulations of both compressive tests and TPB tests were performed varying three mesoscale static parameters of concrete, i.e. the mesoscale tensile strength, the mesoscale shear-strength ratio and the mesoscale initial friction. Once the mesoscale static parameters that provided the best match with the material characterization tests were determined, five simulations of compression tests and five TPB tests were performed using a different distribution of the aggregates in the concrete volume.

The comparison between the average value of the compressive strength determined through numerical simulations at 300 days and the predicted trend determined from experimental tests is showed in Figure 69a. The average compressive strength determined from simulations resulted equal to 30.7 MPa, i.e. 0.2% lower than the estimated experimental value at 300 days. The average peak load obtained from simulations resulted equal to 8.48 kN, i.e. 2.8% greater than the average experimental value (equal to 8.25 kN).

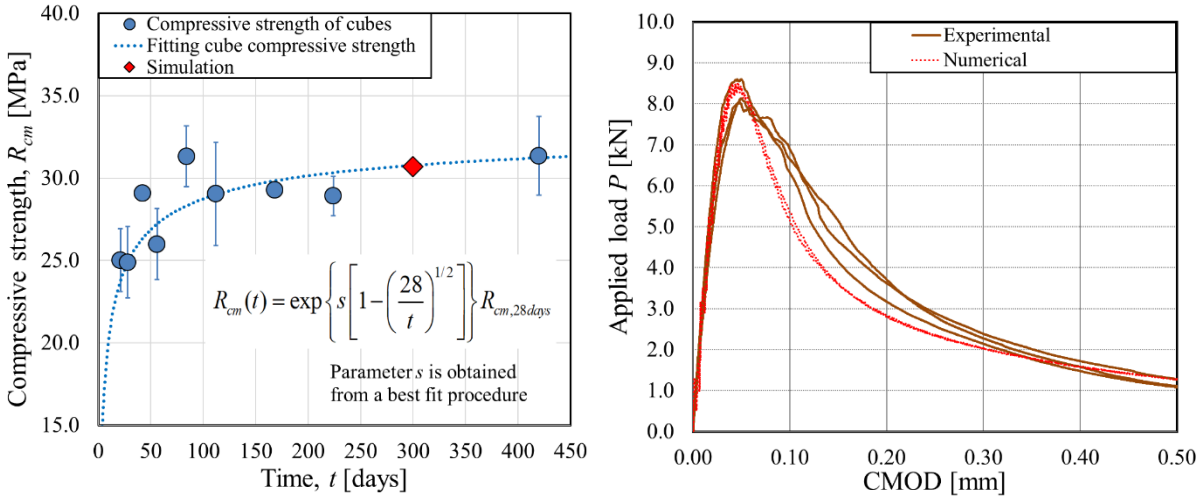

a. b.

Figure 69. a) Compressive strength versus time response; b) Fracture mechanics tests response.

4.1.1.14.4 SRP strip modeling

The numerical analysis was performed to simulate specimens strengthened with HD steel fibers. The SRP strip was modelled using quadrilateral shell elements. In particular, QPH 4-node shell elements with physical hourglass control were employed, adopting the formulation proposed by [110]. The SRP strip was discretized using square shell elements with a side equal to approximatively 3 mm. The behavior of the shell elements was linear-elastic. A thickness equal to 4 mm, i.e. the nominal thickness employed in experimental tests, was assigned to the shell elements. The elastic modulus used for the shell elements, E_{shell}, was determined referring the average value $\overline{E_{f,SRP}^{HD}}$ obtained experimentally to the nominal area of the SRP strip, considering a nominal thickness ($t_{nominal}$) of 4 mm:

$$E_{shell} = \frac{\overline{E_{f,SRP}^{HD}} \cdot t_{f,HD}^{*}}{t_{nominal}} = 16.4\text{GPa} \tag{76}$$

In order to verify the value obtained from experimental results, the elastic modulus of the composite strip was also determined theoretically, using the following relation:

$$E_{theor,shell} = E_f \frac{t_{f,HD}^{*}}{t_{nominal}} + E_{m,c} \frac{t_{nominal} - t_{f,HD}^{*}}{t_{nominal}} = 17.0\text{GPa} \tag{77}$$

Since the theoretical value $E_{theor,shell}$ is only the 4% higher than the experimental value E_{shell}, the latter was considered reliable and used in numerical simulations.

4.1.1.14.5 SRP-concrete joint modeling

The SRP strip was bonded to the concrete prism without using any interface (Figure 70a). Since the fracture process developed on the concrete substrate, as observed from the failure modes presented in section 4.1.1.4, the SRP-concrete joint was modelled supposing a perfect bond between the SRP strip and the concrete surface. The perfect bond was achieved using a master-slave formulation. The concrete particles, located on the external surface in the bonded area were considered as master particles, while the quadrilateral shells, used to model the SRP strip, were considered as slave elements along the bonded region. Relative rotations between the master particles and the slave shell elements were not allowed. The nodes of the shell were placed on the same plane of the concrete surface, i.e. the midplane of the SRP strip was considered exactly on the external concrete surface, neglecting the offset due to the thickness of the shell. Since the present dissertation aims to investigate the capability of the model to predict the overall behavior of the debonding phenomenon, secondary-order effects, as the moment due to the 2 mm eccentricity between the midplane of the SRP strip and the concrete surface, will not be discussed.

4.1.1.14.6 Numerical analysis

In this section the results of numerical simulations are presented. The entire single-lap shear test set-up was modeled. Finite element method (FEM) formulation was adopted for the steel elements of the test set-up, i.e. top and bottom steel plates, and the four bars connecting the steel plates. The nodes of the steel cylinder fixed to the bottom plate were restrained against movements and rotations in each direction in order to simulate the clamping of the testing machine grips. The 4 steel bars were connected both to the top and to the bottom plate using a master slave formulation. The nodes of the bars located in the holes of the steel plates were considered as slaves and they were tied to the corresponding points (master) inside the hexahedral element meshes used to model the steel plates. Friction was assigned between the concrete nodes of the square faces of the concrete prism and the faces of the steel plates. The resistance to sliding within the plane was treated with a stick-slip friction model. When the node is sliding, the friction factor f_f is computed using the expression:

$$f_f = f_k + (f_s - f_k)\frac{A}{A+d} \tag{78}$$

Where f_k is the kinematic friction factor, f_s is the static friction factor, A is a characteristic length (derived from fitting available test data), and d is the cumulative slip resulting from slippage computed during the simulation. f_k, f_s and A were assumed equal to 0.13, 0.015, and 1.3 mm, respectively.

Simulations were performed increasing the displacement of the SRP shell. The displacement was increased at a constant rate and applied to the first alignment of the shell nodes, characterized by the same coordinate y, just outside the beginning of the bonded region (loaded end).

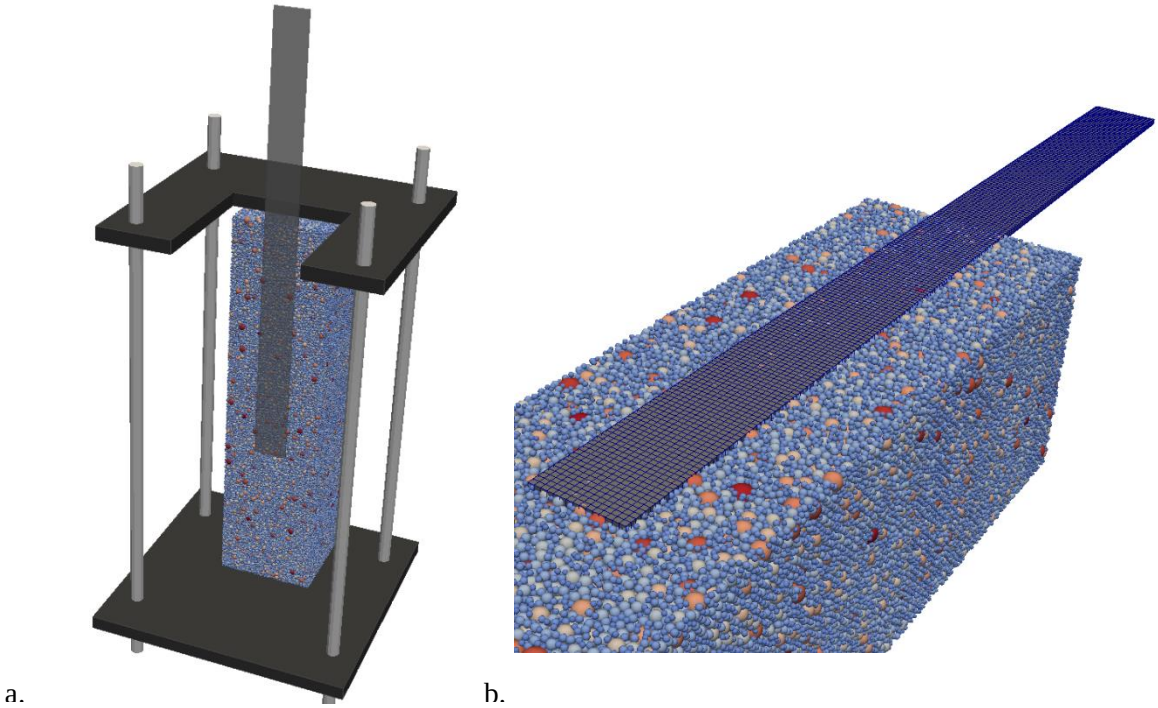

a. b.

Figure 70. a) Direct single-lap shear tests modeled for the numerical analysis; b) Particular of the SRP-concrete joint modeled using LDPM.

Simulations were performed using a standard bonded length equal to 300 mm and eight different bonded widths, i.e. 15 mm, 30 mm, 40 mm, 50 mm, 75 mm, 90 mm, 120 mm, and 150 mm. For each bonded width, five different simulations were performed varying the disposition of the aggregates in the concrete prism. A representative load response obtained from the numerical analysis for a bonded width equal to 50 mm is represented in Figure 71a. It can be noted that, similarly to what observed in section 4.1.1.3, the numerical load response had an initial linear portion, followed by a non-linear branch until the peak load was reached. After the peak was reached, the load response had an approximatively constant portion until failure. The constant plateau was characterized by little drops due to the non-uniform distribution of the aggregates along the bonded region that implies different values of the load needed to propagate the

cohesive crack. For each simulation, the failure consisted in the detachment of the composite strip from the concrete prism. Similar load responses can be observed for representative simulations of the other widths, showed in Figure 71b, that reported the load per unit width – global slip response. Simulations performed with a bonded width equal to 15 mm showed the highest values of load carrying capacity per unit width (average value equal to 370 N/mm) and the highest value of global slip at failure (average value equal to 1.40 mm). High values of the load carry capacity per unit width can be observed also for specimens with a bonded width equal to 30 mm, while for the remaining widths no large changes in the plateau value were observed.

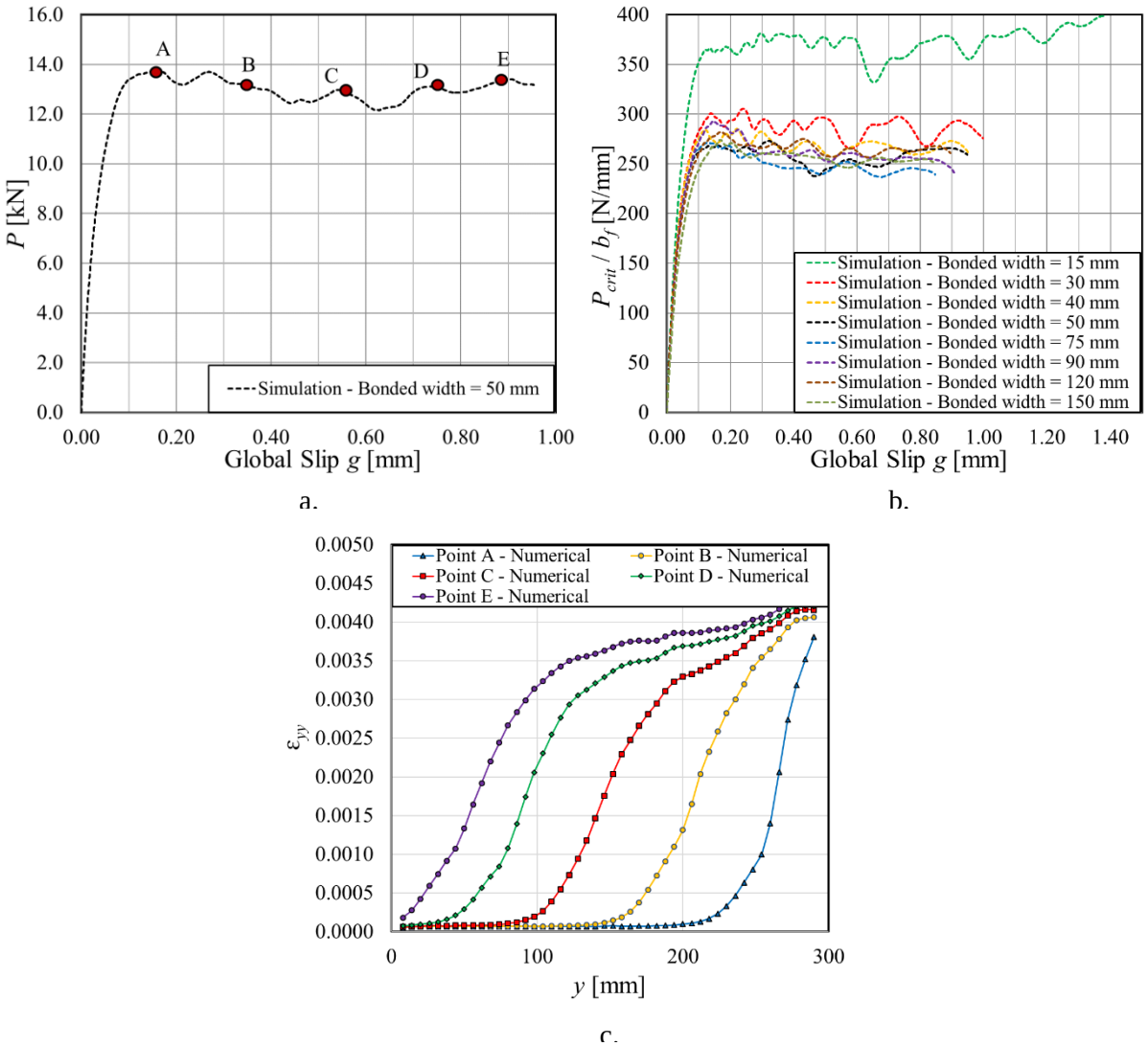

Figure 71. a) Numerical simulation of a specimen with a bonded width equal to 50 mm; b) Representative load responses of numerical analysis performed using different widths; c) ε_{yy} strain profile corresponding to points A, B, C, D, and E of Figure 71a.

Table 18 reported the average value of the load carrying capacity per unit width for each group of simulations performed with the same bonded width. Similarly to what was done for experimental tests (see section 4.1.1.3), the value of P_{crit} was determined as the average value of the load in the global slip range [g_1,g_2], where the load maintained an almost constant value. For each bonded width, a global slip range [g_1,g_2] was determined, individuating directly on the numerical load-global slip response the interval where the load remained nominally constant. The global slip range [g_1,g_2] used for each bonded width simulated in the numerical analysis was reported in Table 18.

Figure 72 reported the fracture propagation in the concrete substrate for the simulation represented in Figure 71a. It can be noted as the interfacial cohesive crack propagated from the loaded end to the free end of the composite strip, damaging also the concrete adjacent to the SRP strip. The propagation of the cohesive crack can be observed also referring to the longitudinal strains ε_{yy} along the center line of the SRP strip in the numerical simulations (Figure 71a). The ε_{yy} profile was characterized by an S-shaped behavior that moved gradually from the loaded end to the free end of the strip. The portion of the strip characterized by the S-shaped strain profile was the region were the shear stresses were transferred. Analyzing the strain profile, it was possible to see that the debonding phenomenon propagated in a self-similar way from the loaded end to the free end of the SRP strip. This fact was observed also in experimental tests by Carloni et al. [92].

Table 18. Comparison between experimental and numerical results.

Bonded width	b_f/b [mm]	$\overline{P_{crit}^{Y,C}/b_{f,actual}}$ Face S [N/mm] (CoV)	$\overline{P_{crit}^{Y,C}/b_{f,actual}}$ Face B [N/mm] (CoV)	$\overline{P_{crit}^{Y}/b_f}$ Numerical [N/mm] (CoV)	Range [g_1,g_2] Numerical simulations [mm]
15 mm	0.1	270 (0.09)	329 (0.00)	370 (0.03)	[0.60,1.30]
30 mm	0.2	230 (0.09)	279 (0.04)	287 (0.03)	[0.20,1.00]
40 mm	0.27	218 (0.04)	277 (0.05)	269 (0.02)	[0.20,0.90]
50 mm	0.33	231 (0.07)	250 (0.07)	258 (0.00)	[0.20,0.90]
75 mm	0.5	225 (0.10)	272 (0.05)	246 (0.01)	[0.30,0.80]
90 mm	0.6	/	267 (0.05)	260 (0.01)	[0.30,0.80]
120 mm	0.8	/	/	259 (0.01)	[0.30,0.80]
150 mm	1.0	/	/	253 (0.01)	[0.30,0.80]

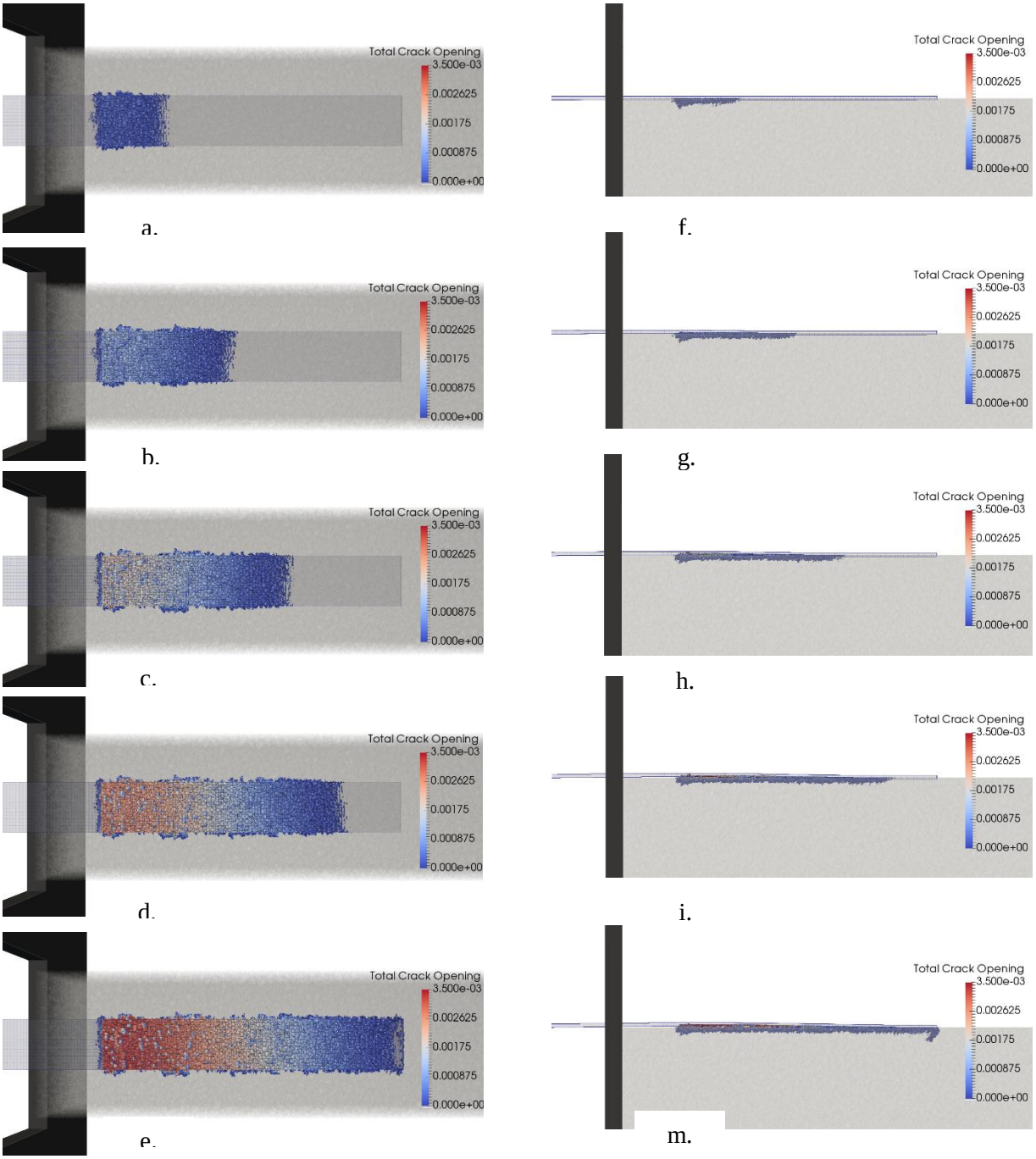

Figure 72. Plan view of the crack propagation in numerical analysis for point A (a), B (b), C (c), D (d), and E (e) of Figure 71a. Side view of the crack propagation in numerical analysis for point A (f), B (g), C (h), D (i), and E (m) of Figure 71a.

4.1.1.14.7 Comparison between experimental results and numerical analysis

The results obtained from numerical simulations (section 4.1.1.14.6) will be compared with the experimental results (section 4.1.1.3) in this section. Figure 73a-b showed a comparison between five numerical simulations conducted on a 50 mm-wide strip and the corresponding experimental results for S-face and B-face specimens, respectively. It can be observed that the numerical simulations are in good agreement with the experimental tests. In particular, the numerical response matched better the experimental data obtained for B-face specimens than the results obtained for S-face specimens. The average value of P_{crit} for a 50-mm wide strip is equal to 12.92 kN that is 0.8% lower than the average value $\overline{P}_{crit}^{50,B}$ obtained for B-face specimens (13.02 kN), and 7.8% higher than the average value $\overline{P}_{crit}^{50,S}$ obtained for S-face specimens (11.98 kN). This fact can be explained considering that in the numerical analysis the distribution of the aggregates in the concrete volume was performed without considering the influence of the mold configuration during the casting procedure. It has been observed by Carloni et al. [92] that S-face specimens presented a lower amount of aggregates on the concrete surface than B-face specimens, determining lower values of the load carrying capacity. Since the numerical model didn't take into account the low amount of large aggregates that characterized the surface of S-face specimens, numerical results will be closer to what obtained for B-face specimens. It is worth noting that load responses obtained from the numerical analysis showed a slightly higher initial stiffness than experimental tests. In numerical analysis, the global slip was measured considering the relative displacement between the nodes of the SRP shell where the constant displacement was applied and the nodes on the concrete surface corresponding to the locations of the actual LVDT holders. As described in section 4.1.1.2, the global slip in experimental tests was measured through two LVDTs that reacted off of a thin aluminum Ω-shaped plate. It is possible that in actual tests, the aluminum plate undergoes little out-of-plane rotations due to the set-up adjustments in the initial phases of the test. The little movements of the Ω-shaped plate determined a slight variation in the initial slope of the load response, determining probably the difference between the numerical and the experimental initial stiffness.

The average load carrying capacity per unit width obtained from numerical analysis, S-face specimens, and B-face specimens was showed in Figure 74 for different b_f/b ratios. Observing Figure 74 it is confirmed that results obtained from numerical simulations are closer to B-face specimens than to S-face specimens. Both from the numerical analysis and from experimental results, the load carrying capacity per unit width tends to decrease for increasing b_f/b ratios until a value of b_f/b equal to 0.33, after that the load carrying capacity per unit width seems to maintain a constant trend until a ratio b_f/b equal to 1. When the ratio b_f/b is equal to 0.1 a large scatter can be observed between the numerical results and the experimental ones.

Finally, a comparison can be done between the ε_{yy} profiles along the composite strip during the debonding phenomenon obtained from the numerical analysis and experimental tests. The ε_{yy} profile of specimen DS_300_50_HD_D_S_1 during the debonding phenomenon is compared with the strain profile at point C of the numerical simulation represented in Figure 71a. The ε_{yy} profile of experimental tests was obtained through the digital image correlation (DIC) analysis using the procedure described in [92]. A part for the inevitable scatter of the experimental values, due to the non-homogeneous surface, the shape and the strain values attained by numerical results are in good agreement with what obtained experimentally, confirming the capability of this model to reproduce the debonding phenomenon in SRP-concrete joints.

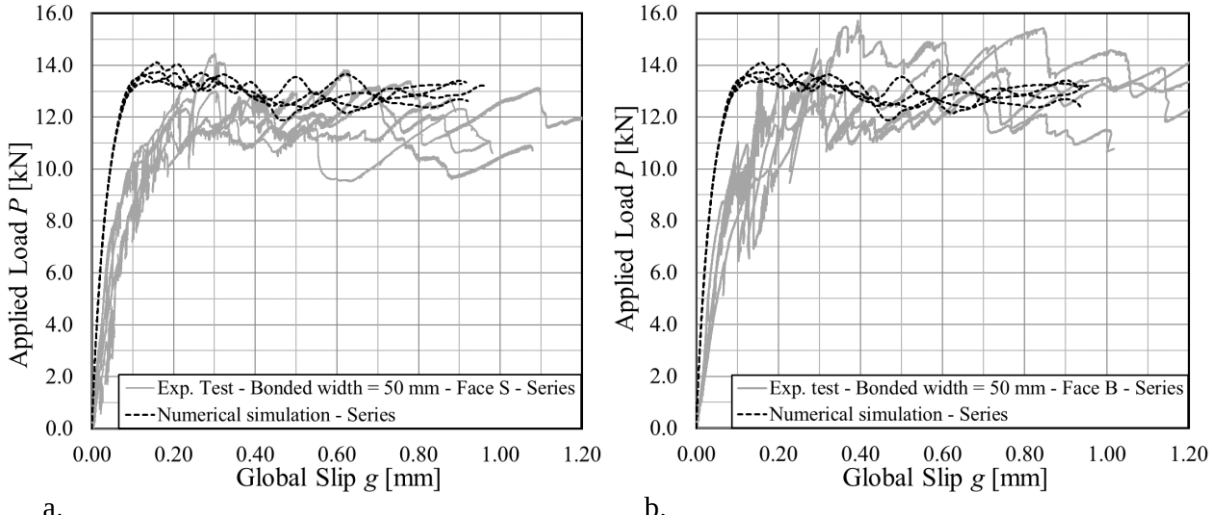

Figure 73. Comparison between experimental results and numerical simulation for a 50 mm-wide HD strip: a) Experimental S-face results; b) Experimental B-face results.

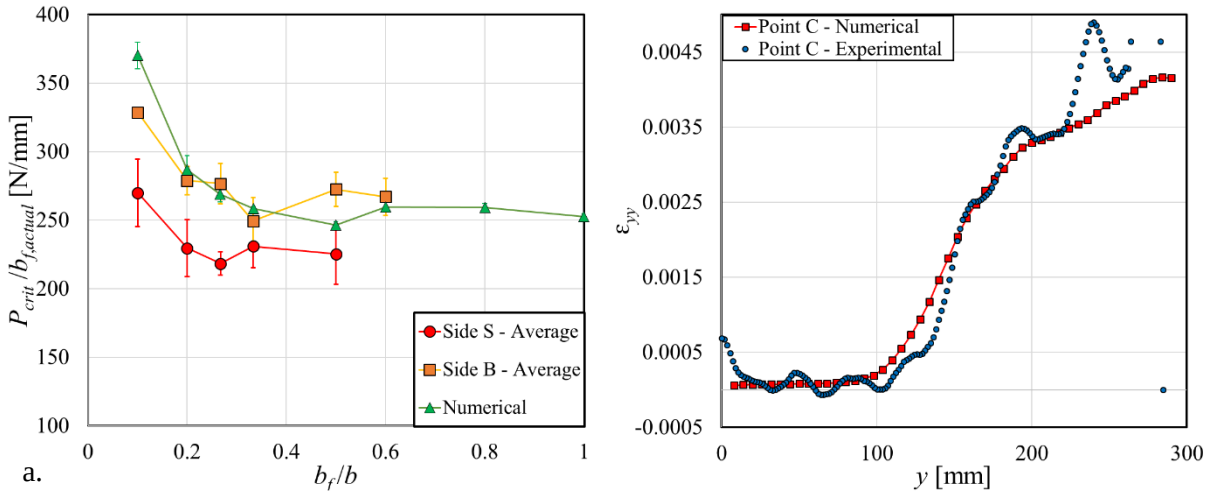

Figure 74. a) Load-carrying capacity per unit width; b) Comparison between experimental and numerical strains.

4.1.1.15 Conclusions

In this section, single-lap shear tests were performed to determine directly the interfacial fracture properties of SRP strips bonded to a concrete substrate. Debonding of the SRP composite occurred for all specimens. Strain profiles along the SRP strip determined from DIC measurements were fitted with three different functions. Out of the three functions selected, two functions were proposed by the author in this dissertation. Those two functions were proposed in order to obtain a finite effective bond length. Different densities of the SRP strip were considered. The SRP strips were bonded to different faces of the concrete prism in order to investigate the effect of concrete surface quality on the bond behavior. Different widths of the composite strip were employed. A numerical analysis was performed using LDPM. The following observations can be made:

1) The bond behavior of SRP composites is very similar to, if not the same as, the behavior of FRP composites
2) The fracture energy G_F of SRP-concrete joints is independent of the composite density, whereas the effective bond length depends on the density of the strip.
3) The fracture energy G_F varies as the composite is bonded to different faces of the concrete prism.
4) The effective bond length is not strongly affected by the face to which the SRP composite is applied.
5) The Mode-II interfacial fracture energy is roughly four times the Mode-I fracture energy of concrete.
6) The width effect should be considered in the evaluation of the load carrying capacity.
7) The numerical analysis performed with LDPM is capable to simulate the behavior of SRP strip bonded to B-faces.

Notched beams were strengthened with SRP strips and tested in a three-point bending set-up. Debonding of the strip occurred for all specimens. The experimental debonding forces obtained from single-lap shear tests and notched beam tests are different.

Finally, an alternative method to compute the fracture energy using an energy balance approach was proposed. The value of the fracture energy obtained is in good agreement with the value obtained from a direct approach. However, the width effect cannot be separated and identified with the energy balance approach.

4.1.2 SRG-concrete joints

4.1.2.1 Background

In the field of structural rehabilitation, SRG systems achieved success since they were able to overcome some drawbacks related to SRP composites, such as the low vapor permeability and the low performances at high temperatures. SRG applications recently captured the interest of the scientific community. The experimental works in literature were mainly focused to investigate the flexural [71] [79] [111] [70] [112] and shear [113] behavior of RC beams strengthened with SRG systems. Few studies were performed to determine the bond [114] [115] behavior of concrete members strengthened with SRG composites. Several failure modes were observed for SRG composites bonded to a quasi-brittle substrate and they can be summarized as follow (Figure 75):

- Debonding with cohesive fracture of the support;
- Interlaminar failure at the matrix-substrate interface;
- Interlaminar failure at the matrix-fiber interface;
- Sliding of the fibers within the matrix;
- Fibers rupture outside from the bonded region;
- Fibers rupture within the matrix.

In this section, the stress transfer mechanism between SRG composites and a concrete substrate is investigated. SRG strips were bonded to concrete prisms and tested using a single-lap shear test set-up. Load responses are presented and failure modes are discussed.

4.1.2.2 Experimental program

All concrete prisms of this experimental program can be classified as “Concrete – Type B” (see section 3.1.2). The SRG composite consisted in one layer of steel fibers (described in section 3.3.1) embedded in a cement-based mortar matrix (described in section 3.3.4.2). The property of the composite strip are described in section 3.3.7.

Twenty-one concrete prisms were tested using a single-lap shear test set-up, described in section 4.1.1.2. SRG composite strips with different bonded lengths and fiber densities were externally-bonded to one face of the concrete prisms. The classical push-pull configuration was adopted where the fibers were pulled while the concrete prism was restrained (Figure 76).

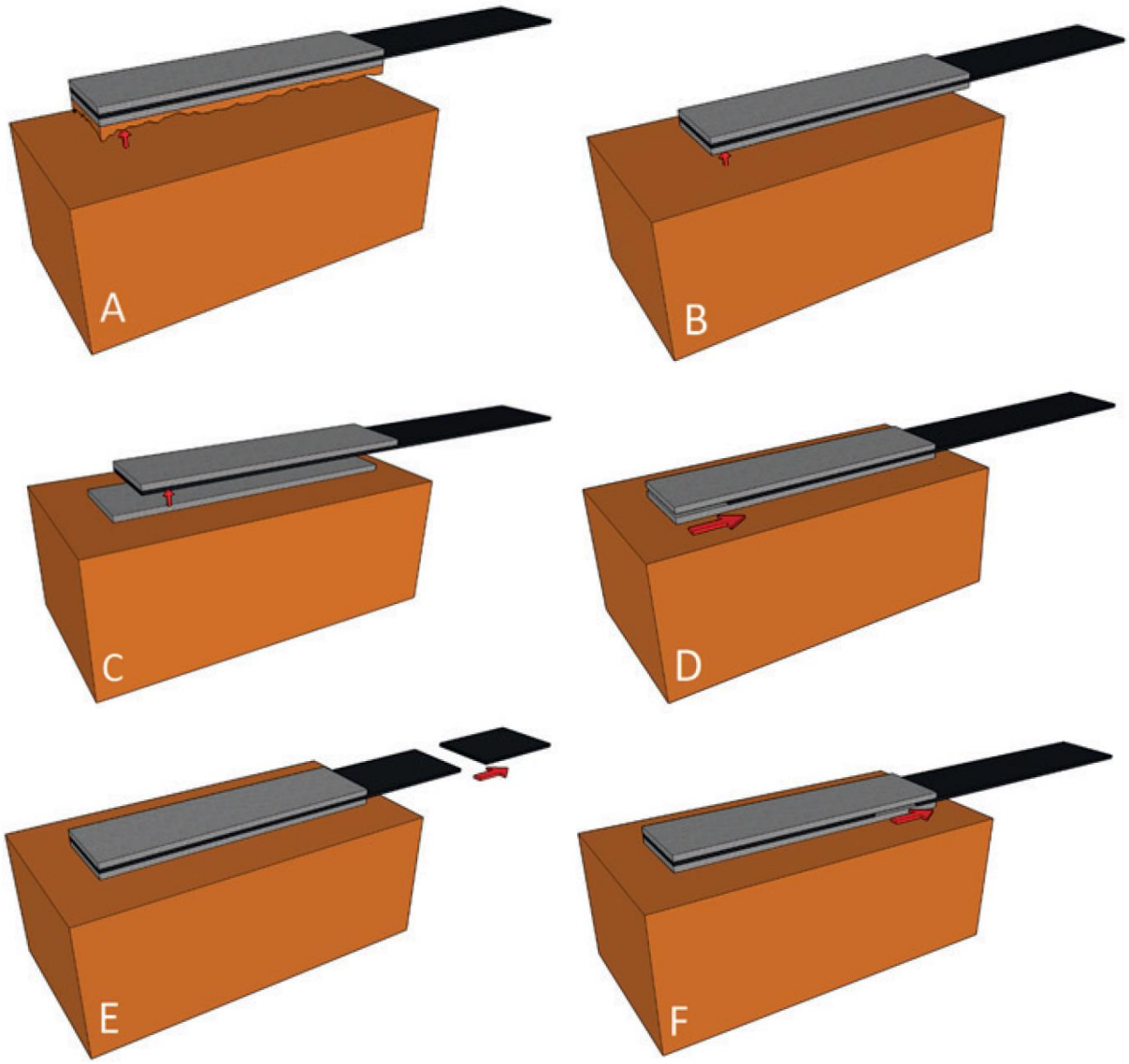

Figure 75. a) Debonding with cohesive fracture of the support; b) Interlaminar failure at the matrix-substrate interface; c) Interlaminar failure at the matrix-fiber interface; d) Sliding of the fibers within the matrix; e) Fibers rupture outside from the bonded region; f) Fibers rupture within the matrix.

The dimensions of all concrete blocks were 150 mm (width) × 150 mm (depth) × 600 mm (length). Three types of fibers were used, i.e. low density (LD), medium-low density (MLD), and medium density (MD) steel fibers. The mortar matrix was used only in the bonded area to embed the fibers and bond the composite to the concrete substrate, while fibers were bare outside the bonded area. The thickness of each layer of mortar was 4 mm, thus, the total thickness of the composite strip was equal to 8 mm. The bonded area started 50 mm from the top edge (loaded end of the fibers) of the concrete prism, to obtain an initial interfacial notch. A 75 mm-long epoxy tab was constructed with a thermosetting epoxy at the end of the fiber strip and used to improve gripping during testing. SRG strips were cured for 28 days after application

at a constant temperature of 20°C but with changeable humidity conditions. The variation of the humidity during the 28 days of curing may have affected the results. The test set-up was the same described in section 4.1.1.2, a part for the fact that the Ω-shaped aluminum plate was attached directly to the bare fibers. The standard test rate was keep equal to 0.00084 mm/s. Out of twenty-one tests, six were performed at a test rate that was ten times the standard rate, while five were performed at a test rate that was half the standard rate. All specimens strengthened with LD steel fibers were tested with the following set of parameters: load rate equal to 0.00084 mm/s, bonded length equal to 200 mm and bonded width equal to 50 mm. Specimens strengthened with MLD and MD steel fibers were tested with three different rates and had a composite width equal to 50 mm and a composite length equal to 450 mm. Specimens were named following the notation DS_F_X_Y_A_E_Z, where F indicates the type of matrix (CM = cement-based mortar matrix), X = bonded length (ℓ) in mm; Y = bonded width (b_f) in mm; A represents the steel fiber density (LD = low density, MLD = medium-low density, MD = medium density); E (if present) indicates that the loading rate was different from the standard rate (0.00084 mm/s) used for the majority of the specimens (10R = ten times the standard rate, 0.5R = 0.5 times the standard rate); and Z = specimen number Table 19.

Table 19. Experimental results of direct shear tests on SRG specimens.

Specimen	Slip at failure [mm]	Peak Load [kN]	Average Peak Load [kN]	Failure Mode	Number of cords
DS_CM_200_50_LD_1	1.33	13.15	13.23	FR	8
DS_CM_200_50_LD_2	1.32	13.23		FR	8
DS_CM_200_50_LD_3	1.25	13.31		FR	8
DS_CM_450_50_MLD_1	2.65	10.98	11.67	MF	12
DS_CM_450_50_MLD_2	3.42	13.18		MF	12
DS_CM_450_50_MLD_3	3.42	10.84		MF	12
DS_CM_450_50_MD_1	1.54	7.90	8.10	MF	16
DS_CM_450_50_MD_2	1.24	7.58		MF	16
DS_MR_450_50_MD_3	1.78	8.69		MF	16
DS_CM_450_50_MD_4	1.60	8.24		MF	16
DS_CM_450_50_MLD_10R_1	3.34	12.21	12.25	MF	12
DS_CM_450_50_MLD_10R_2	3.48	11.73		MF	12
DS_CM_450_50_MLD_10R_3	3.29	12.82		MF	12
DS_CM_450_50_MD_10R_1	0.89	7.90	8.64	MF	16
DS_CM_450_50_MD_10R_2	1.27	9.02		MF	16

DS_CM_450_50_MD_10R_3	0.72	8.99		MF	16
DS_CM_450_50_MLD_0.5R_1	3.02	11.42	11.19	MF	12
DS_CM_450_50_MLD_0.5R_2	3.36	10.96		MF	12
DS_CM_450_50_MD_0.5R_1	1.64	6.75	6.87	MF	16
DS_CM_450_50_MD_0.5R_2	1.36	5.70		MF	16
DS_CM_450_50_MD_0.5R_3	1.50	8.16		MF	16

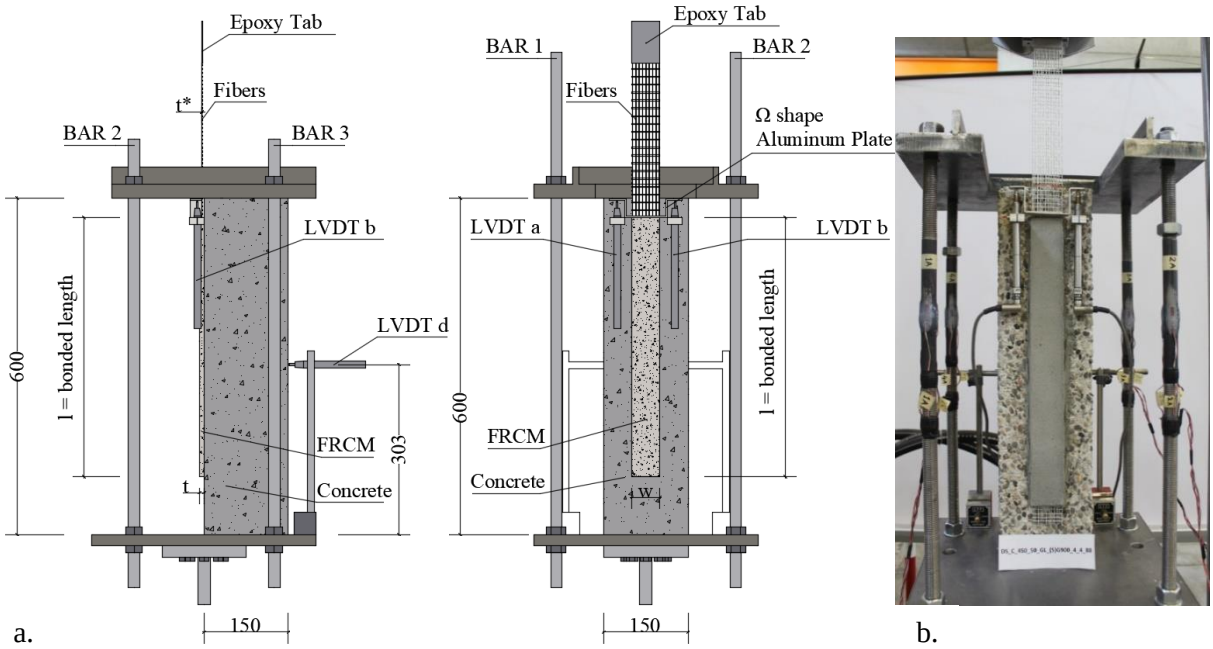

Figure 76. Single lap-shear test set-up for SRG composite strips bonded to a concrete substrate: a) Front view; b) Photograph of specimen DS_CM_450_50_MLD_1.

4.1.2.3 Experimental results

The stress-global slip responses of representative specimens with SRG composite corresponding to different steel fiber densities are plotted in Figure 77a. Stress was evaluated dividing the applied load by the nominal area of the fibers. SRG specimens reinforced with LD steel fibers show an initial linear portion followed by a non-linear behavior before the peak load is reached. The failure of these specimens consists in the rupture of the fibers (denoted by FR in Table 19) and the stress-global slip response show an always-increasing behavior up to the peak load. SRG specimens strengthened with MLD and MD steel fibers show a plateau in the non-linear branch of the stress-global slip response, reaching high values of the global slip before failure. The failure of these specimens consists in delamination (denoted by MF in Table 19) of the external layer of matrix from the internal one. Figure 77b shows the global slip response

of specimen DS_CM_200_50_LD_3. The blue and the red curves refer to the measurements of LVDT a and LVDT b mounted on the front face of the concrete prism. The green curve is the average of the two measurements, which has been named global slip. The displacement of the concrete prism in the direction perpendicular to the face to which the SRG strip is applied, was measured by LVDT c (light blue curve) and LVDT d (violet curve) and reported in Figure 77b. It should be noted that the displacements recorded by LVDT c and LVDT d are consistent, which implies that twisting of the concrete block did not occur during the tests.

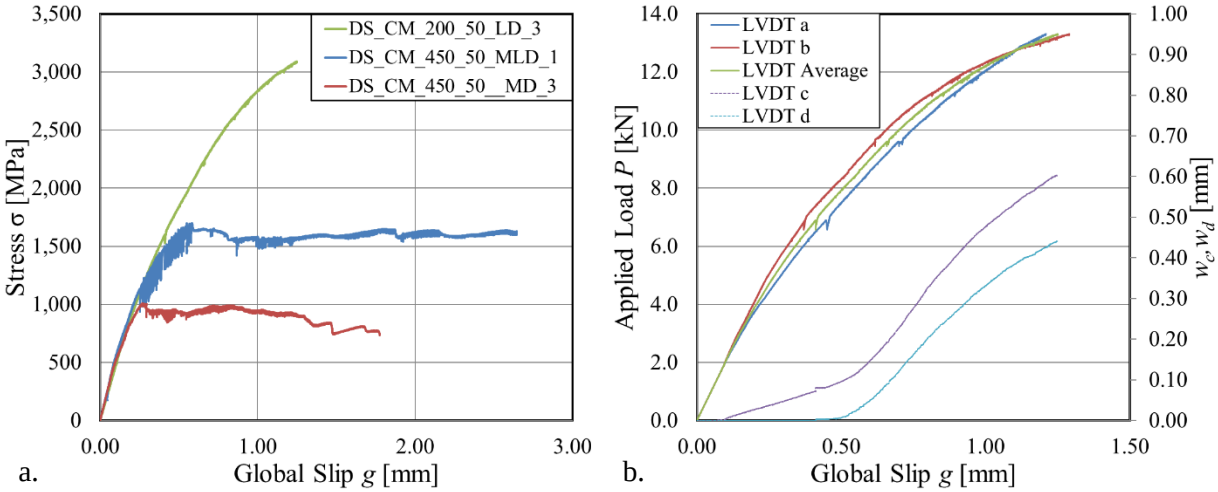

Figure 77. a) Stress – global slip response for representative SRG specimens; b) Load response for specimen DS_CM_200_50_LD_3.

4.1.2.4 Discussion and failure modes

Test results are discussed in this section. Table 19 reports for each specimen the corresponding failure mode. The failure mode of LD steel fibers consists in the rupture of the fibers (FR), while for MLD and MD steel fibers the failure consists in the detachment of the top (external) layer of the mortar matrix from the bottom (internal) one (MF), as showed in Figure 78. The analysis of the failure modes outlines that the density of the fibers plays a key role in the outcome of the tests conducted on SRG composites. The difference in the type of rupture is mainly due to the reduced area of mortar in between the fibers bundles, that causes in addition a lower peak load for MD specimens with respect to MLD specimens. The test rate has a slight influence on the test results for specimens reinforced with MLD and MD steel fibers. Table 19 shows the average peak loads reached for each density at a defined load rate. Comparing the peak loads for different values of the test rate, it is possible to deduce that an increase in the load rate entails an increase in the peak value. This phenomenon is connected to creep in the cementitious matrix, fairly affected by the load rate.

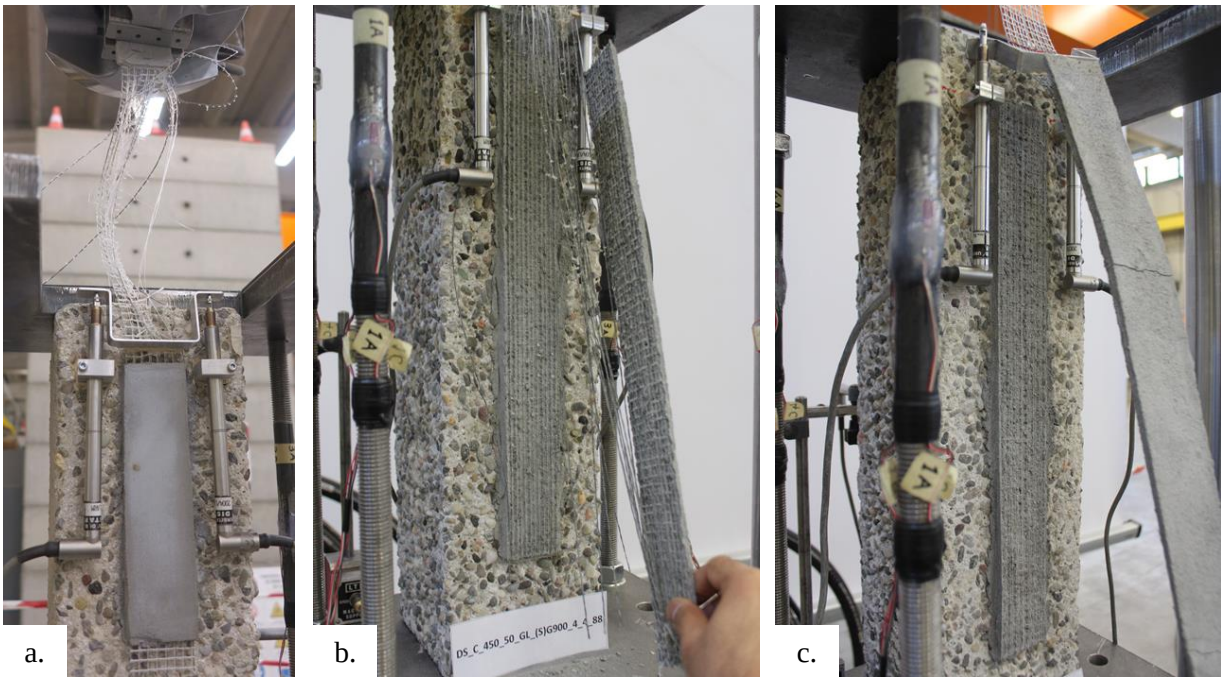

Figure 78. a) Rupture of the fibers for specimen DS_CM_200_50_LD_3; b) Delamination at the fiber-matrix interface for specimen DS_CM_450_50_MLD_1; c) Delamination at the fiber-matrix interface for specimen DS_CM_450_50_MD_1.

4.1.2.5 Conclusions

Results of single-lap shear tests conducted on SRG-concrete joints were presented in this section. Three different densities of steel fibers were employed together with a cement-based mortar matrix. The following conclusions can be drawn:

- Rupture of the fibers occurred for SRG-concrete joints with LD steel fibers while detachment (delamination) of the external layer of mortar matrix from the bottom layer of mortar matrix occurred for specimens with MLD and MD steel fibers;
- The load rate has an influence on the peak load of SRG specimens. An increase in the test rate entails an increase of the maximum load.

4.1.3 FRGM-concrete joints

4.1.3.1 Background

Reinforced concrete (RC) is the most commonly used construction material, supported by an extensive global production of cement, which was estimated to be approximately 4.6 Gt in 2015 [116]. However, due to durability issues or damages caused by external events, strengthening or repair interventions of RC structures are often required in order to preserve the load-carrying capacity of existing structures or to extend their service life. In the last few decades, externally bonded composite materials have been widely and successfully used to strengthen RC structures. In particular, the so called fiber reinforced cementitious matrix (FRCM) composites were recently introduced as an alternative to traditional fiber reinforced polymer (FRP) composites [117] [118] [119] [120] [121] as described in section 4.1.2.1.

In the last few years, a new class of materials known as geopolymers [122], which are part of the broad category of inorganic matrices named alkali activated materials, have raised some interest. Geopolymers are a new attractive class of material synthesized through a reaction between a highly concentrated aqueous alkali solution and a low calcium aluminosilicate powder, which acts as precursor of the geopolymerization process. The main precursors used to produce geopolymers are metakaolin and coal fly ash, usually activated with hydroxide and/or silicate solutions containing sodium or potassium as the alkali cation. The geopolymerization process consists in the dissolution of the aluminosilicate powder by alkaline hydrolysis and a consecutive polycondensation, which leads to the formation of three dimensional aluminosilicate network [123] [124].

Because of their inorganic nature, geopolymers are often compared to ordinary portland cement (OPC) based materials. A large number of studies highlights the satisfactory mechanical properties and durability performance of geopolymers, especially in terms of sulfate and acid attack, which suggests their use as binder in mortar and/or concrete [124] [125] [126] [127] [128]. However, the remarkable growth of research on geopolymers over the last few years can be ascribed to their widely advertised low CO_2 emissions when compared to OPC. Indeed, several types of industrial wastes (e.g. brick powder, agricultural waste, clay sediments, incineration fly ash, coal fly ash, etc.) can be used as raw material for geopolymers production, because of their amorphous aluminosilicate nature [129] [130] [131]. Moreover, both the reactions and the consolidation process can take place at low temperature ($T \leq 100$ °C), which makes the production of geopolymers energy and cost efficient [132].

Sustainability is only one of the advantages of this class of materials. In fact, if properly designed, geopolymers perform better than OPC and epoxy when exposed to high temperature. The dehydration process do not cause significant changes in the geopolymer structure, which presents a high degree of

thermal stability and retains its binding properties during a heating process [133] [134] [135] [136]. Furthermore, geopolymers do not produce either combustion or toxic gases [137] and, in some cases, an increase in mechanical properties can be observed after thermal exposure [138].

Considering geopolymers as a repair material, a previous study [139] showed an excellent bond behavior and adequate compatibility with concrete substrates, independently of the roughness of the surface and the curing time. The same study also highlighted the cost efficiency of geopolymer, which resulted 6.9 times less expensive than the commercial repair product considered in the study. In addition, the bond capacity of properly designed geopolymers applied to cement mortar substrates is barely affected by the thermal exposure up to 300°C [140]. Only in few studies, geopolymers have been successfully used as matrix in composites to strengthen RC elements [52] [141]. However, there is a lack of detailed data on geopolymer matrices and in most cases metakaolin was used as precursor [142] [143], which reduces the environmental benefit of using geopolymer instead of cementitious matrix.

In this section, an interdisciplinary approach to study newly developed steel fiber reinforced geopolymer matrix (S-FRGM) composites for strengthening applications of RC structures is adopted. Three S-FRGM composites are investigated, which correspond to three different geopolymer matrices, obtained by room temperature alkali activation of coal fly ash. The geopolymer matrix embeds high-strength galvanized steel fibers. As geopolymerization process involves a high level of alkalinity (pH varies from 14 to 12 during the process) and galvanized steel fibers are sensitive to the pH environment, the geopolymer matrices are prepared using NaOH solutions with different molarity (8M, 6M and 4M, respectively). Physical, mechanical, and microstructural properties of the geopolymer matrices are characterized in section 3.3.5. Results of FRGM strips bonded to concrete prisms and tested using a single-lap direct shear test set-up are here presented in order to study the stress transfer mechanism between the composite and the concrete.

4.1.3.2 Experimental program

All concrete prisms of this experimental program can be classified as “Concrete – Type B” (see section 3.1.2). The FRGM composite consisted in one layer of steel fibers (described in section 3.3.1) embedded in three different geopolymer matrices (described in section 3.3.5), characterized by a different molarity. FRGM composite strips were bonded to eight concrete prisms (150 mm × 150 mm × 600 mm). The FRGM-concrete joints were tested using the single-lap shear test set-up described in section 4.1.1.2 in order to investigate the debonding mechanism between the FRGM composite and the concrete substrate. The FRGM composite strip was comprised of one layer of LD steel fibers embedded in a geopolymer matrix (GEO4, GEO6, and GEO8). The matrix was used only in the bonded area to embed the fibers and bond the composite to the concrete substrate. All strips had a bonded length equal to 450 mm and a bonded

width equal to 50 mm. The thickness of each layer of the matrix was 4 mm, thus, the total thickness of the composite was equal to 8 mm. Fibers were left bare outside the bonded area, which started 50 mm from the top edge (loaded end of the fibers) of the specimen to avoid spalling of the edge of the concrete prism. As for SRG specimens, the Ω-shaped aluminum plate was attached directly to the bare fibers. A 75 mm-long epoxy tab was constructed with a thermosetting epoxy at the end of the fiber sheet and used to improve gripping during testing. FRGM strips were cured for at least 7 days at room temperature (T = 21 ± 2°C) covered by a PVC film until the day of test. Tests were performed increasing the global slip at a constant rate equal to 0.00084 mm/s. The microstructure of the FRGM strips after the direct shear tests were performed was investigated using a scanner electron microscope (SEM, EVO 40XVP-M, Carl Zeiss Microscopy GmbH).

4.1.3.3 Experimental results and discussion

In this section, the results of single-lap shear tests are presented to analyze the behavior of steel FRGM composites bonded to concrete prisms. Out of eight FRGM-concrete joints, three specimens were used to conduct preliminary direct shear tests to define which geopolymer matrix showed the best bond behavior. Thus, one direct shear test was performed for each type of geopolymer matrix (the corresponding direct shear specimens were named DS_GEO4_1, DS_GEO6_1 and DS_GEO8_1). The applied load-global slip responses of those three tests are reported in Figure 79a. For all specimens, failure was associated with the debonding of the external layer of matrix and fibers from the internal layer of matrix (interlaminar failure) that remained bonded to the concrete substrate. For all three specimens, the applied load-global slip response showed an initial linear portion followed by a non-linear branch before the peak load P^* was reached. During the linear and non-linear phases, drops in the load, mainly due to micro-damage at the matrix-fiber interface, were observed. Once the peak load was reached, an interfacial longitudinal crack initiated and propagated in the matrix and the load response showed a nominally constant trend up to failure. The peak load, P^*, for specimens DS_GEO4_1, DS_GEO6_1 and DS_GEO8_1 is equal to 9.48 kN, 6.97 kN and 7.77 kN, respectively. Specimen DS_GEO4_1 showed also a higher value of the global slip g at the peak load (3.21 mm) if compared with DS_GEO6_1 (1.99 mm) and DS_GEO8_1 (2.37 mm). Specimens DS_GEO4_1 and DS_GEO8_1 exhibited similar values of slip at failure (4.07 mm and 4.30 mm, respectively), which are higher than specimen DS_GEO6_1 (2.83 mm). From the experimental results of the preliminary direct shear tests, it appears that specimen DS_GEO4_1 exhibited the best bond behavior among the three specimens.

On the basis of the results of the three preliminary tests, five additional tests were performed (Figure 79b). The GEO4 matrix was used to manufacture the strips of the five remaining FRGM-concrete joints, in order to further investigate its bond behavior. The additional five specimens were named DS_GEO4_2,

DS_GEO4_3, DS_GEO4_4, DS_GEO4_5 and DS_GEO4_6 and their load-global slip responses are reported in Figure 6b. The applied load-global slip responses were similar to the responses of the preliminary tests. After the peak was reached, the applied load-global slip response showed a drop of the load, due to the onset of the interfacial longitudinal crack inside the matrix, followed by an approximately constant branch. For all specimens, interlaminar failure (at the matrix-fiber interface) was observed. After the longitudinal crack started to propagate along the bonded area, high values of the global slip were reached. The average value of the peak load, *P**, for the five tests was equal to 8.65 kN (CoV = 0.081). Therefore, the maximum stress in the fibers was equal to 2010 MPa, i.e. the 67% of the tensile strength provided by the manufacturer.

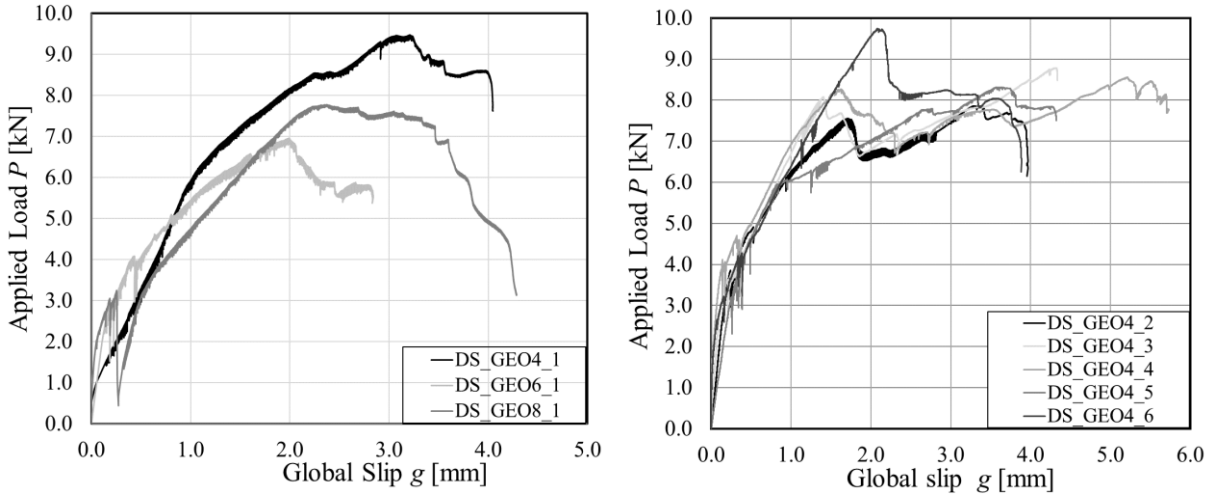

a. b.

Figure 79. Applied load-global slip response of FRGM composites: a) DS_GEO4_1, DS_GEO6_1, and DS_GEO8_1; b) DS_GEO_4_2, DS_GEO4_3, DS_GEO4_4, DS_GEO4_5, and DS_GEO4_6.

SEM micrographs of FRGM composites (Figure 80), after direct shear tests were performed, helped to explain why the different matrices behaved differently. According to the results reported in section 3.3.5, GEO8 is the least porous formulation investigated, which has also the best mechanical and physical properties. Moreover, GEO4 exhibits a large portion of unreacted fly ash particles (Figure 80a); whereas in GEO8, geopolymer gel is prevalent (Figure 80b) with only few unreacted fly ash particles. The presence of unreacted or partially reacted fly ash particles is common in fly ash based geopolymers, especially when they are cured at room temperature, and their presence strongly influence the performances of the final product [144] [145].

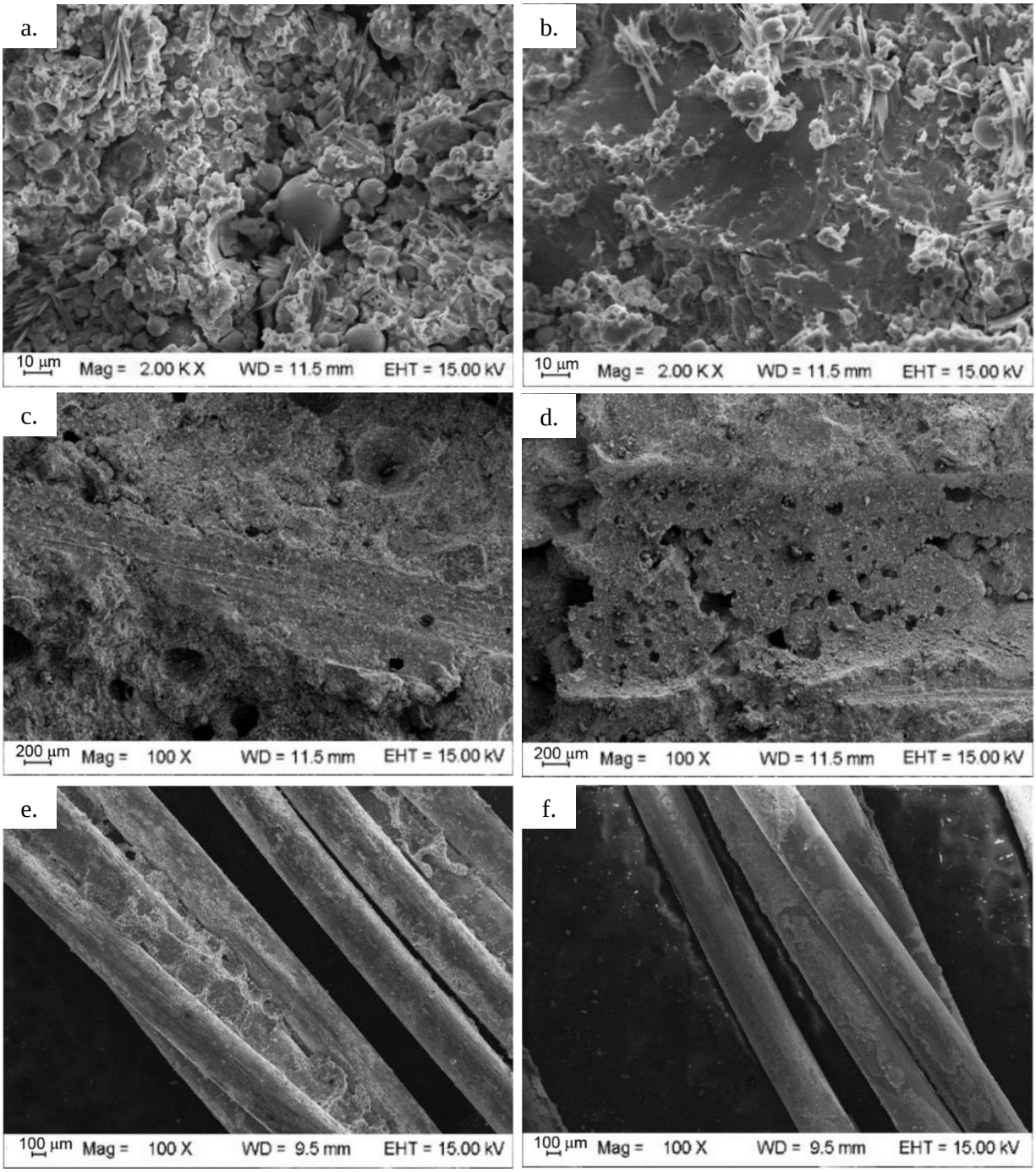

Figure 80. SEM micrographs of FRGM composites constructed with GEO4 (a, c, e) and GEO8 (b, d, f) after single lap direct shear test. (a, b) = Matrix microstructures; (c, d) = matrix at the interface with galvanized steel fibers after debonding; (e, f) = fibers after debonding.

However, for the GEO8 matrix many large pores are localized in the matrix at the interface with the fibers (Figure 80d); whereas, only few pores are visible in the GEO4 matrix (Figure 80c). The pores localized at the fiber/matrix interface suggest that a chemical reaction between the galvanization layer and the

matrix occurred when the composites strips were cast. According to its amphoteric behavior, Zn dissolution also occurs for pH greater than 12 [146]. Thus, a decrease of the molarity of NaOH solution in the geopolymer mix design implies a degradation of the physical and mechanical properties of the matrix and an improvement of the adhesion between fibers and matrix. The improved interfacial interaction between the fibers and the GEO4 matrix is also confirmed by the geopolymer fragments that were still attached to the fibers (Figure 80e) after the shear test. Fragments are not present at all on the fibers from specimens cast with the GEO8 matrix (Figure 80f).

4.1.3.4 Conclusions

Based on the experimental evidence, the following conclusions can be drawn:

- When galvanized steel fibers are used in FRGM composites it is important to limit the reaction between the alkaline environment of the matrix and the zinc coating of the fibers. Therefore, the mix design of the geopolymer matrix has to be tailored in order to avoid a detrimental interaction between the matrix and the fibers. A decrease of the molar concentration of sodium hydroxide activator produced an improvement of the adhesion between the materials, which in turn enhanced the composite performance;
- An adequate compatibility and adhesion between the composite and the concrete substrate was found. Indeed, for all direct shear test specimens, the failure mode was debonding (interlaminar failure) of the external layer of matrix from the internal layer rather than debonding at the matrix-concrete interface. Moreover, in the case of the best performing composite (DS_GEO4_series), the average value of the maximum stress in the fibers in direct shear tests resulted equal to 67% of the tensile strength provided by the manufacturer [6].

4.2 Bond between steel fiber reinforced composite materials and a masonry substrate

In this section the bond performances of SRG composite materials bonded to a masonry surface will be investigated. SRG composites were bonded to a masonry substrate and tested in direct-shear varying several parameters, i.e. the density of steel fibers, the bonded width, the bonded length, the test rate, and the type of mortar matrix. SRG composites were also subjected to degradation cycles using a saline solution in order to investigate the bond performances after salt attack.

4.2.1 SRG-masonry joints

4.2.1.1 Background

Strengthening solutions to rehabilitate existing masonry buildings have always attracted the interest of the scientific community since they allow to preserve historical constructions through an understanding of the original structural configuration. Strengthening applications are useful to guarantee serviceability of a damaged or deficient structure and are considered a sustainable choice to avoid the demolition of existing buildings. In the last decades, strengthening solutions gained a renewed interest due to the seismic events that hit several European countries (Italy, Greece and Turkey). Natural hazards, such as earthquakes, have shown the inadequacy of certain masonry structures to withstand horizontal loads, and brought up the need for an adequate strengthening intervention to avoid certain collapse mechanisms of the structure. In recent years, new strengthening systems, such as fiber reinforced polymer (FRP) composites, have been employed to avoid the onset of a collapse mechanisms of some structural components of the construction and increase the load-carrying capacity. Several researchers conducted experimental campaigns to investigate the debonding mechanism of FRP systems bonded to a masonry substrate [147] [148] [149] [150] [151] [152] [153] . It was observed that failure usually occurred in the masonry substrate, and was characterized by a cohesive crack that propagated both in the bricks and in the mortar joints. Despite FRP systems are able to enhance the load-carrying capacity of a masonry structure, they feature several disadvantages when applied to existing structures, such as the poor behavior at elevated temperatures and lack of reversibility of the application. In addition, FRP composites have a low vapor compatibility with masonry substrates. In an attempt to overcome the disadvantages of traditional FRP systems, a new family of composites, known as fiber reinforced cementitious matrix (FRCM) or textile-reinforced mortar (TRM) composites, was recently developed. FRCM composites consist of high strength fibers embedded within an inorganic matrix and offer several advantages when compared to traditional FRPs: 1) high resistance to fire and high temperatures; 2) resistance to UV

radiation; 3) ease of handling during the application because the inorganic binder is water-based; 4) permeability compatible with concrete and masonry substrates; and 5) unvarying workability time (between 4°C and 40°C) [154]. Experimental tests on FRCM composites bonded to a masonry substrate have been also reported in literature, using carbon, PBO, glass or basalt fibers [155] [156] [157]. Experimental results have shown that the typical failure of FRCM composites bonded to a masonry substrate consisted in the rupture of the fibers or in the delamination at the fiber-matrix interface. Newly-developed high-strength steel fibers were recently employed in FRCM systems and are referred to as steel reinforced grout (SRG) composites. SRG composites consisted in high strength steel fibers embedded in a cementitious or lime-based grout. The low cost of the steel fibers compared to carbon or aramid fibers and the possibility to apply steel fibers also to sharp corners of masonry and concrete structures [158] determined the success of this new strengthening system. Despite the available studies carried out to investigate the bond behavior of SRG-masonry joints [159] [160] [161] and of SRG-brick interfaces [162] [66], which highlighted the effectiveness of this strengthening system, some of the most important aspects of the SRG-masonry debonding mechanism, such as the definition of the cohesive material law or the influence of the bonded length and width on the load responses, are still not fully investigated for this type of composites.

This section presents the result of an extensive experimental campaign designed to study the bond mechanism of SRG-masonry joints. Single-lap shear test are performed. Length and width of the bonded area and loading rate of the tests are varied. Two types of matrices were employed, i.e. a lime-based mortar and a cement-based mortar. Two steel fiber densities were employed, i.e. LD steel fibers and MD steel fibers. An indirect method is then used to determine the interfacial cohesive material law that describes the debonding phenomenon.

4.2.1.2 Experimental program

All masonry blocks of this experimental program were constructed with the bricks and the mortar characterized in section 3.2. The SRG composite consisted in LD and MD steel fibers (described in section 3.3.1) embedded in a lime-based mortar (described in section 3.3.4.1) or cement-based mortar (described in section 3.3.4.2). The property of the composite strips are described in section 3.3.7.

One hundred and twelve SRG-masonry joints were tested using a single-lap shear test set-up. The parameters investigated for the lime-based mortar matrix were the bonded length, the bonded width, the fiber density and the test rate. Out of one hundred and twelve specimens, ninety-seven were strengthened with a lime-based mortar matrix, while fifteen were tested with a cement-based mortar matrix. SRG composites were externally bonded to one face of the masonry blocks. The nominal dimensions of almost all masonry blocks were equal to 120 mm × 120 mm × 445 mm, i.e. each block consisted of 7 half bricks and 6 1 mm-thick mortar joints. Few specimens were made of 6 half bricks and 5 mortar joints. Prior to

applying the SRG strip, the faces of each specimen were wetted by soaking completely each masonry block in a bucket of water for twenty minutes. The water immersion of each specimen was needed to avoid water absorption by the masonry surfaces during the application of the composite strip. Three phases can be identified during the application of the SRG composite strip: 1) application of the first layer of mortar matrix on the designated bonded area of the masonry block (Figure 81c); 2) the steel fiber sheet is placed on top of the first layer of mortar and gently pressured against it in order to guarantee the impregnation of the fibers (Figure 81d); 3) application of the external layer of mortar matrix in order to cover completely the fiber sheet (Figure 81e). After the application of the second layer of matrix, SRG strips were cured for 28 days under wet cloths. Both the 300 mm × 70 mm × 70 mm notched mortar matrix prisms and the 40 mm × 40 mm × 160 mm mortar matrix prisms, cast from the different batches of mortar described in section 3.3.4.1 and 3.3.4.2 and employed to characterize the two matrices of the SRG system, were cured under wet cloths, as well, for 28 days. Out of ninety-seven specimens tested with the lime-based mortar, eighty-three specimens had a bonded width, b_f, equal to 50 mm, five specimens had a bonded width equal to 70 mm, four specimens had a bonded width equal to 75mm, and five specimens had a bonded width equal to 90 mm. Out of eighty-tree specimens with a bonded width equal to 50 mm, seventy-eight specimens were strengthened with a 50 mm-wide LD steel fiber sheet (i.e. 8 cords were employed), while five specimens were strengthened with a 50 mm-wide MD steel fiber sheet (i.e. 16 cords were employed). For specimens with a bonded width equal to 70 mm and 90 mm, the LD fiber sheet width was left equal to 50 mm (i.e. 8 cords were employed), while for specimens with a bonded width equal to 75 mm, the LD fiber sheet width was maintained equal to the bonded width (i.e. 12 cords were employed). All the fifteen specimens strengthened with the cement-based mortar matrix had the same bonded width equal to 50 mm and were reinforced with a 50 mm-wide LD steel fiber sheet (i.e. 8 cords were employed). For specimens in which the width of the fiber sheet was equal to the bonded width, the cords were arranged across the width of the SRG strip in order to have approximatively a distance between the external cords of the fiber sheet and the edges of the mortar matrix equal to half of the fiber spacing. For the ten specimens that had a fiber sheet width narrower than the bonded width, the fiber sheet was centered with respect to the mortar matrix. Both the internal and the external layer of matrix had a thickness equal to 4 mm, which in turn determine a total thickness of the SRG composite strip equal to 8 mm. Fibers were left bare outside the bonded area, i.e. the matrix was only used in the bonded area. The length of the bare fiber portion of the SRG strip was approximately equal to 350 mm. A 75 mm-long epoxy tab was constructed with a thermosetting epoxy at the end of the fiber strip and used to facilitate gripping within the wedges of the testing machine. A distance of 35 mm was left between the top edge of the masonry block and the beginning of the bonded area to avoid spalling of the first brick of the specimen.

Specimens with eleven different bonded lengths were tested, i.e. 75 mm, 100 mm, 125 mm, 150 mm, 175 mm, 200 mm, 215 mm, 250 mm, 280 mm, 315 mm, and 345 mm.

Specimens were named following the notation DS_X_Y_G_A_B_C_D_Z, where X = bonded length (ℓ) in mm; Y = bonded width (b_f) in mm; A represents the steel fiber density (LD = low density); B indicates the type of matrix (LM = lime-based mortar, CM = cement-based mortar); G (if present) indicates the width of the fiber sheet when it results different from the bonded width, C (if present) denotes the type of mortar matrix batch (B1, B2, B3 or B4), D (if present) indicates the test rate different from the standard rate (0.00084 mm/s) used for the majority of the specimens (10R = ten times the standard rate) and Z = specimen number (Table 20).

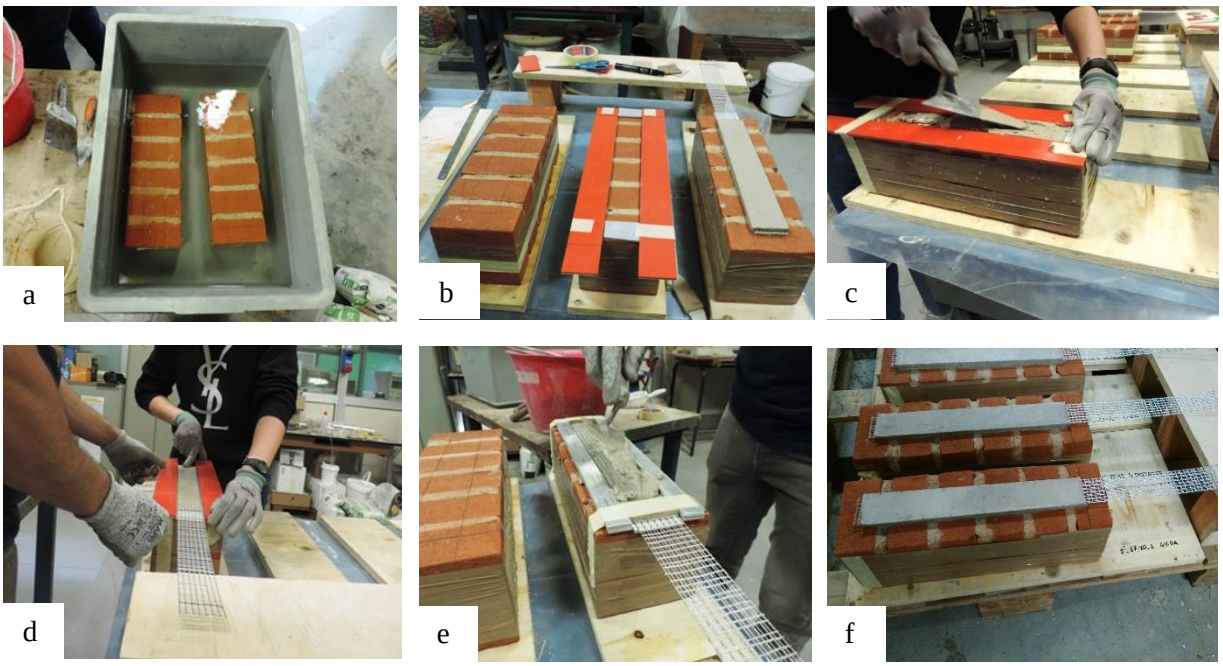

Figure 81. Appliction of the SRG composite to the masonry block: a) Water immersion of the masonry block; b) definition of the bonded area; c) application of the internal layer of mortar matrix; d) application of the steel fiber sheet; e) application of the external layer of mortar matrix; f) SRG-masonry joint after curing.

Direct single-lap shear tests were conducted under displacement control using a closed-loop servo-hydraulic universal testing machine with a capacity of 100 kN. The classical push-pull configuration was adopted, i.e. the masonry block was restrained against movements by two steel plates while fibers were pulled. The sketch and a photo of the test set-up is shown in Figure 82. A cylindrical steel element, fixed to the bottom square plate, was directly clamped by the bottom wedges of the testing machine. The bottom steel plate and the top rectangular steel plate were connected by four steel bars through bolts. On each

steel bar, three strain gages were mounted. The strain gages were aligned with the longitudinal axis of the bar and were arranged 120° apart one another. The average value of the three strain measurements on each bar, was used to evaluate the strain along the bar and consequently the pre-stresing load applied to the masonry block prior to starting the single lap-shear test. The same pre-stressing load (approximatively 1 MPa) was applied to all the specimens at the beginning of the test and the stress along each bar was monitored during the test. Thin neoprene sheets were placed in between the square faces of the masonry block and the steel plates, in order to provide an even distribution of the load.

One hundred and twelve single-lap shear tests were performed in this experimental campaign. Two LVDTs (LVDT a and LVDT b) were mounted on the masonry surface close to the beginning of the bonded area. The LVDTs reacted of a thin aluminum Ω-shaped plate that was glued directly to the bare fibers surface adjacent to the loaded end of the SRG strip. The average value of the LVDT measurements is referred to as global slip, *g*, in this paper and was used to control the test at a constant rate equal to 0.00084 mm/s, which has been considered as the standard rate. Out of 112 specimens, 3 were tested with a rate equal to 0.0084 mm/s, i.e. ten times the standard rate. Two additional LVDTs (LVDT c and LVDT d) were mounted against the face of the masonry block opposite to the surface where the SRG strip was applied, and were used to monitor the horizontal displacements of the masonry block. LVDT c and LVDT d were fixed to the bottom plate by means of two magnets. All specimens were arranged 1 mm forward with respect to the position corresponding to the vertical alignment of the fibers with the machine grips. This expedient was used to balance the inevitable initial backward rotation of the block due to the deformation of the mortar joints and the adjustment of the test fixture and it allowed the fibers to remain almost aligned with the top grips of the testing machine for the entire duration of the single-lap shear test.

Table 20. Test results of single-lap direct shear tests

Specimen Name	Bonded length [mm]	g_1 [mm]	g_2 [mm]	P^* [kN]	P_{crit} [kN]	$\overline{P_{crit}}$ [kN]	Failure mode	$\overline{w_c}$ [mm]	$\overline{w_d}$ [mm]
DS_75_50_LD_LM_1	75	\	\	4.70	\	\	MM	\	\
DS_75_50_LD_LM_2	75	\	\	2.98	\		MM	\	\
DS_75_50_LD_LM_3	75	\	\	3.38	\		MM	\	\
DS_75_50_LD_LM_4	75	\	\	3.84	\		MM	\	\
DS_100_50_LD_LM_1	100	\	\	2.97	\	\	MM	\	\
DS_100_50_LD_LM_2	100	\	\	4.03	\		MM	\	\
DS_100_50_LD_LM_3	100	\	\	7.26	\		MM	\	\
DS_100_50_LD_LM_4	100	\	\	5.65	\		MM	\	\
DS_125_50_LD_LM_1	125	\	\	4.41	\	\	MF	\	\
DS_125_50_LD_LM_2	125	\	\	6.44	\		MF	\	\

DS_125_50_LD_LM_3	125	\	\	8.08	\		MF	\	\
DS_125_50_LD_LM_4	125	\	\	6.20	\		MF	\	\
DS_125_50_LD_LM_5	125	\	\	7.12	\		MF	\	\
DS_150_50_LD_LM_1	150	\	\	6.23	\	\	MF	\	\
DS_150_50_LD_LM_2	150	\	\	4.53	\		MF	\	\
DS_150_50_LD_LM_3	150	\	\	3.58	\		MF	\	\
DS_150_50_LD_LM_4	150	\	\	4.97	\		MF	\	\
DS_175_50_LD_LM_1	175	1.05	1.65	7.74	6.81	6.30	MF	0.67	0.83
DS_175_50_LD_LM_2	175	\	\	5.80	\		MM/MF	\	\
DS_175_50_LD_LM_3	175	1.27	1.49	7.76	6.85		MF	1.01	0.94
DS_175_50_LD_LM_4	175	1.20	1.50	8.12	7.08		MF	1.63	1.76
DS_175_50_LD_LM_5	175	1.20	1.98	9.04	7.35		MF	1.77	1.78
DS_175_50_LD_LM_6	175	0.62	0.67	6.22	5.75		MF	1.37	1.42
DS_175_50_LD_LM_7	175	\	\	10.44	\		SF/MM	\	\
DS_175_50_LD_LM_8	175	0.84	1.04	5.30	3.97		MF	0.87	1.04
DS_175_50_LD_LM_9	175	\	\	5.44	\		MF	\	\
DS_175_50_LD_LM_10	175	\	\	8.34	\		MM	\	\
DS_200_50_LD_LM_1	200	0.58	1.16	7.28	5.64	5.57	MF	1.08	1.59
DS_200_50_LD_LM_2	200	\	\	8.80	\		MF	\	\
DS_200_50_LD_LM_3	200	0.48	1.06	6.04	5.50		MF	1.30	1.42
DS_215_50_LD_LM_1	215	\	\	13.15	\	\	FR	\	\
DS_215_50_LD_LM_2	215	\	\	13.20	\		FR	\	\
DS_215_50_LD_LM_3	215	\	\	12.84	\		MF	\	\
DS_250_50_LD_LM_B2_1	250	0.70	1.57	7.06	6.16	4.95	MF	0.39	0.49
DS_250_50_LD_LM_B2_2	250	0.40	1.30	5.06	4.71		MF	0.91	1.10
DS_250_50_LD_LM_B2_3	250	0.61	1.48	5.42	4.67		MF	2.29	2.33
DS_250_50_LD_LM_B2_4	250	0.60	1.33	5.70	5.60		MF	1.45	1.23
DS_250_50_LD_LM_B2_5	250	0.39	0.62	4.68	3.64		MF	1.94	1.87
DS_280_50_LD_LM_1	280	\	\	10.88	\	4.92	MF	\	\
DS_280_50_LD_LM_2	280	\	\	7.81	\		MF	\	\
DS_280_50_LD_LM_3	280	\	\	9.25	\		MF	\	\
DS_280_50_LD_LM_4	280	0.75	1.59	5.92	4.92		MF	0.68	0.70
DS_315_50_LD_LM_B2_1	315	0.73	1.30	7.49	5.27	6.22	MF	1.69	1.44
DS_315_50_LD_LM_B2_2	315	\	\	12.75	\		FR	\	\
DS_315_50_LD_LM_B2_3	315	\	\	6.21	\		MF	\	\
DS_315_50_LD_LM_B2_4	315	1.00	2.30	6.78	6.33		MF	1.51	1.79
DS_315_50_LD_LM_5	315	\	\	5.05	\		MF	\	\
DS_315_50_LD_LM_6	315	1.03	2.49	7.76	6.85		MF	1.60	1.69
DS_315_50_LD_LM_7	315	1.54	2.35	7.83	6.67		MF	1.22	1.39
DS_315_50_LD_LM_8	315	1.12	2.22	7.52	5.84		MF	0.92	1.15
DS_315_50_LD_LM_9	315	\	\	6.50	\		MF	\	\
DS_315_50_LD_LM_10	315	0.58	1.92	5.88	5.48		MF	1.74	1.66
DS_315_50_LD_LM_11	315	1.18	2.29	6.36	5.84		MF	1.14	0.99

DS_315_50_LD_LM_12	315	1.90	2.30	7.79	7.50		MF	1.47	1.34
DS_315_50_LD_LM_B3_13	315	1.33	2.18	6.07	5.75		MF	1.25	1.40
DS_315_50_LD_LM_B3_14	315	\	\	11.40	\		MF	\	\
DS_315_50_LD_LM_B4_15	315	1.15	2.26	8.12	6.65		MF	0.80	0.94
DS_315_50_LD_LM_B1_10R_1	315	\	\	8.46	\		MF	\	\
DS_315_50_LD_LM_B1_10R_2	315	\	\	10.31	\	\	MF	\	\
DS_315_50_LD_LM_B1_10R_3	315	\	\	12.46	\		MF	\	\
DS_315_50_MD_LM_B1_1	315	0.45	1.05	5.77	5.29		MF	1.94	2.20
DS_315_50_MD_LM_B1_2	315	0.62	0.82	6.22	5.17		MF	0.83	0.90
DS_315_50_MD_LM_B1_3	315	0.45	0.96	4.59	5.42	5.25	MF	1.34	1.46
DS_315_50_MD_LM_B1_4	315	0.40	0.71	6.05	4.28		MF	1.41	1.61
DS_315_50_MD_LM_B1_5	315	0.35	1.12	6.39	6.10		MF	0.74	1.08
DS_315_70_50_LD_LM_B3_1	315	\	\	12.66	\		FR	\	\
DS_315_70_50_LD_LM_B3_2	315	1.08	1.58	7.04	6.82		MF	1.89	1.85
DS_315_70_50_LD_LM_B4_3	315	\	\	12.68	\	8.79	FR	\	\
DS_315_70_50_LD_LM_B5_4	315	3.68	5.52	10.99	10.75		MF	2.08	2.18
DS_315_70_50_LD_LM_B6_5	315	\	\	12.62	\		FR	\	\
DS_315_90_50_LD_LM_B4_1	315	1.17	2.22	10.34	9.94		MF	2.63	1.65
DS_315_90_50_LD_LM_B5_2	315	1.45	2.13	11.41	10.87		MF	2.81	2.63
DS_315_90_50_LD_LM_B5_3	315	1.11	1.53	9.04	8.56	9.79	MF	2.33	2.38
DS_315_90_50_LD_LM_B7_4	315	\	\	12.99	\		FR	\	\
DS_315_90_50_LD_LM_B6_5	315	\	\	13.10	\		FR	\	\
DS_345_50_LD_LM_1	345	\	\	9.85	\		MF	\	\
DS_345_50_LD_LM_2	345	\	\	11.26	\		MF	\	\
DS_345_50_LD_LM_3	345	1.25	2.90	9.17	8.53		MF	2.80	2.99
DS_345_50_LD_LM_4	345	0.97	1.62	9.56	8.84		MF	1.45	1.54
DS_345_50_LD_LM_5	345	\	\	12.30	\		MF	\	\
DS_345_50_LD_LM_6	345	\	\	11.74	\		FR (1)	\	\
DS_345_50_LD_LM_7	345	\	\	10.18	\		MF	\	\
DS_345_50_LD_LM_8	345	1.17	2.44	7.06	6.42		MF	1.43	1.41
DS_345_50_LD_LM_9	345	\	\	13.14	\	7.91	FR (1)	\	\
DS_345_50_LD_LM_10	345	\	\	13.18	\		FR (1)	\	\
DS_345_50_LD_LM_11	345	0.54	2.87	9.05	8.47		MF	0.89	0.79
DS_345_50_LD_LM_12	345	0.64	1.11	7.15	6.31		MF	1.08	1.04
DS_345_50_LD_LM_13	345	1.02	2.18	10.75	8.96		MF	1.37	1.55
DS_345_50_LD_LM_14	345	0.91	1.38	7.98	7.38		MF	1.13	1.13
DS_345_50_LD_LM_15	345	\	\	12.22	\		MF	\	\
DS_345_50_LD_LM_16	345	\	\	10.30	\		MF	\	\
DS_345_50_LD_LM_17	345	1.65	2.82	9.25	8.33		MF	1.82	1.81
DS_345_50_LD_LM_18	345	\	\	8.59	\		MF	\	\
DS_345_75_LD_LM_1	345	\	\	17.43	\		MF	\	\
DS_345_75_LD_LM_2	345	0.82	1.62	14.93	13.58	13.33	MF	3.92	3.70
DS_345_75_LD_LM_3	345	\	\	14.39	\		MF/FR	\	\

DS_345_75_LD_LM_4	345	1.62	2.73	16.47	13.07		MF	0.99	0.58
DS_200_50_LD_CM_C1_1	200	0.37	1.16	6.93	6.16		SF/MF	0.48	0.53
DS_200_50_LD_CM_C1_2	200	0.25	1.18	7.28	6.33		SF/MF	1.50	1.59
DS_200_50_LD_CM_C1_3	200	0.50	1.04	7.39	6.95	6.34	SF/MF	0.95	0.97
DS_200_50_LD_CM_4	200	0.54	0.99	6.08	5.48		SF	1.07	0.97
DS_200_50_LD_CM_C1_5	200	0.26	0.82	7.34	6.80		SF	0.86	0.94
DS_250_50_LD_CM_1	250	1.00	1.70	8.36	8.09		MF	\	\
DS_250_50_LD_CM_C1_2	250	1.15	1.60	8.85	8.17		SF/MF	0.56	1.31
DS_250_50_LD_CM_3	250	0.64	1.44	8.02	7.48	8.14	SF/MF	1.09	1.45
DS_250_50_LD_CM_4	250	0.80	1.88	8.83	7.97		SF/MF	1.20	1.34
DS_250_50_LD_CM_C1_5	250	0.80	2.25	9.77	8.97		SF/MF	2.14	2.32
DS_315_50_LD_CM_C1_1	315	0.65	1.10	10.88	6.17		SF	1.20	1.27
DS_315_50_LD_CM_C1_2	315	0.98	2.55	8.66	7.85		MF	0.31	0.28
DS_315_50_LD_CM_C1_3	315	1.20	2.60	8.55	7.86	7.63	MF	1.63	1.66
DS_315_50_LD_CM_C1_4	315	0.90	2.30	8.72	7.97		MF	1.46	1.57
DS_315_50_LD_CM_C1_5	315	0.98	2.20	8.59	8.30		MF	1.13	1.69

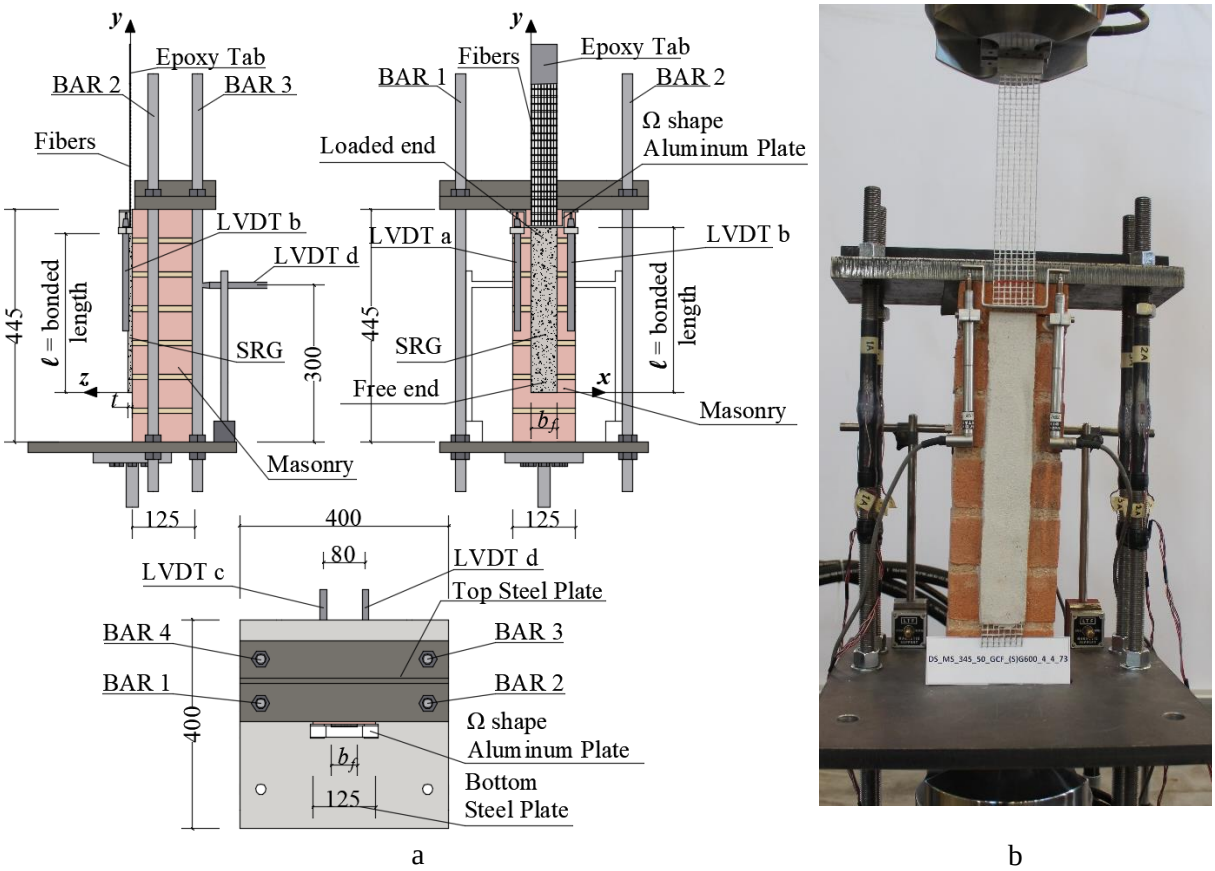

Figure 82. Single-lap shear test setup: sketch (a) and photo of specimen DS_345_50_LD_LM_9 (b).

4.2.1.3 Experimental results: lime-based mortar matrix

In this section the direct-single lap shear test results of specimens that employed a lime-based mortar matrix will be shown. For the sake of clarity, the influence of the different parameters will be discussed separately.

4.2.1.3.1 Influence of the bonded length and test rate

In this section the results of direct shear tests performed on specimens strengthened with a lime-based mortar matrix varying the bonded length and the test rate are presented. All specimens analyzed in this section have the same bonded width and employs LD steel fibers.

The applied load *P* versus global slip *g* response of representative specimens are presented in Figure 83a for different bonded lengths.

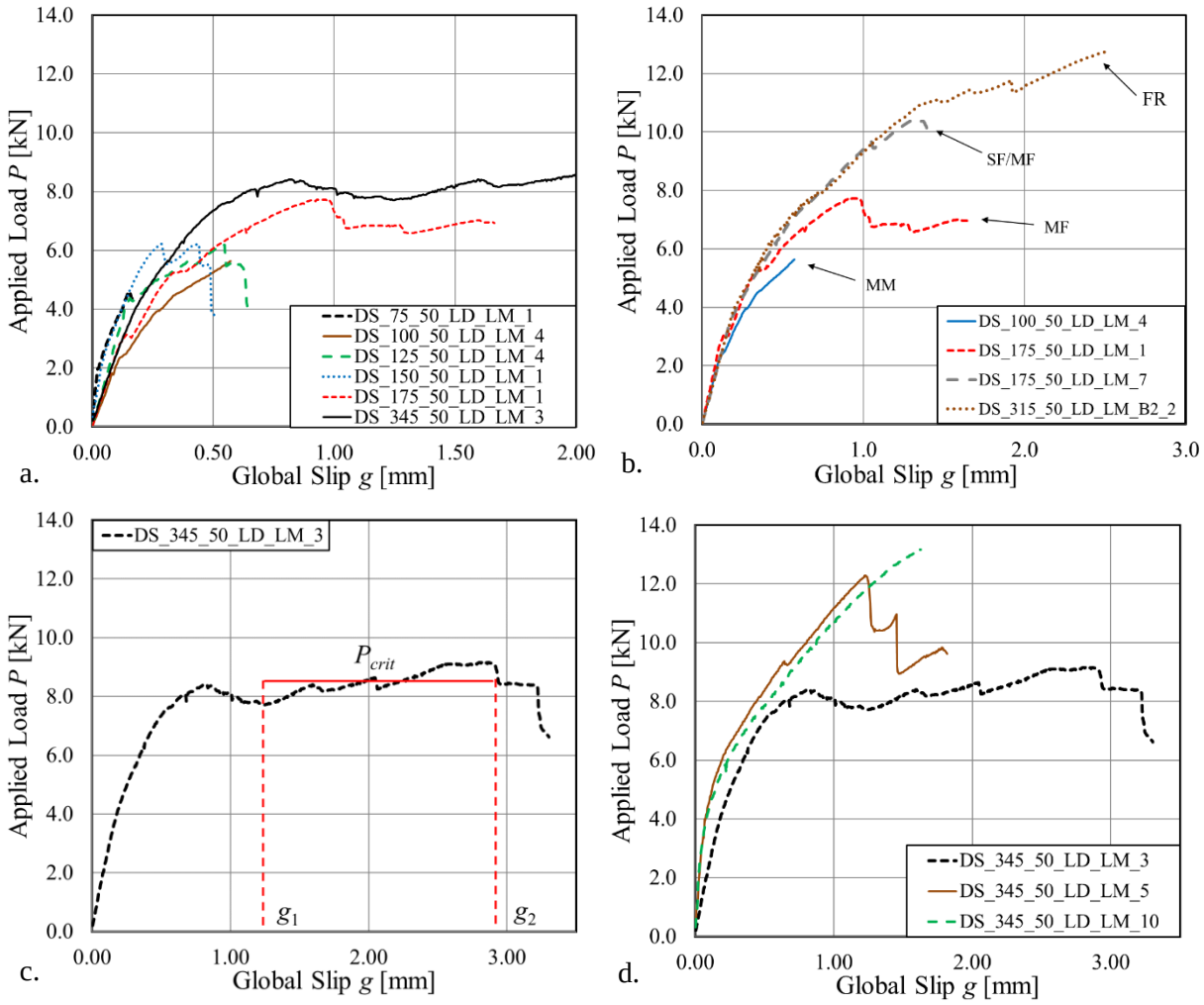

Figure 83. a) Representative load responses for different bonded length; b) Representative load responses for different failure modes, c) Load response of specimen DS_345_50_LD_LM_3; d) Representative load responses for a bonded length equal to 345 mm.

The behavior of the load responses was affected by the bonded length of the SRG strip and by the type of failure. Four different failure modes were observed (Figure 84): a) debonding of the SRG strip from the masonry substrate without a thin layer of masonry attached to the strip (MM), b) interlaminar failure with delamination at the matrix-fiber interface (MF), c) rupture of the steel fibers (FR), and d) mixed failure mode (SF/MF) characterized by the detachment of the SRG strip from the substrate with a thin layer of masonry attached to it (SF) in a limited portion of the bonded region and by the interlaminar failure (MF) in the remaining portions of the bonded region. It should be observed that type d) failure was observed only for specimen DS_175_50_LD_LM_7 (Figure 83b).

For all specimens, the load response was characterized by an initial linear branch followed by a non-linear portion until the peak load, P^*, was reached. Specimens with a bonded length equal or lower than 150 mm failed after the peak load was reached. The failure mode for specimens with a bonded length equal to 75 mm and 100 mm was always type a), i.e. MM, while the failure mode for specimens with ℓ = 125 mm and ℓ = 150 mm was delamination at the fiber-matrix interface (MF). Out of ten specimens with ℓ = 175 mm, four specimens failed after the peak load was reached while six specimens presented a drop in the load response when the peak was reached, followed by a nominally constant load portion (plateau) until failure. The load responses of specimens with long bonded length ($\ell \geq$ 200 mm) had generally three different behaviors depending on the failure mode. Twenty-six specimens with long bonded length presented a drop after the peak was reached followed by an approximatively constant load branch (plateau). For these specimens, which failed at the matrix-fiber interface (MF), the load carrying capacity or plateau load, P_{crit}, was evaluated as the average value of the applied load in the range of global slips $[g_1,g_2]$. The value g_1 was defined as the value of global slip that corresponded to the first substantial drop in the load response after the peak was reached, while the value g_2 was defined as the last value of global slip that preceded the failure of the specimen (Figure 83c). For all specimens that presented a constant plateau in the load response, i.e. the aforementioned twenty-six specimens with $\ell \geq$ 200 mm and the six specimens with a bonded length equal to 175 mm, the values of g_1, g_2 and P_{crit} are reported in Table 20. These specimens were referred to as "Plateau specimens". In addition, for these specimens, the average value of LVDT c ($\overline{w_c}$) and LVDT d ($\overline{w_d}$) in the range $[g_1,g_2]$ was reported in Table 20. The maximum value of $\overline{w_c}$ and $\overline{w_c}$ resulted equal to 2.80 mm and 2.99 mm, respectively, which supports the choice of arranging the masonry block 1 mm forward with respect to the initial alignment (see Section 4.2.1.2). Generally, the longer is the bonded length the longer is the plateau. Six specimens with long bonded length failed because of the rupture of the fibers (FR) and showed an always increasing load response until failure. Twenty-two specimens with $\ell \geq$ 200 mm showed a type b) failure mode (MF) with an always increasing load response or with a load response characterized by large drops without a constant plateau. In Figure 83d, the load responses for specimens DS_345_50_LD_LM_3, DS_345_50_LD_LM_5, and

DS_345_50_LD_LM_10 are reported. It can be observed that the load responses had a similar trend until approximatively 8 kN. After 8 kN, delamination started in specimen DS_345_50_LD_LM_3 and the cohesive crack at the matrix-fiber interface continued to propagate gradually until failure, which resulted in the presence of a plateau in the response. Specimen DS_345_50_LD_LM_5 had a behavior similar to specimen DS_345_50_LD_LM_10 until approximatively 12 kN, after which the interlaminar failure quickly propagated (MF) with sudden drops in the load response. Specimen DS_345_50_LD_LM_10 showed a monotonic increasing load response until the rupture of the fibers. Only the value of the peak load, *P**, was reported in Table 20 for all the specimens whose load response didn't show a constant plateau. The plots of Figure 83d are symptomatic of how the variability of the mortar properties and the impregnation of the fibers could entail for different load responses. A large scatter in the experimental results can be observed in Table 20. Considering specimens DS_315_50_LD_LM_B2_2 and DS_315_50_LD_LM_B2_3, which were cast using the same batch of mortar matrix (B2) and using the same bonded length equal to 315 mm, the peak load, *P**, was equal to 12.75 kN and 6.21 kN, respectively.

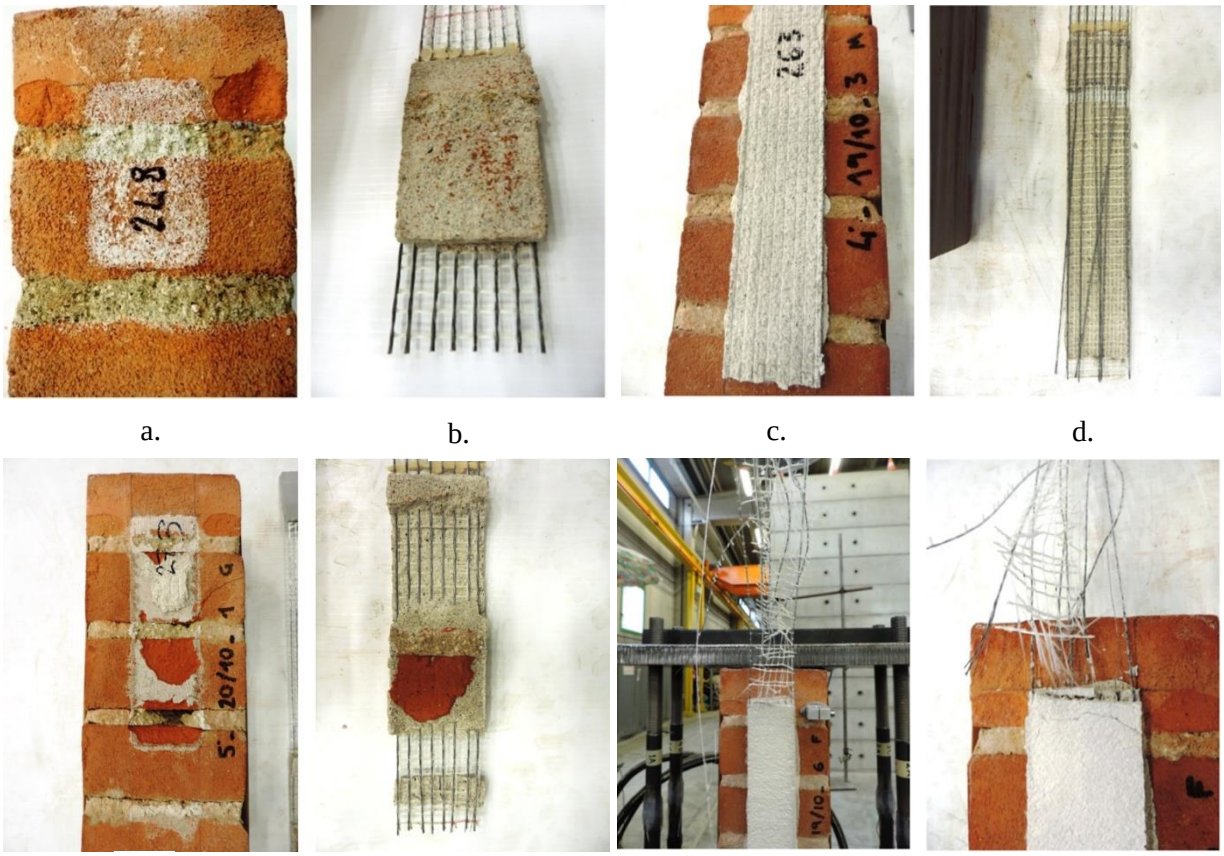

a. b. c. d.

e. f. g. h.

Figure 84. Failure modes: a) and b) debonding at the masonry substrate (MM), c) and d) delamination at the matrix-fiber interface (MF), e) and f) mixed failure mode (SF/MF), g) and h) rupture of the fibers (FR).

The different response can be ascribed in part to different saturation levels of the masonry blocks prior to applying the SRG strip. It is possible that the masonry block that resulted less wetted, absorbed part of the water of the mortar matrix during and after application of the composite strip, which caused a reduction of the mortar matrix mechanical properties that translated into low bond properties. In addition, as reported in section 3.3.4.1, it can be observed that both the compressive and fracture properties of the mortar were quite scattered among the different batches. Batch B3 had a compressive strength equal to 15.7 MPa that was 39% higher than the compressive strength of batch B4, and a fracture energy equal to 30 N/m that was 3% higher that the value found for batch B4. The scatter of the mortar matrix properties among different batches contributed to the scatter of the experimental single-lap shear test results. A third reason for the scatter in the experimental results is related to the application of the SRG composite to the masonry substrate, since for all specimens it was difficult to control that the mortar matrix was fully penetrating through and impregnating each steel fiber during casting of SRG strips.

Figure 85a reported the average peak load and the average plateau load for different bonded lengths. The load response shown in Figure 85a is referred to as $P_{crit}(\ell)$ in the remainder of the dissertation. The average value of the peak load is represented with a blue circular marker in Figure 85a for $\boldsymbol{\ell} \leq 175$ mm, while the average value of the plateau load is represented with a red triangular marker for $\boldsymbol{\ell} > 175$ mm. The average value of the plateau load for specimens with $\boldsymbol{\ell} = 280$ mm was omitted because it was possible to evaluate P_{crit} only for specimen DS_280_50_LD_LM_4, which cannot be considered statistically relevant. The choice of plotting the peak load for specimens with short bonded lengths was determined by the fact that for these specimens the test failed prior to observing a plateau in the load response. Figure 85a shows an increase of the average value of the peak load with the bonded length until $\boldsymbol{\ell} = 175$ mm, then the average value of the plateau load has an approximatively constant trend between $\boldsymbol{\ell} = 175$ mm and $\boldsymbol{\ell} = 315$ mm, with values that range from 4.92 kN to 6.30 kN. The maximum value of the average plateau load is observed for $\boldsymbol{\ell} = 345$ mm and results equal to 7.91 kN. Due to the trend observed in Figure 85a, it can be stated that, for the SRG composite studied in this experimental work, the effective bond length, i.e. the length of the composite strip needed to fully establish the stress transfer between the composite strip and the substrate, is between 175 mm and 200 mm. This fact is confirmed from the load responses analyzed in Figure 83b, that feature a constant plateau starting from a bonded length equal to 175 mm. This evaluation of the effective bond length didn't take into account those specimens with $\boldsymbol{\ell} \geq 200$ mm that didn't show a constant plateau in the load response. These specimens usually reached the rupture of the fibers or values of the peak load close to the value that caused the rupture of the fibers. The author choses to neglect these specimens for the determination of the effective bond length since they were not representative of the actual interlaminar debonding phenomenon and thus can entail for misleading results.

For the sake of completeness, Figure 85b shows the average value of the peak load for different bonded lengths, considering all specimens tested at the standard rate (0.00084 mm/s). The load response shown in Figure 85b is referred to as $P^*(\ell)$ in the remainder of the dissertation. It could be noted that values of the load in the $P^*(\ell)$ response of Figure 85b are in general higher than the ones in the $P_{crit}(\ell)$ response for the same bonded length, since the former includes also specimens that didn't show a constant plateau in the load response, i.e. specimens that failed reaching a value of the load close to the one corresponding to the rupture of the fibers.

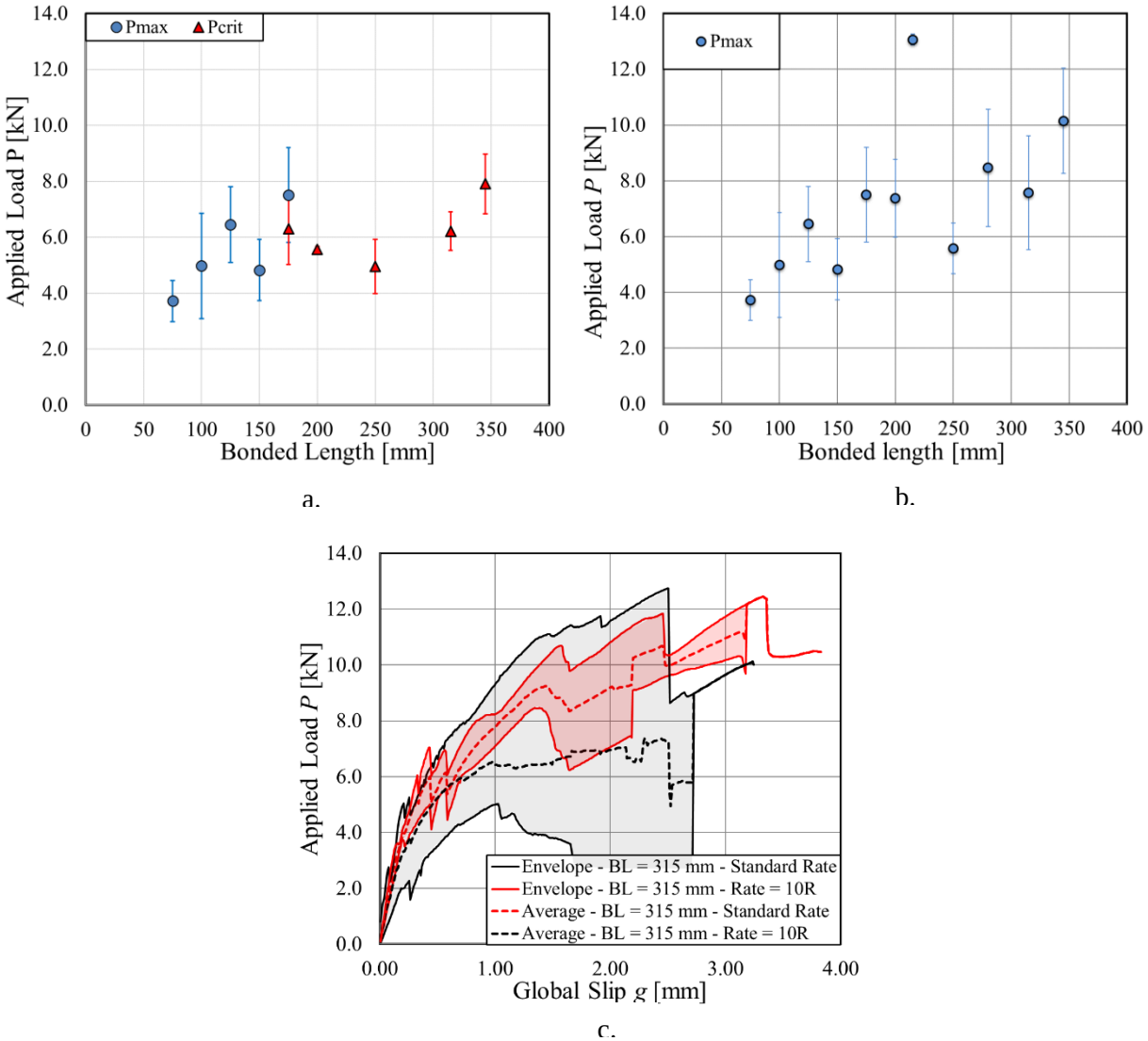

Figure 85. a) $P_{crit}(\ell)$ response; b) $P^*(\ell)$ response; c) Load-global slip envelope for specimens with a bonded length equal to 315 mm and two different rates (0.00084 mm/s and 0.0084 mm/s).

Figure 85c shows a comparison between direct single-lap shear tests performed using two different test rates and a constant bonded length equal to 315 mm. The grey area represents the envelope of the experimental tests performed at the standard rate (0.00084 mm/s), while the black dashed line is the average response of those tests, which is obtained by averaging the values of P for each value of g. Similarly, the red area represents the envelope of the experimental tests performed at a rate that was ten times the standard one (0.0084 mm/s), while the red dashed line is the average response. The average peak load for specimens tested at standard rate and ten times the standard rate resulted equal to 7.57 kN and 10.41 kN, respectively. It appears that this type of composites exhibits a rate effect [120]. As shown in Figure 85c, the average curve of specimens tested at a rate equal to 0.0084 mm/s is well above the average curve of specimens tested at standard rate. On the other hand, it should also be pointed out that only three specimens were tested with a higher rate and therefore more results are needed to confirm this trend.

4.2.1.3.2 Influence of the fiber density

In this section masonry blocks strengthened with LD steel fibers and MD steel fibers will be compared. Since all specimens with MD steel fibers had a nominal bonded length and width equal to 315 mm and 50 mm, respectively, only LD specimens with the same geometrical characteristics of the SRG strip will be considered. The load responses of all MD specimens had the same behavior (Figure 86a), characterized by an initial linear portion, followed by a non-linear branch until the peak load P* was reached. After the peak load was reached, all specimens showed a nominally constant portion of the load response until failure. The values of the plateau load, P_{crit}, evaluated as described in section 4.2.1.3.1 and global slip ranges $[g_1,g_2]$ for specimens with MD steel fibers are reported in Table 20. The failure mode for all masonry blocks strengthened with MD steel fibers consisted in the delamination at the fiber-matrix interface (Figure 86b). The average debonding stress, obtained dividing the load P_{crit} by the nominal area of the fibers is equal to 610 MPa and 1445 MPa for MD and LD specimens, respectively, while the load carrying capacity is equal to 5.25 kN and 6.22 kN for MD and LD specimens, respectively. It appeared that an increase in the density of the steel fibers caused a decrease of the load carrying capacity. This fact is due to the reduced amount of mortar matrix between two consecutive steel fibers in MD specimens with respect to LD specimens. The reduced amount of mortar matrix caused a lower value of the applied load needed to initiate and propagate the cohesive crack.

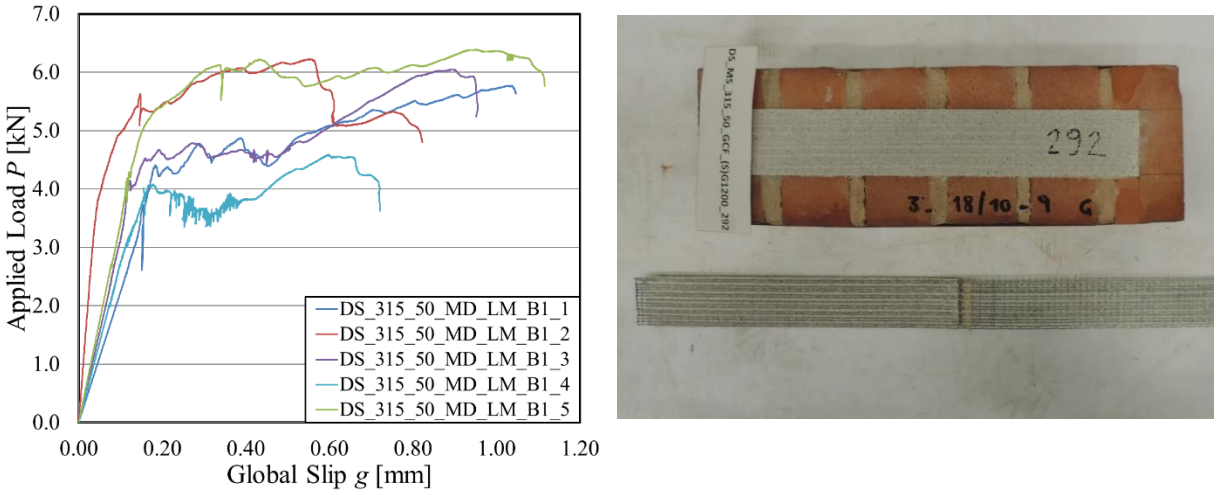

a. b.

Figure 86. a) Load responses of specimens strengthened with MD steel fibers embedded in a lime-based mortar matrix; b) Failure mode of specimen DS_315_50_MD_LM_B1_1.

4.2.1.3.3 Influence of the bonded width

In this section masonry blocks strengthened with LD steel fibers using different bonded widths will be compared. Figure 87a shows the load responses of specimens reinforced with LD steel fibers that have a bonded width equal to 75 mm and a bonded length equal to 345 mm. For these specimens, the width of the fiber sheet is equal to the bonded width. All load responses had an initial linear portion followed by a non-linear branch until the peak load was reached. After the peak load was reached, specimens DS_345_75_LD_LM_1 and DS_345_75_LD_LM_3 failed suddenly, while the load response of specimens DS_345_75_LD_LM_2 and DS_345_75_LD_LM_4 had a drop followed by a nominally constant plateau until failure was reached. Except for specimen DS_345_75_LD_LM_3 that experienced a mixed mode failure characterized by both rupture of some micro-cords and delamination at the fiber-matrix interface (Figure 87b), the remaining specimens had a failure characterized by the detachment of the external layer of matrix and fibers from the internal layer of matrix (MF). The average value of the load carrying capacity per unit width (P_{crit}/b_f) evaluated for specimens with a bonded width equal to 75 mm, resulted equal to 178 N/mm. The corresponding value evaluated for specimens with a bonded length and width equal to 345 mm and 50 mm, respectively, resulted equal to 158 N/mm. Considering the high scatter of experimental results, the two values are quite similar, suggesting that for SRG composites bonded to a masonry substrate there is no “width effect”, i.e. for this type of reinforcements the fibers work independently one another.

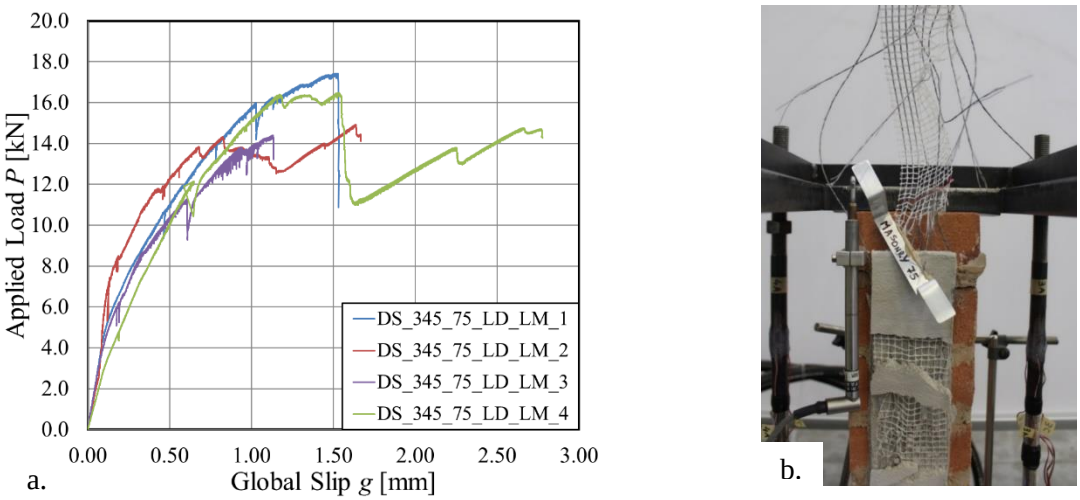

Figure 87. a) Load responses of specimens with a bonded width equal to 75 mm; b) Failure mode of specimen DS_345_75_LD_LM_3.

The influence of the composite width on the load responses was investigated also varying the bonded width, b_f, of the SRG composite and maintaining a constant width of the fibers sheet (equal to 50 mm). The load responses for specimens with a bonded with equal to 70 mm and 90 mm are showed in Figure 89a and Figure 90a, respectively. Specimens with a bonded with equal to 70 mm had an average load carrying capacity equal to 8.79 kN that was 41% higher than the value obtained for specimens with a bonded width and a bonded length equal to 50 mm and 315 mm, respectively (6.22 kN). In addition, out of five specimens with a bonded width equal to 70 mm, three specimens reached the rupture of the fibers (Figure 89b). It appeared that, for a constant width of the fiber sheet, an increase in bonded width of the SRG composite entails for increasing values of the load carrying capacity, since it is required a higher amount of energy to initiate and propagate the crack due to the additional mortar matrix area of the cross-section. This statement is valid only for certain widths of the SRG composite. Observing the average load carrying capacity of specimens with a bonded width equal to 90 mm (Table 20), it can be noted that the value is 57 % higher than the one obtained for specimens with a bonded width and a bonded length equal to 50 mm and 315 mm, respectively. Out of five specimens with a bonded length equal to 90 mm, three specimens experienced a failure characterized by delamination at the fiber matrix-interface with longitudinal cracks along the mortar matrix at approximately 10 mm from the matrix edges (Figure 90b). Even if the average load-carrying capacity of specimens with a 90 mm bonded width was higher than specimens with a 70 mm bonded width, the average peak load for specimens with a bonded width equal to 90 mm was lower than the corresponding value for specimens with a bonded width equal to 70 mm, which reached in most of cases the rupture of the fibers. It appeared that for a 50 mm-wide fiber sheet, a 70 mm bonded width is enough to improve the bond performances, while larger increases of the bonded width didn't provide any benefit to the bond performances.

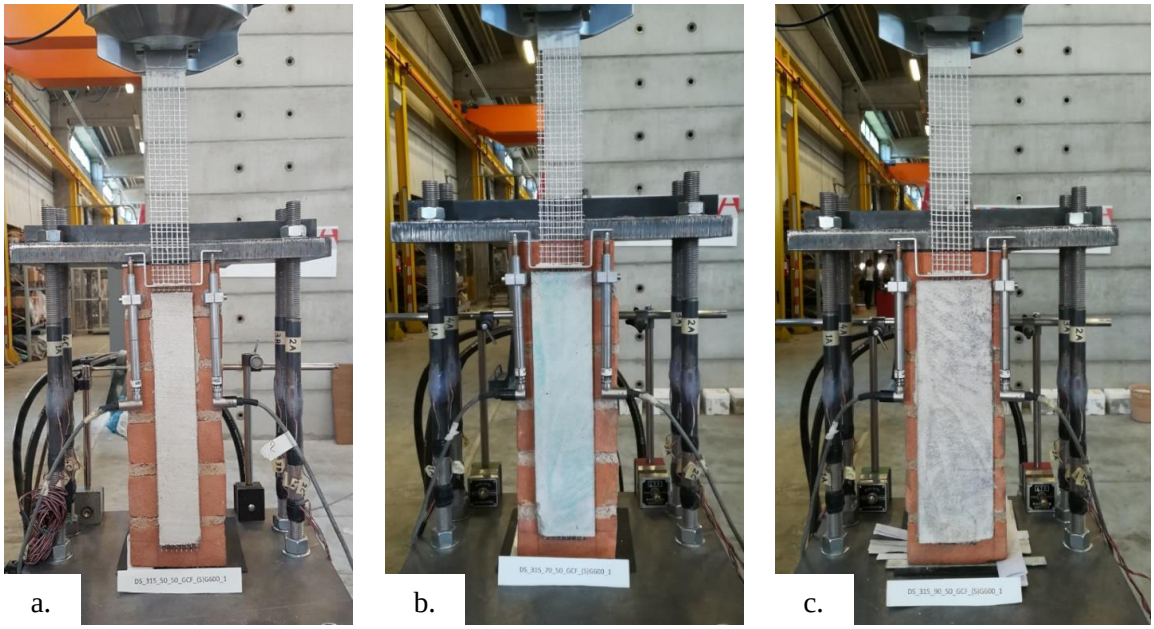

Figure 88. Direct-shear test set-up: a) Specimen DS_315_50_LD_LM_B3_13; b) Specimen DS_315_70_50_LD_LM_B3_1; c) Specimen DS_315_90_50_LD_LM_B4_1.

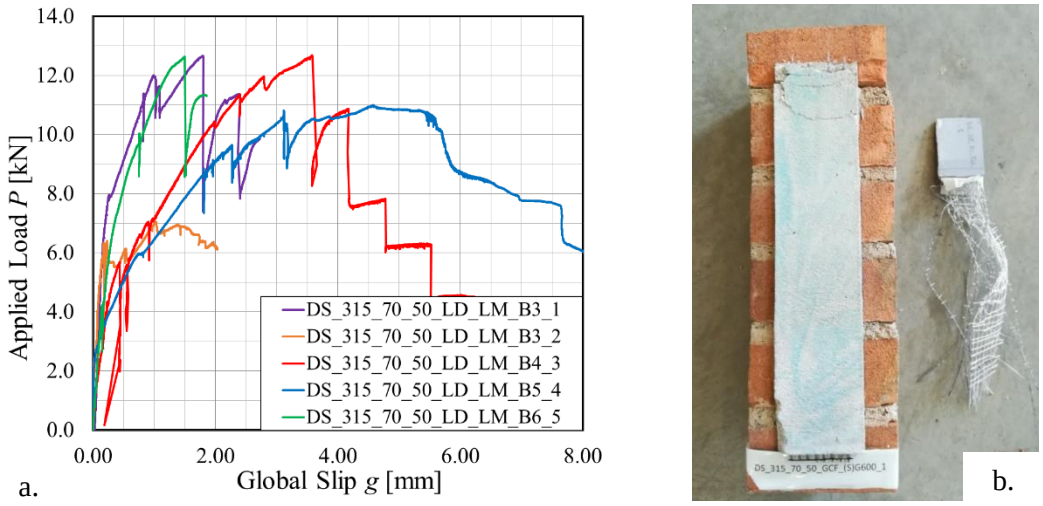

Figure 89. a) Load responses for specimens with a bonded width equal to 70 mm and a 50 mm-wide fiber sheet; b) Failure mode of specimen DS_315_70_50_LD_LM_B3_1.

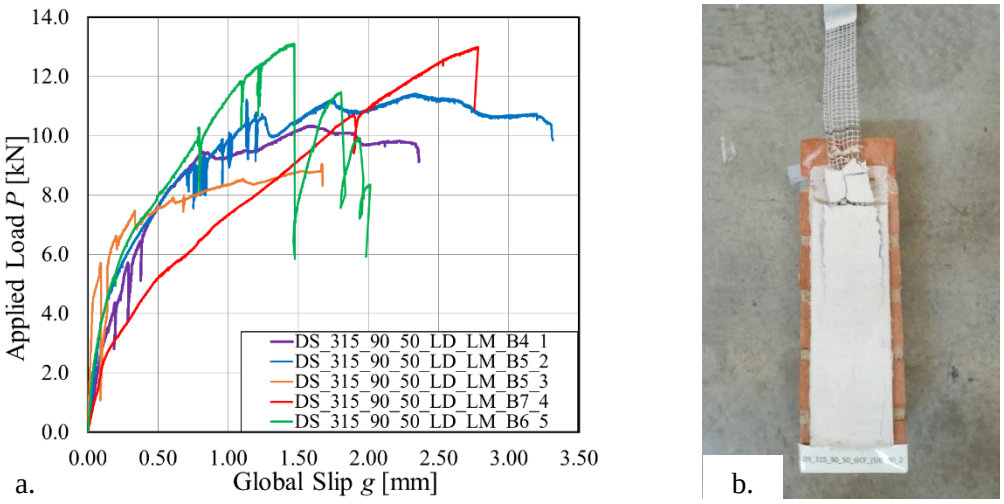

Figure 90. a) Load responses for specimens with a bonded width equal to 90 mm and a 50 mm-wide fiber sheet; b) Failure mode of specimen DS_315_90_50_LD_LM_B5_2.

4.2.1.4 Experimental results: cement-based mortar matrix

In this section the direct-single lap shear test results of specimens that employed LD steel fibers embedded in a cement-based mortar matrix will be shown. Three different bonded length were investigated, i.e. 200 mm, 250 mm, and 315 mm, while the bonded width was maintained constant and equal to 50 mm. Figure 91a showed the load response of representative specimens for each bonded length. It can be observed that each load response had an initial linear branch, followed by a non-linear portion until a peak load, P*, was reached. After the peak load, all the graphs had a nominally constant branch until failure. Generally, longer values of the bonded length are associated with a longer plateau. Three failure modes were observed, i.e. delamination at the fiber-matrix interface (MF), detachment of the SRG strip with a thin layer of masonry attached to it (SF), and a mixed mode with some portions of the bonded region the failed at the matrix-fiber interface and some portions that failed with the fracture that propagated into the masonry substrate (MF/SF). For each specimen, the load carrying capacity was evaluated as described in section 4.2.1.3.1. The average load carrying capacity for specimens with a bonded length equal to 200 mm, 250 mm, and 315 mm was equal to 6.34 kN, 8.14 kN, and 7.63 kN, respectively (Table 20). Figure 91b shows the average value of the load carrying capacity for each bonded length. It can be observed that the average value of the load carrying capacity seemed to increase until a bonded length equal to 250 mm. After 250 mm, an increase in the bonded length didn't cause an increase of the load carrying capacity. For that reasons it appeared that the effective bonded length, i.e. the length needed to establish completely the shear stress transfer between the SRG composite strip and the masonry substrate is between 200 mm and 250 mm.

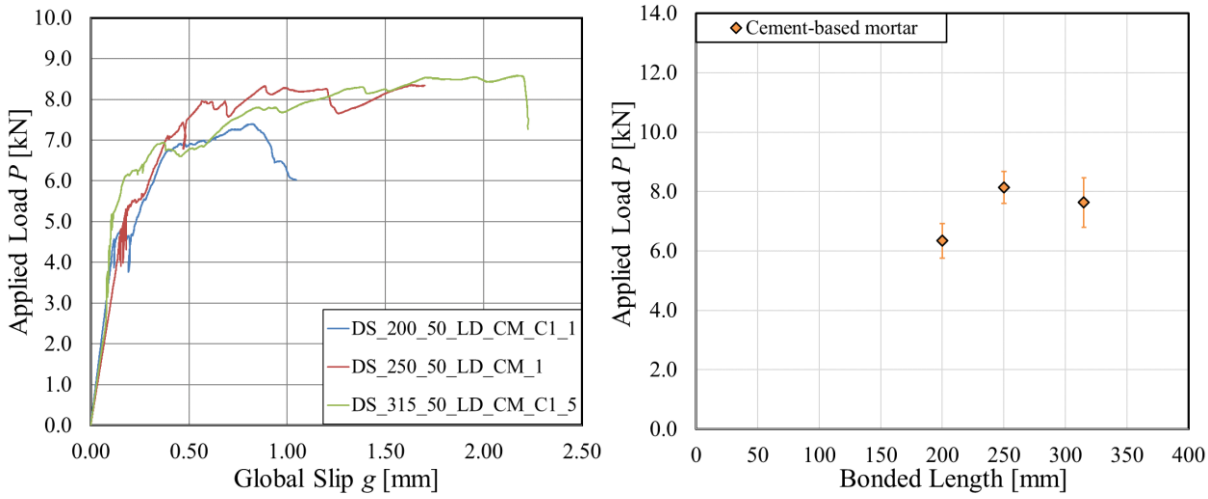

a. b.

Figure 91. a) Load responses of representative specimens strenghtend with a cement-based mortar matrix a three different bonded length; b) Load versus bonded length response for specimens strengthened with LD steel fibers and a cement based mortar matrix.

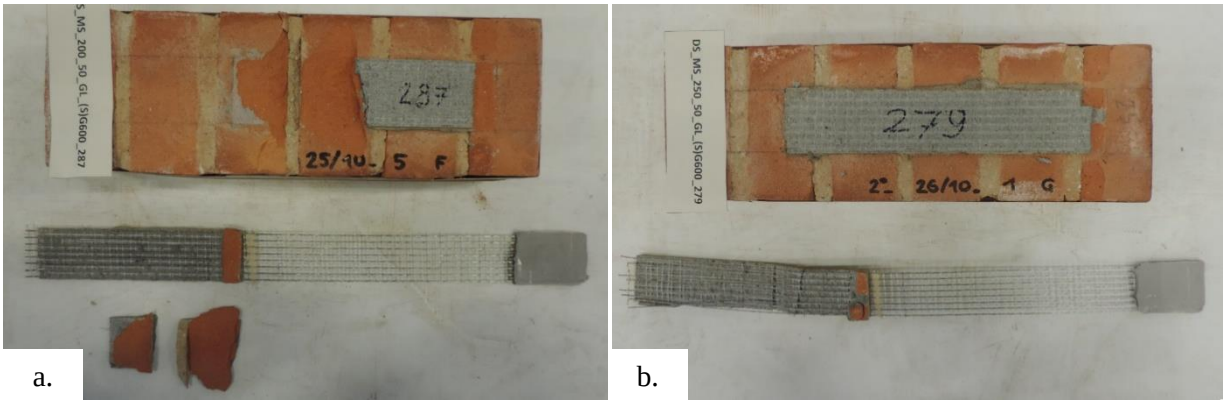

a. b.

Figure 92. a) Failure mode for specimen DS_200_50_LD_CM_C1_1; b) Failure mode for specimen DS_250_50_LD_CM_1.

4.2.1.5 Indirect calibration of the cohesive material law

In this section the cohesive material law (CML) of SRG-masonry joints will be calibrated through two different indirect methods. Only specimens with a bonded width equal to 50 mm and strengthened with LD steel fibers embedded in a lime based mortar, i.e. the specimens described in section 4.2.1.3.1 (except for the three specimens tested at a different rate), will be considered in this section. The first method calibrates the CML using the load versus bonded length response, while the second method allows to obtain the CML from the average load-global slip response. It should be noted that the CML obtained will be representative of the interfacial crack propagation at the fiber-matrix interface, which is the

interface that plays the main role for this SRG composite. A CML for the matrix-substrate interface cannot be obtained as only few specimens exhibited crack propagation at this interface and they were typically characterized by small bonded lengths.

4.2.1.5.1 Functions adopted for the definition of the cohesive material law

Both methods require the adoption of a CML. The CML, i.e. the relationship between the slip *s* of the steel fibers with respect to the matrix, and the corresponding shear stress τ at the matrix-fiber interface, will be referred to as τ(*s*) relationship in this work. Two different shapes of the cohesive material law will be used in this study. The first CML is derived from the expression proposed by Dai et al. [35]:

$$\tau(s) = \mathrm{A}\left(e^{-\alpha s} - e^{-2\alpha s}\right) \tag{79}$$

Where **p** = [A, α] is the set of unknown parameters, arbitrarily assigned at the beginning of the procedure. Using Eq. (79), the maximum value of the slip, s_f, beyond which no stress transfer occurs approaches infinity ($s_f \to +\infty$). Eq. (79) represents a cohesive material law characterized by shear stress equal to zero when $s = 0$ ($\tau(0)=0$).

The second CML is a tri-linear function, proposed by Focacci et al. [91]:

$$\tau(s) = \begin{cases} \tau_0 + \dfrac{\tau_m - \tau_0}{s_m} s & \text{if} \quad 0 \le s \le s_m \\ \tau_{01} - \dfrac{\tau_{01}}{s_{01}} s & \text{if} \quad s_m \le s \le s_c \\ \tau_{02} - \dfrac{\tau_{02}}{s_f} s & \text{if} \quad s_c \le s \le s_f \end{cases} \tag{80}$$

Where **p** = [τ_0, τ_{01}, τ_{02}, τ_m, s_{01}, s_f, s_m] is the set of unknown parameters, arbitrarily assigned at the beginning of the procedure. Eq. (80) represents a CML characterized by shear stress equal to τ_0 when $s = 0$. Eq. (79) implies an infinite effective bond length, while Eq. (80) implies a finite effective bond length.

4.2.1.5.2 Indirect calibration from the load-bonded length response

The first method for the indirect calibration of the CML was proposed by Focacci et al. [163] and is employed in the present section to fit the load versus bonded length response $P_{crit}(\ell)$ and $P^*(\ell)$ showed in Figure 85a-b. In this work, the indirect calibration obtained from the $P_{crit}(\ell)$ response is referred to as $CAL_{Pcrit(\ell)}$ while the indirect calibration obtained from the $P^*(\ell)$ response is referred to as $CAL_{P^*(\ell)}$. The

steel fibers are considered evenly distributed across the width of the composite strip, b_f. Based on this assumption, the area of the fiber sheet can be evaluated as $A_f = b_f t^*_{f,LD}$.

As described in section 4.2.1.3.1, the most common type of failure of SRG-masonry joints observed in the present study is delamination at the matrix-fiber interface. Once the shape of the CML is chosen, the differential equation that governs the debonding phenomenon can be expressed as:

$$\frac{d^2 s}{dy^2} = \frac{b_f}{E_f A_f} \tau(s) \tag{81}$$

where $s = s(y)$ is the slip at location y. The location y refers to the Cartesian system shown in Figure 82. Eq. (81) can be solved once the boundary conditions are assigned (for example at the free end, i.e. $y = 0$). The procedure aims to define for each bonded length that has been tested, the analytical load response $P(g)$, determined with the assigned cohesive material law. The load response $P(g)$ is characterized by two branches, i.e. a first branch, $P_1(g)$, that corresponds to null slips at the free end and a second branch, $P_2(g)$, that corresponds to nonzero slips at the free end. Then, for each bonded length, the maximum value of the analytical load response, $P_{max}(\ell)$, is evaluated and compared with the experimental value. Finally, the unknown parameters of the cohesive material law are calibrated through a best fit procedure in order to minimize for each bonded length the gap between the average experimental value and the analytical one. The procedure to define the $P(g)$ response for each bonded length consisted of 4 steps.

Step 1: determination of the applied load $\overline{P}$ and the relative loaded end slip $\overline{g}$ at the onset of nonzero slip at the free end, solving Eq. (81) with the following boundary conditions at the free end ($y = 0$):

$$\begin{cases} s(0) = 0 \\ \varepsilon(0) = \left.\dfrac{ds}{dy}\right|_{y=0} = 0 \end{cases} \tag{82a,b}$$

The applied load $\overline{P}$ and the relative loaded end slip $\overline{g}$ are then evaluated as:

$$\begin{aligned} \overline{g} &= \overline{s}(\ell) \\ \overline{P} &= E_f A_f \left.\frac{d\overline{s}}{dy}\right|_{y=\ell} \end{aligned} \tag{83}$$

Where $\bar{s}(y)$ is the slip value obtained solving Eq. (81) enforcing the boundary conditions expressed in Eq. (82a,b).

Step 2: evaluation of the first portion $P_1(g)$ of the load response $P(g)$ in the global slip range $\left[0, \bar{g}\right]$, using Eq. (84a,b):

$$\begin{aligned} g &= s(\ell) \\ P_1(g) &= \sqrt{2 b_f E_f A_f \int_0^g \tau(s)\, ds} \end{aligned} \tag{84a,b}$$

Step 3: evaluation of the second portion $P_2(g)$ of the load response $P(g)$. In order to define the second branch $P_2(g)$, Eq. (81) was solved considering a set of values of the free end slip, s_F, with the following boundary conditions:

$$\begin{cases} s(0) = s_F \\ \varepsilon(0) = \left.\dfrac{ds}{dy}\right|_{y=0} = 0 \end{cases} \tag{85a,b}$$

The solution $s(y) = s_{sF}(y)$ can be defined for each value of the free end slip s_F. The subscript s_F specifies that the slip profile $s(y) = s_{sF}(y)$ is referred to a certain slip value s_F at free end. Both the loaded end slip g and the applied load P can be determined for each value of s_F:

$$\begin{aligned} g(s_F) &= s_{sF}(\ell) \\ P(s_F) &= E_f A_f \left.\frac{ds_{sF}}{dy}\right|_{y=\ell} \end{aligned} \tag{86a,b}$$

The second portion $P_2(g)$ of the load response $P(g)$ can be then defined by eliminating the parameter s_F between the two functions $P(s_F)$ and $g(s_F)$.

Step 4: The entire $P(g)$ response can be obtained as the union of the two branches $P_1(g)$ and $P_2(g)$, determined in Step 2 and Step 3, respectively.

Once the entire $P(g)$ response was determined for each bonded length, the maximum value of the load corresponding to a defined bonded length, $P_{max}(\ell)$, can be obtained as:

$$P_{max}(\ell) = \max\left\{P(g)\right\} \tag{87}$$

For $CAL_{Pcrit(\ell)}$ the analytical $P_{max}(\boldsymbol{\ell})$ response is compared with the $P_{crit}(\ell)$ response shown in Figure 85a, while for $CAL_{P^*(\ell)}$ the analytical $P_{max}(\boldsymbol{\ell})$ response is compared with the $P^*(\ell)$ response shown in Figure 85b. The unknown parameters are determined by minimizing the distance between the analytical and experimental response using the least square method, i.e. minimizing the error between the analytical value $P_{max}(\boldsymbol{\ell})$ and the average experimental value of the debonding load for each bonded length.
The analytical $P_{max}(\boldsymbol{\ell})$ response was obtained by determining, for each bonded length, the analytical $P(g)$ response. It is worth noting that using this procedure, the analytical $P(g)$ response associated with a certain bonded length, $\boldsymbol{\ell}_1$, coincides with the $P(g)$ response of a shorter bonded length, $\boldsymbol{\ell}_2$, up to the point $(\overline{g}_2, \overline{P}_2)$, defined as:

$$\overline{g}_2 = \bar{s}(\ell_2)$$
$$\overline{P}_2 = E_f A_f \left.\frac{d\bar{s}}{dy}\right|_{y=\ell_2} \qquad (88a,b)$$

This is true when all the specimens exhibit the same type of failure, i.e. the fracture process is governed by the same CML, regardless of the bonded length. It has been observed in section 4.2.1.3.1 that specimens with a bonded length shorter than 125 mm had a failure mode characterized by the detachment of the SRG strip from the masonry substrate (MM). All the remaining specimens considered in the best fit procedure had a failure mode characterized by delamination at matrix-fiber interface (MF). Thus, specimens with a bonded length equal to 75 mm and 100 mm, should not be considered for the fitting, since the cohesive material law that governs the fracture process is different with respect to the other specimens. The author decided to include these specimens in the best fit procedure. Because of the hierarchy of interface failures, it is possible that the interlaminar failure for short bonded length cannot be obtained experimentally. Thus, this would mean that that type of failure would require a higher load than the MM failure. Keeping this mind, the author used all data to determine the CML through the best fit procedure, although it might not be fully representative of specimens with $\boldsymbol{\ell} \leq 100$ mm.

4.2.1.5.3 Indirect calibration from the load-global slip response

The second method, introduced earlier to calibrate indirectly the CML employs the load-global slip response. Once the CML is chosen (see section 4.2.1.5.1), which is associated with an arbitrary set **p** of parameters, the analytical $P(g)$ response corresponding to a bonded length equal to 345 mm, $P(g)_{\ell=345}$,

is evaluated through the procedure described in section 4.2.1.5.2. The CML is then calibrated minimizing the error between the analytical $P(g)_{\ell=345}$ response and the average experimental response. The average experimental response is evaluated considering two different sets of data. The experimental response referred to as $\overline{P^{ALL}(g)}$ is determined considering all the load-global slip responses of specimens with $\ell \geq$ 175 mm while the average experimental response referred to as $\overline{P^{PLAT}(g)}$ is determined considering the load-global slip responses of the "Plateau specimens", i.e. the specimens that feature a constant plateau (P_{crit}) and therefore characterized by an interlaminar failure mode at the matrix-fiber interface (MF).

The average load-global slip response $\overline{P^{ALL}(g)}$ is reported in Figure 93a while the average load-global slip response $\overline{P^{PLAT}(g)}$ is reported in Figure 93b. The unknown parameters of the CML are calibrated through a best fit procedure that employs the least square method to minimize the error between the analytical value of the $P(g)$ response for a bonded length equal to 345 mm, $P(g)_{\ell=345}$, and $\overline{P^{ALL}(g)}$ or $\overline{P^{PLAT}(g)}$, respectively. The indirect calibration obtained from the $\overline{P^{ALL}(g)}$ response is referred to as $CAL_{\overline{PALL(g)}}$; while the indirect calibration obtained from the $\overline{P^{PLAT}(g)}$ response is referred to as $CAL_{\overline{PPLAT(g)}}$. The calibration criterion is described in section 4.2.1.5.4.

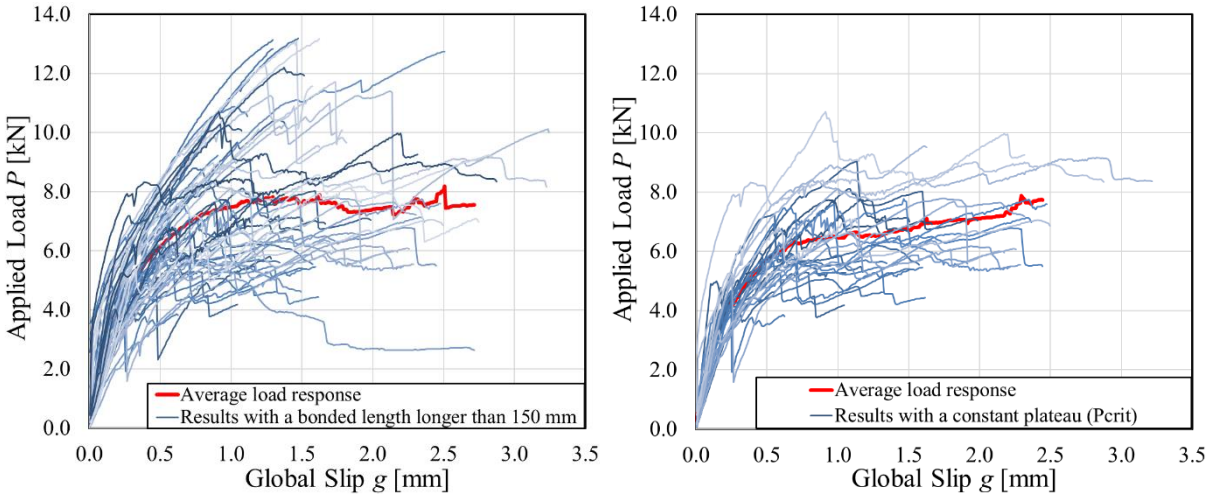

Figure 93. Average experimental response: a) $\overline{P^{ALL}(g)}$ response; b) $\overline{P^{PLAT}(g)}$ response.

4.2.1.5.4 Calibration criterion

The indirect calibration of the CML aims to define, among the possible set **p** of parameters that can describe the CML, the set **p** that provides the best fit between the analytical and experimental responses. The set **p** of unknown parameters can be obtained by minimizing the distance between the analytical and experimental responses. For the indirect method described in section 4.2.1.5.2 the calibration criteria aimed to determine the set **p** of parameters that minimize the distance between $P_{\max}(\boldsymbol{\ell})$ and $P_{crit}(\ell)$ or $P^*(\ell)$:

$$d\left(P_{crit}(\ell), P_{\max,\underline{\mathbf{p}}}(\ell)\right) \le d\left(P_{crit}(\ell), P_{\max,\mathbf{p}}(\ell)\right) \quad \forall \mathbf{p} \tag{89}$$

$$d\left(P^*(\ell), P_{\max,\underline{\mathbf{p}}}(\ell)\right) \le d\left(P*(\ell), P_{\max,\mathbf{p}}(\ell)\right) \quad \forall \mathbf{p} \tag{90}$$

Where the subscript **p** is used to specify that the analytical load response depends on the choice of the set **p** of unknown parameters, while $d\left(P_{crit}(\ell), P_{\max,\mathbf{p}}(\ell)\right)$ and $d\left(P*(\ell), P_{\max,\mathbf{p}}(\ell)\right)$ is the distance between the experimental $P_{crit}(\ell)$ and analytical $P_{\max,\mathbf{p}}(\ell)$ responses and the experimental $P^*(\ell)$ and analytical $P_{\max,\mathbf{p}}(\ell)$ responses, respectively, determined as:

$$d\left(P_{crit}(\ell), P_{\max,\mathbf{p}}(\ell)\right) = \sum_{j=1}^{N}\left[P_{crit}\left(\ell_j\right) - P_{\max,\mathbf{p}}\left(\ell_j\right)\right]^2 \tag{91}$$

$$d\left(P^*(\ell), P_{\max,\mathbf{p}}(\ell)\right) = \sum_{j=1}^{N}\left[P^*\left(\ell_j\right) - P_{\max,\mathbf{p}}\left(\ell_j\right)\right]^2 \tag{92}$$

Where N is the number of bonded lengths $\boldsymbol{\ell}_1, \boldsymbol{\ell}_2, \ldots, \boldsymbol{\ell}_N$ investigated in the experimental work, $P_{crit}\left(\ell_j\right)$ (j = 1, 2, …N) is the average value of the debonding load of specimens having bonded lengths $\boldsymbol{\ell}_j$, while $P*\left(\ell_j\right)$ (j = 1, 2, …N) is the average value of the peak load of specimens having bonded lengths $\boldsymbol{\ell}_j$.

For the indirect method described in section 4.2.1.5.3 the calibration criteria aimed to define the set **p** of parameters that minimize the distance between $P(g)_{\ell=345}$ and $\overline{P^{ALL}(g)}$ or $\overline{P^{PLAT}(g)}$:

$$d\left(\overline{P^{ALL}(g)}, P(g)_{\ell=345,\underline{\mathbf{p}}}\right) \le d\left(\overline{P^{ALL}(g)}, P(g)_{\ell=345,\mathbf{p}}\right) \quad \forall \mathbf{p} \tag{93}$$

$$d\left(\overline{P^{PLAT}(g)}, P(g)_{\ell=345,\underline{\mathbf{p}}}\right) \leq d\left(\overline{P^{PLAT}(g)}, P(g)_{\ell=345,\mathbf{p}}\right) \quad \forall \mathbf{p} \tag{94}$$

Where $d\left(\overline{P^{ALL}(g)}, P(g)_{\ell=345,\mathbf{p}}\right)$ is the distance between the experimental $\overline{P^{ALL}(g)}$ response and the analytical $P(g)_{\ell=345,\mathbf{p}}$ while $d\left(\overline{P^{PLAT}(g)}, P(g)_{\ell=345,\mathbf{p}}\right)$ is the distance between the experimental $\overline{P^{PLAT}(g)}$ and the analytical $P(g)_{\ell=345,\mathbf{p}}$:

$$d\left(\overline{P^{ALL}(g)}, P(g)_{\ell=345,\mathbf{p}}\right) = \sum_{j=1}^{N}\left[\overline{P^{ALL}(g_j)} - P(g_j)_{\ell=345,\mathbf{p}}\right]^2 \tag{95}$$

$$d\left(\overline{P^{PLAT}(g)}, P(g)_{\ell=345,\mathbf{p}}\right) = \sum_{j=1}^{N}\left[\overline{P^{PLAT}(g_j)} - P(g_j)_{\ell=345,\mathbf{p}}\right]^2 \tag{96}$$

Where $g_1, g_2, \ldots g_N$ are the slips enforced at the loaded end, while $\overline{P^{ALL}(g_j)}$ and $\overline{P^{PLAT}(g_j)}$ ($j = 1, 2, \ldots N$) the corresponding average loads.

4.2.1.5.5 Results of the indirect calibration of the CML

In this section, the results of the indirect calibration of the CML described in section 4.2.1.5.2 and section 4.2.1.5.3 are presented.

Figure 94a-b shows a comparison between the CML calibrated through different load-responses using both the tri-linear function [91] and the Dai et al. [35] function. From Figure 94a it can be observed that the CML obtained from $CAL_{P^*(\ell)}$ reaches greater values of s_f than the CML obtained from $CAL_{Pcrit(\ell)}$. This fact can be explained considering that the experimental $P^*(\ell)$ response does not show a constant trend as the bonded length increases (Figure 94g), as observed for the $P_{crit}(\ell)$ response (Figure 94h).

a showed that the maximum shear stress τ_{max} obtained through the $CAL_{P^*(\ell)}$ is similar to the one obtained through the $CAL_{Pcrit(\ell)}$, if the same function is employed. The tri-linear and Dai et al. [35] CMLs obtained from $CAL_{Pcrit(\ell)}$ and $CAL_{\overline{PPLAT(g)}}$ are similar (Figure 94c), whether the comparison is made in terms of the same calibration method or same CML function. This observation suggests that if the plateau load is considered, the method selected to obtain the CML or the shape of the CML itself are not crucial to obtain

the fracture properties of the interface. A similar comment cannot be made when $CAL_{P^*(\ell)}$ and $CAL_{\overline{PALL(g)}}$ (Figure 94b) are considered. A possible explanation stems from what observed earlier about Figure 94g. The CMLs obtained from the $CAL_{\overline{PALL(g)}}$ calibration reached greater values of the maximum shear stress τ_{max} than the CMLs obtained from the $CAL_{\overline{PPLAT(g)}}$ calibration (Figure 94d), for both CML functions. This is partially connected to the fact that the average response $\overline{P^{ALL}(g)}$ reaches greater values of the applied load P with respect to the $\overline{P^{PLAT}(g)}$ response, for any value of the global slip g. Overall, it should be noted that the values of the maximum shear stress τ_{max} are roughly comprised between 1.0 MPa and 1.5 MPa, while the values of the slip corresponding to the complete debonding are consistent with the values of g1 reported in Table 20.

Figure 94e-f compare the experimental $P(g)$ responses and the analytical $P(g)$ responses obtained from the indirect calibrations. As expected, the best match is obtained when the analytical response is best fitted from the corresponding experimental response. For example, the *P-g* curve obtained from $CAL_{P^*(\ell)}$ employing either CML functions does not agree well with the experimental $\overline{P^{ALL}(g)}$ curve. On the other hand, independently of the CML chosen, the *P-g* curve obtained from $CAL_{\overline{PALL(g)}}$ agrees very well with the experimental $\overline{P^{ALL}(g)}$ curve. In Figure 94g-h a comparison between the experimental $P(\boldsymbol{\ell})$ responses and the analytical $P(\boldsymbol{\ell})$ responses obtained from the indirect calibrations is made. Similarly to what observed for Figure 94e-f, the best match between the response obtained from the calibration and the experimental response occurs when the calibration is made against the same experimental curve used to compare the results. The shape of the CML function does not influence this match.

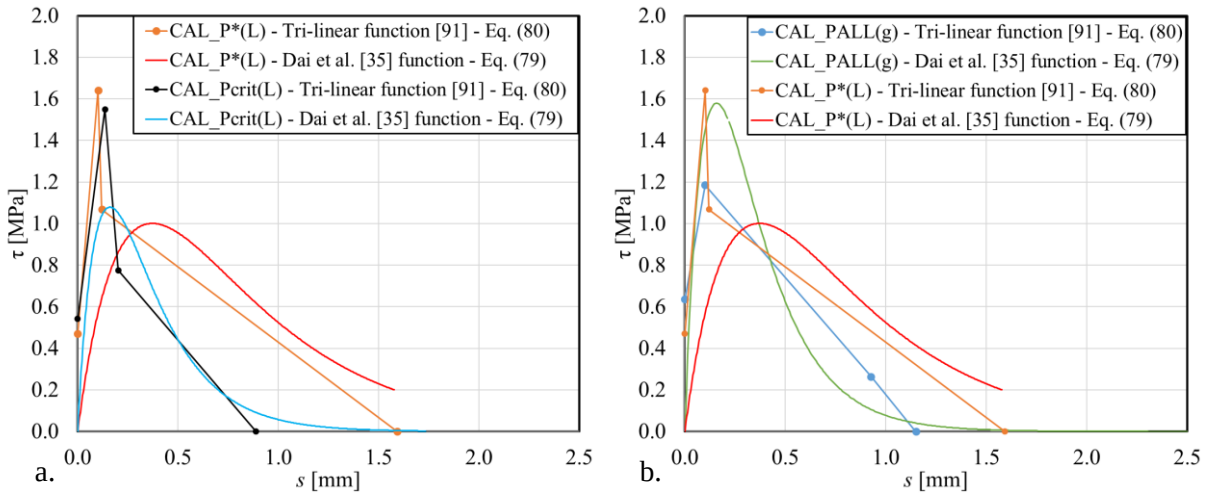

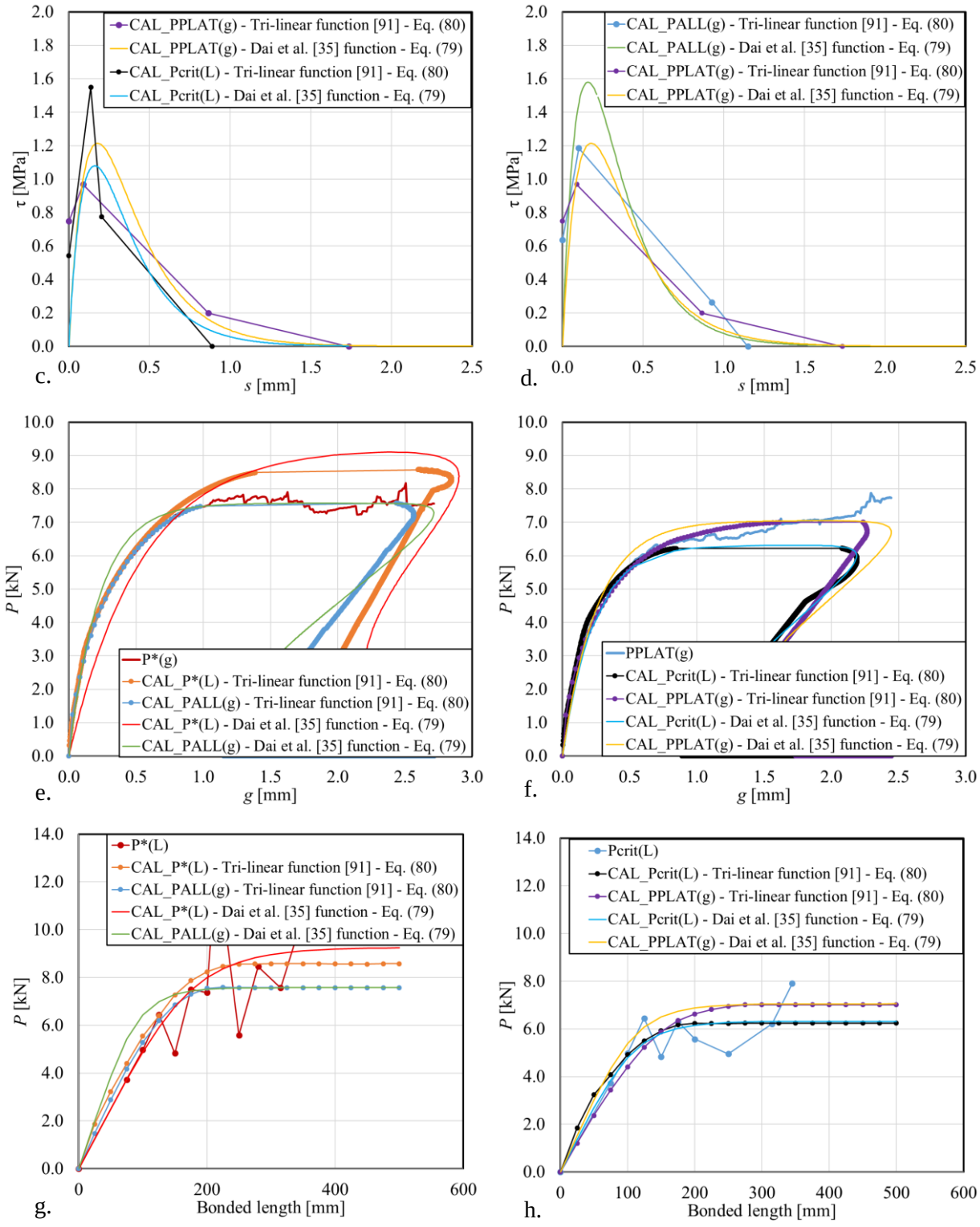

Figure 94. Results of the indirect calibration.

Table 21 summarizes the most important fracture mechanics parameters obtained from the indirect calibration. Lower values of the fracture energy, i.e. the area under the CML curve, are obtained when the experimental responses that employ the plateau load are used with respect to the peak load. The values of the fracture are consistent between the calibrations that employ two different CML functions. The values of the effective bond length, L_{eff}, which represents the minimum length to fully establish the stress transfer, are very similar among the different calibrations when the tri-linear CML is employed. A similar comment can be made for Dai et al. function [35], when the plateau load is used. For Dai et al. [35] CML an arbitrary criterion for the effective bond length should be established.

Table 21. Fracture mechanics parameters obtained from the indirect calibration

Calibration	*Tri-linear function* [91]				*Dai et al.* [35] *function*			
	G_F [N/m]	L_{eff} [mm]	τ_{max} [MPa]	s_m [mm]	G_F [N/m]	L_{eff} [mm]	τ_{max} [MPa]	s_m [mm]
$CAL_{Pcrit(\ell)}$	485	217	1.55	0.14	500	226	1.08	0.16
$CAL_{P*(\ell)}$	918	267	1.64	0.10	964	381	1.00	0.37
$CAL_{PALL(g)}$	719	209	1.19	0.10	719	191	1.58	0.16
$CAL_{PPLAT(g)}$	616	287	0.97	0.09	623	224	1.21	0.18

4.2.1.6 Conclusions

In this section, direct single lap shear tests were performed on SRG-masonry joints. The following conclusions can be drawn for SRG systems that employed a lime-based mortar matrix:

- Failure mode depends on the bonded length of the composite strip.
- The effective bond length when interlaminar failure occurs is in the range 175 mm – 200 mm.
- No width effect was observed for these strengthening systems.
- When the width of the fiber sheet is maintained constant, an increase of the matrix width caused an increase of the load carrying capacity.
- The load carrying capacity of the matrix-fiber interface decreases as the fiber density increases.
- An increase of the loading rate might entail for an increase of the load-carrying capacity of the matrix-fiber interface.
- The cohesive material law (CML) can be determined using an indirect calibration.

Tests performed on SRG systems that employed a cement-based mortar showed that the effective bond length is in the range 200 mm – 250 mm.

4.2.2 Durability of SRG-masonry joints: effect of water and salt crystallization

4.2.2.1 Background

Several studies that dealt with the debonding mechanism of FRCM composites bonded to a masonry substrate have shown that the effectiveness of the FRCM systems in strengthening applications depends on the stress transfer between the substrate and the composite [164] [165] [119] [166]. Conversely, a limited number of studies has investigated the durability of FRCM composites applied to a masonry substrate [167] [168] [169]. Inorganic and porous matrices of FRCM composites expose them to a series of weathering processes that are entirely different from those affecting FRPs. In particular, moisture-related deterioration mechanisms such as freeze-thaw cycles, salt crystallization cycles, and dissolution of soluble fractions may affect the matrices, as historic buildings are commonly exposed to rising damp, rain, and condensation [170] [171]. It is well known that salt attack is one of the most common causes of weathering in masonry materials. Salt damage involves complex mechanisms, which depend mainly on the microstructure of the materials, nature of the salt or mixture of salts as well as environmental conditions (evaporation rate, deliquescence cycles, etc.). Several papers in the literature have investigated such mechanisms [172]. Water and salts are often supplied from the ground (rising damp). The subsequent water evaporation inside the wall may result in the precipitation of crystals beneath the surface (subflorescence). The salts that accumulate in the pores of brick and/or mortar result in a pressure in the pores that modifies the existing stress field. If locally the stress components exceed specific thresholds, fracture processes may initiate [173]. When FRCM composites are applied to masonry, given the porous nature of the composite matrices, salt attack might damage the substrate and the composite, which in turn could affect the mechanical properties of the composite and cause the loss of adhesion from the substrate. The aim of the present study is to investigate the effects of salt crystallization on the stress transfer between SRG composites and masonry. Twenty-five SRG-masonry joints were considered in order to investigate the degradation process. Out of the twenty-five specimens, ten were subjected to wetting-drying cycles in a saline solution. Sodium sulfate was selected because it is one of the most damaging salts and is frequently used for accelerated salt crystallization tests [174] [175]. Ten specimens were subjected to the same weathering cycles in deionised water. Finally, five out of the twenty-five specimens were used as control and therefore they were not subjected to any conditioning cycle. The five specimens used as control specimens correspond to specimens DS_315_50_LD_LM_5, DS_315_50_LD_LM_6, DS_315_50_LD_LM_7, DS_315_50_LD_LM_8, and DS_315_50_LD_LM_9 described in section 4.2.1.3.1 that where cast using the same batch of lime-based mortar matrix used to strengthen the twenty specimens that were subjected to degradation cycles. The accelerated weathering protocol adopted in this

study was carefully designed so that in five specimens, the salt was forced to crystallize on the entire face of the masonry block where the SRG composite was bonded; whereas, in the remaining five specimens, the salt was forced to crystallize only on the bonded area. For comparison, the same configuration was used for the ten specimens cycled with deionised water. Forcing the salt to crystallize in selected areas allowed to investigate different damage mechanisms that might occur once the composite is applied to masonry walls. In fact, salts in buildings do not crystallize uniformly across the walls, but they rather follow unpredictable paths, which depend on the permeability of the masonry surface [176]. For instance, the presence of scarcely permeable layers applied to a wall (such as water-repellents, consolidating materials, and organic paints) may lead to salt crystallization beneath those layers that could lead to their detachment from the substrate [177] [178] [179]. When rendered bricks are subjected to rising damp, the capillary water transport is altered by the presence of the interface between brick and render; this alteration has to be ascribed to the hydric resistance at the interface (i.e. difference of capillary pressure of the two materials, which may cause a slowing of the wetting process and a maximum transmitted flow) or to the change of the water transport properties of the two layers [180]. In addition, the presence of compact finishing materials (renders, plasters, etc.) on portions of the masonry surface may lead to a concentration of salts in the remaining permeable zones, that can cause severe differential deteriorations [181].

After the wetting-drying cycles were completed, direct shear tests were performed using the single-lap test set-up to assess the effect of salt crystallization on the stress transfer mechanism at the FRCM-masonry interface. After the direct shear tests were performed, salt distribution was measured to investigate where sulfate accumulated. Pore distribution was evaluated to investigate the presence of micro-cracks in the SRG due to the presence of salt.

4.2.2.2 Experimental program

All masonry blocks of this experimental program were constructed with the bricks and the mortar characterized in section 3.2. The SRG composite consisted in LD steel fibers (described in section 3.3.1) embedded in a lime-based mortar (described in section 3.3.4.1) The property of the composite strips are described in section 3.3.7.

All masonry blocks have the same nominal dimensions equal to 120 mm × 120 mm × 380 mm. The bonded width and bonded length were equal to 50 mm and 300 mm, respectively.

As introduced in section 4.2.2.1 twenty specimens were tested to investigate how the degradation process affected the bond performances of SRG-masonry joints. Out of twenty specimens, ten FRCM-masonry joints (labelled SALT) were subjected to an artificially weathering protocol purposely designed to reproduce the damage mechanism associated with salt crystallization cycles. Each cycle was comprised of a wetting phase and a drying phase. In the wetting phase, specimens were laid in trays that contained

a 20 mm deep aqueous saline solution of sodium sulfate decahydrate $Na_2SO_4 \cdot 10H_2O$ (8 wt.%) for two days, in order to allow the capillary absorption of the saline solution (Figure 95b and Figure 95c). The level of the saline solution was kept constant by periodically refilling the tray. Preliminary tests showed that 8 hours are necessary to obtain a complete water saturation of the specimens by capillary absorption, thus a two days period was determined to be a suitable amount of time for the wetting phase to obtain sulfate accumulation. The face where the composite was applied (top face) was positioned upward, i.e. opposite to the bottom face in contact with the saline solution, in order to induce salt crystallization (efflorescence and/or subflorescence) on the top face itself, i.e. where it occurs in masonry walls [182] [183]. A similar approach was suggested by RILEM Technical Committee 127-MS ‘’Determination of the resistance of wallettes against sulfates and chlorides” [184].

In order to make salt crystallize in different areas, two different configurations of the ten SALT SRG-masonry joints were used:

- Five specimens were partially wrapped (labelled SALT-PW), i.e. duct tape was placed on the 4 lateral faces of the block to make evaporation (and hence salt crystallization) occur through the entire top face of the masonry block where the composite strip was applied. Partial wrapping was designed to investigate if a different permeability of the top face due to the presence of the strip could cause a sulfate accumulation outside the bonded area (Figure 95b);
- Five specimens were totally wrapped (labelled SALT-TW), i.e. duct tape was placed on the 4 lateral faces of the block and on the portion of the top face that was not covered by the composite strip to make evaporation (and hence salt crystallization) occur through the SRG strip. Totally wrapped specimens were used to investigate if salt accumulates beneath the composite strip, which might cause the detachment of the composite (Figure 95c).

The two days wetting phase was followed by a drying phase in which the specimens were placed in a ventilated oven at 60 °C (±5°C) for two days. The duration of the drying phase was determined after preliminary tests that showed that such period of time was sufficient to dry completely the specimens (moisture < 2 wt.%). A dry condition of the specimen was considered essential to assure an effective absorption of the saline solution in the following wetting phase.

Four wetting-drying cycles were carried out. The number of cycles was selected on the basis of previous experimental works [182] [183] and because they caused a remarkable amount of efflorescence on the surface of specimens.

The accelerated protocol developed in this study is aimed at complying with some key requirements [185]: *i*) to obtain a realistic type of damage, i.e. similar to the deterioration observed in practice, in a

relatively short period of time (few weeks or months); as well as *ii*) to jointly test the substrate and the SRG composite and not the composite alone, which allows to investigate the influence of salt crystallization on the debonding behavior.

In the first requirement, a compromise between the need of a short weathering procedure and the need of producing realistic damage must be found. To this aim, the drying cycle in oven at 60°C was selected, as it is supposed to accelerate the crystallization of salts without changing the deterioration mechanism; moreover, this temperature may be found in real building façades due to solar radiation (in European climates and during summer, surfaces may reach 40-60°C, but in some cases even 80°C [186]). The possibility of a drying stage at room temperature, suggested for example in [184], was discarded in the present experimental campaign, as the drying of salt-laden specimens would be too slow and time-consuming.

For the same reasons, a standard 28-day curing time was selected for the SRG composite strips, although it is well known that four weeks are usually not enough to produce a complete hardening of the inorganic matrix and longer curing periods may be necessary, depending on the nature of the binder. This aspect is extremely important, because the alternation of water imbibition and high temperature might alter the mechanical properties of the matrix by enhancing its curing or, conversely, it could cause the dissolution of soluble phases still present in the matrix (e.g. not carbonated lime). As a consequence, ten specimens, out of the twenty-five specimens, were subjected to the same number of cycles (four) with deionised water rather than with saline solution (labelled WATER), in order to separate the effect of the water and the salt during the cycles. These specimens were labelled WATER-PW for partially wrapped specimens (5 specimens, Figure 95b) and WATER-TW for totally wrapped specimens (5 specimens, Figure 95c).

This expedient allows to fully compare SALT and WATER specimens, as the effect of a possible incomplete hardening of the FRCM matrix during the first 28-day curing period is eliminated, and a considerable time saving is achieved.

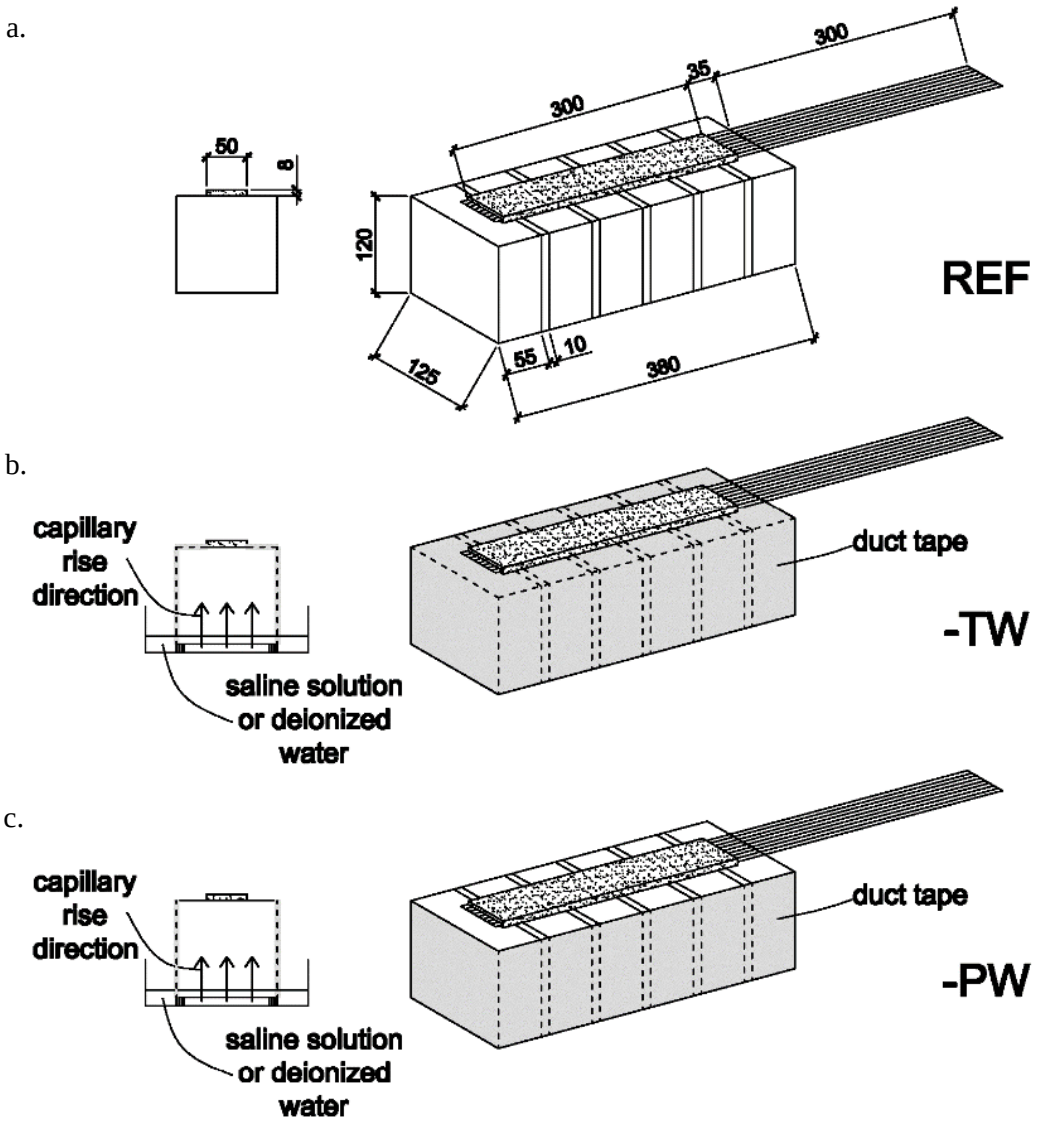

Figure 95. Reference specimens (a) and duct tape configuration for totally wrapped (-TW) specimens (b) and partially wrapped (-PW) specimens (c). Dimensions in mm.

Finally, five control specimens, named DS_315_50_LD_LM_5, DS_315_50_LD_LM_6, DS_315_50_LD_LM_7, DS_315_50_LD_LM_8, and DS_315_50_LD_LM_9 in Table 20 and cast within the same batch of mortar matrix used for the twenty specimens subjected to cycles, were left to cure in laboratory conditions for the same duration of the artificial weathering cycles for comparison purposes. These specimens were referred to as REF in this section.

Specimens were tested using a single-lap shear test set-up described in section 4.2.1.2. Tests were performed increasing the global slip *g* at a constant rate equal to 0.00084 mm/s.

4.2.2.3 Determination of salt amount and pore size distribution

After the direct shear tests were performed, samples of brick, mortar joint, and matrix were extracted with a chisel at different locations in the SALT and REF specimens, according to the sampling scheme of Figure 96 (two samples were extracted at each location). It should be noted that the extraction of the samples was done in dry conditions with no water added. The amount of salt in these samples was determined in terms of $SO_4^{=}$ percentage, after powdering (<0.075 mm), extraction with deionised boiling water (electrical conductivity <0.02 μS), and filtration by blue ribbon filter by ion chromatography, IC (Dionex ICS-1000, equipped with Ion Pac AG14A guard column and Ion Pac AS14A inorganic anion-exchange column kept at 30 °C; measuring cell temperature 35 °C). The investigation of the distribution of sulfate at different locations throughout the specimen was necessary to determine if salt accumulated in some specific areas.

Mercury intrusion porosimetry, MIP (Porosimeter 2000 with a Fisons Macropore Unit 120), was also carried out on some samples of brick, mortar joint, and matrix collected from SALT and REF specimens, in order to assess their total porosity and pore size distribution. MIP is a valuable tool to investigate the opening of micro-cracks due to the pressure in pores caused by salt crystallization. However, when salts accumulate inside porous materials, a pore-filling effect occurs, which hinders the evaluation of the actual negative effects of artificial weathering. For this reason, the removal of salt crystals from the pores may be necessary [176]. For the samples of matrix from SALT-TW specimens, MIP was performed both before and after salt removal by poultice (cellulose pulp and deionised water in the weight proportions 1:6).

The mineralogical composition of the SRG matrix in the SALT-TW specimens was investigated by powder X-ray diffraction, XRD (Philips Diffractometer PW 1840, 40 kV/20 mA, Cu Kα radiation), in order to assess the possible formation of ettringite associated with the presence of sulfate [187].

Finally, the condition of the steel fibers in SALT-TW specimens was investigated by optical microscopy (SOM Wild M3 Heerbrugg). The composite strip was cut in order to expose the cross-section of the fibers. Particular attention was paid to detect any possible presence of surface alteration of the steel fibers after the conditioning cycles.

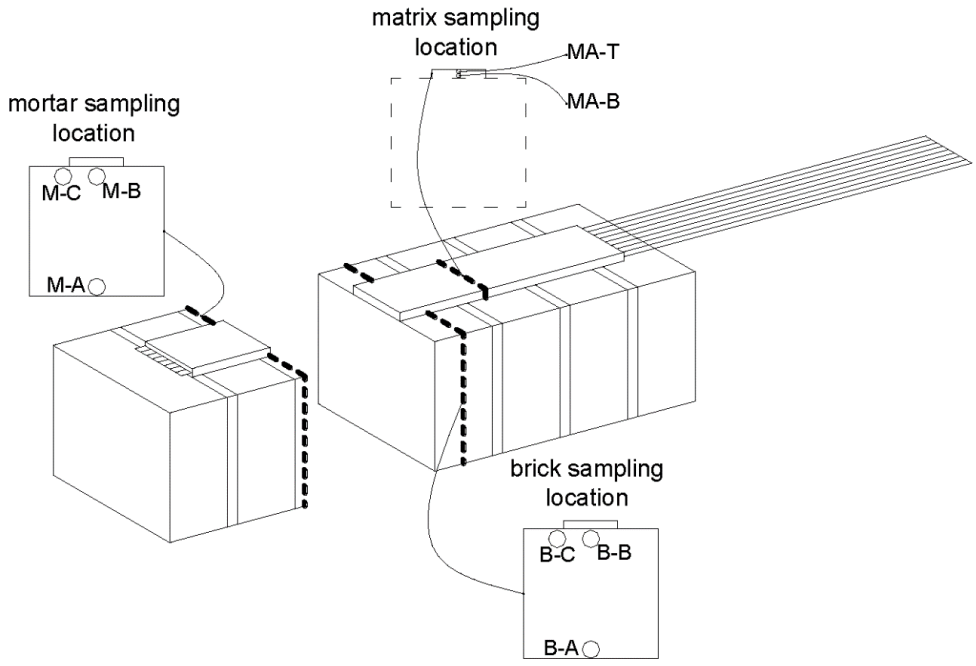

Figure 96. Sampling locations for material characterization. Mortar samples: M-A = center of the bottom face of the mortar joint, M-B = center of the top face of the mortar joint.

4.2.2.4 Experimental results

4.2.2.4.1 Visual inspection

Photos of two representative SALT-TW and SALT-PW specimens at the end of the weathering cycles are shown in Figure 97a and Figure 97b, respectively, where copious efflorescence is clearly visible on the composite surface (for SALT-TW) and on the entire top face of the specimen where the composite strip was applied (for SALT-PW). Photos of two representative WATER-TW and WATER-PW specimens are shown in Figure 97c and Figure 97d, respectively. Notwithstanding the absence of salts in the solution, a thin layer of efflorescence is visible on both specimens (especially on the composite) at the end of the 4th cycle, independently of the wrapping configuration. The formation of efflorescence in WATER specimens suggests the presence of salts in the materials used to manufacture the masonry block and/or the composite.

Interestingly, all specimens of the same group exhibited a similar amount of efflorescence on the surface, which suggests that the accelerated weathering protocol proposed is replicable.

No severe deterioration phenomena linked to salt attack (such as flaking or crumbling of the composite matrix) were observed in the specimens. In particular, no detachment of the composite from the substrate was noted. Some surface powdering of the composite matrix was the only deterioration pattern observed.

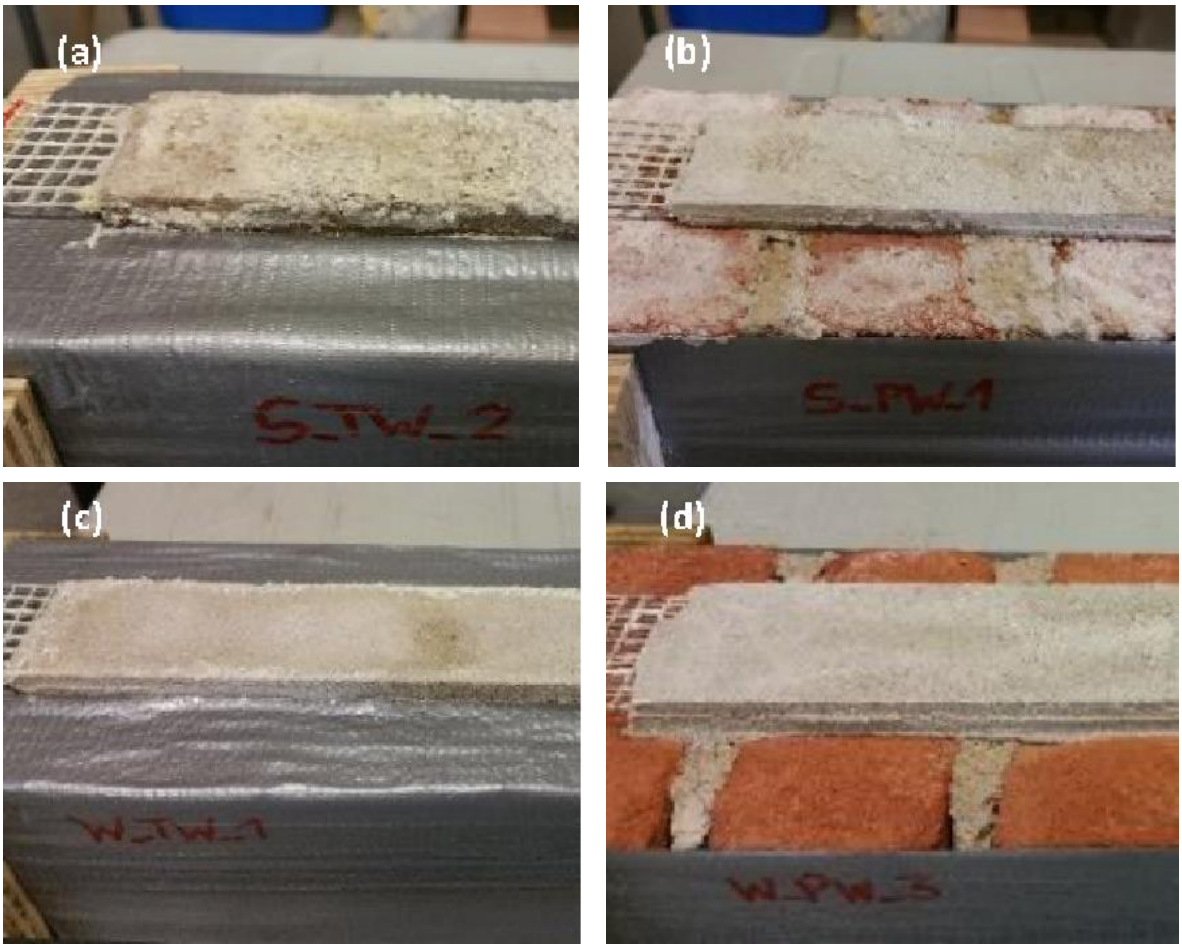

Figure 97. Specimens SALT-TW-2 (a), SALT-PW-1 (b), WATER-TW-1 (c), and WATER-PW-3 at the end of the conditioning procedure.

4.2.2.4.2 Direct shear test results

In this section, the results of the single-lap shear tests are presented. For all specimens, failure was associated with slippage of the fibers from the internal layer of matrix, while the external layer of matrix remained attached to the fibers, which in turn resulted in an interlaminar fracture (MF) [118]. The internal layer of matrix bonded to the surface of the masonry block did not experience any detachment from the substrate (Figure 98). All specimens exhibited a similar load response. In Figure 99, the load-global slip response of a representative REF specimen (DS_315_50_LD_LM_7) is plotted. The dark grey and the light grey curves are the plots of the applied load versus displacements g_a (measured by LVDTa) and g_b (measured by LVDTb), respectively. The applied load P - global slip g curve is represented by the black line in Fig. 5. Displacements w_c and w_d, measured by LVDTc and LVDTd, respectively, are plotted versus global slip g in the same figure. Displacements recorded by LVDTc and LVDTd are similar for any value of g, which implies that no twisting of the masonry block occurred during the test.

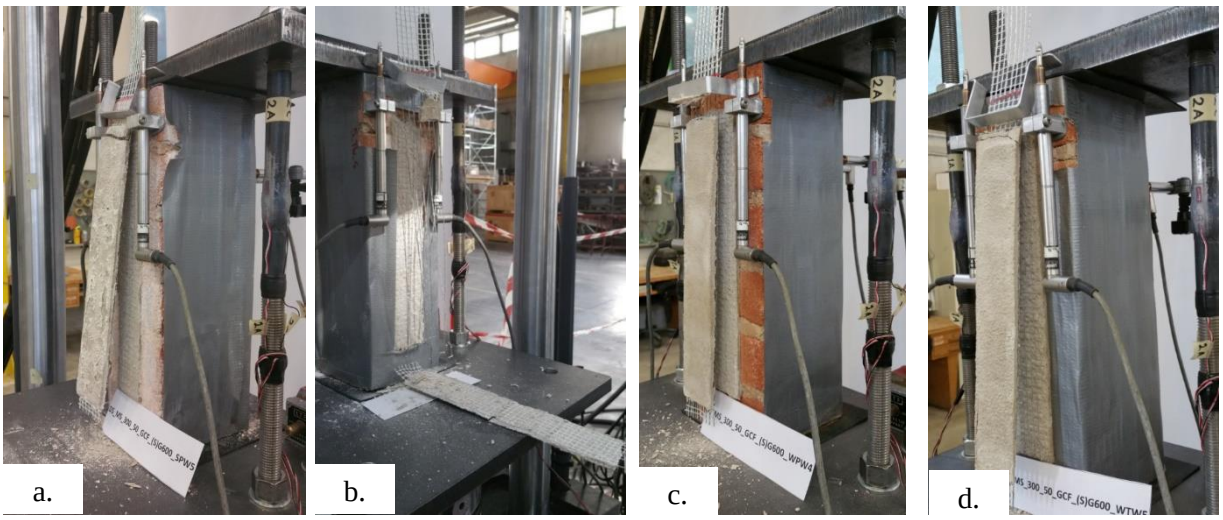

Figure 98. Failure mode for specimens SALT-PW-5 (a), SALT-TW-5 (b), WATER-PW-4 (c), and WATER-TW-5 (d).

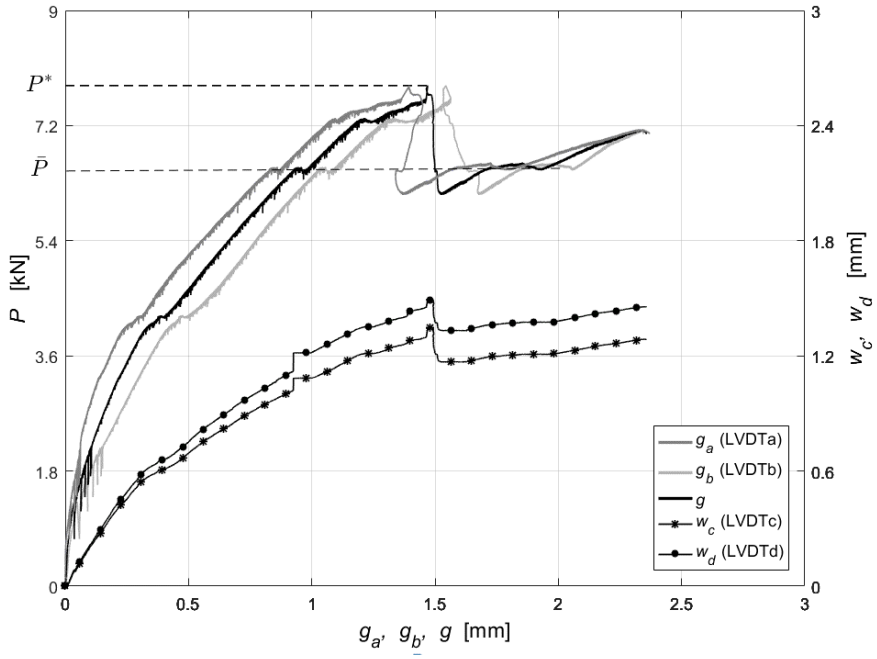

Figure 99. Load – global slip response of specimen DS_315_50_LD_LM_7.

The P - g response shows an initial linear portion followed by a non-linear behavior before the peak load P^* is reached. During the linear and non-linear phases, minor drops in the load are observed, which are due to the formation of micro-cracks in the matrix and their coalescence. Once a macro-crack has formed, i.e. the peak load has been reached, a substantial drop in the load occurs. The drop is related to the type of control of the test. In fact, as the global slip is increased at a constant rate, when coalescence of micro-cracks results in the onset of an interfacial macro-crack, the global slip suddenly increases, and the servo-

hydraulic valve reduces the flow to adjust the rate of the slip. After the load drop, fibers start to slip with respect to the internal layer of matrix and the interfacial crack shifts toward the free end. The load is nominally constant as the interfacial crack propagates.

In Figure 100, five *P* - *g* curves that are representative of the five groups of specimens described above (REF, SALT-TW, SALT-PW, WATER-TW, and WATER-PW) are reported. Considering the initial part of the curves, the REF specimen shows a lower slope with respect to the other specimens. All specimens that were subjected to the conditioning procedure (in water or salt) share the same slope, slightly greater than that of the REF specimen, which suggests that no degradation of the initial stiffness related to the cycles occurred. Moreover, WATER-PW and WATER-TW specimens exhibit a similar or even higher peak loads than REF specimen, which indicates that the cycles in water and oven not only do not deteriorate the composite, but also slightly improve the load-carrying capacity. It should be noted that for specimens conditioned in saline solution (SALT-TW and SALT-PW), the presence of salt does not appear to influence the bond behavior between the composite and the substrate. In fact, no significant difference was found in the shape of the *P* - *g* curves (Figure 100), among REF, SALT-TW, and SALT-PW specimens.

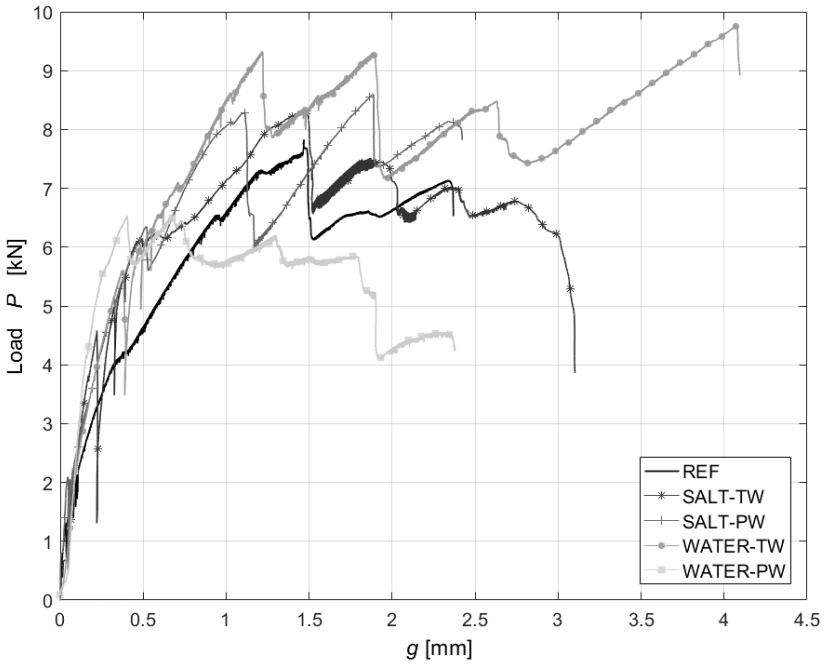

Figure 100. Load-global slip response of representative REF, SALT-TW, SALT-PW, WATER-TW, and WATER-PW specimens.

The mechanical parameters of the direct shear tests for all the specimens are provided in Table 22. In particular, P_{avg}^{*} represents the average peak load for each group of specimens. In each curve, an almost

horizontal branch, defined by the global slip range (g_1,g_2), can be observed after the main load drop described above occurs. For each specimen, the values of g_1 and g_2 are reported in Table 22. The average of the load $\overline{P_{crit}}$ in the range (g_1,g_2) has been also computed and provided in the same table for each specimen. $\bar{P}_{avg}$ and $g_{1(avg)}$ are the mean values of $\bar{P}$ and g_1, respectively, for each group of specimens. The average w^*_{avg} of the displacements measured by LVDTc, w^*_c, and LVDTd, w^*_d, which correspond to the peak load P^*, is also reported. If the specimen didn't show a constant plateau, the value of P_{crit}, g_1, g_2, $\overline{w_c}$, and $\overline{w_d}$, were not reported in Table 22.

Table 22. Test results of single-lap direct shear tests

Specimen Name	Bonded length [mm]	g_1 [mm]	g_2 [mm]	P^* [kN]	P_{crit} [kN]	$\overline{P_{crit}}$ [kN]	Failure mode	$\overline{w_c}$ [mm]	$\overline{w_d}$ [mm]
DS_315_50_LD_LM_5	315	\	\	5.05	\		MF	\	\
DS_315_50_LD_LM_6	315	1.03	2.49	7.76	6.85		MF	1.60	1.69
DS_315_50_LD_LM_7	315	1.54	2.35	7.83	6.67	6.45	MF	1.22	1.39
DS_315_50_LD_LM_8	315	1.12	2.22	7.52	5.84		MF	0.92	1.15
DS_315_50_LD_LM_9	315	\	\	6.50	\		MF	\	\
WATER-PW-1	300	0.81	1.18	7.18	6.41		MF	1.99	1.96
WATER-PW-2	300	0.52	1.52	4.65	4.18		MF	0.69	0.81
WATER-PW-3	300	\	\	4.92	\	5.87	MF	\	\
WATER-PW-4	300	0.97	1.87	6.54	5.83		MF	2.21	2.06
WATER-PW-5	300	1.30	1.73	6.68	7.07		MF	1.53	1.47
WATER-TW-1	300	0.92	1.51	8.57	7.49		MF	1.95	2.10
WATER-TW-2	300	1.32	3.23	9.33	8.04		MF	2.91	2.89
WATER-TW-3	300	\	\	10.21	\	7.16	MF	\	\
WATER-TW-4	300	3.74	4.34	9.42	7.74		MF	2.02	2.15
WATER-TW-5	300	0.92	1.92	7.89	5.36		MF	1.67	1.85
SALT-PW-1	300	0.84	1.31	8.23	5.81		MF	2.06	2.02
SALT-PW-2	300	\	\	11.14	\		MF	\	\
SALT-PW-3	300	1.96	2.50	8.29	7.78	6.21	MF	1.87	2.08
SALT-PW-4	300	1.19	1.59	6.07	5.72		MF	1.43	1.77
SALT-PW-5	300	1.95	2.24	6.98	5.52		MF	1.85	2.10
SALT-TW-1	300	\	\	6.63	\		MF	\	\
SALT-TW-2	300	1.24	2.39	9.20	7.34		MF	2.40	2.73
SALT-TW-3	300	0.57	1.26	6.34	4.71	6.02	MF	1.10	1.28
SALT-TW-4	300	0.64	1.36	5.26	5.30		MF	1.24	1.31
SALT-TW-5	300	2.00	2.80	8.30	6.72		MF	2.21	2.18

Considering the values in Table 22, a slight improvement in terms of peak load is observed for SALT specimens with respect to REF ones, which confirms the positive role of water in the composite curing process (rather than the occurrence of deterioration associated with salt).

4.2.2.4.3 Specimens characterization after weathering cycles

As described in section 4.2.2.3, samples were extracted from specimens after single-lap shear tests were performed, for a further characterization in terms of salt content and pore distribution.

The sulfate distribution across representative specimens is reported in Figure 101, together with the location where samples were extracted. The characterization of REF specimens revealed that all materials contained a slight amount of salts, namely sulfates, which are common for this kind of building materials especially for the mortars herein selected. The $SO_4^=$ amount resulted on average 0.014 wt.% in the brick, 0.165 wt.% in the mortar joint, and 0.410 wt.% in the matrix. This confirms that the efflorescence observed on the top surface where the composite was applied for WATER specimens (Figure 97c and Figure 97d) is due to the presence of salts in the materials prior to conditioning that were transported by rising water. The amount of efflorescence was particularly visible on the surface of the composite, as observed in section 4.2.2.4.1, due to the high content of salt in the matrix. However, efflorescence on the SRG composites of WATER specimens was simply due to the salts originally present in the materials (with very low percentages), that were washed out by deionized water flowing through the specimen and were transported to the upper surface. Hence, they were expected not to play a significant role in the deterioration process and they were not further investigated in the following analyses by ion chromatography.

Specimens subjected to cycles with saline solution (SALT) exhibited thick efflorescence on the surface (Figure 97a and Figure 97b) and a remarkable amount of sulfate in the matrix (Figure 101).

The results reported in Figure 101 allow to make the following considerations:

- The amount of sulfate in the matrix for the SALT specimens (between 1.8 and 2.5 wt. %) is similar to that observed in several historic buildings in ordinary conditions of salt damage occurrence [188] [189]. Thus, the conditioning protocol was able to reproduce a realistic salt accumulation;
- Specimens that were totally wrapped had an accumulation of salt in the matrix that was only slightly greater than the amount of salt found in partially wrapped specimens. Thus, the application of different finishing layers next to the composite strips is expected to have a negligible effect on the salt accumulation;
- In SALT-PW specimens, no preferential direction for salt crystallization was found in the bulk of masonry, i.e. in the brick or in the mortar joint;

- In SALT-TW and SALT-PW specimens, no accumulation of salts occurred at the SRG-masonry interface, which suggests that the composite does not hinder the migration of the saline solution towards the external surface, which in turn also indicates that premature salt precipitation did not occur. This is the key point in this study because the accumulation of salts beneath finishing layers applied on the surface of masonry walls is one of the major causes for their detachment after long-term exposure to crystallization cycles.

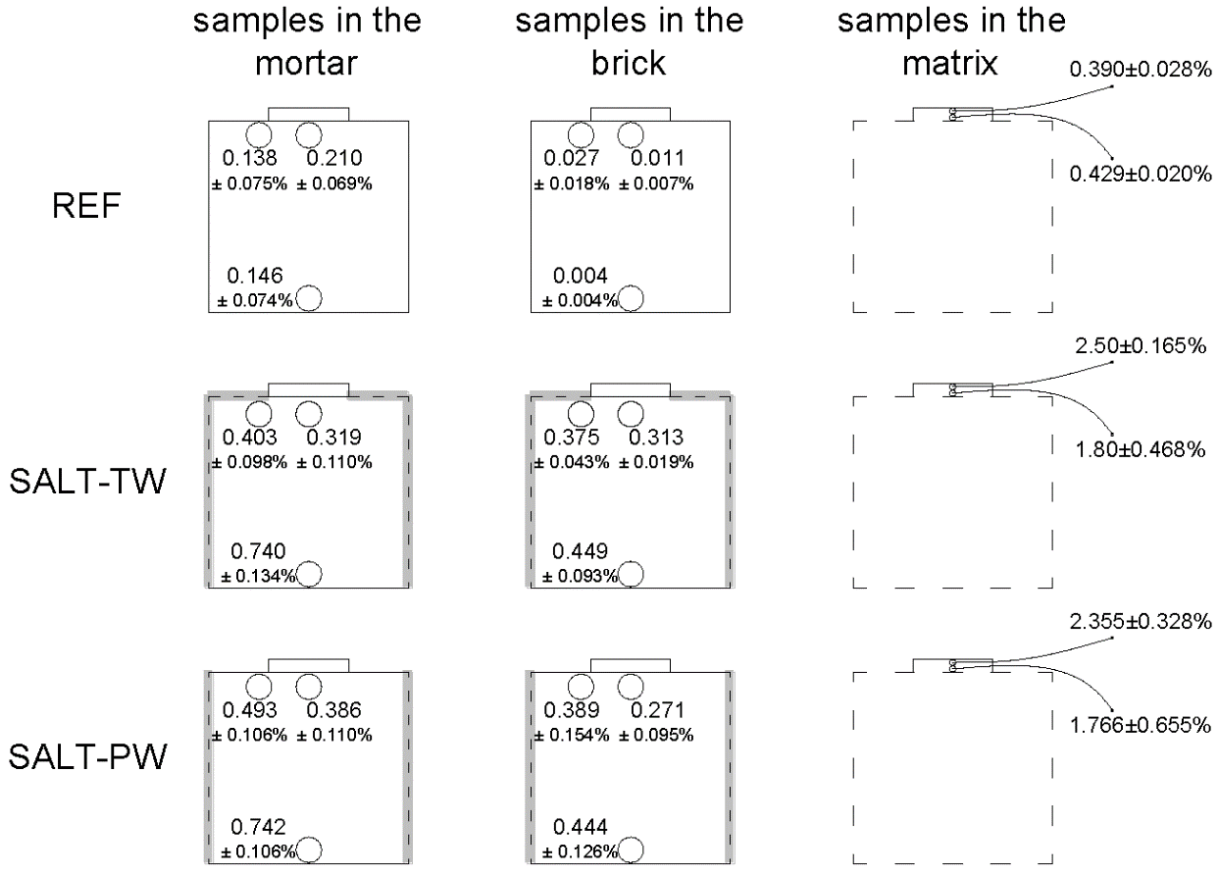

Figure 101. Sulfate anion amount ($SO_4^=$, wt%) in mortar, brick and matrix for representative REF, SALT-TW, and SALT-PW specimens (see sampling scheme of Figure 96).

After the salt distribution was measured at some specific locations, possible local damage mechanisms due to pressure in the pores associated with salt crystallization were investigated by means of MIP. The pore size distribution curves of the materials from a representative REF specimen (Figure 102) indicate that porosity of the brick (total porosity 43%) is very high if compared with the porosity of the mortar joint and the matrix (total porosity equal to 22% and 26%, respectively). The matrix exhibits a relatively large pore mean radius (7.7 μm), which probably facilitated salt migration through the composite. In fact, an accumulation of salt at the substrate/matrix interface was not detected. Conversely, a more compact

matrix with smaller pore radius with respect to the bricks is expected to cause an accumulation of salts beneath the composite that may result in the detachment of the composite [190] [191]. This aspect will be the object of a future research study.

A comparison of the porosity of the matrix before and after the conditioning procedures (Figure 102), indicates that cycles in water (WATER-TW matrix) caused a significant decrease of the porosity and pore size of the matrix with respect to unconditioned samples of matrix (REF matrix). This effect is also highlighted by the results of bond tests. Some possible pore occlusions given by the moderate efflorescence formation in the WATER-TW matrix cannot be excluded, but it is considered an ancillary effect with respect to the effect of curing. The exposure of the matrix to the most severe weathering condition (SALT-TW matrix) caused a further decrease of the porosity, which is due to salt accumulation inside the pores (especially for pores smaller than 1 μm). When salts are removed (SALT-TW matrix (desalinated)), the pore size distribution curve almost overlaps with the WATER-TW matrix curve, which suggests that no micro-crack opening occurred in the matrix after cycles with saline solution.

No ettringite formation was detected in the matrix by XRD and no surface alterations or corrosion were observed with the optical microscope in the steel fibers of SALT-TW specimens.

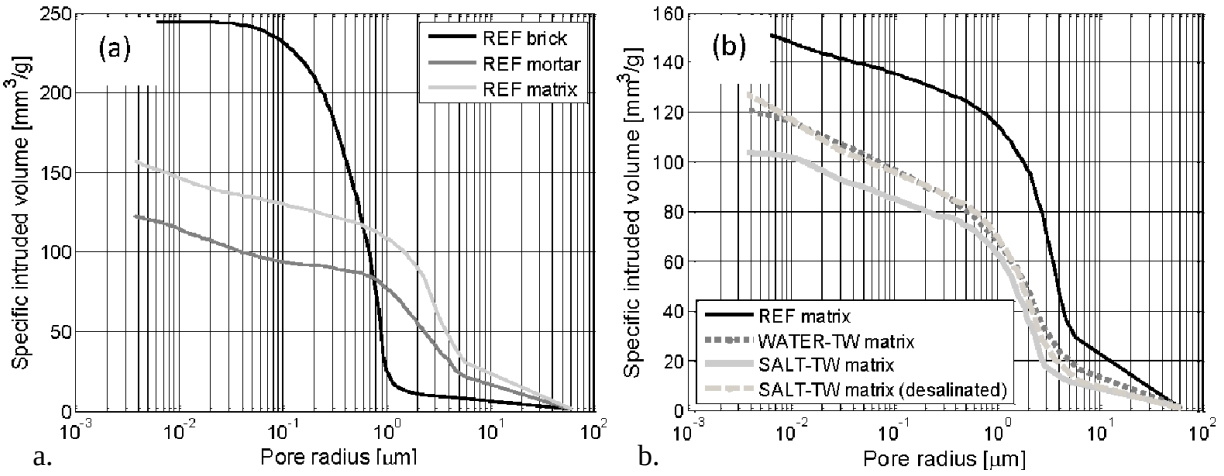

Figure 102. Pore size distribution of: (a) samples of brick, mortar, and matrix extracted from a representative REF specimen and of (b) samples of matrix extracted from representative REF, WATER-TW, SALT-TW and SALT-TW specimens after salt removal.

4.2.2.5 Conclusions

In this section, the results of twenty single-lap shear tests performed on SRG-masonry joints were presented. Prior to testing, ten specimens were subjected to cyclic wetting phases with saline solution and drying phases in oven, in order to reproduce artificially on-site damage that is typically found in existing masonry buildings. Ten additional specimens were subjected to the same cycles in deionised water.

Porosity of the materials and distribution of salt across specimens were measured after testing and used to discuss peak load, failure mode, and slip at failure of the direct shear tests.

The main purpose of this study was to investigate the effect of salt crystallization cycles on the SRG-masonry bond behaviour. The following conclusions can be drawn:

- The accelerated weathering protocol herein proposed, which consisted of four wetting and drying phases, caused a remarkable amount of efflorescence on the face of the masonry block where the composite was applied, and the amount of salt was comparable with the amount typically found in masonry buildings. Hence, the protocol successfully produced a realistic salt accumulation in the specimens. The number of cycles was selected based on some previous tests and by visually inspecting the efflorescence formation on the specimens. A fixed number of salt crystallization cycles cannot be recommended in advance for any testing protocol (for example, no total number of cycles is given in [184]), as the level of damage depends on the nature of the materials investigated. However, in the present protocol, two general criteria are suggested for the selection of the number of cycles: *i*) Visual observation of the surface of the reinforced specimens (efflorescence extent and thickness, surface powdering, visible damage); *ii*) Quantitative determination of the salts amount in the FRCM composite during the cycles, which can be delivered by collecting small samples that are analyzed via ion chromatography (for example, some "dummy specimens" can be devoted to this aim);
- The failure mode of all direct shear tests, independently of the weathering cycles, was characterized by interlaminar failure, i.e. the external layer of matrix remained attached to the fibers and detached from the internal layer;
- For specimens subjected to cycles both in water and in saline solution, a slight increase of the peak load was observed with respect to REF specimens, which could be related to the inorganic nature of the matrix (since it is a hydraulic lime-based mortar). In fact, the presence of water due to the cycles might induce additional curing of the matrix;
- Salt crystallization and accumulation in the pores occurred almost uniformly within the brick and the mortar of the SALT specimens. No significant difference was noted between the totally wrapped (-TW) and partially wrapped (-PW) configurations;
- The SRG composite employed did not hinder the capillary flow of the saline solution and did not cause local accumulation of salts at the SRG-masonry interface;
- Mercury intrusion porosimetry was employed to measure pore size and pore distribution. No micro-crack opening in the matrix after cycles with saline solution (and after salt removal by poulticing) was inferred from the measurements.

The results herein presented indicate a limited effect of sulfate exposure on the stress-transfer between SRG composites and masonry, at least for the artificial weathering protocol applied in this section.

5. Confinement of concrete columns with SRP or SRG systems

This chapter presents the result of an experimental study on concrete columns wrapped with SRP or SRG composites. SRP jackets were applied to concrete members that had several shapes (square cross-sections or circular cross-sections) and several dimensions in order to investigate their influence on the load responses. Different fiber densities and number of composite layers were employed. SRG jackets were applied to concrete prisms with the same nominal dimensions and a square cross-section. Different parameters were investigated, i.e. the density of steel fibers, the number of layers, the corner condition, the number of overlapping faces, and the length of the reinforcement.

5.1. Confinement of concrete columns with SRP systems

In this section the behavior of concrete members confined by steel reinforced polymer (SRP) composites is investigated. Two different dimensions of the columns were employed in order to investigate the scale effect. Two different shapes of the concrete columns were used in order to study the influence of the shapes on the load responses. Two additional parameters were considered, i.e. the density of steel fibers and the number of layers. The effectiveness of the confinement was evaluated in terms of load-bearing capacity and ultimate strain with respect to unconfined prisms. Digital image correlation (DIC) is used to study qualitatively and quantitatively the displacement and strain fields on one face of the composite during the test.

5.1.1. Introduction

In recent decades, the use of innovative fiber reinforced composite materials has gained popularity in structural strengthening applications. Confinement of concentrically or eccentrically loaded columns has played a key role in strengthening existing structures given the more stringent code requirements and the beam-column hierarchical relationship in a frame subjected to seismic loading. Fiber reinforced polymer (FRP) composites offer certain advantages when compared to traditional materials in confinement applications of structural elements. Features such as ease of installation, relatively short curing time, high strength-to-weight ratio, high corrosion resistance, and minimal change in dimension of the strengthened member make FRP composites an appealing alternative to other techniques such as concrete or steel jackets or external steel ties. The composite is typically wrapped around the column with fibers oriented perpendicular to the longitudinal axis of the column or with an angle if the sheets are continuously wrapped around the column. The use of composite materials as a confinement system has been proven to

be effective in terms of improving the load-bearing capacity and deformability of confined elements (e.g. [192] [193]).

Numerous experimental works have been carried out to study the behavior of plain or reinforced concrete columns confined by FRP composites (the reader is referred to [194] [195], which present comprehensive databases of test results on FRP-confined plain or reinforced concrete specimens collected from the literature). It has been observed that the type of fiber can affect the behavior of the confined concrete in terms of failure mode and enhancement of compressive strength and ultimate strain [192] [193]. Rochette and Labossière [193] compared the results of FRP-confined plain concrete columns with carbon or aramid fibers and found that the axial stiffness of the confining material influences the concrete cracking pattern and also plays a key role in enhancing the ductility of the column. Pessiki et al. [196] observed that the axial stress and axial strain capacity of FRP-confined reinforced concrete columns increases with increasing jacket strength and stiffness, which are a function of the FRP composite material.

Different axial stress-strain responses have been observed for FRP-confined specimens with different cross-sectional shapes, with circular cross-sections having a larger ultimate stress and strain than comparable square cross-sections [197]. For rectangular cross-sections, a variable transverse strain distribution around the section has been observed [193]. For non-circular sections, the confinement is not as effective as for circular sections due to arching action. It has been observed that for a given axial stress level, the transverse strains measured at the mid-width of the column face are higher than those close to the corners [193]. This indicates that the confinement pressure at the mid-width of the column faces is lower than at the corners. Rounding the corners of the cross-section has been shown to enhance the ultimate strength and ultimate strain of carbon or aramid FRP-confined plain concrete relative to a similar confined cross-section with sharp corners [193].

The failure mode of most concrete specimens confined by FRP with carbon, glass, or aramid fibers has been reported to be tensile fracture of the fibers. Failure has been observed to be sudden and preceded by noises attributed to micro cracking of the concrete and shifting of the aggregates, as well as changes in the appearance of the composite [198]. Rupture of the fibers for FRP-confined columns with a circular cross-section is generally reported to initiate near the mid-length of the specimen and extend towards the top and bottom surfaces, whereas for columns with a rectangular cross-section, rupture has occurred at one corner of the specimen [193]. Premature failure of the confining composite, that is, rupture of the fibers at a strain level lower than the ultimate strain of fibers, has been observed in some studies [199]. Studies have also shown that inadequate length of the overlap at the end of wrapping may result in premature failure due to debonding of the overlapped region prior to tensile rupture of the fibers [199].

A new type of FRP composite that is being explored for structural strengthening applications includes steel fiber sheets. The use of steel fibers was proposed as a lower-cost alternative to other fiber types, such as carbon or aramid. The resulting composite has been referred to in the recent literature as steel reinforced polymer (SRP) composite. Different authors have studied the use of SRP composite for flexural strengthening of RC beams [71] [200] [72] [73] [74] [75] [76] [77] [201] [78] and RC slabs [79], and confinement of concrete columns [81] [82] [202].

5.1.2. Experimental program

The experimental campaign was designed in order to study the effect of SRP confinement on concrete members investigating several variables, i.e. the steel fiber density, the number of SRP layers, the shape of the specimens (circular cross-sections or square cross cross-sections were employed), and the specimen dimensions. All concrete columns of this experimental program were cast from the same batch of concrete, i.e. "Concrete – Type C" (see section 3.1.3). The SRP composite consisted in HD or UHD steel fibers (described in section 3.3.1) embedded in a cement-based mortar matrix (described in section 3.3.4.2). The properties of the composite strip are described in section 3.3.7.

Forty-four specimens were tested to investigate the influence of SRP jacketing on the behavior of concrete members subjected to a concentric compressive load. Specimens were divided in three series depending on the specimen dimensions. The first series (I) included 17 prisms with nominal dimensions equal to 150 mm (width) × 150 mm (depth) × 450 mm (length) with an aspect ratio equal to 3. The second series (II) included 12 prisms with nominal dimensions equal to 250 mm (width) × 250 mm (depth) × 750 mm (length) with an aspect ratio equal to 3. The third series (III) included 12 cylinders with nominal dimensions equal to 150 mm (diameter) × 300 mm (length). Specimens of each series were dived into 4 groups, i.e. G0, G1, G2, and G3, based on the type of confinement. Specimens of group G0 were left unconfined and referred to as control specimens in this section. Specimens of group G1, G2, and G3 were confined with one layer of medium density (MD) steel fibers, three layers of medium density (MD) steel fibers, and one layer of ultra-high density (UHD) steel fibers. The characteristics of the SRP jacketing are reported in Table 23 for specimens with a square cross-section, while are reported in Table 24 for specimens with a circular cross-section.

Table 23. Series I and II: test specimen characteristics.

Specimens				Fiber density	Number of Layers
Series		Group	Name		
I	Control	G0	SQ-I-UC-S-1	-	-
			SQ-I-UC-S-2	-	-
			SQ-I-UC-S-3	-	-
			SQ-I-UC-S-4	-	-
			SQ-I-UC-S-5	-	-
			SQ-I-UC-S-6	-	-
	Confined	G1	SQ-I-CE-MD-S-1L-1	MD	1
			SQ-I-CE-MD-S-1L-2	MD	1
			SQ-I-CE-MD-S-1L-3	MD	1
			SQ-I-CE-MD-S-1L-4	MD	1
		G2	SQ-I-CE-MD-S-3L-1	MD	3
			SQ-I-CE-MD-S-3L-2	MD	3
			SQ-I-CE-MD-S-3L-3	MD	3
		G3	SQ-I-CE-UHD-S-1L-1	UHD	1
			SQ-I-CE-UHD-S-1L-2	UHD	1
			SQ-I-CE-UHD-S-1L-3	UHD	1
			SQ-I-CE-UHD-S-1L-4	UHD	1
II	Control	G0	SQ-II-UC-S-1	-	-
			SQ-II-UC-S-2	-	-
			SQ-II-UC-S-3	-	-
			SQ-II-UC-S-4	-	-
	Confined	G1	SQ-II-CE-MD-S-1L-1	MD	1
			SQ-II-CE-MD-S-1L-2	MD	1
			SQ-II-CE-MD-S-1L-3	MD	1
		G2	SQ-II-CE-MD-S-3L-1	MD	3
			SQ-II-CE-MD-S-3L-2	MD	3
			SQ-II-CE-MD-S-3L-3	MD	3
			SQ-II-CE-MD-S-3L-4	MD	3
		G3	SQ-II-CE-UHD-S-1L-1	UHD	1
			SQ-II-CE-UHD-S-1L-2	UHD	1
			SQ-II-CE-UHD-S-1L-3	UHD	1
			SQ-II-CE-UHD-S-1L-4	UHD	1

Table 24. Series III: test specimen characteristics.

Specimens				Fiber density	Number of Layers
Series		Group	Name		
III	Control	G0	C-III-UC-1	-	-
			C-III-UC-2	-	-
			C-III-UC-3	-	-
	Confined	G1	C-III-CE-MD-1L-1	MD	1
			C-III-CE-MD-1L-2	MD	1
			C-III-CE-MD-1L-3	MD	1
		G2	C-III-CE-MD-3L-1	MD	3
			C-III-CE-MD-3L-2	MD	3
			C-III-CE-MD-3L-3	MD	3
		G3	C-III-CE-UHD-1L-1	UHD	1
			C-III-CE-UHD-1L-2	UHD	1
			C-III-CE-UHD-1L-3	UHD	1

For each Series, specimens from the same group were characterized by same parameters. Confined specimens were named following the notation L-M-B-A-C-Y-Z, where L indicates the type of cross-section (SQ = square cross-section, C = circular cross-section); M denotes the series (I = first series, II = second series, III = third series); B indicates the specimen was confined (UC = unconfined, CE = confined with an epoxy matrix); A denotes the fiber density (MD = medium density, UHD = ultra-high density); C (if present) indicates the concrete corner condition (S = sharp, i.e. corner radius $r = 0$), Y indicates the number of confinement layers (1L = one layer, 3L = three layers), and Z = specimen number. Confined specimens were named following the notation L-M-B-C-Z with the parameters L, M, B, C, and Z defined above.

The confined members were wrapped following the manufacturer's recommendations [6]. The SRP was applied using a wet layup process shown in Figure 103. Steel fiber sheets, with fibers oriented perpendicular to the longitudinal axis of the member, were wrapped around the concrete member. For specimens of series I and II, since the width of the fiber sheet was not the same as the length of the prism, the prisms were wrapped with two or three segments of the fiber sheet with no overlap of the different segments along the specimen length. For cylinders of series III, one segment of the fiber sheet was employed since the width of the fiber sheet was equal to the length of the cylinder (300 mm). For all series, the fiber sheets were bent before wrapping so that they were able to conform to the surface (Figure 103). For specimens of series I and II an overlap length equal to 150 mm and 250 mm, respectively, was provided. The overlap length corresponded to the width of one prism face. For cylinders of series III, an overlap length equal to half of the cylinder circumference was provided.

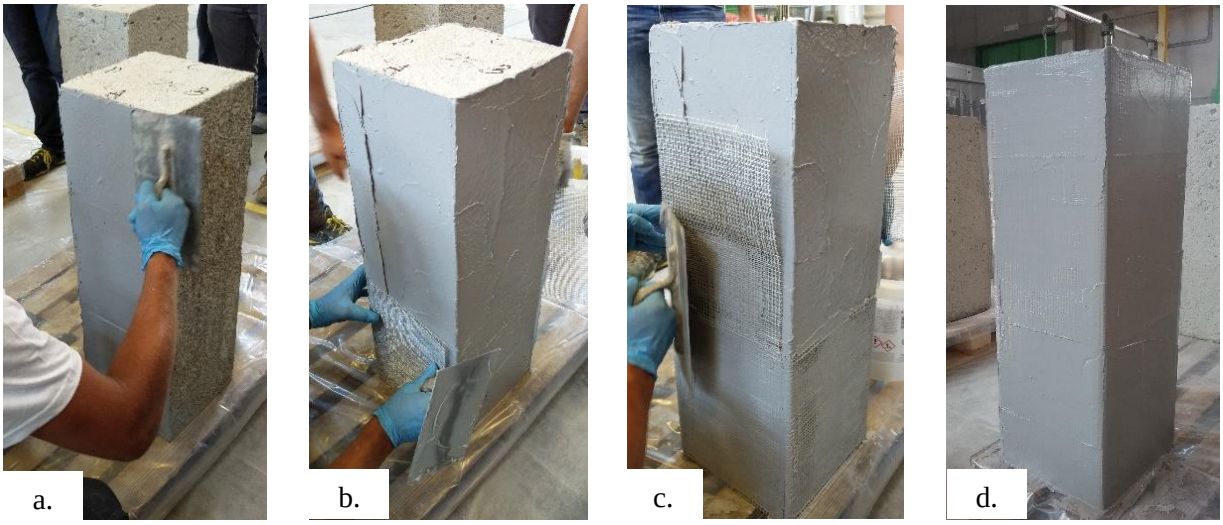

Figure 103. Application of reinforcement: a) Application of the first layer of matrix; b) Application of steel fiber sheet; c) Application of the second layer of matrix; d) Finished specimen.

Prior to testing, both ends of each concrete specimen (both confined and control) were capped with a 25 mm thick layer of high strength mortar to ensure that ends were flat and parallel to one another. The compression tests were performed using a 4000 kN capacity compression testing machine. The bottom pressing plate was fixed, and the top pressing plate was able to rotate. A photo of the test set-up is shown in Figure 104. The specimens were tested under monotonically increasing displacement until failure. The distance between the two pressing plates was measured using four LVDTs named LVDT 0, LVDT 1, LVDT 2, and LVDT 3 mounted between the pressing plates at each corner (see Figure 104). The displacement rate, determined by average value of the two LVDTs, was maintained at 0.2 mm/min by continuously monitoring and controlling the machine stroke. Testing was completed when a significant drop in load occurred in the post-peak response or when a significant damage was observed in the specimen.

For six specimens of series I and six specimens of series II, digital image correlation (DIC) was used to analyze the displacement in the axial and hoop directions on one face (front face) of the confined prism during the loading process. The surface strains were determined as the gradients of the displacements after interpolating the displacement contours with a quantic B-spline collocation method [84]. To enable the DIC measurements, the composite surface was covered uniformly with white nonreflective paint prior to testing. Black paint was then sprayed on the composite surface to create a speckle pattern, which is recognized and employed by the DIC software to obtain the displacement field. During testing specimens were illuminated with normal white light to assure uniform light intensity on the composite surface.

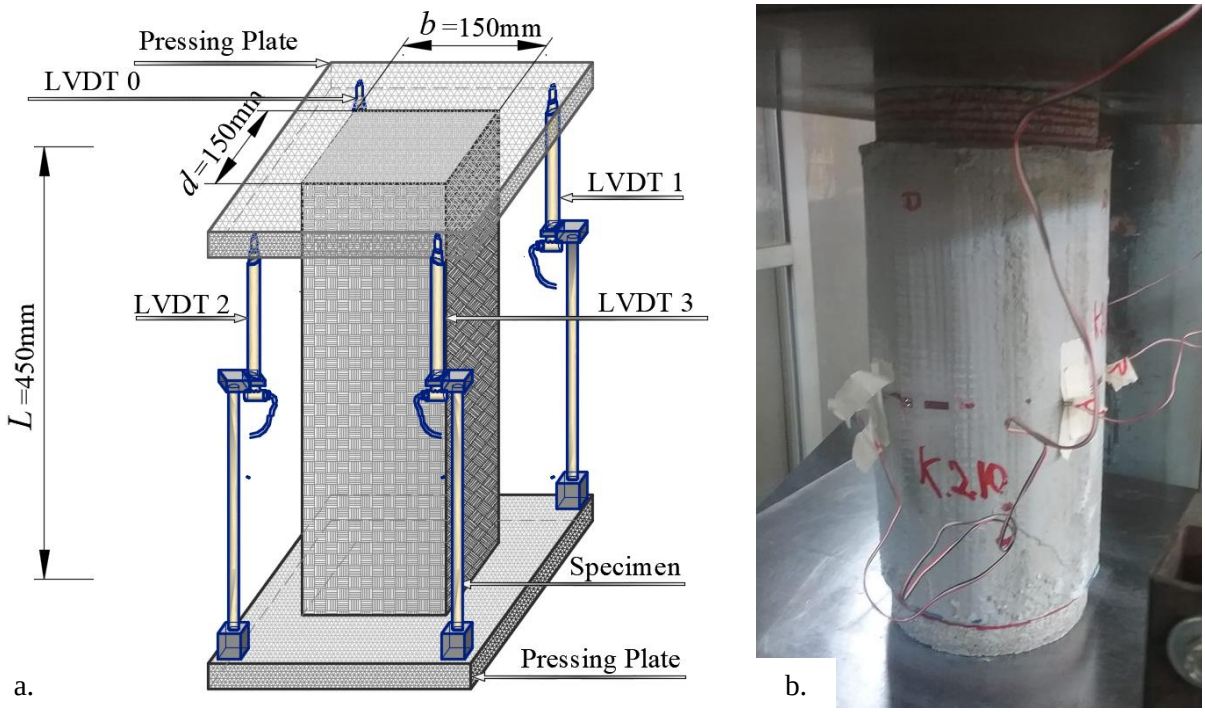

Figure 104. Test set-up: a) sketch of a confined specimen of series I; b) C-III-CE-MD-1L-1.

Image were taken at a frequency of 0.1 Hz and were processed considering the origin of the Cartesian axes located at the top left edge of the specimen front face. Due to the potentially brittle nature of the failure, readings were recorded only until shortly after the peak load was achieved in order to protect the DIC equipment.

Six cylinders of series III (two for each group) were instrumented with strain gages. On each cylinder four strain gages were mounted on the composite surface in the direction perpendicular with respect to the longitudinal axis of the specimen in order to measure the hoop strains. The four strain gages were arranged 90° apart one another.

5.1.3. Experimental results

5.1.3.1. Failure modes

The peak load of all unconfined specimens was associated with crushing of concrete (C) (Figure 105a-b-c). After the peak load was achieved, the confined specimens of series I and II continued to deform under decreasing applied load until failure occurred by separation of the SRP jacket at the vertical lap joint or rupture of the fibers. All confined specimens of series I except for specimen SQ-I-CE-MD-S-1L-2 and specimen SQ-I-CE-MD-S-3L-3, experienced the same type of failure characterized by opening (O) of the SRP jacket at the vertical lap joint. Failure was generally sudden but preceded by noises associated with cracking of the epoxy in the composite matrix. For most confined specimens of series I, failure initiated

near the middle third of the specimen length, and the SRP jacket was completely opened with transverse cracks (parallel to the fiber direction) that extended from the failed face to other faces of the specimen. Some of the transverse cracks were consistent with the locations where different steel fiber sheet segments abutted one another. Detachment of the overlapping layer of the jacket occurred along a limited portion of the specimen length. For several specimens, failure started in the layer of epoxy in between the two overlapping layers, and both layers of fibers opened with the internal layer having some concrete from the substrate attached. For specimen SQ-I-CE-MD-S-1L-2 the failure consisted in the rupture of the fibers (R) at one corner while for specimen SQ-I-CE-MD-S-3L-3 a mixed failure mode was observed characterized by both rupture of the fibers and opening of the SRP jacket. Specimens of group G2 and G3 of series II experienced the same type of failure characterized by the opening of the SRP jacket at the vertical lap joint, except for specimen SQ-II-CE-MD-S-3L-3 for which the rupture of the fibers occurred. Specimen of Group G1 of series II experienced the same type of failure characterized by the rupture of the fibers close to one corner.

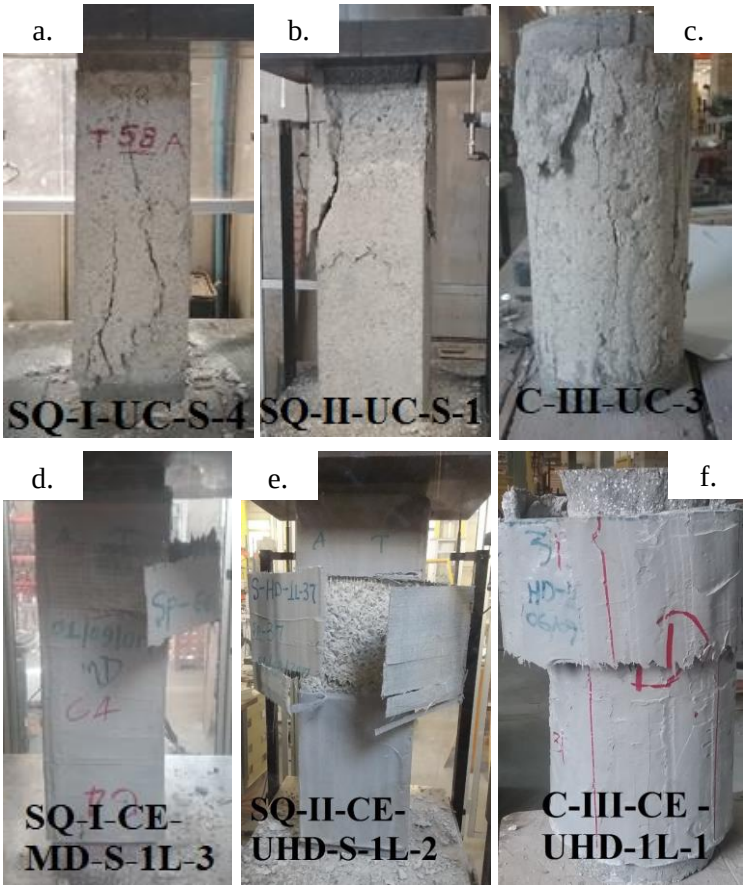

Figure 105. Typical failure modes of confined and control specimens: a) SQ-I-UC-S-4; b) SQ-II-UC-S-1 c) C-III-UC-3; d) SQ-I-CE-MD-S-1L-3; e) SQ-II-CE-UHD-S-1L-2; f) C-III-CE-UHD-1L-1.

The load responses of cylinders confined with SRP jackets showed the same behavior, characterized by an increasing branch after the peak load was reached. All confined cylinders strengthened with MD steel fibers experienced the same type of failure characterized by the rupture of the steel fibers, while cylinders confined with UHD steel fibers had a failure mode that consisted in the opening of the SRP jacket. Table 25 and Table 26 summarizes the key experimental results obtained for each test specimen. Values provided for the unconfined specimens include the unconfined compressive strength (peak stress) f'_{co}, the unconfined ultimate compressive stress $f'_{co,u}$, and the corresponding values of strain ε_{co} and $\varepsilon_{co,u}$, respectively. Values provided for the confined specimens include the confined compressive strength (peak stress) f'_{cc}, the confined ultimate compressive stress $f'_{cc,u}$, and the corresponding values of strain ε_{cc} and $\varepsilon_{cc,u}$, respectively. It should be noted that for confined cylinders, the ultimate axial strain coincided with the axial strain at peak stress. Therefore, only ε_{co} was reported in Table 26 for confined cylinders. Both for control and confined square specimens, the ultimate compressive stress was chosen as the value corresponding to the 85% of the peak stress, if a softening branch was observed after the peak. Values of stress were determined by dividing the force by the cross-sectional area of the concrete prism (neglecting the thickness of the composite). Values of strain were determined by dividing the average of displacement readings from the four LVDTs by the initial distance between the pressing plates. Accordingly, the values of strain determined in this manner are considered to be *global* strain. Values of the ratios $f'_{cc}/\overline{f'_{co}}$ and $\varepsilon_{cc,u}/\overline{\varepsilon_{co}}$ are provided in Table 25 and Table 26 for each confined specimen. Average values of the ratios $f'_{cc}/\overline{f'_{co}}$ and $\varepsilon_{cc,u}/\overline{\varepsilon_{co}}$ are also reported for each group in each series. Control specimens for series I, II and III had an average compressive strength $\overline{f'_{co}}$ equal to 19.88 MPa, 18.16 MPa, and 20.47 MPa, respectively, while had an average compressive strain at peak load $\overline{\varepsilon_{co}}$ equal to 0.293, 0.295, and 0.297, respectively. The highest values of the ratios $f'_{cc}/\overline{f'_{co}}$ and $\varepsilon_{cc,u}/\overline{\varepsilon_{co}}$ belong to cylinders of group G2 (confined with 3 layers of MD steel fibers). For these specimens the ratio $f'_{cc}/\overline{f'_{co}}$ ranged between 3.43 and 3.99 while the ratio $\varepsilon_{cc,u}/\overline{\varepsilon_{co}}$ ranged from 1.02 to 1.40. The highest average values of the ratios $f'_{cc}/\overline{f'_{co}}$ and $\varepsilon_{cc,u}/\overline{\varepsilon_{co}}$ were obtained for specimens of group G2 in each series.

Test results for series I and series II

Specimens			f'_{co} or f'_{cc}	$\frac{f'_{cc}}{f'_{co}}$	$f'_{co,u}$ or $f'_{cc,u}$	Avg	ε_{co} or ε_{cc}	$\varepsilon_{co,u}$ or $\varepsilon_{cc,u}$	$\frac{\varepsilon_{cc,u}}{\varepsilon_{co}}$	Avg	Failure Mode	A_{total}	A_{peak}
			[MPa]		[MPa]	[MPa]	%	%				[MPa]	[MPa]
	Group	Name											
Control	G0	SQ-I-UC-S-1	21.13	-	17.96	-	0.31	0.43	-	-	C	0.067	0.043
		SQ-I-UC-S-2	17.73	-	15.07		0.3	0.38	-		C	0.049	0.036
		SQ-I-UC-S-3	22.26	-	18.92		0.29	0.40	-		C	0.065	0.043
		SQ-I-UC-S-4	17.88	-	15.20		0.29	0.44	-		C	0.058	0.034
		SQ-I-UC-S-5	20.83	-	17.71		0.3	0.43	-		C	0.066	0.040
		SQ-I-UC-S-6	19.48	-	16.56		0.27	0.40	-		C	0.057	0.034
Confined	G1	SQ-I-CE-MD-S-1L-1	26.40	1.33	22.44	1.29	0.76	2.49	8.48	8.93	O	0.661	0.158
		SQ-I-CE-MD-S-1L-2	25.58	1.29	22.89		0.53	3.29	11.22		R	0.751	0.099
		SQ-I-CE-MD-S-1L-3	25.03	1.26	22.51		0.61	2.55	8.69		O	0.563	0.113
		SQ-I-CE-MD-S-1L-4	25.61	1.29	22.16		0.79	2.15	7.34		O	0.495	0.163
	G2	SQ-I-CE-MD-S-3L-1	37.52	1.89	36.99	1.86	1.29	3.38	11.53	10.72	O	0.651	0.392
		SQ-I-CE-MD-S-3L-2	37.53	1.89	36.11		1.38	3.04	10.38		O	1.916	0.427
		SQ-I-CE-MD-S-3L-3	35.77	1.80	34.70		1.49	3.00	10.25		R/O	2.404	0.441
	G3	SQ-I-CE-UHD-S-1L-1	29.88	1.50	25.61	1.45	0.78	2.21	7.52	6.56	O	0.595	0.182
		SQ-I-CE-UHD-S-1L-2	31.10	1.56	28.42		0.74	1.52	5.19		O	0.407	0.171
		SQ-I-CE-UHD-S-1L-3	25.89	1.30	22.01		0.51	2.32	7.90		O	0.519	0.097
		SQ-I-CE-UHD-S-1L-4	28.42	1.43	27.19		0.56	1.65	5.62		O	0.479	0.120

Table 25. Test results for series I and series II.

Specimens			f'_{co} or f'_{cc}	$\frac{f'_{cc}}{f'_{co}}$	$f'_{co,u}$ or $f'_{cc,u}$	Avg	ε_{co} or ε_{cc}	$\varepsilon_{co,u}$ or $\varepsilon_{cc,u}$	$\frac{\varepsilon_{cc,u}}{\varepsilon_{co}}$	Avg	Failure Mode	A_{total}	A_{peak}
			[MPa]		[MPa]	[MPa]	%	%				[MPa]	[MPa]
	Group	Name											
Control	G0	SQ-II-UC-S-1	17.64	-	14.99	-	0.26	0.41	-	-	C	0.054	0.029
		SQ-II-UC-S-2	18.57	-	15.78		0.30	0.42	-		C	0.061	0.039
		SQ-II-UC-S-3	16.42	-	13.96		0.27	0.37	-		C	0.046	0.031
		SQ-II-UC-S-4	19.99	-	16.99		0.35	0.49	-		C	0.072	0.047
Confined	G1	SQ-II-CE-MD-S-1L-1	21.98	1.21	18.68	1.13	0.35	0.62	2.10	2.37	R	0.110	0.055
		SQ-II-CE-MD-S-1L-2	21.23	1.17	18.05		0.36	0.68	2.30		R	0.119	0.057
		SQ-II-CE-MD-S-1L-3	18.61	1.02	15.82		0.34	0.80	2.71		R	0.127	0.047
	G2	SQ-II-CE-MD-S-3L-1	25.47	1.40	21.65	1.33	0.46	1.21	4.11	5.59	O	0.263	0.088
		SQ-II-CE-MD-S-3L-2	25.04	1.38	21.28		0.68	1.52	5.15		O	0.326	0.133
		SQ-II-CE-MD-S-3L-3	22.49	1.24	19.12		0.59	1.84	6.23		R	0.367	0.106
	G3	SQ-II-CE-MD-S-3L-4	23.91	1.32	20.33		0.52	2.03	6.89		O	0.432	0.097
		SQ-II-CE-UHD-S-1L-1	23.44	1.29	19.92	1.31	0.41	0.94	3.18	3.16	O	0.184	0.071
		SQ-II-CE-UHD-S-1L-2	24.26	1.34	20.62		0.36	0.69	2.34		O	0.135	0.063
		SQ-II-CE-UHD-S-1L-3	23.10	1.27	19.63		0.42	1.17	3.97		O	0.233	0.059
		SQ-II-CE-UHD-S-1L-4	24.47	1.35	20.80		0.40	0.93	3.16		O	0.188	0.068

Test results for series III

Specimens			f'_{co} or f'_{cc}	$\frac{f'_{cc}}{f'_{co}}$	Avg	ε_{co} or ε_{cc}	$\frac{\varepsilon_{cc}}{\varepsilon_{co}}$	Avg	$\varepsilon_{j,u}$	Failure Mode	A_{total}
			[MPa]		[MPa]	%			%		[MPa]
	Group	Name									
Control	G0	C-III-UC-1	20.78	-	-	0.313	-	-	-	C	0.060
		C-III-UC-2	19.90	-		0.308	-		-	C	0.052
		C-III-UC-3	20.73	-		0.270	-		-	C	0.066
Confined	G1	C-III-CE-MD-1L-1	39.77	1.94	1.93	2.414	8.13	8.47	0.804	R	0.953
		C-III-CE-MD-1L-2	38.80	1.90		2.210	7.44		-	R	0.700
		C-III-CE-MD-1L-3	39.88	1.95		2.920	9.83		1.439	R	1.084
	G2	C-III-CE-MD-3L-1	70.28	3.43	3.72	3.492	11.76	11.93	1.376	R	2.143
		C-III-CE-MD-3L-2	81.67	3.99		3.789	12.76		-	R	2.249
		C-III-CE-MD-3L-3	76.73	3.75		3.346	11.27		0.716	R	1.877
	G3	C-III-CE-UHD-1L-1	44.55	2.18	2.12	2.584	8.70	7.3	-	O	0.920
		C-III-CE-UHD-1L-2	43.39	2.12		2.264	7.62		0.471	O	0.802
		C-III-C.E-UHD-1L-3	42.37	2.07		1.654	5.57		1.110	O	0.932

Table 26. Test results for series III.

5.1.3.2. Axial stress – axial strain response

As explained in section 5.1.2, four LVDTs measured the axial displacements between the pressing plates. Figure 106 shows the axial load – axial displacement response of two representative specimens SQ-II-CE-HD-S-1L-2 and SQ-II-CE-HD-S-1L-1, determined by the individual LVDT. Figure 106a shows a consistent behavior of the four LVDTs until the failure of the specimen, while in Figure 106b it is clear that although the behavior of the four LVDTs was consistent up to the peak load, the post peak behavior of LVDTs 1 and 2 differed from LVDTs 0 and 3. For each confined and unconfined specimen, the axial stress versus axial strain response was observed in order to understand the number of specimens for which the four LVDTs have a consistent behavior up to the failure. Thirty specimens out of forty-four specimens showed a consistent behavior up to failure, while the remaining specimens showed a consistent behavior up to the peak load.

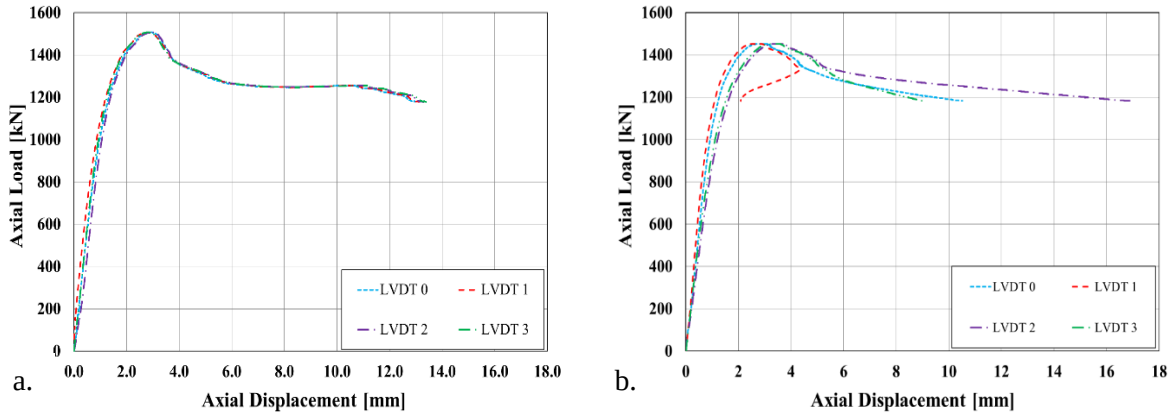

Figure 106. Axial stress-axial strain response: a) Specimen SQ-II-CE-HD-S-1L-2; b) Specimen SQ-II-CE-HD-S-1L-1.

5.1.3.2.1. Series I and II

Figure 107 and Figure 108 show the axial stress – axial strain response of square specimens (Series I and II) confined with different number of SRP layers. Control specimens are included for comparison. The behavior of specimens can be divided into three phases. The general behavior of the confined columns is characterized by an initial linear response that follows the unconfined behavior. After the unconfined strength is reached, the behavior becomes non-linear and the axial stress continues to increase until the peak stress is reached. After the peak stress, different behavior for each series are observed. For specimens of group G1 and G3 of series I and specimens of series II, the third phase is characterized by a descending branch until failure that occurs with a significant drop of the axial stress due to the opening of the SRP jacket. For specimens of group G2 of series I, the third phase is characterized by an increment of the axial strain with an almost constant axial stress up to the failure.

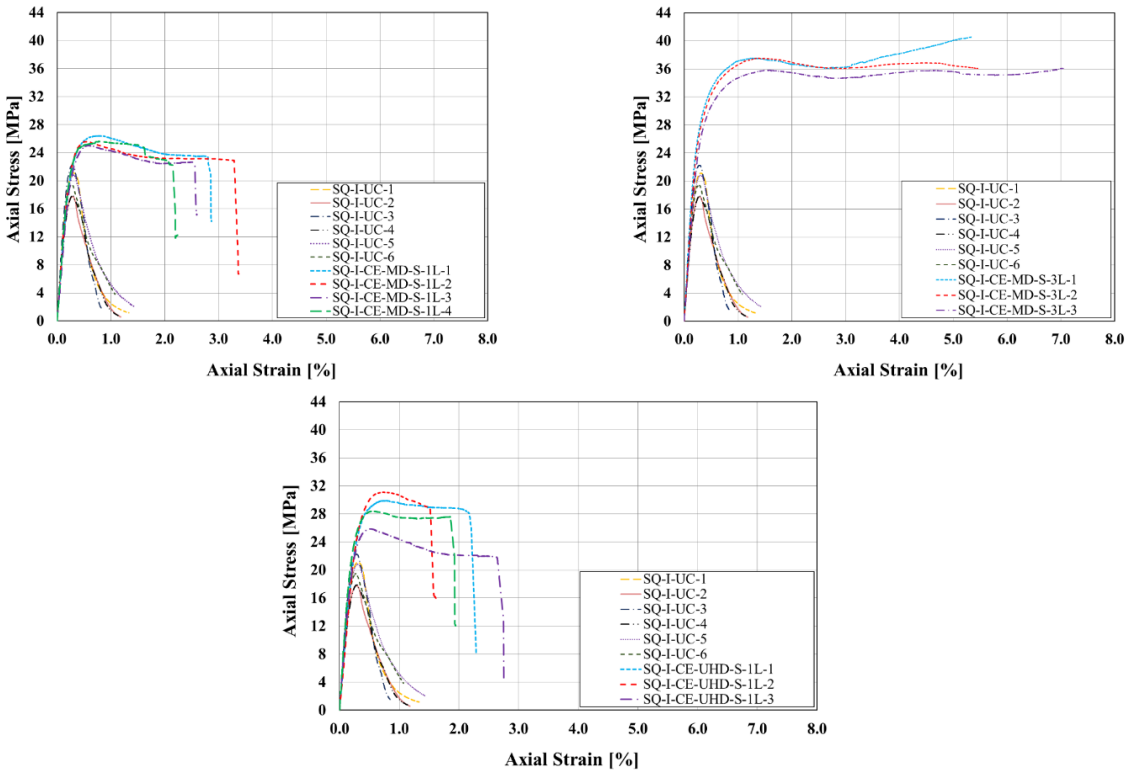

Figure 107. Axial stress- axial strain response for series I specimens.

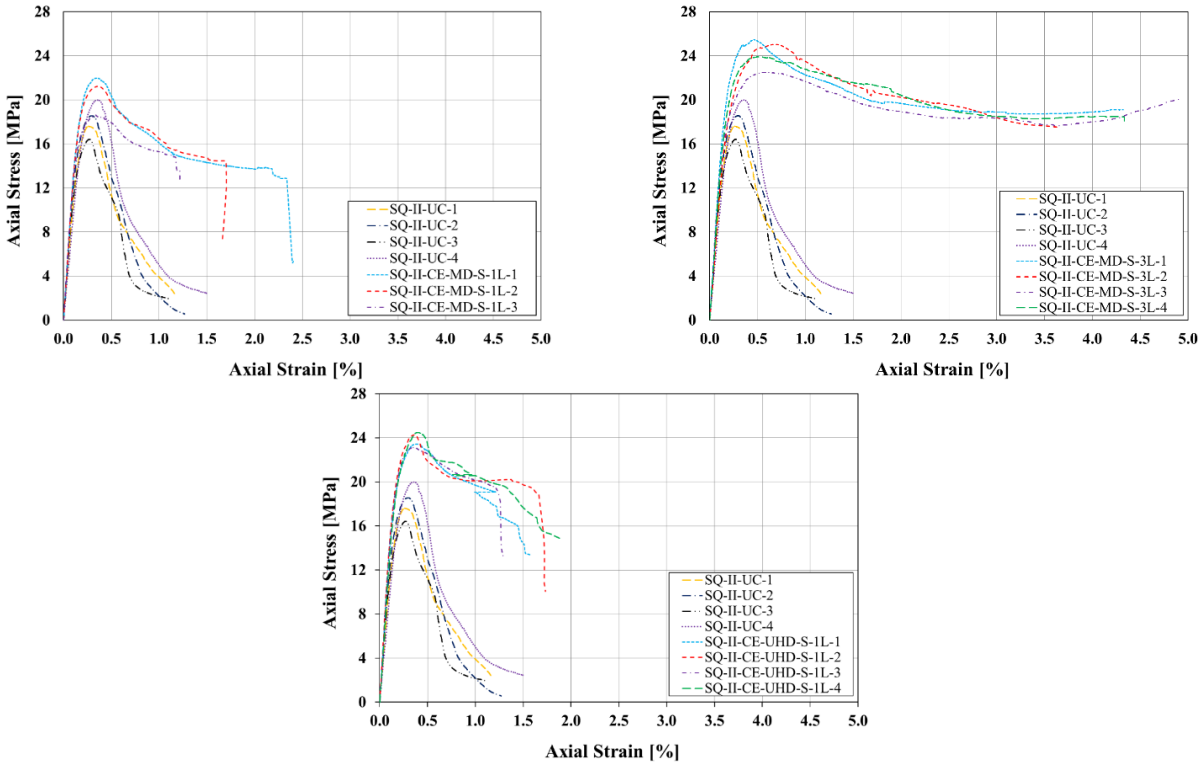

Figure 108. Axial stress- axial strain response for series II specimens.

5.1.3.2.2. Series III

Figure 109 shows the axial stress – axial strain response of specimens of Series III together with the corresponding control specimens. The first linear branch of the response of the confined specimens overlaps with that of the unconfined cylinders. Once the curve reaches the peak stress of the unconfined specimens, a non-linear branch begins in which the concrete core starts to damage while the SRP jacket is activated. The third phase of the response, that follows the non-linear branch, is almost linear until failure of the specimen occurs.

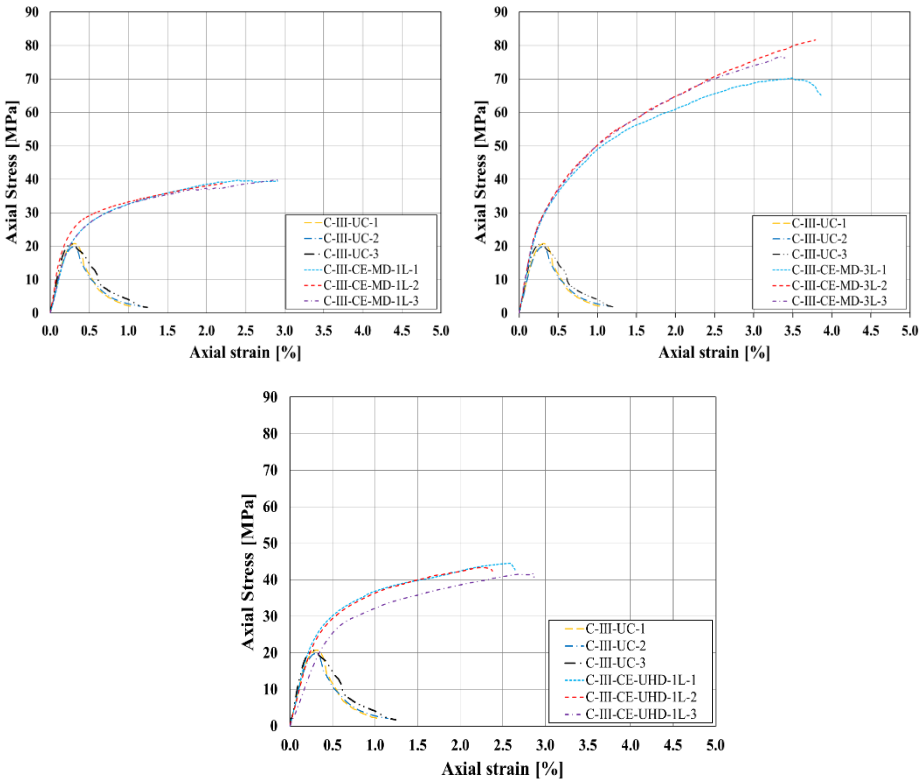

Figure 109. Axial stress- axial strain response for series III specimens.

5.1.3.3. Evaluation of hoop strains

5.1.3.3.1. Series I and II

As explained in section 5.1.2, vertical and hoop strain components of some square columns (Series I and II) were obtained using DIC. Values of hoop and axial strains were obtained for eight square areas (Figure 110) in the central third of the column height, for a 5 pixel step size and subset 31 pixels. Each square was 30mm width, the horizontal spacing between adjacent squares was 30mm, and the vertical spacing measured 10mm. Therefore, the average of the strains within these eights squares was considered

representative of the longitudinal and hoop strain component of the column. Figure 111 and Figure 112 show the axial stress versus axial strain response obtained from the four LVDTs, and axial stress versus hoop strain response determined by DIC for specimens of Series I and II. The accuracy of the axial strain values obtained by the four LVDTs was compared with the axial strain values determined by DIC, in order to validate the DIC measurements (Figure 113).

The axial stress versus hoop strain response of SRP confined concrete specimens can be divided in two parts. In the first part, axial stress increases while hoop strain remains almost equal to zero. As the average compressive strength of the unconfined columns is reached (i.e. 19.9 MPa and 18.2 MPa for series I and II respectively), the hoop strain component starts to increase, which corresponds to the second part of the curve when activation of the SRP jacket initiates. The second part is characterized by an always increasing trend for the hoop strain component.

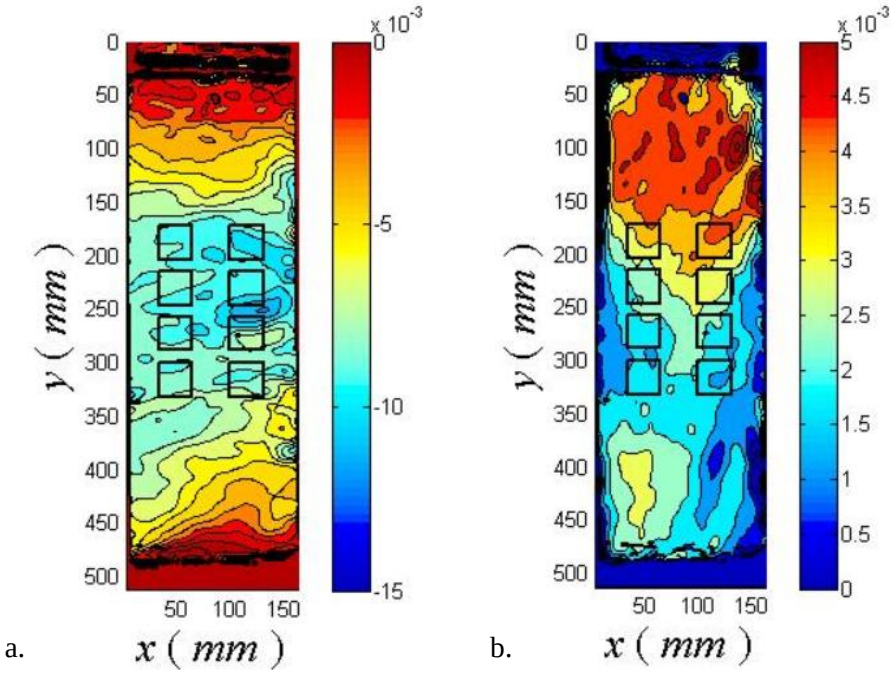

Figure 110. Representation of the eight squares used to calculate the values of the strain using DIC technique for specimen SQ-I-CE-MD-S-3L-1 at peak stress: a) axial strain; b) hoop strain.

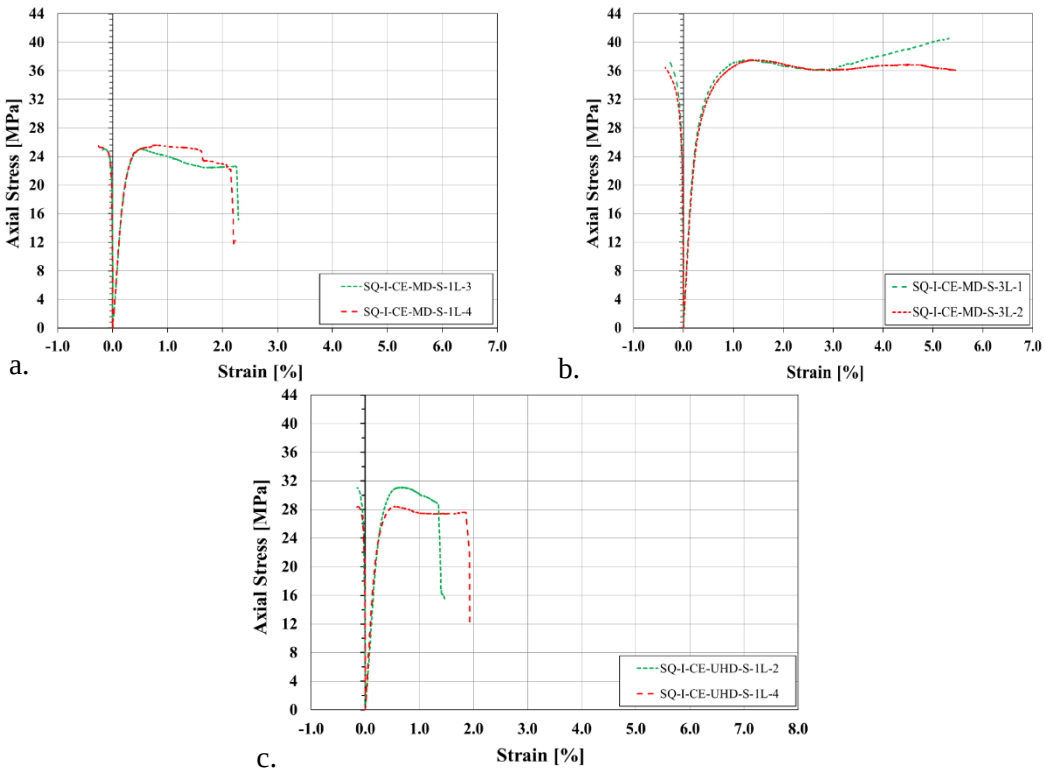

Figure 111. Axial and hoop stress versus axial strain for series I specimens: a) G1; b) G2; c) G3.

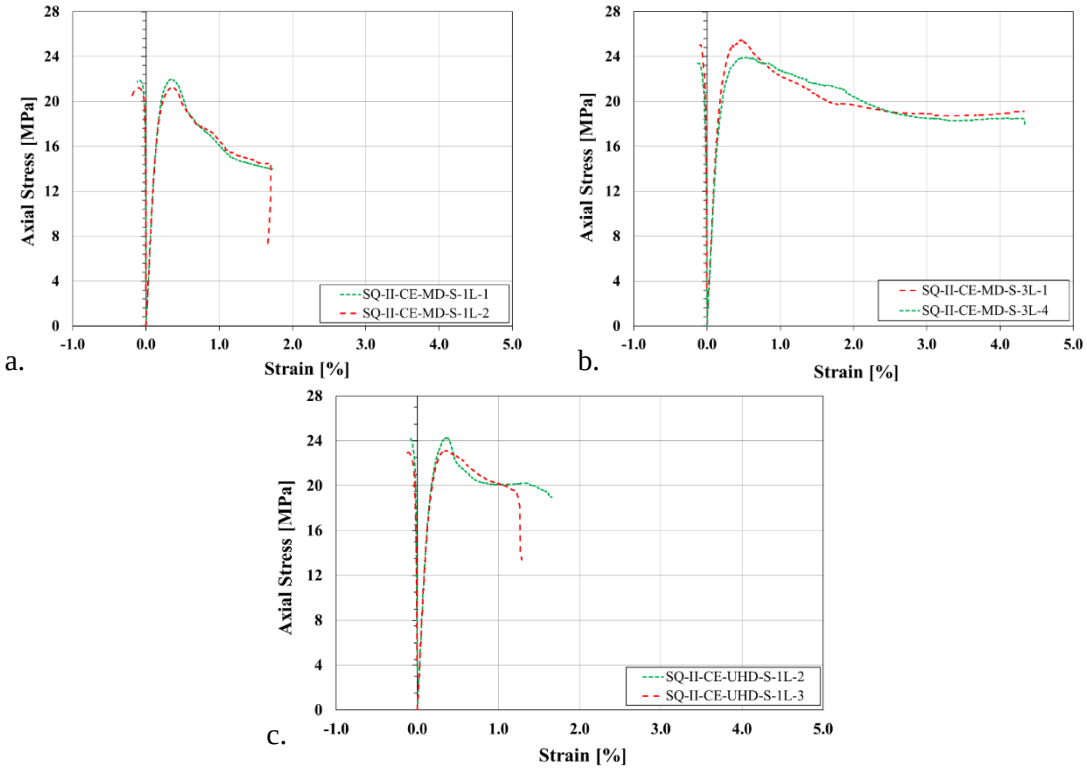

Figure 112. Axial and hoop stress versus axial strain for series II specimens: a) G1; b) G2; c) G3.

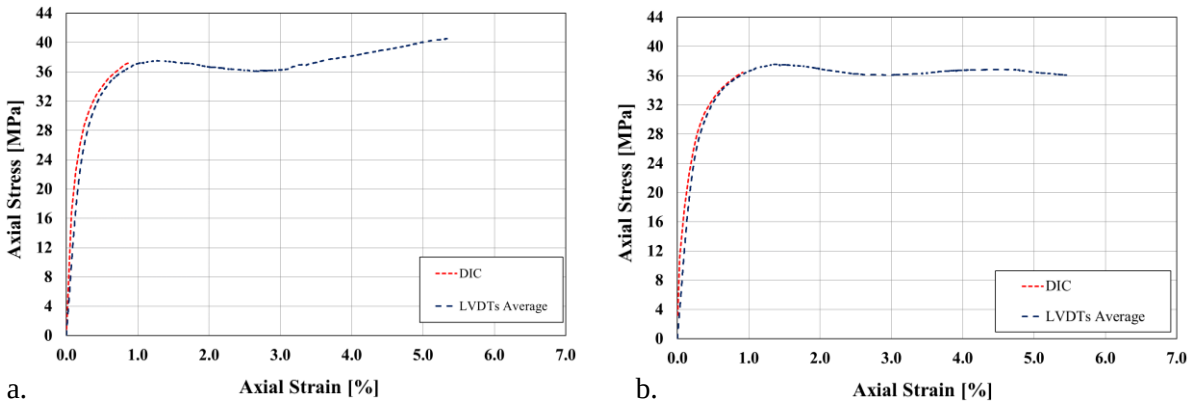

Figure 113. Comparison of axial stress – axial strain response determined by LVDTs and DIC: specimen SQ-I-CE-MD-S-3L-1 (a), specimen SQ-I-CE-MD-S-3L-2 (b).

5.1.3.3.2. Series III

As mentioned in section 5.1.2, four strain gauges were installed on the surface of the six SRP confined concrete specimens of series III to measure the hoop strains. Figure 114 shows the axial stress versus hoop strain curves, measured by individual strain gauge, and axial stress versus axial strain response, determined by individual LVDT, of representative specimen C-III-CE-MD-3L-3. Furthermore, the axial stress-strain behavior of those specimens instrumented with strain gages are presented in Figure 115. The axial stress – hoop strain curve of SRP confined concrete cylinders can be divided in two parts. The first part is characterized by an almost vertical branch corresponding to negligible strain values in the hoop direction. After the average compressive strength of the control specimens is reached, the SRP jacket is activated and hoop strain increases, which correspond to the second branch of the curve.

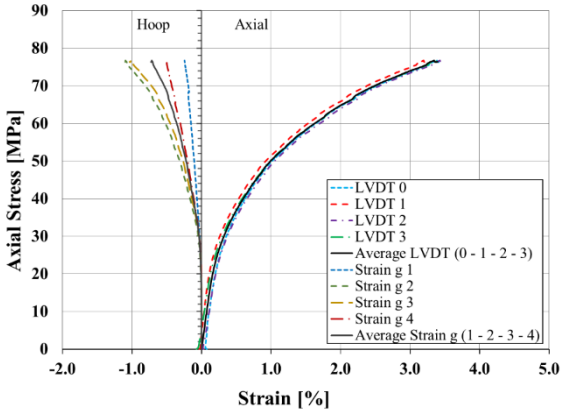

Figure 114. Axial stress – strain response determined by individual LVDT and each strain gauge for representative specimens: C-III-CE-MD-3L-3.

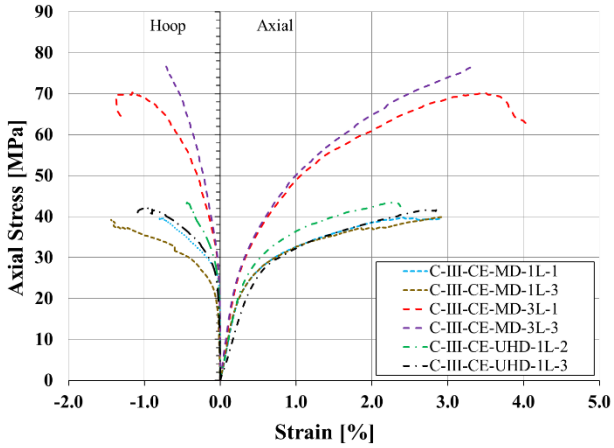

Figure 115. Axial stress – strain response determined by LVDTs and strain gauges for six confined specimens in series III.

5.1.4. Discussion

5.1.4.1. Influence of test variables

5.1.4.1.1. Effect of the dimension of the column

One of the objectives of this study is to examine the size effect of the size of the column on the behavior of confined columns, which is investigated by comparing the results of the specimens in Series I and Series II. Some comments can be made by comparing the results plotted in Figure 116 and summarized in Table 25:

- Increasing the dimension of the specimen, resulted in a 8.7% decrease of the average unconfined strength f'_{co}. Only 2.0% difference was observed between the average ultimate axial strain $\varepsilon_{co,u}$ of control specimens of Series I and II, which indicates a similar behavior of the post-peak region of the stress – strain curve for the unconfined specimens in Series I and II. It should be pointed out that the average compressive strength of the control square specimens of Series I and II was respectively 18.5% and 23.4% lower than the compressive strength obtained from the 150 mm cubes at the day of testing, which indicates the existence of the size effect, as reported by Turkel and Ozkul [203].
- An increase of the dimension of the specimen, from Series I to Series II, resulted in a decrease of the confined compressive strength f'_{cc} for groups G1, G2 and G3 by 19.7%, 34.4% and 17.4% respectively. Moreover, the average axial strain at ultimate stress $\varepsilon_{cc,u}$ obtained by increasing the dimension of the specimen, from Series I to Series II, declined significantly for groups G1, G2 and G3 by 73.3%, 47.5% and 37.3% respectively.

Figure 116 summarizes the effect of the dimension of the specimens and points out that higher peak stresses are reached in small columns although the trend between the groups is the same between the two dimensions, as concluded by Wang and Wu [204]. It should be noted that size effect can be examined only by comparing specimens in which the amount of confinement is scaled proportionally to the specimen dimension, while in this study specimens with the same amount of composite and two different dimensions were investigated. Thus, the results indicate that a predictive formula for confined columns should take into account the reinforcement ratio rather than the absolute amount of composite. These results also point out the need of additional data to clarify the size effect.

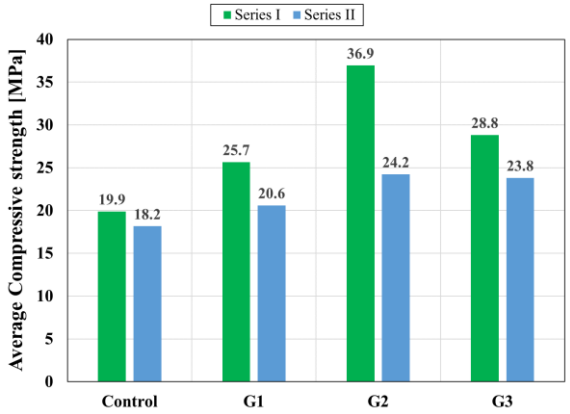

Figure 116. Variation in the average compressive strength with specimens size.

5.1.4.1.2. Shape effect

The effect of the shape of the cross-section on the compressive strength and the ultimate axial strain of the confined and unconfined specimens is investigated by comparing the results of Series I and III. The average compressive strength of square and circular columns for control and confined specimens is shown in Figure 117. The following comments can be made (see Table 25, Table 26, and Figure 117):

- There is just a negligible difference (2.9%) between the average compressive strength of control specimens of Series I (19.9 MPa) and Series III (20.5 MPa). However, the average ultimate axial strain of control specimens dropped considerably from Series I to Series III by 27.7%.
- The average peak stress of confined specimens in Series III is greater than Series I, by 53.9%, 106.4% and 50.7% for groups G1, G2, and G3, respectively. A 12.0% increase of the average ultimate axial strain is observed for groups G2 and G3 of Series III when compared with the corresponding groups of Series I; whereas, for group G1 of Series III, the average ultimate axial strain decreased by 4% with respect to the same group of Series I.

Evidently, the shape of the cross-section influences the compressive strength of confined specimens, while there is not a substantial difference between the two shapes of the cross-section in terms of ultimate axial strain of confined specimens.

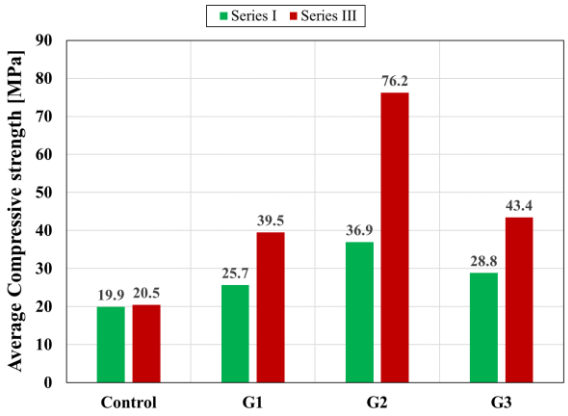

Figure 117. Variation in the average compressive strength with specimens shape.

5.1.4.1.3. Influence of the number of SRP layers

The influence of the number of SRP layers is investigated by comparing the average compressive strength and the average ultimate strain of columns confined with one layer and three layers of SRP with MD steel fiber sheet, within each Series. Figure 118 shows the comparison between the average compressive strength of the specimens confined with one or three fiber sheet layers for Series I, II and III. Table 25 and Table 26 show that the average compressive strength increases as the number of SRP layers increases. For Series I specimens, the average compressive strength of columns confined with three layers of MD steel fiber sheets is 44% greater than the average strength of columns confined with one layer of MD steel fiber sheets. Similarly, the average ultimate axial strain increases roughly by 20.0% for group G2, with respect to the average ultimate strain of group G1 specimens. For Series II specimens, the increment of the average compressive strength of group G2 with respect to group G1 is 17.6%. The average ultimate axial strain for group G2 is roughly 2.4 times greater than the average ultimate strain of group G1 specimens. For Series III specimens, the difference between the increment of the average compressive strength for group G2 is more evident. In fact, for G2 specimens, the increase of the average compressive strength with respect to G1 specimens is equal to 93.1%. The average ultimate axial strain for Series III specimens, which coincides with the peak strain, increase roughly by 40.9% from group G1 to group G2. The increase of the average compressive strength is not linearly related to the number of SRP layers as already noted by El-Hacha et al. [202].

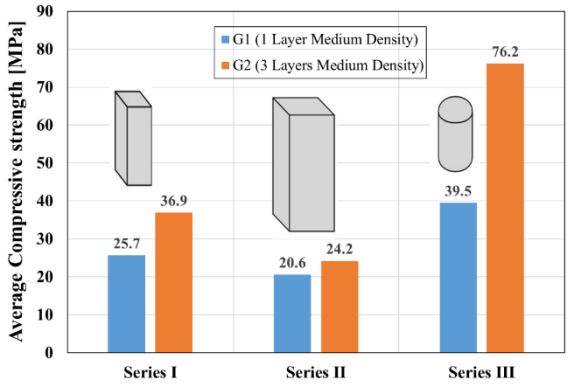

Figure 118. Variation in the average compressive strength with unconfined specimens, one layer and three SRP layers for series I, II and III.

5.1.4.1.4. Effect of steel fiber sheet density

Results from groups G1 and G3, are compared within each Series to investigate the influence of the steel fiber sheet density on the average compressive strength and the average ultimate axial strain. Figure 119 shows that with one layer of SRP composite, the average compressive strength increases not proportionally as the increase in the fiber sheet density. For series I, the average compressive strength of specimens confined with one layer of MD fiber sheet is 12.3% lower than the average compressive strength of specimens confined with one layer of UHD fiber sheet. Similarly, for Series II and III the increase between groups G1 and G3 is 15.6% and 10.0%, respectively.

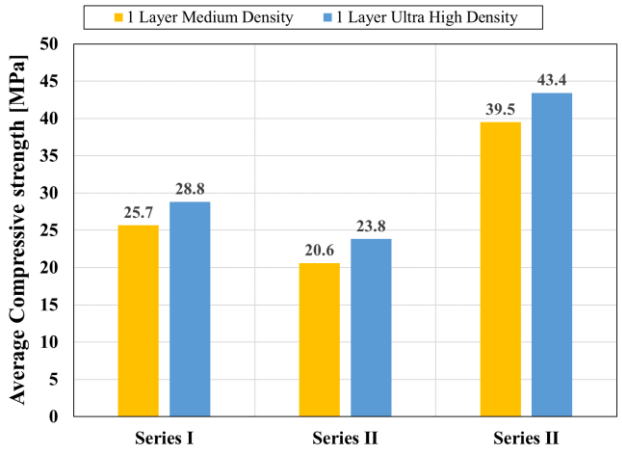

Figure 119. Variation in the average compressive strength with SRP sheets density.

5.1.4.2. Energy absorption

One of the key aspects to understand the efficiency of the confining system is the energy absorption, which can be identified as the total area under the axial stress – axial strain curve up to the ultimate stress and its corresponding strain (A_{total}). The area under the axial stress – axial strain curve up to the peak strength and its corresponding strain is named A_{peak}. The values of A_{peak} and A_{total} are reported in Table 25 for each square specimen. It was already mentioned in section 5.1.3.1 that the ultimate stress and the compressive strength of confined cylindrical specimens coincide. Thus, only A_{total} is reported in Table 26 for each cylindrical specimen. The average total energy for control specimens of each Series is equal to 0.06 MPa, which appears to suggest that the energy absorption of plain concrete is independent of the dimension and shape of the specimen.

The ratio between the average total area of confined specimens and control specimens for each group of each Series is presented in Figure 120 which demonstrates the effectiveness of SRP fiber sheets in improving the deformability of the specimens. The most increase of energy absorption is observed for confined cylindrical specimens (Series III) in which the average energy absorption for specimens confined with 3 layers of MD SRP fiber sheet is 35 times greater than control specimens.

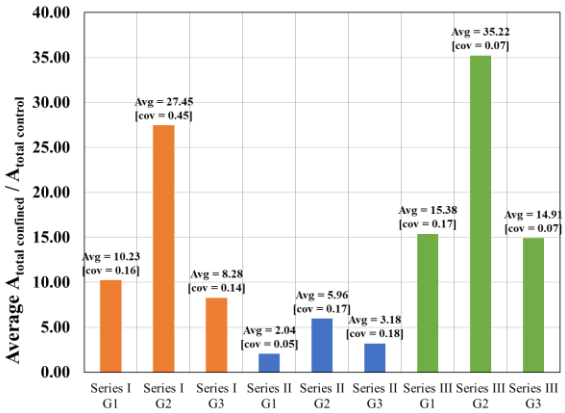

Figure 120. Comparison of $\frac{\bar{A}_{tot\ confined}}{\bar{A}_{tot\ control}}$ for each group of each Series.

Moreover, it is obvious that the most ductile behavior in each Series is related to the specimens confined with three plies of MD SRP fiber sheet because of both high strength capacity and deformability of these specimens. For Series I, II and III, the average value of energy absorption increases from group G1 to G2 by 168.1%, 194.1% and 136.2% respectively. Accordingly, the average energy absorption grows not proportionally with the increase of the number of SRP layers, as noted by El-Hacha and Mashrik [81]. The average energy absorption for Series I and III decreases from group G1 to G3 by 19.1% and 3% respectively, though this value for Series II, increases by 56.3%. Consequently, these results suggest that

the composite stiffness does not have a specific and predictable effect on energy absorption of the confined specimens.

5.1.4.3. Arch effect

After testing, in order to study the condition of the concrete, the specimens were saw cut near the middle length. Three general observations can be summarized as follows: (1) The area of crushing of concrete near the surface of confinement was noticeable; (2) In the case of square cross-section, an arch effect was observed. The arch effect appeared by formation of the parabolic zones of crushing, mostly along the four side faces of the specimens. However, for groups G1 and G3 specimens, particularly for specimens confined with UHD SRP fiber sheet, the parabolic zones rarely formed along the four sides. Moreover, the parabolas started from each corner and continued up to the following corner. (3) In the case of circular specimens, no parabolic region appeared which indicates that the full area of concrete enclosed in SRP wraps was effectively confined which, in turn, plays an important role in determining the peak strength of the confined concrete. Sharp corners of the square specimen led in starting parabolas from each corner, which caused a reduction in the effective confined area due to the arch effect. An increase in parabola height corresponds to in an increase in parabola length, as noted by Sneed et al. [69]. In the case of rounded corners, as the length of parabolas decreases due to its starting point, the arch effect is less remarkable and eventually the effective confined area increases.

Figure 121 shows the cut cross-section of specimen SQ-II-CE-MD-S-1L-1 (confined with 1 layer of MD SRP fiber sheet), specimen SQ-II-CE-MD-S-3L-1 (confined with 3 layers of MD SRP fiber sheet), specimen SQ-I-CE-UHD-S-1L-3 (confined with HD SRP fiber sheet), and specimen C-III-CE-UHD-1L-1 (with a circular cross-section). For each specimen, the height of the formed parabolas for each cross-section was measured, and its average height was determined. The specimens confined with 3 layers of MD SRP fiber sheet, has the largest average height of the parabolas. There is a correlation between the profile of the parabola and the compressive strength of the confined specimens. Accordingly, higher values of the compressive strength for confined specimens are related to larger average height of the parabolas in the cross-section areas.

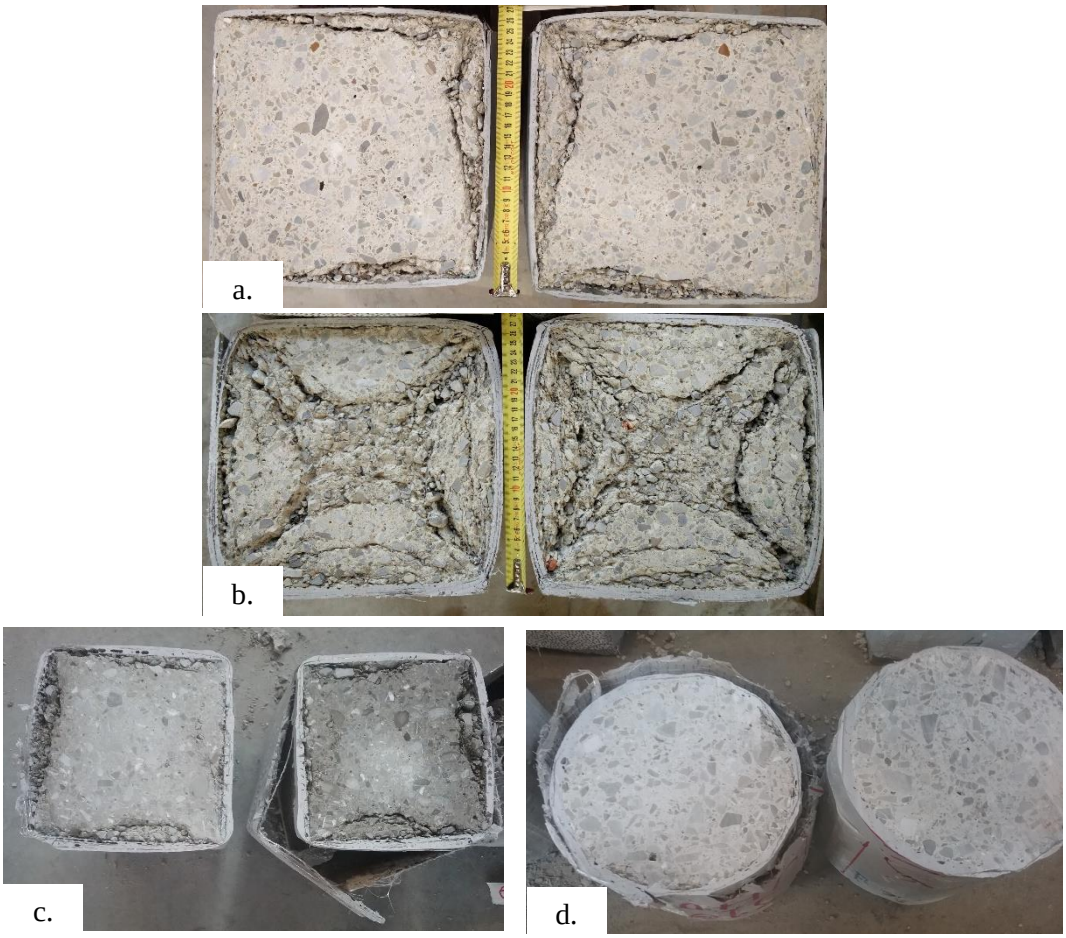

Figure 121. Photos of cut cross-sections after failure: a) SQ-II-CE-MD-S-1L-1; b) SQ-II-CE-MD-S-3L-1; c) SQ-I-CE-UHD-S-1L-3; d) C-III-CE-UHD-1L-1.

5.1.5.Conclusions

Results of monotonic compressive tests conducted on concrete members confined with SRP composites were presented in this section. The following conclusions can be drawn:

- Specimens of different sizes with the same SRP jacket showed a significant size effect. High failure stresses were observed in small columns with respect to large columns.
- The geometric shape influenced the compressive strength of confined specimens, while there is a not noticeable shape effect on the ultimate axial strain of SRP confined specimens.
- Increases in fiber density were not proportional to increases in confined compressive strength.
- The use of three layers of steel fibers provides a significant increase of the energy absorption.

5.2. Confinement of concrete columns with SRG systems

In this section the behavior of concrete compressive members confined by steel reinforced grout (SRG) is investigated. An experimental study was carried out to understand the behavior of short concrete prisms with a square cross-section confined by SRG subjected to a monotonic concentric compressive load. Test parameters considered in this study are the density of steel fibers, number of layers, corner condition, number of overlapping faces, and length of the reinforcement. The effectiveness of the confinement is evaluated in terms of peak stress with respect to unconfined prisms.

5.2.1. Introduction

The use of innovative strengthening techniques for existing concrete structures has gained attention in the last decades. The more stringent code requirements, designed with the primary aim of preserving existing buildings against natural hazards, such as earthquakes, entail that beams and columns must be strengthened in order to satisfy the beam-column hierarchical relationship in a frame subjected to seismic loadings. Among the new strengthening techniques, steel reinforced polymer (SRP) composite and steel reinforced grout (SRG) composites became appealing strengthening materials since they provided the advantages of traditional FRP systems employing low cost steel fibers. The available literature is mainly focused on the study of SRP composites (see section 5.1.1). The relatively fewer studies on SRG composites indicate that they can be used to increase the flexural [71] [70] and shear [205] capacity of RC members or to enhance the ultimate strength and deformability of concrete columns through external jacketing [206] [207]. The studies related to the SRG technique have been mainly focused on the bond behavior of SRG-concrete joints [115].

5.2.2. Experimental program

All concrete columns of this experimental program were cast from the same batch of concrete, i.e. "Concrete – Type A" (see section 3.1.1). The SRG composite consisted in MD or HD steel fibers (described in section 3.3.1) embedded in a cement-based mortar matrix (described in section 3.3.4.2). The property of the composite strip are described in section 3.3.7.

The experimental program included 22 concrete prisms tested under a concentric compressive loading condition. All prisms had a square cross-section. Seventeen concrete prisms were confined with SRG, while five were left unconfined and used as control specimens. The nominal dimensions of prisms were width (b) = 150 mm × depth (h) = 150 mm × length (L) = 450 mm, with an aspect ratio of approximately 3. All prisms were axially unreinforced, i.e., no internal reinforcement was provided since jacket-internal reinforcement interaction was outside the scope of this study. The 17 confined specimens were classified in seven groups. Specimens from the same group were characterized by same parameters. Specimens

were named following the notation SQ-X-A-B-C-W-Y-Z, where SQ indicates a square cross-section, X indicates the confined length (h_c) in mm, i.e. the portion of the prism length wrapped with composite material, A indicates the fiber density (MD = medium density, HD = high density), B indicates the composite matrix (UC = unconfined, CM = confined with mortar-based matrix), C indicates the concrete corner condition (R = rounded to a radius r = 17.5 mm, S = sharp), W indicates the number of overlapping faces (1F = 1 face, 2F = 2 faces), Y indicates the number of confinement layers (1L or 2L), and Z = specimen number. The unconfined specimens were named following the notation SQ-B-C-Z with the parameters B, C, D, and Z defined above. The details of the specimens and test parameters are summarized in Table 27.

Table 27. Test Specimen Characteristics

Specimen			Jacket Length	Fiber Density	Corner		Instrumentation	
Group		Name	[mm]		Edge Type	Radius [mm]	LVDT-a and LVDT-b	LVDT-c and LVDT-d
Control		SQ-UC-S-1	-	-	Sharp	0	✓	×
		SQ-UC-S-2	-	-	Sharp	0	✓	×
		SQ-UC-S-3	-	-	Sharp	0	✓	×
		SQ-UC-S-4	-	-	Sharp	0	✓	×
		SQ-UC-S-5	-	-	Sharp	0	✓	×
SRG-Confined	Group 1	SQ-450-HD-CM-S-1F-1L-1	450	High Density	Sharp	0	✓	✓
		SQ-450-HD-CM-S-1F-1L-2	450	High Density	Sharp	0	✓	×
		SQ-450-HD-CM-S-1F-1L-3	450	High Density	Sharp	0	✓	✓
	Group 2	SQ-450-HD-CM-R-1F-1L-1	450	High Density	Rounded	17.5	✓	✓
		SQ-450-HD-CM-R-1F-1L-2	450	High Density	Rounded	17.5	✓	×
	Group 3	SQ-450-HD-CM-R-2F-1L-1	450	High Density	Rounded	17.5	✓	✓
		SQ-450-HD-CM-R-2F-1L-2	450	High Density	Rounded	17.5	✓	×
	Group 4	SQ-450-MD-CM-S-2F-1L-1	450	Medium Density	Sharp	0	✓	✓
		SQ-450-MD-CM-S-2F-1L-2	450	Medium Density	Sharp	0	✓	✓
		SQ-450-MD-CM-S-2F-1L-3	450	Medium Density	Sharp	0	✓	✓
	Group 5	SQ-450-HD-CM-S-2F-1L-1	450	High Density	Sharp	0	✓	✓
		SQ-450-HD-CM-S-2F-1L-2	450	High Density	Sharp	0	✓	✓
	Group 6	SQ-440-MD-CM-S-2F-1L-1	440	Medium Density	Sharp	0	✓	×
		SQ-440-MD-CM-S-2F-1L-2	440	Medium Density	Sharp	0	✓	✓
	Group 7	SQ-450-MD-CM-S-2F-2L-1	450	Medium Density	Sharp	0	✓	✓
		SQ-450-MD-CM-S-2F-2L-2	450	Medium Density	Sharp	0	✓	✓
		SQ-450-MD-CM-S-2F-2L-3	450	Medium Density	Sharp	0	✓	×

The confined prisms were wrapped following the manufacturer's recommendations [6]. All confined specimens were sandblasted prior to applying the SRG jacket. The SRG was applied using a wet layup process (Figure 122). Steel fiber sheets, with fibers oriented perpendicular to the longitudinal axis of the prism, were wrapped around the specimens. Since the width of the fiber sheet was not the same as the length of the columns, the columns were wrapped with several segments of the fiber sheet with no overlap of the different segments along the columns length. The steel fiber sheets were pre-bent in order to conform to the surface. An overlap length of 150 mm or 300 mm, corresponding to the width of one or two prism faces, respectively, was provided for specimens depending on the specimen group. Confined concrete prisms were kept in the laboratory and cured at ambient conditions for 28 days after the application of the SRG composite. Prior to testing, both ends of each prism were capped with an 8 mm thick layer of high strength mortar to ensure that the ends were flat and parallel to one another.

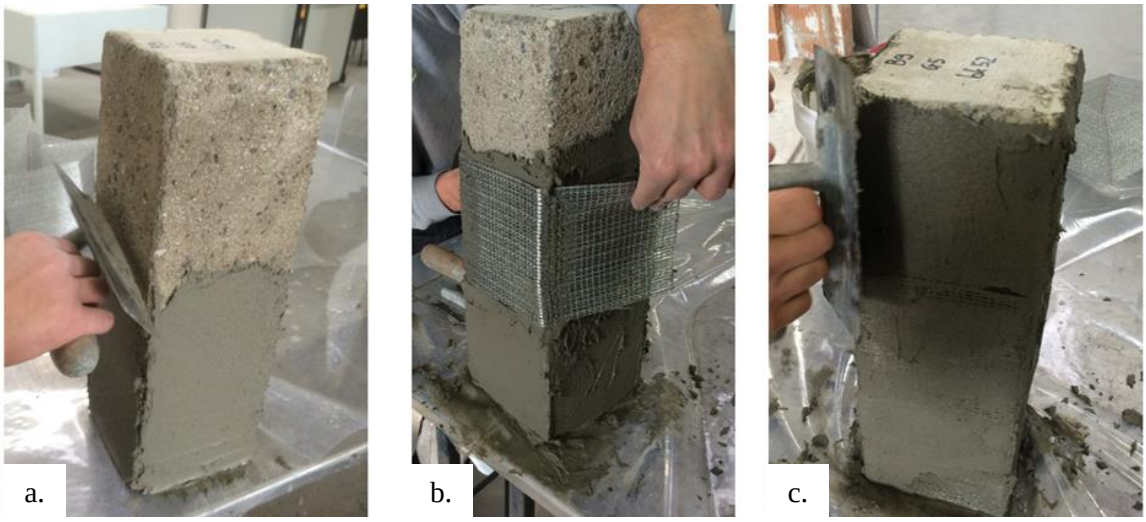

Figure 122. Specimen preparation: a) application of matrix to concrete surface; b) application of steel fiber sheet around the prism; c) application of external layer of matrix.

Concrete prisms were tested using a 4000 kN capacity compression testing machine. Prisms were tested under monotonically increasing displacement until failure. The distance between the two pressing plates was measured using two linear variable displacement transducers (LVDT), named LVDT-a and LVDT-b, mounted between the pressing plates at opposite corners (Figure 123). The displacement rate, determined by average value of the two LVDTs, was maintained at 0.2 mm/min by continuously monitoring and controlling the machine stroke. Testing was completed when a significant drop in load occurred in the post-peak response. Axial strains were calculated from the LVDT measurements from LVDT-a and LVDT-b. Some specimens also included two additional LVDTs mounted directly to the specimen with bolts drilled into the concrete core (LVDT-c and LVDT-d in Figure 123b). LVDT-c and LVDT-d were oriented in the axial direction of the specimen and were located in the central third of the

specimen length on opposite sides. Readings of applied load and displacement were acquired with a data acquisition system and stored on a personal computer.

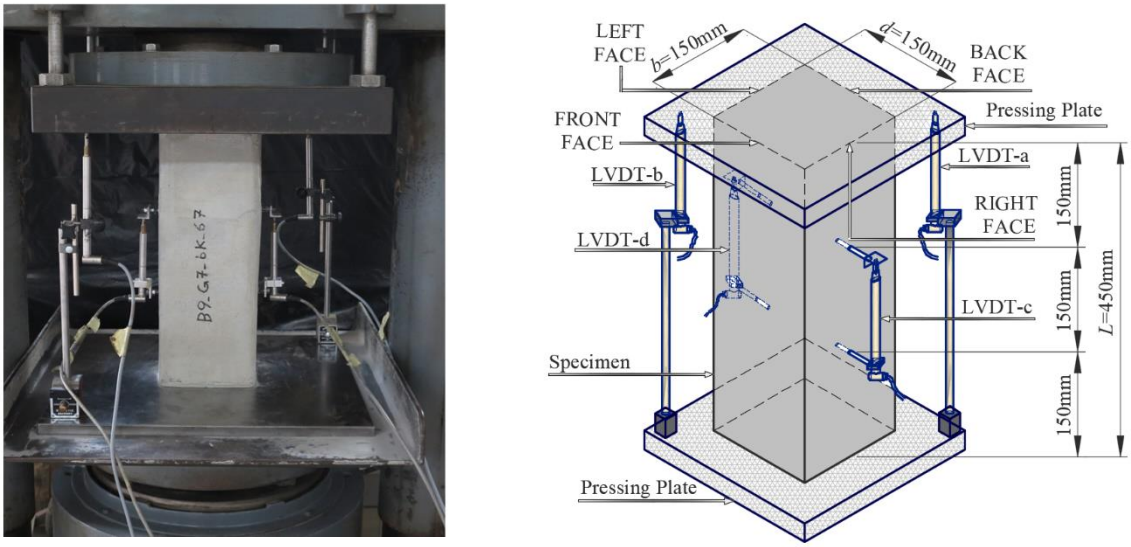

a. b.

Figure 123. a) Photo of specimen; b) Test set-up.

5.2.3. Experimental results

The peak load of all unconfined and confined specimens was associated with crushing of concrete. After the peak load was reached, the confined specimens continued to deform under decreasing applied load until failure occurred by separation of the SRG jacket at the vertical lap joint. For all confined specimens, failure initiated with the detachment of the SRG jacket with transverse cracks (parallel to the fiber direction) that extended from the failed face to other faces of the specimen. Some of the transverse cracks were consistent with the locations where different steel fiber sheet segments abutted one another. Detachment of the overlapping layer of the jacket usually occurred along a limited portion of the specimen length, and in few cases occurred for the entire length of the specimen. Failure started in the layer of mortar in between the two overlapping layers of fibers, and usually only the external layer tended to open, while the internal layer remained attached to the prism surface. Photographs of a representative specimen at failure are shown in Figure 124.

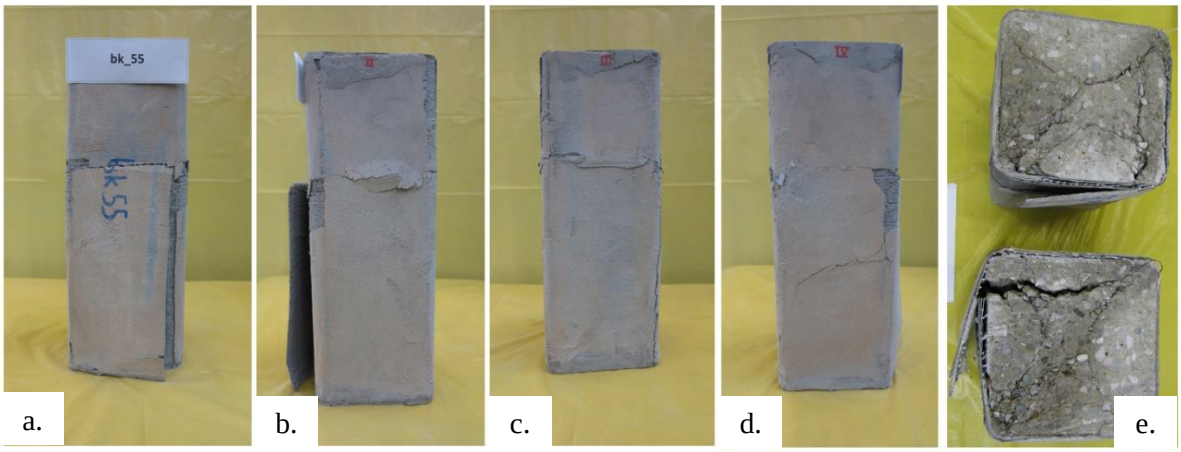

Figure 124. Failure mode of steel-FRCM confined specimen (specimen SQ-450-HD-CM-R-1F-1L-2 shown): a) front face; b) right face; c) back face; d) left face; e) cut section.

After testing, the conditions of the concrete core and jacket were documented. Crushed concrete was observed near the side surfaces of each specimen. Each specimen was sawcut near the midlength to observe the condition of the concrete cross-section. A representative cut section is shown in Figure 124e. Table 28 summarizes the key experimental results obtained for each test specimen. Values provided for the unconfined specimens include the unconfined compressive strength (peak stress) f'_{co} and the unconfined ultimate compressive stress $f'_{co,u}$. Values provided for the confined specimens include the confined compressive strength (peak stress) f'_{cc} and the confined ultimate compressive stress $f'_{cc,u}$. Values of the ultimate stress correspond to the stress at which a significant drop in load occurred in the post-peak load response and are associated with specimen failure. Values of stress were determined by dividing the force by the cross-sectional area of the prism (22,500 mm^2 and 22,237 mm^2 for specimens with sharp and rounded corners, respectively).

The axial stress – axial strain responses of one representative specimen from each group of the confined prisms are plotted in Figure 125. The response of all unconfined specimens is provided for comparison. It should be noted that values of strain were determined by dividing the average of displacement readings from LVDT-a and LVDT-b by the initial distance between the pressing plates. Accordingly, the values of strain determined in this manner are considered to be *global* strain. It was observed that, for most specimens, the individual readings of LVDT-a, LVDT-b, LVDT-c, and LVDT-d were consistent until the peak load was reached. After the peak was reached, the measurements obtained from LVDT-a and LVDT-b continued to be consistent with each other, while different values were registered by LVDT-c and LVDT-d with respect to each other and to LVDT-a and LVDT-b. This difference in the readings by LVDT-c and LVDT-d was mainly due to localized effects at the location of LVDT-c and LVDT-d after the peak load was achieved. Therefore, only the readings obtained from LVDT-a and LVDT-b were

considered. The general behavior of the SRG confined specimens in Figure 125 can be described as having an initial linear response that follows the unconfined behavior. After the unconfined strength is reached, the response of the confined specimens becomes non-linear, and the axial stress continues to increase until the peak stress is reached. Then, all specimens show a descending response until failure occurs with a drop in the axial stress, where failure is associated with jacket opening.

Table 28. Summary of Test Results.

Specimen			f'_{co} or f'_{cc}	$f'_{co,u}$ or f'_{ccu}	$\frac{f'_{cc}}{f'_{co}}$	Average (CoV)	$\frac{A_{tot}}{A_{peak}}$	Average (CoV)
Group		Name	[MPa]	[MPa]				
Control		SQ-UC-S-1	28.9	13.6	-	-	-	-
		SQ-UC-S-2	24.1	19.1	-		-	
		SQ-UC-S-3	27.6	21.0	-		-	
		SQ-UC-S-4	25.8	20.5	-		-	
		SQ-UC-S-5	23.4	21.0	-		-	
SRG Confined	Group 1	SQ-450-HD-CM-S-1F-1L-1	30.0	16.3	1.16	1.20 (0.060)	2.56	2.01
		SQ-450-HD-CM-S-1F-1L-2	33.3	22.7	1.28		1.81	
		SQ-450-HD-CM-S-1F-1L-3	30.1	28	1.16		1.65	
	Group 2	SQ-450-HD-CM-R-1F-1L-1	29.7	28.8	1.14	1.16 (0.014)	1.38	1.58
		SQ-450-HD-CM-R-1F-1L-2	30.3	17.1	1.17		1.78	
	Group 3	SQ-450-HD-CM-R-2F-1L-1	35.5	10	1.37	1.34 (0.035)	1.96	2.22
		SQ-450-HD-CM-R-2F-1L-2	33.8	24.6	1.30		2.48	
	Group 4	SQ-450-MD-CM-S-2F-1L-1	33.5	25	1.29	1.29 (0.027)	2.39	3.96
		SQ-450-MD-CM-S-2F-1L-2	32.5	13.5	1.25		7.53	
		SQ-450-MD-CM-S-2F-1L-3	34.3	24.7	1.32		1.95	
	Group 5	SQ-450-HD-CM-S-2F-1L-1	37.1	30	1.43	1.44 (0.009)	2.18	1.89
		SQ-450-HD-CM-S-2F-1L-2	37.6	31.4	1.45		1.59	
	Group 6	SQ-440-MD-CM-S-2F-1L-1	30.8	20.1	1.19	1.16 (0.033)	3.67	3.84
		SQ-440-MD-CM-S-2F-1L-2	29.4	18.4	1.13		4.02	
	Group 7	SQ-450-MD-CM-S-2F-2L-1	37.2	25	1.43	1.45 (0.012)	4.56	4.87
		SQ-450-MD-CM-S-2F-2L-2	38	21	1.46		4.55	
		SQ-450-MD-CM-S-2F-2L-3	37.9	25	1.46		5.49	

The influence of corner condition is examined by comparing the results of specimens in Groups 1 and 2. Results in Table 28 indicate that specimens with sharp corners (Group 1) had an average compressive strength slightly higher (4%) than those with corners rounded to a radius of 17.5 mm (Group 2). Due to the limited number of tests, additional research is needed to establish a general trend.

The influence of overlapping faces is examined by comparing the results of specimens in Groups 2 and 3, with one and two overlapping faces, respectively. Average values of compressive strength for Group 3 are 16% higher than those of Group 2, which indicates that the number of overlapping faces influenced the compressive strength.

The influence of fiber density is examined by comparing the results of Groups 4 and 5, with medium and high density fibers, respectively. Specimens reinforced with high density fibers (Group 5) had an average compressive strength 12% higher than specimens reinforced with medium density fibers (Group 4).

The influence of the jacket length is examined by comparing specimens in Group 4 and 6. Specimens in Group 4 had an average compressive strength 11% higher than those in Group 6.

The influence of the number of jacket layers is examined by comparing the results of specimens in Group 4 and 7, with one and two layers of medium density fibers, respectively. Specimens in Group 7 had an average compressive strength 13% higher than those in Group 4. These results suggest that increasing the number of jackets layers increased the axial strength; however, the increase in axial strength was not proportional to the number of jackets layers.

The maximum increase in the compressive strength was observed for specimens of Group 7 (Table 28 and Figure 125), with two layers of medium density fibers and two overlapping faces, which exhibited an average compressive strength 45% higher than the control specimens. Similarly, Group 5, with one layer high of density fibers and two overlapping layers, exhibited an average compressive strength of 44% higher than the control specimens. Similar increases in the maximum compressive strength with respect to control specimens were found by Thermou et al. [207] who tested concrete prisms in compression (aspect ratio equal to 4) confined with ultra-low density steel fibers (1 cord/cm) with three faces of overlapping.

As mentioned in the previous section, failure of the confined prisms consisted of the opening of the SRG jacket, which started on the overlapping face(s). Since the failure mode was the same for all confined specimens, it is possible to compare the influence of the different parameters by evaluating the energy absorption, i.e. the area under the axial stress – axial strain curve (e.g., Figure 125). For each confined specimen, Table 28 tabulates the value of the ratio $\frac{A_{tot}}{A_{peak}}$, where A_{tot} is the area under the stress-strain response up to the ultimate strain and corresponding stress, and A_{peak} is the area under the stress-strain response up to the peak stress and corresponding strain. Average values of the ratio $\frac{A_{tot}}{A_{peak}}$ for each group are also summarized in Table 28.

Specimens of Groups 1, 2, 3, 4, and 5 have similar values of the ratio $\frac{A_{tot}}{A_{peak}}$, ranging from 1.38 to 2.56, with the exception of specimen SQ-450-MD-CM-S-2F-1L-2, which had a value of the ratio $\frac{A_{tot}}{A_{peak}}$ (7.56) that was significantly larger than other specimens of the same group; therefore it was not considered representative of Group 4 specimens. Specimens of Group 6 (confined length equal to 440 mm) and Group 7 (two layers of composite and two overlapping faces) showed the best performance in terms of energy absorption, with an average ratio of $\frac{A_{tot}}{A_{peak}}$ equal to 3.84 and 4.87, respectively. For specimens of Group 6, large values of the ratio $\frac{A_{tot}}{A_{peak}}$ are due to the additional deformability of the unconfined regions at the specimen ends, whereas the large values of the ratio $\frac{A_{tot}}{A_{peak}}$ for specimens of Group 7 are mainly due to the increase in the composite stiffness. Therefore, it can be concluded that the use of two layers of SRG composite, instead of one, had a significant effect on the energy absorption.

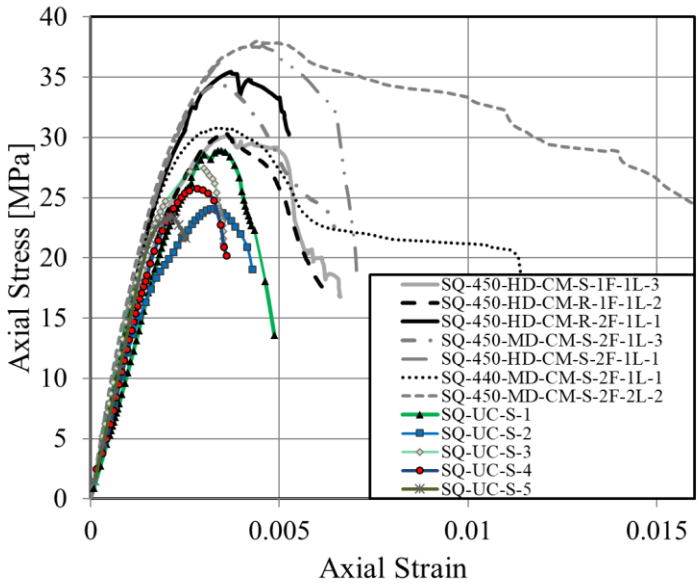

Figure 125. Axial stress – axial strain response for representative confined specimens and control specimens.

5.2.4. Conclusions

In this section, an experimental study aimed to investigate the effectiveness of SRG as a confinement technique is presented. Concrete prisms were wrapped with SRG composite, and parameters investigated were the corner condition, fiber density, length of the overlap, length of the confinement, and number of layers of confinement. The following conclusions can be drawn:

- The limited results available indicate that sharp corners are not detrimental for SRG confinement;
- Specimens reinforced with high density fibers had slightly higher compressive strength than specimens reinforced with medium density fibers;
- The length of the overlap affects the effectiveness of the SRG confinement;
- An increase of the confined strength is associated with an increase of the number of layer of confinement. However, the increase in axial strength is not proportional to the number of jackets layers;
- The use of two layers of steel fibers provides a significant increase of the energy absorption.

6. Bond between Basalt-fiber reinforced cementitious matrix (B-FRCM) and a masonry substrate

This chapter presents an investigation of the bond between Basalt-fiber reinforced cementitious matrix (B-FRCM) material and a masonry substrate. The first section is focused on the study of the debonding phenomenon through single-lap shear tests. The second section analyzed the behavior of large-scale masonry columns wrapped with B-FRCM composites. The last section investigated a B-FRCM application on existing masonry arches.

6.1. Direct single-lap shear tests on B-FRCM-masonry joints

6.1.1. Experimental program

In this section the bond performances of B-FRCM composite materials bonded to a masonry substrate are investigated through single-lap shear tests. All masonry blocks of this experimental program were constructed with the bricks and the mortar characterized in section 3.2. The B-FRCM composite consisted in low-density basalt (LDB) fibers and high-density basalt (HDB) fibers (described in section 3.3.2) embedded in a lime-based mortar matrix (described in section 3.3.4.1).

Five B-FRCM-joints were tested using a single-lap shear test set-up. The parameter investigated was the density of the basalt fibers. Out of five specimens, two were tested with LDB fibers (Figure 126a), while three were tested with HDB fibers (Figure 126b). B-FRGM-masonry joints were cast using the same procedure described in section 4.2.1.2 for SRG-masonry joints. All masonry blocks have the same nominal dimensions equal to 120 mm × 120 mm × 380 mm. The bonded width and bonded length were equal to 50 mm and 300 mm, respectively. Specimens were tested using a single-lap shear test set-up described in section 4.2.1.2. Tests were performed increasing the global slip g at a constant rate equal to 0.00084 mm/s.

Specimens were named following the notation DS_X_Y _A_B_Z, where X = bonded length (ℓ) in mm; Y = bonded width (b_f) in mm; A represents the steel fiber density (LDB = low density basalt, HDB = high density basalt); B indicates the type of matrix (LM = lime-based mortar); and Z = specimen number (Table 29).

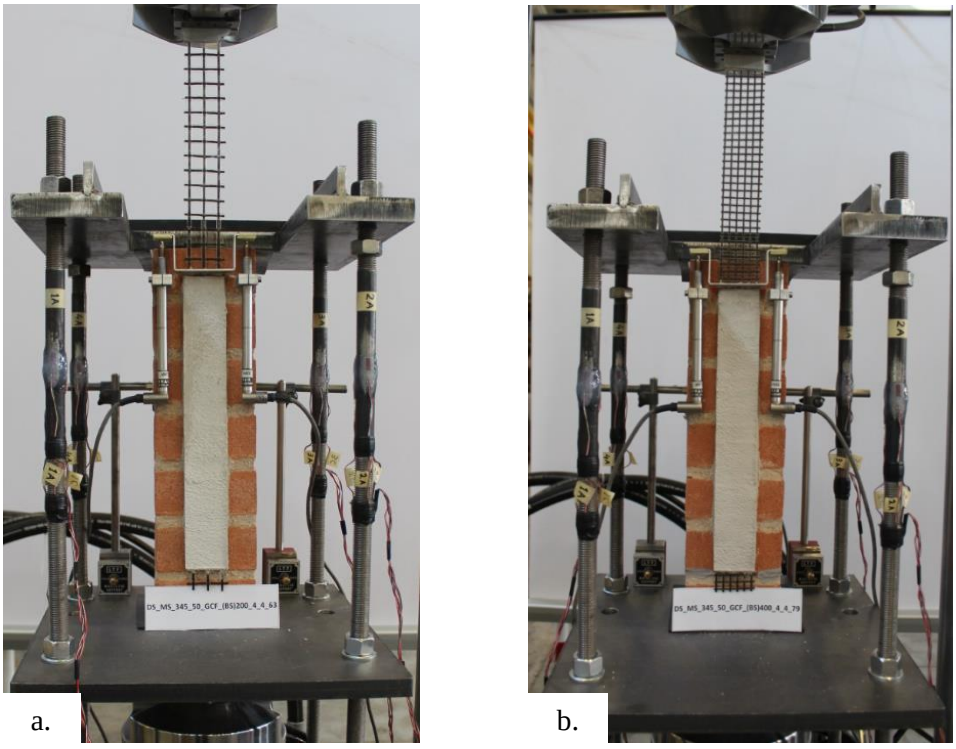

a. b.

Figure 126. Single-lap shear test set-up: specimen DS_345_50_LDB_LM_1 (a) and specimen DS_345_50_HDB_LM_1 (b).

6.1.2. Experimental results

Figure 127 shows the load-global slip response of specimens DS_345_50_LDB_LM_1 and DS_345_50_HDB_LM_1. The blue and the red curves refer to the measurements of LVDT a and LVDT b mounted on the front face of the masonry block. The green curve is the average of the two readings, which has been named global slip. The displacement of the masonry block perpendicular to the face of the B-FRCM strip is measured by LVDT c (displacement w_c, light blue curve) and LVDT d (displacement w_d, violet curve). It should be noted that the displacements recorded by LVDT c and LVDT d are consistent, which implies that twisting of the masonry block did not occur during the test. The load response of specimens strengthened with LDB fibers is characterized by an initial linear portion followed by a non-linear branch until the peak load, P^*, was reached. After the peak load was reached, some fibers broke, causing large drops in the load responses. The test finished when the last fiber of the B-FRCM composite broke. Fibers usually broke close to the beginning of the bonded region or close to the epoxy tabs gripped by the wedges of the testing machine Figure 128a. The load response of specimens strengthened with HDB fibers is characterized by an initial linear portion, followed by a non-linear branch until a peak was reached. After the peak a drop in the load response was observed, which corresponded to the delamination close to the loaded end of the bonded region. Delamination occurred at the matrix-

fiber interface (Figure 128b-c). After the first portion of the B-FRCM composite detached, the load response showed a second increasing branch, followed by a second drop that correspond to the detachment of the second portion of the reinforcement on the middle region of the bonded area. Finally, the load response showed a third increasing branch that ended when the last portion of the reinforcement completely detached and the specimen failed.

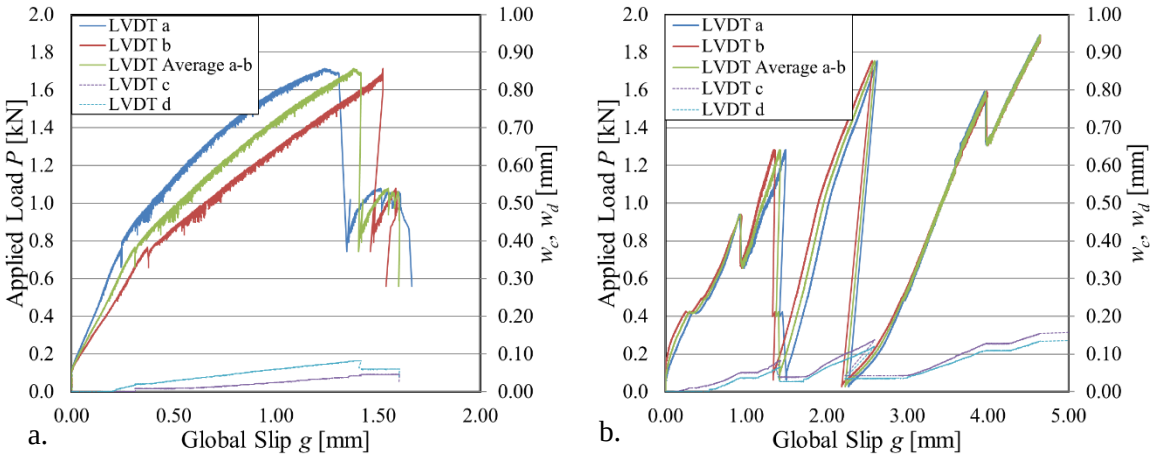

Figure 127. Load-global slip response for specimen DS_345_50_LDB_LM_1 (a) and for specimen DS_345_50_HDB_LM_1 (b).

Table 29. Test results of single-lap direct shear tests

Specimen Name	Bonded length [mm]	Bonded width [mm]	Fiber density	P^* [kN]	g_u [mm]	Failure mode
DS_345_50_LDB_LM_1	345	50	LDB	1.71	1.60	FR
DS_345_50_LDB_LM_2	345	50	LDB	1.74	1.75	FR
DS_345_50_HDB_LM_1	345	50	HDB	1.89	4.65	MF
DS_345_50_HDB_LM_2	345	50	HDB	1.96	3.46	MF
DS_345_50_HDB_LM_3	345	50	HDB	1.82	3.90	MF

Specimens strengthened with LDB fibers show a failure mode that consisted in the rupture of the fibers (FR) (Figure 128a). Specimens DS_345_50_LDB_LM_1 and DS_345_50_LDB_LM_2 reached a maximum tensile stress in the fibers equal to 1070 MPa and 1090 MPa, respectively, which is lower than the tensile strength provided by the manufacturer [6] and reported in section 3.3.2. Stress concentration might have occurred as observed by other researchers with glass fibers [164]. Specimens strengthened with HDB fibers failed at the fiber-matrix interface and the debonding mechanism consisted in the

detachment of the top (external) mortar layer of composite from the internal layer (FIGURE). This type of rupture differs from the one obtained for LDB specimens and it is mainly due to the reduced area of mortar matrix in between the fiber bundles.

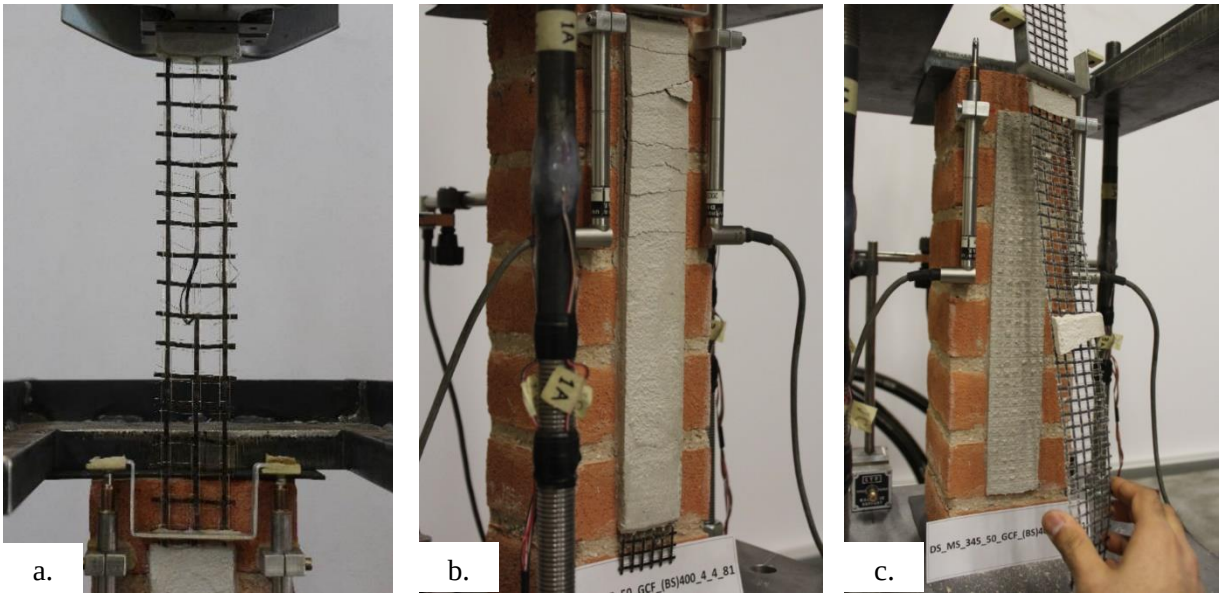

Figure 128. a) Rupture of the fibers (FR) for specimen DS_345_50_LDB_LM_1, b) debonding process during test for specimen DS_345_50_HDB_LM_3, c) delamination (MF) at the fiber-matrix interface for specimen DS_345_50_HDB_LM_3.

6.1.1. Conclusions

Results of single-lap shear tests conducted on specimens with B-FRCM composite strips bonded to masonry blocks were presented in this section. Two types of fibers were employed, i.e. LDB fibers and HDB fibers, together with a lime-based mortar matrix. Failure of B-FRCM masonry joints with LDB fibers consisted in the rupture of the fibers (RF) while HDB specimens exhibited the detachment (delamination) of the external layer of matrix from the internal one (MF). The maximum tensile stress reached by LDB fibers was lower than the tensile strength provided by the manufacturer [6]. This fact is probably due to the not uniform distribution of the stresses among the LDB fibers.

6.2. Confinement of masonry columns with B-FRCM composites

In this section, the behavior of masonry columns confined with B-FRCM composites is investigated. Columns with a square-cross section confined with B-FRCM composite jacket were subjected to a monotonic concentric compressive load. The effectiveness of the confinement is studied in terms of load-bearing capacity with respect to unconfined columns. The effect of corner radius for columns confined with basalt fibers is investigated.

6.2.1. Experimental program

All masonry columns of this experimental program were constructed with the bricks and the mortar characterized in section 3.2. The B-FRCM composite consisted in low-density basalt (LDB) fibers (described in section 3.3.2) embedded in a lime-based mortar matrix (described in section 3.3.4.1).

The experimental program included sixteen masonry columns tested under a concentric compressive loading condition. Ten masonry columns were confined, while six were left unconfined and used as control columns. The nominal dimensions of the masonry columns were width (b) = 250 mm × depth (h) = 250 mm × length (L) = 770 mm, with an aspect ratio of approximately 3.1. Test parameter considered in this study was the masonry corner condition. Confined specimens were named following the designation C-X-Y-Z, where C indicates the specimen was confined; X indicates the type of fibers (LDB = low density basalt); Y denotes the masonry corner condition (R = rounded to a radius r = 20 mm, S = sharp); and Z indicates the specimen number. All confined specimens were wrapped with one layer of composite. Unconfined specimens were named following the designation UC- Z, where UC indicates the specimen was unconfined, and Z indicates the specimen number. Specimens are listed in Table 30.
All masonry columns had a thickness of the masonry joints equal to 10 mm. For all columns, bricks were arranged to obtain the alternate stretcher and header bond. For the confined specimens with rounded corners, the designated corner radius was achieved using a diamond grinding wheel. All confined columns were prewetted prior to install the composite jacket. The confined columns were wrapped following the manufacturer's recommendations. The B-FRCM composite was applied using a wet layup process (Figure 129). Basalt fibers were wrapped around the masonry columns using a single fiber sheet. No pre-bending was needed because basalt fibers easily conform to column edges. An overlap corresponding to the width of one column face was provided for all specimens, forming a vertical seam near the column corner. Masonry columns were kept in the laboratory under controlled temperature and humidity until they were tested. Prior to testing, both ends of each prism were capped with a 25 mm thick layer of high strength mortar (Figure 130) to ensure that the ends were flat and parallel. For five unconfined columns (UC-1, UC-2, UC-3, UC-4, UC-6) a square 300 mm × 300 mm steel plate was applied with a thin layer

of high strength mortar to both the square bases of the masonry column, to ensure flat and horizontal surfaces for the application of the load during test.

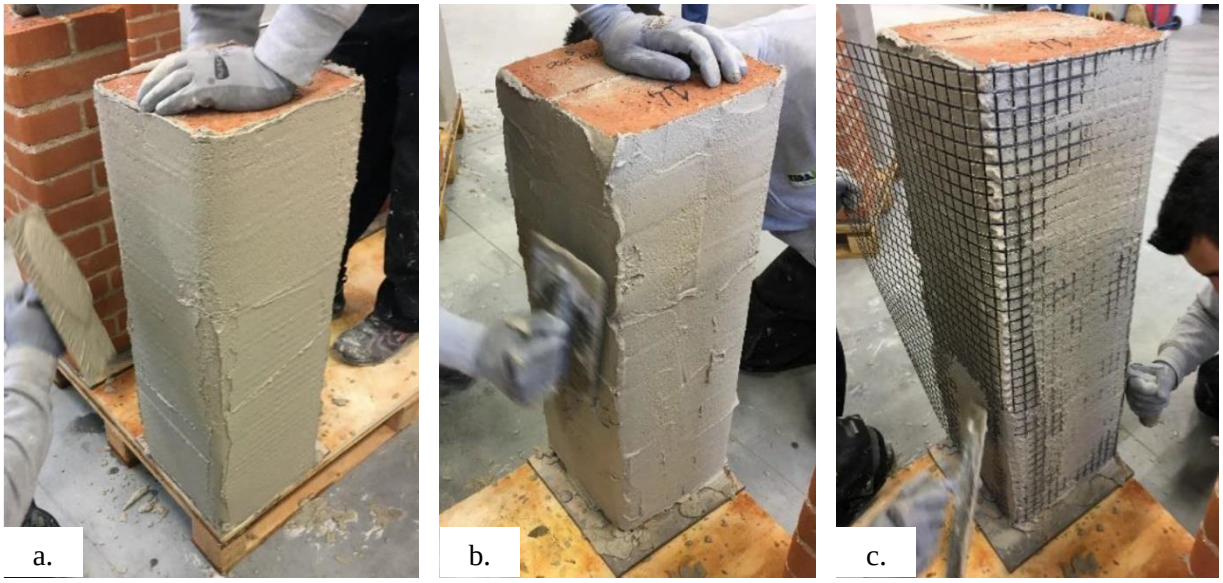

Figure 129. Application of the B-FRCM composite to a masonry column.

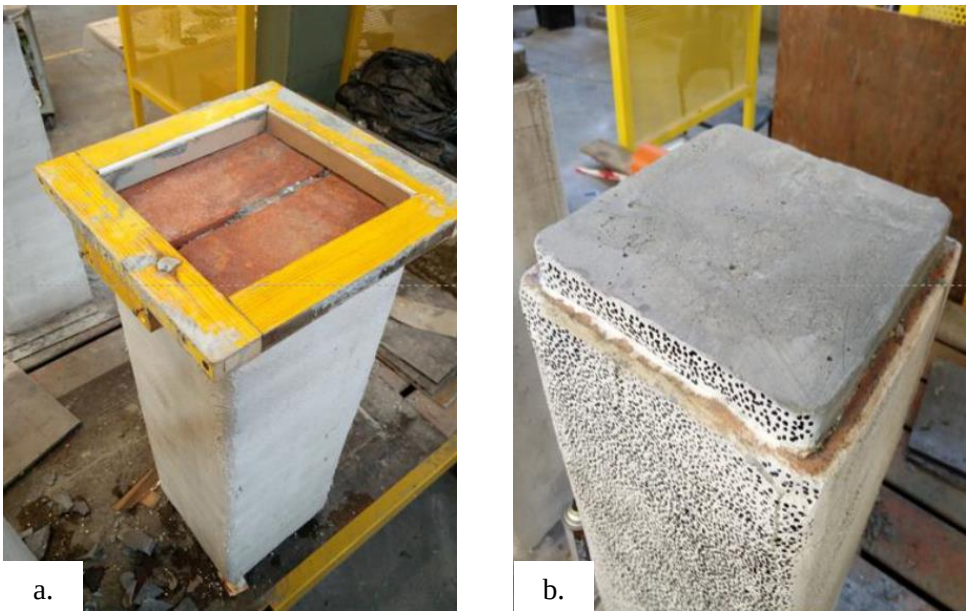

Figure 130. High strength mortar capping.

Masonry columns were tested using a 4000 kN capacity compression testing machine. The columns were tested under monotonically increasing displacement until failure. The distance between the two pressing plates was measured using two linear variable displacement transducers (LVDTs) mounted between the pressing plates at opposite corners. The displacement rate, determined by average value of the two LVDTs (named LVDT-a and LVDT-b), was maintained at 0.2 mm/min by continuously monitoring and

controlling the machine stroke. Testing was completed when a significant drop in load occurred in the post-peak response. Axial strains were calculated from the LVDT measurements. The test setup is shown in Figure 131.

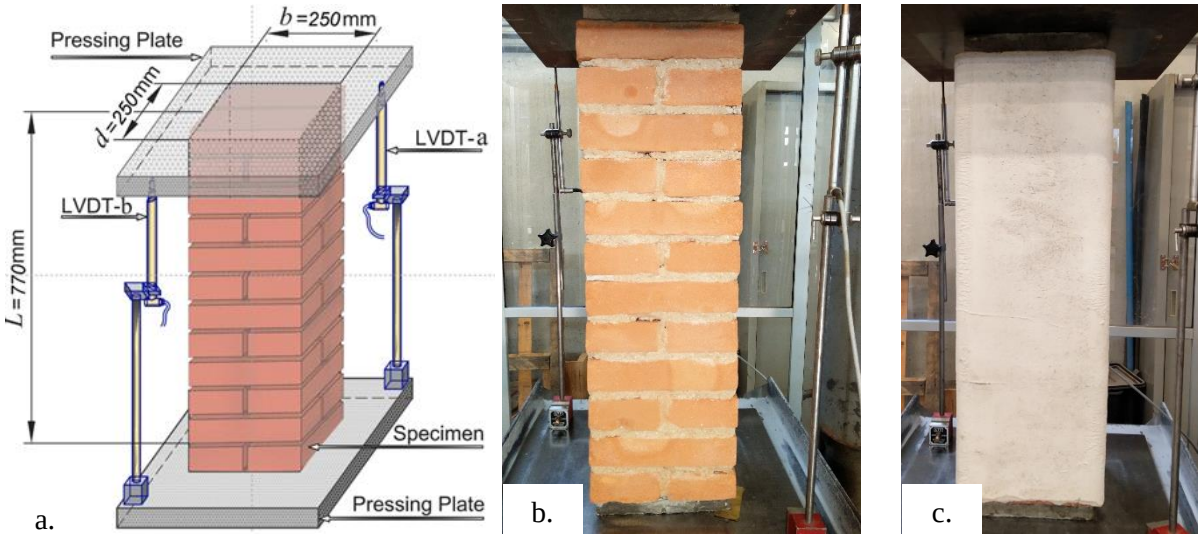

Figure 131. Test set-up: a) Sketch; b) Photo of unconfined specimen (UC-5); c) Photo of confined specimen (C-B-S-1).

6.2.2. Experimental results

The peak load of all unconfined and confined specimens was associated with crushing of the masonry (Figure 132). After the peak load was reached, the confined specimens continued to deform under decreasing applied load until failure occurred by detachment of the B-FRCM jacket. During the softening branch of the load response, longitudinal cracks were observed near the corners. The longitudinal cracks propagated for almost the entire length of the masonry columns and the formation of the cracks was always associated with the rupture of the basalt fibers close to the column corners. Specimens with sharp and rounded corners showed the same failure mode. Photograph of typical failed specimens are shown in Figure 133. After tests were completed, for some specimens it was possible to observe the masonry cores, which revealed that the masonry core was crushed while a thin layer of masonry was bonded to the inner layer of the jacket surface (Figure 133c).

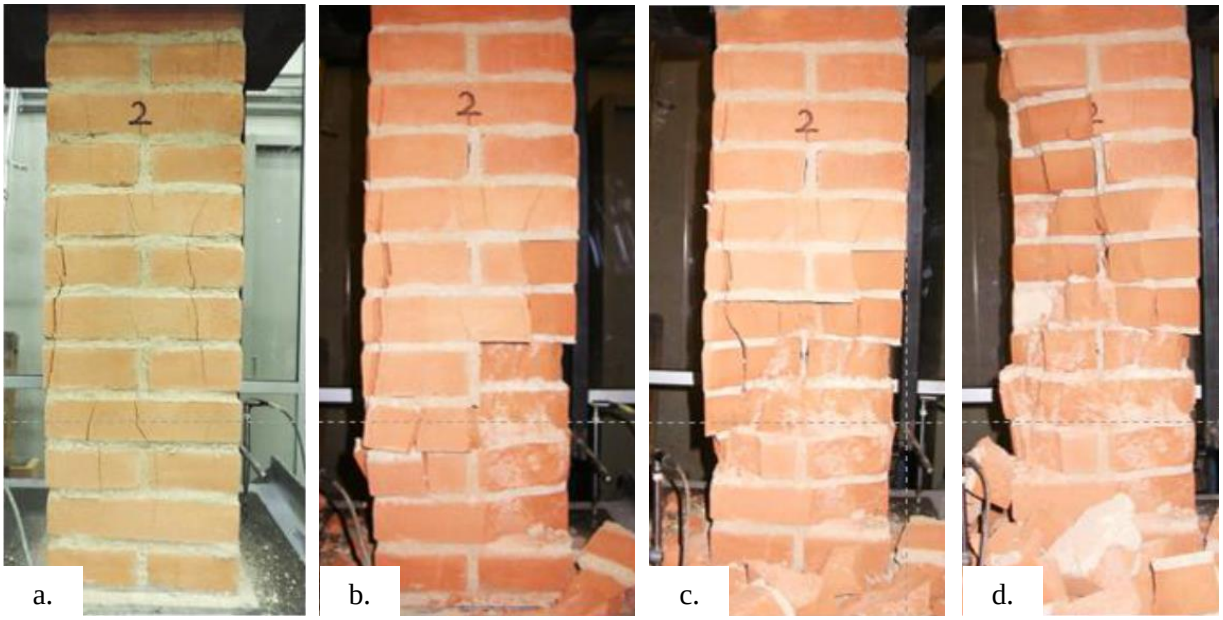

Figure 132. Failure mode of specimen UC-2.

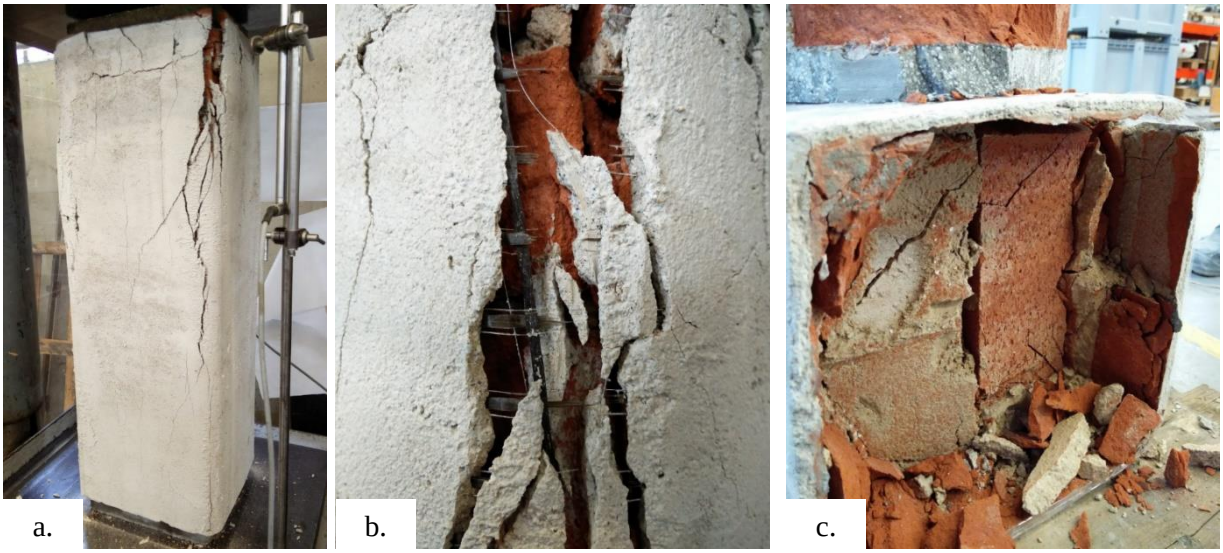

Figure 133. Failure mode of specimen C-LDB-S-5 (a,b) and crushing of the masonry core (c) for specimen C-LDB-R-5.

The peak stress of each specimen is provided in Table 30, where f'_{co} and f'_{cc} are the peak unconfined compressive strength and the peak confined compressive strength, respectively. Values of stress were determined by dividing the force by the cross-sectional area of the masonry column, and considering the corner condition. The control specimens had an average unconfined compressive strength $\overline{f'_{co}}$ of 4.9 MPa, while the confined specimens had an average confined compressive strength $\overline{f'_{cc}}$ ranging from 5.6

MPa to 5.7 MPa. Values of the ratio $\overline{f'_{cc}}/\overline{f'_{co}}$ are also reported for each group of confined specimens. Values of $\overline{f'_{cc}}/\overline{f'_{co}}$ range from 1.14 to 1.16.

Table 30. Summary of test results.

Group	Specimen	Type of steel fibers	Corner radius *r* [mm]	f'_{co} or f'_{cc} [MPa]	$\overline{f'_{cc}}$ $\overline{f'_{co}}$ or $\overline{f'_{cc}}$ (CoV)	$\overline{f'_{cc}}/\overline{f'_{co}}$
Control	UC-1	-	0	5.0	4.9 (0.04)	-
	UC-2	-	0	4.6		
	UC-3	-	0	4.9		
	UC-4	-	0	4.6		
	UC-5	-	0	5.1		
	UC-6	-	0	5.0		
1	C-LDB-R-1	Basalt	20	6.7	5.6 (0.18)	1.14
	C-LDB-R-2	Basalt	20	6.4		
	C-LDB-R-3	Basalt	20	5.6		
	C-LDB-R-4	Basalt	20	4.3		
	C-LDB-R-5	Basalt	20	4.8		
2	C-LDB-S-1	Basalt	0	6.7	5.7 (0.16)	1.16
	C-LDB-S-2	Basalt	0	4.9		
	C-LDB-S-3	Basalt	0	4.9		
	C-LDB-S-4	Basalt	0	5.4		
	C-LDB-S-5	Basalt	0	6.8		

Results showed that basalt fibers provided a slight increase (14% - 16%) of the average compressive strength with respect to control specimens. It should be highlighted that almost half of the specimens confined with basalt fibers had a compressive strength (f'_{cc}) that was equal or lower than the average value obtained from control specimens. Therefore, the observed increase in the average compressive strength of specimens confined with basalt fibers could be simply due to better mechanical properties of some masonry columns and not to an actual benefit due to confinement. The rupture of the basalt fibers along the corners of the masonry columns (both rounded and sharp) is mainly due to the brittle nature of this type of fibers and their relatively low tensile strength.

Axial stress – axial strain responses of specimens confined with basalt fibers are plotted in Figure 134. The unconfined (control) specimens are also plotted in each graph for comparison. The general behavior of the confined columns can be described as having an initial linear response. After the unconfined strength is reached, the response becomes non-linear, and the axial stress continues to increase, although

the increase is small, until the peak stress is reached. After the peak stress, a descending response is observed until failure occurs with a sudden drop in the axial stress. The descending response is very similar to the response of unconfined specimens. It is interesting to note that the presence of a steel plate or a thick capping layer did not change the behavior of the unconfined columns, although the initial stiffness is affected by the presence of the capping layer because LVDTs reacted off of the machine platens.

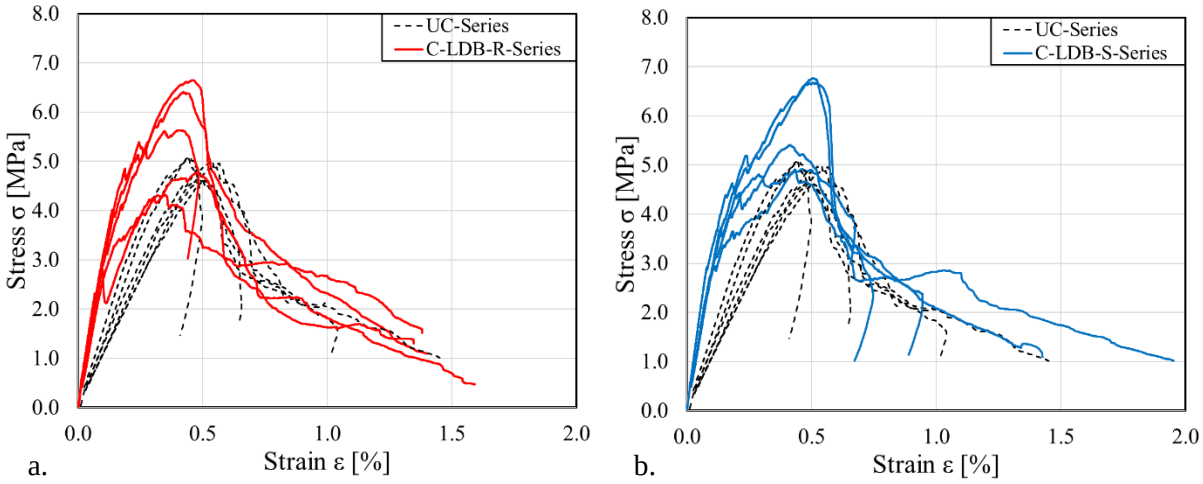

Figure 134. Axial stress vs. axial strain response of LDB specimens with rounded corners (a) and with sharp corners (b) together with control specimens (black dashed line).

6.2.3. Conclusions

This section presented the results of an experimental study carried out to understand the behavior of masonry columns with a square cross-section confined by B-FRCM composite subjected to a monotonic concentric compressive load. Test parameter considered in this study is the corner condition. The following conclusions can be drawn from the results:

- B-FRCM jackets seems to provide a slight increase (14-16%) of the average compressive strength with respect to control specimens;
- The low increase of the average compressive strength for specimens strengthened with LDB fibers with respect to the unconfined specimens is mainly due to the brittle nature and relatively low tensile strength of the basalt fibers that tend to rupture near the corners of the columns.

6.3. Destructive in-situ tests on masonry arches strengthened with B-FRCM composite materials

6.3.1. Introduction

Masonry arches and vaults are widespread structural components in several cities all over Europe and they represent a quite large part of the cultural heritage of historical buildings. These structures can undergo different types of damages due to ageing processes or natural hazards such as earthquakes. Their preservation has recently gained a renewed interest because of the recent seismic events that involved several countries (Italy, Greece and Turkey). Among the new strengthening systems, fiber reinforced polymer (FRP) composites have been widely employed in the last few decades. Several experimental campaigns and analytical studies [208] [88] [91] [148] were carried out to investigate the effectiveness of these new systems as a strengthening tool of existing masonry arches or vaults [209] [210] [211] [212] [213] [214]. The application of FRP strips to masonry arches and vaults can prevent the typical failure mechanism of these unreinforced structures. The strengthening system enhances the ductility and the strength capacity of masonry arches and vaults, which could in turn lead to a switch of the failure mode, i.e. masonry compressive failure, sliding along the mortar joints, and FRP debonding from the masonry [209] [210]. Recently, fiber reinforced cementitious matrix (FRCM) composites have gained a terrific success as a suitable alternative to FRPs. This newly developed strengthening material can overcome several drawbacks related to FRP strengthening technique, such as the low vapor permeability, the poor behavior at elevated temperatures and the lack of reversibility of the installation [215]. FRCMs composites consist of high strength fibers embedded within an inorganic matrix that is responsible for the stress-transfer mechanism between the composite and the substrate. The available literature is mainly focused on the study of bond between FRCMs and masonry surfaces [215] [166] [160] or on the use of FRCMs for strengthening masonry elements [216] [217] [218], and limited experimental works have been published in order to study masonry arches strengthened with FRCM systems [219]. The present study reports the results of destructive in-situ tests performed on existing masonry arches reinforced with B-FRCM composites. B-FRCM strips consist of basalt fibers embedded in an inorganic matrix (lime-based hydraulic mortar). Three different configurations of the strengthening system have been considered. Load responses and failure modes are presented.

6.3.2. Experimental program

The bricks and the mortar of the masonry arches were characterized in section 3.2.1. The B-FRCM composite consisted in low-density basalt (LDB) fibers (described in section 3.3.2) embedded in a lime-based mortar matrix (described in section 3.3.4.1).

Four masonry arches were tested in-situ by applying a vertical load at approximately one-fourth of the net span. One arch was left unstrengthened and used as control, while three arches (Figure 135, Figure 136, and Figure 137) were strengthened using a LDB fiber bi-directional grid embedded within a lime-based hydraulic mortar. The four masonry arches were obtained from the same existing barrel vault by removing five 100 mm wide masonry strips spaced 900 mm apart in order to obtain four masonry arches with the same width equal to 800 mm. The barrel vault strips were removed only in the central portion of the span, while the voussoirs in the haunches where not removed. Each arch consists of bricks placed with their intermediate dimension along the radial direction in the central portion of the element, while close to the haunches, the arch section is increased due to a different arrangement of the bricks (Figure 135). The thickness of each arch in the central portion of the span is approximatively equal to 120 mm. One masonry arch, named V_01, was not strengthened and used as control arch. The remaining arches were strengthened with B-FRCM composite strips. Arch V_02 (Figure 135) was strengthened at the intrados, using two 200 mm wide composite strips applied for the entire length of the arch until the springing. The strips were symmetrically applied with respect to the cross-section of the arch. The distance of the external side of the strip from the edge of the arch was equal to 100 mm. Steel connectors, spaced 300 mm apart, were placed for the entire length of the composite strips in order to prevent premature debonding between the strips and the masonry substrate. Arch V_03 (Figure 136) was strengthened at the extrados, using two 200 mm wide composite strips applied for the entire length of the arch until the haunches. The two strips were symmetrically applied with respect to the cross-section of the arch. The distance of the external side of the strip from the edge of the arch was equal to 100 mm. For each composite strip a steel connector was placed close to the haunches at both ends of the masonry arch. Arch V_04 (Figure 137) was strengthened at both the extrados and intrados, with two 200 mm wide composite strips on each side. The strips were applied at the same distance apart and from the edges of the arch on both side. At the extrados two B-FRCM strips were applied for the entire length of the arch starting from the haunches, while at the intrados two B-FRCM strips were applied starting from the springing. The composite strips were symmetrically applied with respect to the cross-section of the arch. The distance of the external side of the strip from the edge of the arch was equal to 100 mm. Steel connectors, spaced 300 mm apart, were placed at intrados for the entire length of the composite strips. At extrados, for each composite strip a steel connector was placed close to the haunches at both ends of the arch. It should be noted that steel connectors were as long as the thickness of the arch. For Arch_V03 and

Arch_V04, the connectors at the extrados were inserted parallel to the tangent to the arch where the haunches had an increase of the thickness.

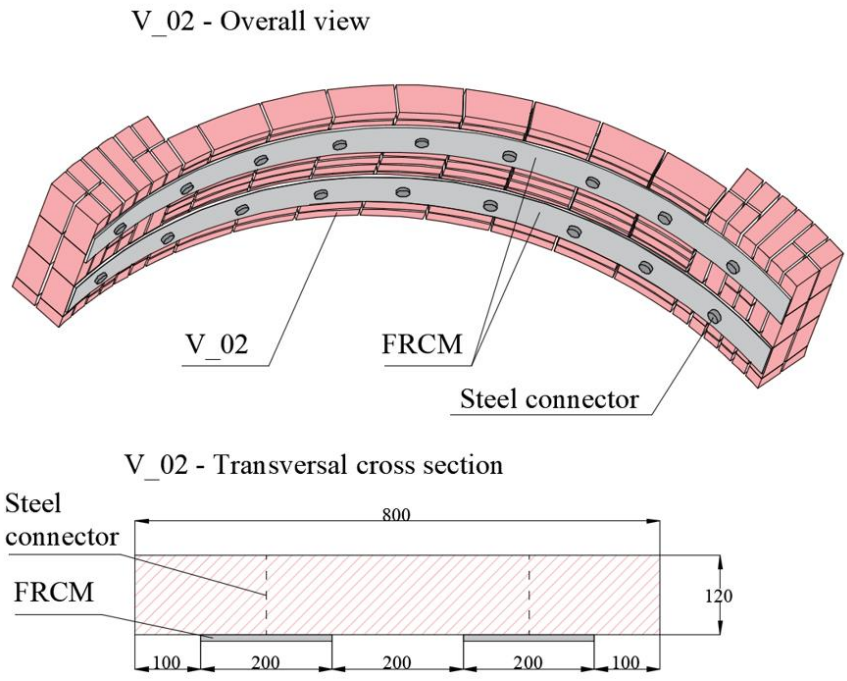

Figure 135. Configuration of the strengthening system of the masonry arch V_02.

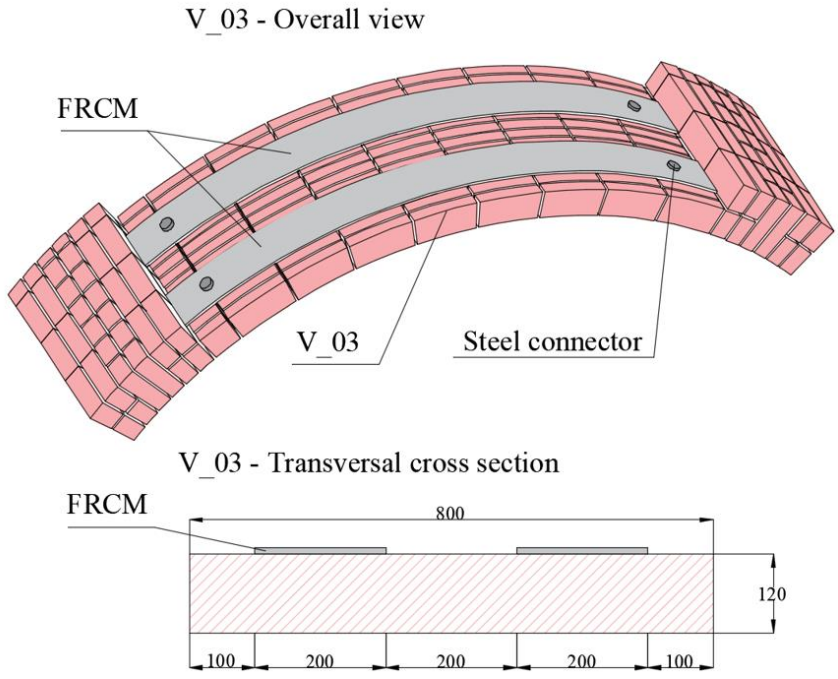

Figure 136. Configuration of the strengthening system of the masonry arch V_03.

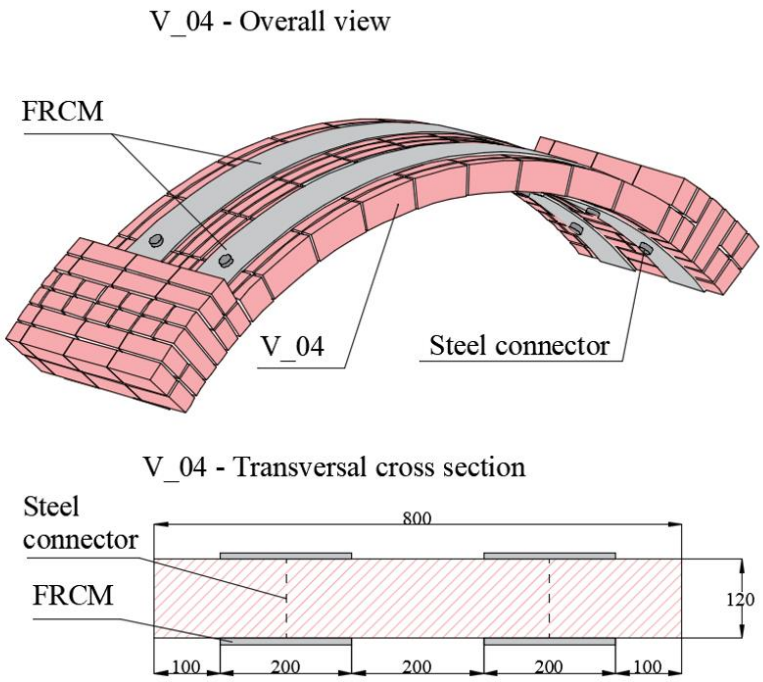

Figure 137. Configuration of the strengthening system of the masonry arch V_04.

The experimental set-up consists of a closed-loop loading apparatus and six linear variable displacement transducers (LVDT) used to monitor the vertical displacements of the masonry arches at several key points (Figure 138 and Figure 139). The load was applied approximately at one-fourth of the total span of each arch. A mechanical jack was used to apply the load to a stiff I-steel beam that applied a uniformly distributed load across the width of the arch (Figure 138). To ensure vertical alignment and even distribution of the applied load, a transversal layer of mortar was cast at the masonry extrados to firmly rest the I-beam. In the first phase of each test, three loading and unloading cycles at low load level were performed to allow possible adjustments of the test set-up and infer the response of the masonry arches. The peak value of each cycle for each test is reported in Table 31. Six LVDTs were mounted at the extrados of the masonry arches to monitor the vertical displacement of key points. LVDT-a and LVDT-f were placed at each haunch of the masonry where the cross-section enlarges. LVDT-b and LVDT-c measured the vertical displacement of the load point. LVDT-d was placed at the mid-span (crown) of the arch, while LVDT-e measured the vertical displacement of the point symmetrical with respect to the one where the load was applied. Figure 138 shows the spacings d_1, d_2, d_3 and d_4 among the LVDTs, reported

in Table 31 for each arch. The average measurement obtained from LVDT-b and LVDT-c was used to control the test. Load was applied in order to keep an approximate constant rate equal to 0.03 mm/s.

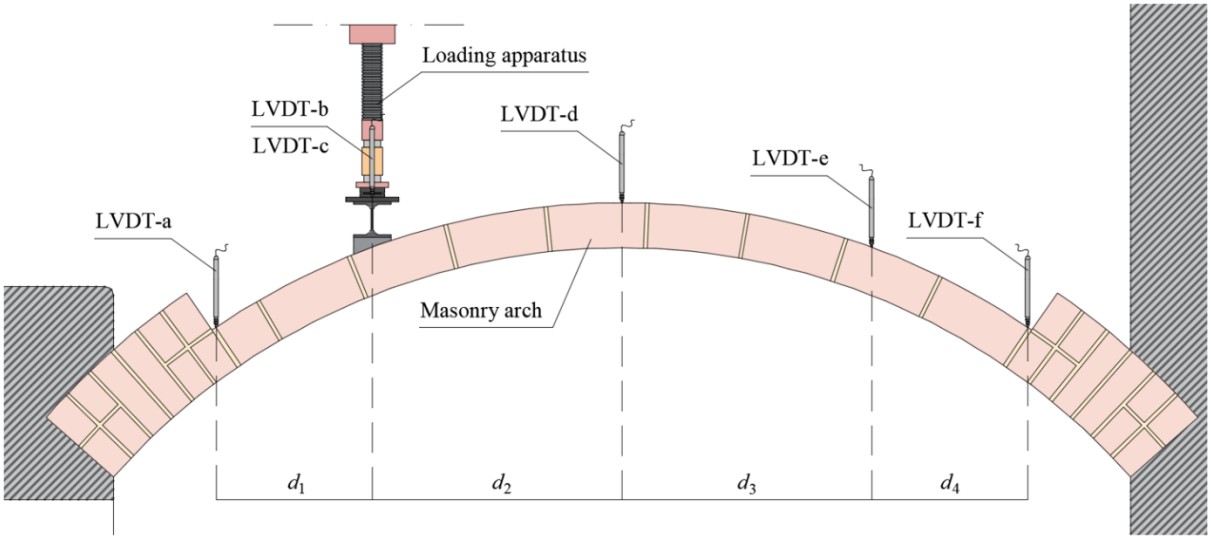

Figure 138. Sketch of the test set-up.

Figure 139. Photo of the experimental set-up.

Table 31- Set-up details and instruments layout.

Arch	d_1 [mm]	d_2 [mm]	d_3 [mm]	d_4 [mm]	Cycle 1 Peak load [kN]	Cycle 2 Peak load [kN]	Cycle 3 Peak load [kN]
V_01	*485*	*665*	*685*	*415*	*2*	*4*	*6*
V_02	*490*	*660*	*680*	*420*	*4*	*8*	*12*
V_03	*480*	*710*	*710*	*360*	*2*	*4*	*12*
V_04	*470*	*675*	*690*	*345*	*2*	*4*	*12*

6.3.3. Experimental results

In this section, the experimental results are presented. Destructive in-situ tests were performed on four masonry arches. One arch was not strengthened and used as control arch, the remaining three arches were strengthened with B-FRCM strips arranged in several configurations. Figure 140a-b-c-d shows the applied load – vertical displacement of the point load curves for arches V_01, V_02, V_03, and V_04, respectively. The vertical displacement of the loading point is obtained as the average of LVDT-b and LVDT-c measurements. Load responses of arches V_01, V_02 and V_03 show an initial linear branch followed by a non-linear portion until the peak load is reached. At peak load one hinge formed in the arch at the point of application of the load. After the peak load, the graphs show a descending branch until failure, i.e. collapse of the arch. As the softening branch progressed, additional hinges formed in each arch (Figure 141). Collapse occurred after the fourth hinge formed. The load response of arch V_04 shows only an increasing branch since the test was interrupted prior to reaching the peak load. Arch V_04 was strengthened at both the intrados and extrados, and therefore it presented a higher load-carrying capacity with respect to other arches. Since the load cell of the loading apparatus had a maximum capacity equal to 50 kN, for arch V_04 test was stopped approximatively at this value of force without reaching the collapse of the arch. The value of the peak load and corresponding vertical displacement is reported in Table 32. Figure 141a shows the load response of arch V_03, together with the measurements obtained from LVDT a, d, e, and f. A large variation in the displacements measured by LVDT a, d, e, and f was observed after the first hinge (point A in Figure 141a) formed in arch V_03.

All three arches strengthened with B-FRCM composite strips show an increase of the load-carrying capacity with respect to the control arch. In particular, arches V_02 and V_03 show a percentage increase of the peak load with respect to arch V_01 equal to 157 % and 128 %, respectively. The higher value of the peak load obtained for specimen V_02 could be justified by the presence of the basalt fibers at the intrados, which delayed the formation of the first plastic hinge that occurred at the load point. In addition, the presence of steel connectors for the entire length of the composite strip prevented the possible early debonding triggered by the curvature of the arch. The stiffness of the system (measured as the slope of the response between 5 kN and 15 kN) is also improved by the presence of the composite. In fact, the stiffness is approximately equal to 9 kN/mm for the unstrengthened arch, 15 kN/mm for arches V_02 and V_03, and 37 kN/mm for arch V_04. The application of the B-FRCM strips does not modify the failure mode, which results in the formation of four consecutive hinges that caused the collapse of the arch (Figure 141).

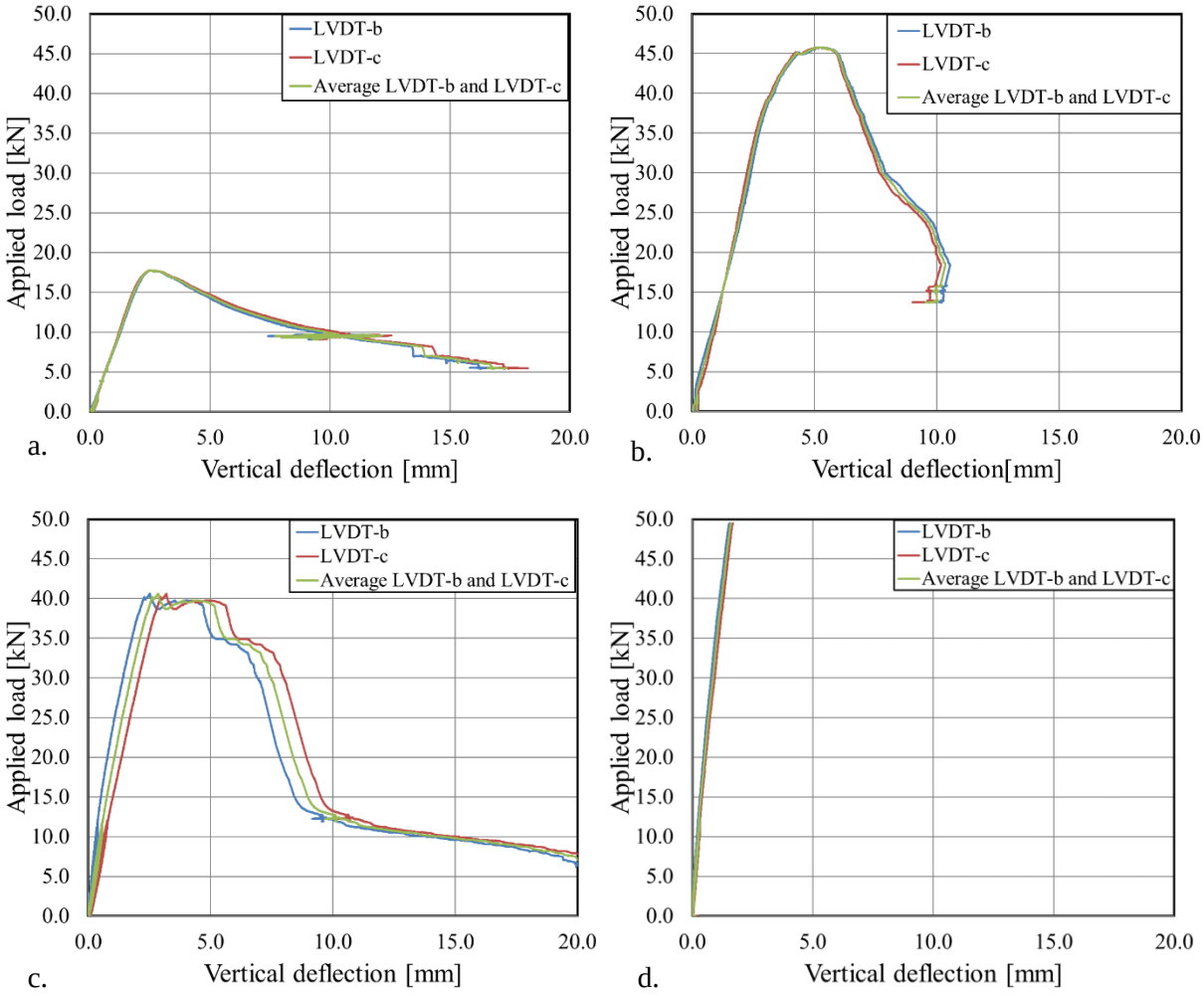

Figure 140. Applied load vs. point load deflection response: a) Arch V_01; b) Arch V_02; c) Arch V_03; d) Arch V_04.

Table 32. Experimental results.

Arch	Load point vertical displacement at peak [mm]	Peak load [kN]	Percentage increase of the peak load with respect to V_01 [%]
V_01	*2.41*	*17.80*	/
V_02	*5.26*	*45.77*	*157 %*
V_03	*2.86*	*40.60*	*128 %*
V_04	*1.62**	*49.51**	/

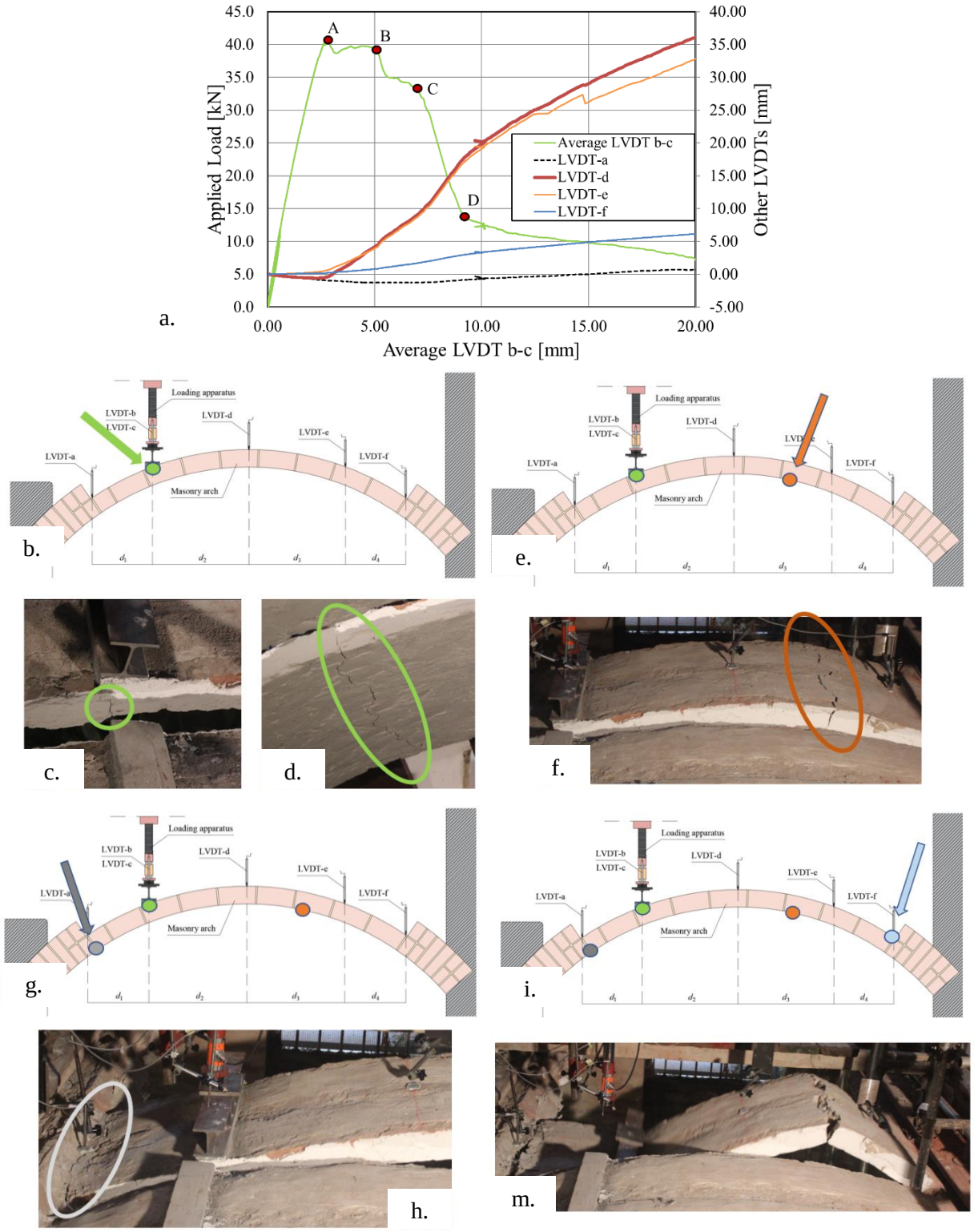

Figure 141. a) Applied load vs. point load deflection response of arch V_03; b), c) and d) First hinge (Point A); e) and f) Second hinge (Point B); g) and h) Third hinge (Point C); i) Fourth hinge (Point D); m) Failure of arch V_03.

However, vaults that were strengthened with B-FRCM strips experienced a delay in the formation of the hinges even though the locations of the hinges were similar with respect to the control arch. It should be noted that fiber rupture was observed where the hinges opened prior to failure of the arch by increasing mechanism. Arch V_02 showed a substantial increase of the point loading vertical displacement at peak load (5.26 mm) with respect to the control arch V_01 (2.41 mm) since the first hinge formation was delayed by the presence of the composite at the intrados and so the load increased until the formation of the second hinge at midspan. Conversely, arch V_03 reached a value of the vertical deflection of the point load at peak load equal to 2.86 mm, similar to that of arch V_01, since the reinforcement was able to delay the formation of the second hinge (at midspan) and not first hinge. Nevertheless, load was maintained almost constant until the formation of the third hinge. As mentioned before, limited discussion can be drawn for arch V_04 because test was stopped prior to the reaching the peak load when no hinges formed yet. As expected, the application of the B-FRCM strips both at the intrados and at the extrados of the arch is more effective than solutions adopted in arches V_02 and V_03.

6.3.4. Conclusions

In this section, destructive in situ tests were performed on existing masonry arches. Three arches were strengthened with B-FRCM composite strips, while one arch was not strengthened and used as control arch. Three different configurations of the strengthening system were considered. Results showed that the application of the composite strips improve the load-carrying capacity of the arch, and entailed for large deflections of the point of application of the load at peak. All four arches collapsed after the formation of four hinges. The application of the basalt FRCM strips both at the intrados and at the extrados of the arch appears to be the most effective solution in terms of load-carrying capacity.

7. Conclusions

In this chapter a summary of the main findings of the present dissertation is presented.

7.1. Summary

A general objective of the present study has been to deepen the knowledge of newly developed composite materials that employed steel or basalt fibers and that are bonded to quasi-brittle surfaces. The study of the experimental strains on SRP strips bonded to concrete, during the debonding phenomenon, allowed for the determination of the cohesive material law, that was determined also for SRG composites bonded to masonry blocks through an indirect calibration. For several composite systems important features were evaluated such as the fracture energy and the effective bond length. In addition, the study of different parameters allowed a comparison between different strengthening solutions providing useful advices for design aspects.

7.2. Conclusions

The present dissertation analyzed the bond performances of newly developed fiber reinforced composite systems applied to quasi-brittle material interfaces.

The debonding phenomenon of SRP composites bonded to a concrete substrate was studied through direct single-lap shear tests and through TPB tests on notched beams. The experimental debonding forces obtained from single-lap shear tests and notched beam tests are different. It was found that the bond behavior of SRP composites was very similar to the behavior of FRP composites. The fracture energy G_F of SRP-concrete joints was independent of the composite density, whereas the effective bond length depends on the density of the strip. The fracture energy G_F varies as the composite was bonded to different faces of the concrete prism. The width effect should be considered in the evaluation of the load-carrying capacity of SRP-concrete joints. The numerical analysis performed with LDPM was capable to simulate the behavior of SRP strips bonded to face B of the concrete prisms.

The bond performances of SRG composites bonded to a concrete substrate were studied perfoming single-lap shear tests. When LD steel fibers were employed, the failure mode consisted in the rupture of the fibers, while delamination at the fiber-matrix interface occurred when MLD and MD steel fibers were employed. The load rate had an influence on the peak load of SRG specimens. An increase in the test rate entailed an increase of the maximum load.

A new composite material, consisting in steel fibers embedded in a newly developed geopolymer matrix, was tested in direct shear. An excellent adhesion between the FRGM composite and the concrete substrate was found and the average value of the maximum stress in the fibers in direct shear tests resulted equal to 67% of the tensile strength provided by the manufacturer [6]. The failure mode was debonding (interlaminar failure) of the external layer of matrix from the internal layer.

Direct single lap shear tests were performed also on SRG-masonry joints. For SRG specimens that employed a cement-based mortar the effective bond length was found to be in the range 200 mm – 250 mm. For specimens that employed a lime-based mortar the effective bond length was found to be in the range 175 mm – 200 mm. The failure mode depended on the bonded length of the strip. No width effect was observed for SRG systems applied to masonry. The load carrying capacity of the matrix-fiber interface decreases as the fiber density increases. The cohesive material law (CML) was found through an indirect calibration. Results showed in the present dissertation indicated a limited effect of sulfate exposure on the stress-transfer between SRG composites and masonry, at least for the artificial weathering protocol that was used.

Monotonic compressive tests were conducted on concrete members confined with SRP composites in order to investigate the effect of the SRP wrapping on the compressive strength and ultimate strain. High failure stresses were observed in small columns with respect to large columns. The geometric shape influenced the compressive strength of confined specimens, while there is a not noticeable shape effect on the ultimate axial strain of specimens confined with SRP composites. Increases in fiber density were not proportional to increases in confined compressive strength. The use of three layers of steel fibers provided a significant increase of the energy absorption.

The effectiveness of SRG jackets applied to small concrete prisms was investigated varying several parameters. Results showed that sharp corners are not detrimental for SRG confinement. Specimens reinforced with high density (HD) fibers had slightly higher compressive strength than specimens reinforced with medium density (MD) steel fibers. The length of the overlap affected the effectiveness of the SRG confinement. An increase of the confined strength was associated with an increase of the number of layers, even the increase in axial strength was not proportional to the number of jacket layers. The use of two layers of steel fibers provided a significant increase of the energy absorption.

Eventually, several applications of basalt-fiber reinforced cementitious matrix (B-FRCM) composites bonded to masonry substrates were analysed. The results of direct-single lap shear tests showed that the failure of B-FRCM-masonry joints strengthened with LDB fibers consisted in the rupture of the fibers (RF) while HDB specimens exhibited the detachment (delamination) of the external layer of matrix from the internal one (MF). Monotonic compressive tests performed on masonry columns strengthened with

B-FRCM composites showed that B-FRCM jackets provided a slight increase (14-16%) of the average compressive strength with respect to control columns. The low increase of the average compressive strength with respect to unconfined specimens is mainly due to the brittle nature and relatively low tensile strength of the basalt fibers that tend to rupture near the corners of the columns. The application of B-FRCM composite to existing masonry arches showed that B-FRCM strips provided a significant increase of the peak load and delayed the formation of the hinges and consequently the activation of the failure mechanism.

7.3. Ongoing and future work

The present dissertation shows several findings related to the bond between newly developed composite materials and quasi-brittle interfaces, but several aspects of the bond phenomenon are still unsolved and need further research.

Until today, it was not found yet a direct reliable method to determine the cohesive material law of SRG composite bonded to quasi-brittle interfaces. The future research will try to investigate the cohesive material law applying optical fibers to the strengthening textile before the casting procedure. Following this procedure, it should be possible to monitor the slip of the strengthening textile at different positions along the bonded length during single-lap shear tests and determine the cohesive material law.

In this work, the SRG composite was applied on masonry blocks constructed with the same type of masonry brick. The future research is aimed to study the debonding phenomenon of SRG composites applied to masonry blocks constructed with historical bricks or tuft elements coming from different Italian regions. In this way, it will be possible to verify the effectiveness of the SRG strengthening system when applied to different substrates.

Since most of the SRG-masonry joints tested in this experimental work showed a interlaminar failure at the matrix-fiber interface, a future aspect that will be studied is the influence of anchorage systems on the bond performances. In particular, SRG-composite strips will be bonded to masonry substrates and anchored at the free end, embedding the steel fibers in a hole in the last brick of the masonry blocks with an epoxy resin. Then, the SRG-masonry joint will be tested in direct shear.

Further studies are also needed to analyze some aspects of the bond phenomenon that have not been deeply investigated from the scientific community, such has creep and fatigue problems. A steel set-up has been designed and will be employed to apply for several months a constant force to SRP-concrete joints in order to study the long-term behavior.

Eventually, a wide experimental study will be performed to investigate the influence of different corner radius on the load response of confined concrete columns tested in compression.

Bibliography

[1] D. B. Miracle, ASM handbook, Volume 21, ASM International, 2001.

[2] National Research Council, "CNR-DT 200. R1: Istruzioni per la Progettazione, l'Esecuzione ed il Controllo di Interventi di Consolidamento Statico mediante l'utilizzo di Compositi Fibrorinforzati," 2013.

[3] F. Berardi, "A study of the load-carrying capacity of SRG- and SRP-masonry interface: the effect of salt crystallization and width of the composite," *Master degree thesis - University of Bologna,* 2017.

[4] G. Daissè, "Interfacial bond behavior of steel-FRCM composites applied to a masonry substrate," *Master degree thesis - University of Bologna,* 2017.

[5] Mapei S.p.A., "http://www.mapei.com," [Online]. [Accessed December 2017].

[6] Kerakoll S.p.A., "www.kerakoll.com," [Online]. [Accessed November 2017].

[7] O. Buyukozturk and B. Hearing, "Failure behavior of precracked concrete beams retrofitted with FRP," *Journal of composites for construction,* vol. 2(3), pp. 138-144, 1998.

[8] J. G. Teng, S. T. Smith, J. Yao and J. F. Chen, "Intermediate crack-induced debonding in RC beams and slabs," *Construction and building materials,* vol. 17(6), pp. 447-462, 2003.

[9] M. Arduini, A. Di Tommaso and A. Nanni, "Brittle failure in FRP plate and sheet bonded beams," *ACI Structural Journal,* vol. 94(4), pp. 363-370, 1997.

[10] C. Carloni, "Analyzing bond characteristics between composites and quasi-brittle substrates in the repair of bridges and other concrete structures.," in *Advanced Composites in Bridge Construction and Repair.*, Sawston, Cambridge, Woodhead Publishing Limited, 2014, pp. 61-93.

[11] W. M. Sebastian, "Significance of midspan debonding failure in FRP-plated concrete beams," *Journal of Structural Engineering,* vol. 127(7), pp. 792-798, 2001.

[12] O. Rosenboom and S. Rizkalla, "Modeling of IC debonding of FRP-strengthened concrete flexural members," *Journal of Composites for Construction,* vol. 12(2), pp. 168-179, 2008.

[13] M. J. Chajes, W. W. Finch and T. A. Thomson, "Bond and force transfer of composite-material plates bonded to concrete," *Structural Journal,* vol. 93(2), pp. 209-217, 1996.

[14] L. Bizindavyi and K. W. Neale, "Transfer lengths and bond strengths for composites bonded to concrete," *Journal of composites for construction,* vol. 3(4), pp. 153-160, 1999.

[15] B. Täljsten, "Defining anchor lengths of steel and CFRP plates bonded to concrete," *International Journal of Adhesion and Adhesives,* vol. 17(4), pp. 319-327, 1997.

[16] D. Van Gemert, "Force transfer in epoxy bonded steel/concrete joints," *International Journal of Adhesion and Adhesives,* vol. 1(2), pp. 67-72, 1980.

[17] R. N. Swamy, R. Jones and A. Charif, "Shear adhesion properties of epoxy resin adhesives," *Adhesion between polymers and concrete/Adhésion entre polymères et béton,* pp. 741-755, 1986.

[18] K. Brosens and D. Van Gemert, "Anchoring stresses between concrete and carbon fibre reinforced laminates," *Composite construction-conventional and innovative. International conference,* pp. 181-186, 1997.

[19] T. Maeda, Y. Asano, Y. Sato, T. Ueda and Y. Kakuta, "A study on bond mechanism of carbon fiber sheet," *Non-Metallic (FRP) Reinforcement for Concrete Structures, Proceedings of the Third Symposium,* vol. 1, pp. 279-286, 1997.

[20] U. Neubauer and F. S. Rostasy, , "Design aspects of concrete structures strengthened with externally bonded CFRP-plates," in *PROCEEDINGS OF THE SEVENTH INTERNATIONAL CONFERENCE ON STRUCTURAL FAULTS AND REPAIR*, 1997.

[21] Y. N. Ziraba, M. H. Baluch, I. A. Basunbul, A. K. Azad, G. J. Al-Sulaimani and A. M. Sharif, "Combined experimental-numerical approach to characterization of steel-glue-concrete interface," *Materials and Structures,* vol. 28(9), pp. 518-525, 1995.

[22] M. S. Mohamed Ali, D. J. Oehlers and M. C. Griffith, "Shear transfer across cracks in FRP strengthened RC members," *Journal of Composites for Construction,* vol. 12(4), pp. 416-424, 2008.

[23] A. Gartner, E. P. Douglas, C. W. Dolan and H. R. Hamilton, "Small beam bond test method for CFRP composites applied to concrete," *Journal of Composites for Construction,* vol. 15(1), pp. 52-61, 2010.

[24] H. Yuan, J. G. Teng, R. Seracino, Z. S. Wu and J. Yao, "Full-range behavior of FRP-to-concrete bonded joints," *Engineering structures,* vol. 26(5), pp. 553-565, 2004.

[25] B. Täljsten, "Plate bonding: Strengthening of existing concrete structures with epoxy bonded plates of steel or fibre reinforced plastics," *Doctoral dissertation, Luleå tekniska universitet,* 1994.

[26] B. Täljsten, "Strengthening of concrete prisms using the plate-bonding technique.," *International journal of Fracture,* vol. 82(3), pp. 253-266, 1996.

[27] M. Ali-Ahmad, K. Subramaniam and M. Ghosn, "Experimental investigation and fracture analysis of debonding between concrete and FRP sheets.," *Journal of engineering mechanics,* vol. 132(9), pp. 914-923, 2006.

[28] Z. Wu and H. Niu, "Prediction of crack-induced debonding failure in R/C structures flexurally strengthened with externally bonded FRP composites," *Doboku Gakkai Ronbunshuu E,* vol. 63(4), pp. 620-639, 2007.

[29] C. Mazzotti, M. Savoia and B. Ferracuti, "An experimental study on delamination of FRP plates bonded to concrete," *Construction and Building Materials,* vol. 22(7), pp. 1409-1421, 2008.

[30] Y. Sato, K. Kimura and Y. Kobatake, "Bond behavior between CFRP sheet and concrete," *Journal of Structural and Construction Engineering,* vol. 500, pp. 75-82, 1997.

[31] L. De Lorenzis, B. Miller and A. Nanni, "Bond of FRP laminates to concrete," *ACI Materials Journal,* vol. 98(3), pp. 256-264, 2001.

[32] H. Yoshizawa, Z. Wu, H. Yuan and T. Kanakubo, "Study on FRP-concrete interface bond performance," *Trans. Jpn. Soc. Civ.,* vol. 662(49), pp. 105-119, 2000.

[33] K. Nakaba, T. Kanakubo, T. Furuta and H. Yoshizawa, "Bond behavior between fiber-reinforced polymer laminates and concrete," *Structural Journal,* vol. 98(3), pp. 359-367, 2001.

[34] Y. Sato, Y. Asano and T. Ueda, "Fundamental study on bond mechanism of carbon fiber sheet," *Concr. Library Int., JSCE,* vol. 648, pp. 71-87, 2000.

[35] J. Dai, T. Ueda and Y. Sato, "Development of the nonlinear bond stress–slip model of fiber reinforced plastics sheet–concrete interfaces with a simple method.," *Journal of Composites for Construction,* vol. 9(1), pp. 52-62, 2005.

[36] CEN, "EN 12390-3 Testing hardened concrete - Part 3: Compressive strength of test specimens.," 2009. A1: 2011..

[37] CEN, "EN 12390-6 Testing hardened concrete - Part 6: Tensile splitting strength of test specimens.," 2009.

[38] British Standards Institution, "Eurocode 2: Design of Concrete Structures," 2004.

[39] M. Elices and J. Planas, "Fracture mechanics parameters of concrete: an overview," *Advanced Cement Based Materials,* vol. 4(3), pp. 116-127, 1996.

[40] A. Hillerborg, "The theoretical basis of a method to determine the fracture energy GF of concrete.," *Materials and structures,* vol. 18(4), pp. 291-296, 1985.

[41] M. Elices, V. G. Guinea and J. Planas, "Measurement of the fracture energy using three-point bend tests: Part 3—influence of cutting the P-δ tail.," *Materials and Structures,* vol. 25(6), pp. 327-334, 1992.

[42] C. G. Hoover and Z. P. Bažant, "Comprehensive concrete fracture tests: size effects of types 1 & 2, crack length effect and postpeak.," *Engineering Fracture Mechanics,* vol. 110, pp. 281-289, 2013.

[43] W. Gerstle, "Progress in developing a standard fracture toughness test for concrete," *Structures Congress 2010,* pp. 1915-1926, 2010.

[44] J. Planas, M. Elices and G. V. Guinea, "Measurement of the fracture energy using three-point bend tests: Part 2—Influence of bulk energy dissipation," *Materials and Structures,* vol. 25(5), pp. 305-312, 1992.

[45] Z. P. Bazant and J. Planas, Fracture and size effect in concrete and other quasibrittle materials, CRC press, 1997.

[46] ACI Committee 308, ACI 308R-16: Guide to External Curing of Concrete, Farmington Hills, MI (USA): American Concrete Institute, 2016.

[47] CEN, EN 772-1, 2011, "Methods of test for masonry units – Part 1: Determination of compressive strength. A1:2015".

[48] C. Carloni, M. Santandrea and R. Wendner, "An investigation on the “width and size effect” in the evaluation of the fracture energy of concrete.," *Procedia Structural Integrity*, vol. 3, pp. 450-458, 2017.

[49] DIN 18555-9:1999-09, "Testing of mortars containing mineral binders - Part 9: Hardened mortars; determination of the mortar compressive strength in the bed joint".

[50] CEN, EN 1015-11:1999, "Methods of test for mortar for masonry – Part 11: Determination of flexural and compressive strength of hardened mortar. A1:2006".

[51] M. C. Bignozzi, S. Manzi, M. E. Natali, W. D. Rickard and A. Van Riessen, "Room temperature alkali activation of fly ash: The effect of Na2O/SiO2 ratio," *Construction and Building Materials*, vol. 69, pp. 262-270, 2014.

[52] F. Bencardino, A. Condello and A. F. Ashour, "Single-lap shear bond tests on Steel Reinforced Geopolymeric Matrix-concrete joints," *Composites Part B: Engineering*, vol. 110, pp. 62-71, 2017.

[53] L. Carabba, M. Santandrea, S. Manzi, C. Carloni and M. C. Bignozzi, "Geopolymer mortars for strengthening existing reinforced concrete structures," in *4th Workshop on The New Boundaries of Structural Concrete*, Anacapri, 2016.

[54] UNI EN 1015 - 3, "Methods of test for mortar for masonry – Part 3: determination of consistence of fresh mortar (by flow table)," 2007.

[55] B. Singh, M. R. Rahman, R. Paswan and S. K. Bhattacharyya, "Effect of activator concentration on the strength, ITZ and drying shrinkage of fly ash/slag geopolymer concrete," *Construction and Building Materials*, vol. 118, pp. 171-179, 2016.

[56] EN 13057, "Products and systems for the protection and repair of concrete structures. Test methods. Determination of resistance of capillary absorption," 2002.

[57] Y. Ma, J. Hu and G. Ye, "The pore structure and permeability of alkali activated fly ash," *Fuel*, vol. 104, pp. 771-780, 2013.

[58] EN 196 - 1 , "Methods of testing cement – part 1: Determination of strength," 2005.

[59] U. Rattanasak and P. Chindaprasirt, "Influence of NaOH solution on the synthesis of fly ash geopolymer," *Minerals Engineering,* vol. 22(12), pp. 1073-1078, 2009.

[60] L. H. Sneed, T. D'Antino and C. Carloni, "Investigation of bond behavior of PBO fiber-reinforced cementitious matrix composite-concrete interface," *ACI Mater J,* vol. 111(5), pp. 569-580, 2014.

[61] EN 12617- 4, "Products and systems for the protection and repair of concrete structures - Test methods - Part 4: Determination of shrinkage and expansion," 2002.

[62] A. Mobili, A. Belli, C. Giosué, T. Bellezze and F. Tittarelli, "Metakaolin and fly ash alkali-activated mortars compared with cementitious mortars at the same strength class," *Cement and Concrete Research,* vol. 88, pp. 198-210, 2016.

[63] ASTM Committee D-30 on Composite Materials, *Standard test method for tensile properties of polymer matrix composite materials.,* ASTM International, 2008.

[64] C. Carloni and K. V. Subramaniam, "Direct determination of cohesive stress transfer during debonding of FRP from concrete.," *Composite Structures,* vol. 93(1), pp. 184-192, 2010.

[65] EN 12190:1998, "Products and systems for the protection and repair of concrete structures. Test methods. Determination of compressive strength of repair mortar".

[66] G. de Felice, S. De Santis, L. Garmendia, B. Ghiassi, P. Larrinaga, P. B. Lourenço, D. V. Oliveira, F. Paolacci and C. G. Papanicolaou, "Mortar-based systems for externally bonded strengthening of masonry," *Materials and structures,* vol. 47(12), pp. 2021-2037, 2014.

[67] S. De Santis and G. de Felice, "Tensile behaviour of mortar-based composites for externally bonded reinforcement systems," *Composites Part B: Engineering,* vol. 68, pp. 401-413, 2015.

[68] D. Arboleda, F. G. Carozzi, A. Nanni and C. Poggi, "Testing procedures for the uniaxial tensile characterization of fabric-reinforced cementitious matrix composites," *Journal of Composites for Construction,* vol. 20(3), 2015.

[69] L. H. Sneed, F. Ravazdezh, M. Santandrea and I. A. O. Imohamed, "A study of the compressive behavior of concrete columns confined with SRP jackets using digital image analysis.," *Composite Structures,* vol. 179, pp. 195-207, 2017.

[70] L. H. Sneed, S. Verre, C. Carloni and L. Ombres, "Flexural behavior of RC beams strengthened with steel-FRCM composite.," *Engineering Structures,* vol. 127, pp. 686-699, 2016.

[71] E. Wobbe, P. Silva, B. L. Barton, L. R. Dharani, V. Birman, A. Nanni, T. Alkhrdaji, J. Thomas and G. Tunis, "Flexural capacity of RC beams externally bonded with SRP and SRG.," in *Proceedings of Society for the Advancement of material and Process Engineering 2004 Symposium*, 2004.

[72] Y. J. Kim, A. Fam, A. Kong and R. El-Hacha, "Flexural strengthening of RC beams using steel reinforced polymer (SRP) composites.," *ACI Special Publication SP-230,* pp. 1647-1664, 2005.

[73] B. Barton, E. Wobbe, L. R. Dharani, P. Silva, V. Birman, A. Nanni, T. Alkhrdaji, J. Thomas and G. Tunis, "Characterization of reinforced concrete beams strengthened by steel reinforced polymer and grout (SRP and SRG) composites.," *Materials Science and Engineering: A,* vol. 412(1), pp. 129-136, 2005.

[74] P. Casadei, A. Nanni, T. Alkhrdaji and J. Thomas, "Performance of double-T prestressed concrete beams strengthened with steel reinforcement polymer.," *Advances in Structural Engineering,* vol. 8(4), pp. 427-442, 2005.

[75] A. Prota, K. Y. Tan, A. Nanni, M. Pecce and G. Manfredi, "Performance of shallow reinforced concrete beams with externally bonded steel-reinforced polymer.," *ACI Structural Journal,* vol. 103(2), p. 163, 2006.

[76] M. Pecce, F. Ceroni, A. Prota and G. Manfredi, "Response prediction of RC beams externally bonded with steel-reinforced polymers.," *Journal of Composites for Construction,* vol. 10(3), pp. 195-203, 2006.

[77] F. Ceroni and M. Pecce, "Cracking behaviour of RC beams externally strengthened with emerging materials.," *Construction and Building Materials,* vol. 21(4), pp. 736-745, 2007.

[78] R. Hawileh, J. Abdalla, W. Nawaz, A. Alzeer, R. Muwafi and A. Faridi, "Strengthening reinforced concrete beams in flexure using hardwire steel fiber sheets.," in *CICE,* Vancouver, 2014.

[79] A. Napoli and R. Realfonzo, "Reinforced concrete beams strengthened with SRP/SRG systems: experimental investigation," *Construction and Building Materials,* vol. 93, pp. 654-677, 2015.

[80] A. Napoli, R. Realfonzo, M. Petracca, F. Candeloro, G. Camata and P. Casadei, "Flexural strengthening of RC slabs with SRP/SRG: an experimental-numerical comparison.," *Applied Mechanics and Materials,* vol. 847, pp. 381-390, 2016.

[81] R. El-Hacha and M. A. Mashrik, "Effect of SFRP confinement on circular and square concrete columns," *Engineering Structures,* vol. 36, pp. 379-393, 2012.

[82] A. Napoli and R. Realfonzo, "Compressive behavior of concrete confined by SRP wraps," *Construction and Building Materials,* vol. 127, pp. 993-1008, 2016.

[83] J. J. Zheng, J. G. Dai and X. L. Fan, "Fracture analysis of FRP-Plated notched concrete beams subjected to three-point bending," *Journal of Engineering Mechanics,* vol. 142(3), 2016.

[84] K. V. Subramaniam, C. Carloni and L. Nobile, "Width effect in the interface fracture during shear debonding of FRP sheets from concrete.," *Engineering Fracture Mechanics,* vol. 74(4), pp. 578-594, 2007.

[85] K. V. Subramaniam, C. Carloni and L. Nobile, "An understanding of the width effect in FRP–concrete debonding," *Strain,* vol. 47(2), pp. 127-137, 2011.

[86] C. Czaderski, K. Soudki and M. Motavalli, "Front and side view image correlation measurements on FRP to concrete pull-off bond tests," *Journal of Composites for Construction,* vol. 14(4), pp. 451-463, 2010.

[87] C. B. Boyer and U. C. Merzbach, A history of mathematics, John Wiley & Sons, 2011.

[88] C. Carloni and F. Focacci, "FRP-masonry interfacial debonding: An energy balance approach to determine the influence of the mortar joints," *European Journal of Mechanics-A/Solids,* vol. 55, pp. 122-133, 2016.

[89] R. Seracino, M. R. Raizal Saifulnaz and D. J. Oehlers, "Generic debonding resistance of EB and NSM plate-to-concrete joints," *Journal of Composites for Construction,* vol. 11(1), pp. 62-70, 2007.

[90] P. Colombi, G. Fava and C. Poggi, "End debonding of CFRP wraps and strips for the strengthening of concrete structures," *Composite Structures,* vol. 111, pp. 510-521, 2014.

[91] F. Focacci and C. Carloni, "Periodic variation of the transferable load at the FRP-masonry interface," *Composite Structures,* vol. 129, pp. 90-100, 2015.

[92] C. Carloni, M. Santandrea and I. A. O. Imohamed, "Determination of the interfacial properties of SRP strips bonded to concrete and comparison between single-lap and notched beam tests.," *Engineering Fracture Mechanics,* vol. 186, pp. 80-104, 2017.

[93] J. F. Chen and J. G. Teng, "Anchorage strength models for FRP and steel plates bonded to concrete.," *Journal of Structural Engineering,* vol. 127(7), pp. 784-791, 2001.

[94] L. De Lorenzis and G. Zavarise, "Modeling of mixed-mode debonding in the peel test applied to superficial reinforcements," *International Journal of Solids and Structures,* vol. 45(20), pp. 5419-5436, 2008.

[95] F. S. Rostasy e U. Neubauer, «Bond behaviour of CFRP-laminates for the strengthening of concrete members.,» in *Composite construction-conventional and innovative. International conference*, 1997.

[96] P. Holzenkämpfer, «Ingenieurmodelle des Verbunds geklebter Bewehrung für Betonbauteile,» *PhD dissertation,* 1994.

[97] K. Brosens and D. Van Gemert, "Anchorage design for externally bonded carbon fiber reinforced polymer laminates," *ACI Special Publication,* vol. 188, pp. 635-646, 1999.

[98] K. Brosens, «Anchorage of externally bonded steel plates and CFRP laminates for the strengthening of concrete elements,» *Dissertation - Department of Civil Engineering, Katholieke University Leuven,* 2001.

[99] X. Z. Lu, J. G. Teng, L. P. Ye and J. J. Jiang, "Bond–slip models for FRP sheets/plates bonded to concrete," *Engineering structures,* vol. 27(6), pp. 920-937, 2005.

[100] Y. F. Wu and C. Jiang, "Quantification of bond-slip relationship for externally bonded FRP-to-concrete joints," *Journal of composites for construction,* vol. 17(5), pp. 673-686, 2013.

[101] J. P. Lin, Y. F. Wu and S. T. Smith, "Width factor for externally bonded FRP-to-concrete joints," *Construction and Building Materials,* vol. 155, pp. 818-829, 2017.

[102] T. Xu, Z. J. He, C. A. Tang, W. C. Zhu e P. G. Ranjith, «Finite element analysis of width effect in interface debonding of FRP plate bonded to concrete,» *Finite elements in analysis and design,* vol. 93, pp. 30-41, 2015.

[103] E. Benvenuti, N. Orlando, D. Ferretti e A. Tralli, «A new 3D experimentally consistent XFEM to simulate delamination in FRP-reinforced concrete,» *Composites Part B: Engineering,* vol. 91, pp. 346-360, 2016.

[104] P. Neto, J. Alfaiate e J. Vinagre, «Assessment of the dependence of CFRP-concrete behaviour on the width of the bonded materials,» *Composites Part B: Engineering,* vol. 91, pp. 448-457, 2016.

[105] V. Salomoni, G. Mazzucco, C. Pellegrino e C. Majorana, «Three-dimensional modelling of bond behaviour between concrete and FRP reinforcement,» *Engineering Computations,* vol. 28(1), pp. 5-29, 2011.

[106] P. Carrara, D. Ferretti, F. Freddi and G. Rosati, "Shear tests of carbon fiber plates bonded to concrete with control of snap-back," *Engineering Fracture Mechanics,* vol. 78(15), pp. 2663-2678, 2011.

[107] G. P. D. &. M. A. Cusatis, "Lattice discrete particle model (LDPM) for failure behavior of concrete. I: Theory.," *Cement and Concrete Composites,* vol. 33(9), pp. 881-890, 2011.

[108] Z. P. Bažant, M. R. Tabbara, M. T. Kazemi and G. Pijaudier-Cabot, "Random particle model for fracture of aggregate or fiber composites," *Journal of engineering mechanics,* vol. 116(8), pp. 1686-1705, 1990.

[109] G. Cusatis, Z. P. Bažant and L. Cedolin, "Confinement-shear lattice model for concrete damage in tension and compression: I. Theory," *Journal of Engineering Mechanics,* vol. 129(12), pp. 1439-1448, 2003.

[110] T. Belytschko and I. Leviathan , "Physical stabilization of the 4-node shell element with one point quadrature," *Computer Methods in Applied Mechanics and Engineering,* Vols. 113(3-4), pp. 321-350, 1994.

[111] F. Bencardino and A. Condello, "Structural behaviour of RC beams externally strengthened in flexure with SRG and SRP systems," *International Journal of Structural Engineering,* vol. 5(4), pp. 346-368, 2014.

[112] C. Escrig, L. Gil and E. Bernat-Maso, "Experimental comparison of reinforced concrete beams strengthened against bending with different types of cementitious-matrix composite materials," *Construction and Building Materials,* vol. 137, pp. 317-329, 2017.

[113] J. H. Gonzalez-Libreros, C. Sabau, L. H. Sneed, C. Pellegrino and G. Sas, "State of research on shear strengthening of RC beams with FRCM composites," *Construction and Building Materials,* vol. 149, pp. 444-458, 2017.

[114] M. Matana, A. Nanni, L. Dharani, P. Silva and G. Tunis, "Bond performance of steel reinforced polymer and steel reinforced grout," *Proceedings of the International Symposium on Bond Behaviour of FRP in Structures,* pp. 125-132, 2005.

[115] M. Santandrea, I. A. O. Imohamed, C. Carloni, C. Mazzotti, S. de Miranda and F. Ubertini, "An Investigation of the Debonding Mechanism in Steel FRP- and FRCM-Concrete Joints.," in *Proceedings of the 4th Workshop on The New Boundaries of Structural Concrete*, Anacapri, Italy, 2016.

[116] 2015 Activity Report - CEMBUREAU, "http://www.cembureau.eu/2015-activity-report," [Online]. [Accessed September 2016].

[117] T. D'Antino, C. Carloni, L. H. Sneed and C. Pellegrino, "Matrix–fiber bond behavior in PBO FRCM composites: A fracture mechanics approach," *Engineering Fracture Mechanics,* vol. 117, pp. 94-111, 2014.

[118] C. Carloni, D. A. Bournas, F. G. Carozzi, T. D'Antino, G. Fava, F. Focacci, G. Giacomin, G. Mantegazza, C. Pellegrino, C. Perinelli and C. Poggi, "Fiber reinforced composites with cementitious (inorganic) matrix," *Design Procedures for the Use of Composites in Strengthening of Reinforced Concrete Structures,* pp. 349-392, 2016.

[119] J. Donnini, V. Corinaldesi and A. Nanni, "Mechanical properties of FRCM using carbon fabrics with different coating treatments," *Composites Part B: Engineering,* vol. 88, pp. 220-228, 2016.

[120] C. Carloni, S. Verre, L. H. Sneed and L. Ombres, "Loading rate effect on the debonding phenomenon in fiber reinforced cementitious matrix-concrete joints.," *Composites Part B: Engineering,* vol. 108, pp. 301-314, 2017.

[121] L. Ombres, "Analysis of the bond between fabric reinforced cementitious mortar (FRCM) strengthening systems and concrete," *Composites Part B: Engineering,* vol. 69, pp. 418-426, 2015.

[122] J. Davidovits, "Geopolymers: inorganic polymeric new materials," *Journal of Thermal Analysis and calorimetry,* vol. 37(8), pp. 1633-1656, 1991.

[123] P. Duxson, A. Fernández-Jiménez, J. L. Provis, G. C. Lukey, A. Palomo and J. S. J. Van Deventer, "Geopolymer technology: the current state of the art," *Journal of Materials Science,* vol. 42(9), pp. 2917-2933, 2007.

[124] J. L. Provis, "Geopolymers and other alkali activated materials: why, how, and what?," *Materials and Structures,* Vols. 47(1-2), pp. 11-25, 2014.

[125] C. Monticelli, M. E. Natali, A. Balbo, C. Chiavari, F. Zanotto, S. Manzi and M. C. Bignozzi, "A study on the corrosion of reinforcing bars in alkali-activated fly ash mortars under wet and dry exposures to chloride solutions," *Cement and Concrete Research,* vol. 87, pp. 53-63, 2016.

[126] L. Carabba, S. Manzi and M. C. Bignozzi, "Superplasticizer Addition to Carbon Fly Ash Geopolymers Activated at Room Temperature," *Materials,* vol. 9(7), p. 586, 2016.

[127] B. Singh, G. Ishwarya, M. Gupta and S. K. Bhattacharyya, "Geopolymer concrete: A review of some recent developments," *Construction and building materials,* vol. 85, pp. 78-90, 2015.

[128] K. H. Mo, U. J. Alengaram and M. Z. Jumaat, "Structural performance of reinforced geopolymer concrete members: A review," *Construction and Building Materials,* vol. 120, pp. 251-264, 2016.

[129] M. S. Reddy, P. Dinakar and B. H. Rao, "A review of the influence of source material's oxide composition on the compressive strength of geopolymer concrete," *Microporous and Mesoporous Materials,* vol. 234, pp. 12-23, 2016.

[130] W. K. Part, M. Ramli and C. B. Cheah, "An overview on the influence of various factors on the properties of geopolymer concrete derived from industrial by-products," *Construction and Building Materials,* vol. 77, pp. 370-395, 2015.

[131] X. Y. Zhuang, L. Chen, S. Komarneni, C. H. Zhou, D. S. Tong, H. M. Yang, W. H. Yu and H. Wang, "Fly ash-based geopolymer: clean production, properties and applications," *Journal of Cleaner Production,* vol. 125, pp. 253-267, 2016.

[132] L. K. Turner and F. G. Collins, "Carbon dioxide equivalent (CO 2-e) emissions: a comparison between geopolymer and OPC cement concrete," *Construction and Building Materials,* vol. 43, pp. 125-130, 2013.

[133] V. F. Barbosa and K. J. MacKenzie, "Thermal behaviour of inorganic geopolymers and composites derived from sodium polysialate," *Materials Research Bulletin,* vol. 38(2), pp. 319-331, 2003.

[134] W. D. Rickard, C. D. Borstel and A. Van Riessen, "The effect of pre-treatment on the thermal performance of fly ash geopolymers," *Thermochimica acta,* vol. 573, pp. 130-137, 2013.

[135] W. D. Rickard, G. J. Gluth and K. Pistol, "In-situ thermo-mechanical testing of fly ash geopolymer concretes made with quartz and expanded clay aggregates," *Cement and Concrete Research,* vol. 80, pp. 33-43, 2016.

[136] G. Masi, W. D. Rickard, M. C. Bignozzi and A. Van Riessen, "The effect of organic and inorganic fibres on the mechanical and thermal properties of aluminate activated geopolymers," *Composites Part B: Engineering,* vol. 76, pp. 218-228, 2015.

[137] K. Mróz, I. Hager and K. Korniejenko, "Material solutions for passive fire protection of buildings and structures and their performances testing," *Procedia Engineering,* vol. 151, pp. 284-291, 2016.

[138] W. D. Rickard, C. S. Kealley and A. Riessen, "Thermally induced microstructural changes in fly ash geopolymers: experimental results and proposed model," *Journal of the American Ceramic Society,* vol. 98(3), pp. 929-939, 2015.

[139] F. Pacheco-Torgal, J. P. Castro-Gomes and S. Jalali, "Adhesion characterization of tungsten mine waste geopolymeric binder. Influence of OPC concrete substrate surface treatment," *Construction and Building Materials,* vol. 22(3), pp. 154-161, 2008.

[140] H. Y. Zhang, V. Kodur, S. L. Qi and B. Wu, "Characterizing the bond strength of geopolymers at ambient and elevated temperatures," *Cement and Concrete Composites,* vol. 58, pp. 40-49, 2015.

[141] K. Katakalos and C. G. Papakonstantinou, "Fatigue of reinforced concrete beams strengthened with steel-reinforced inorganic polymers," *Journal of Composites for Construction,* vol. 13(2), pp. 103-112, 2009.

[142] C. Menna, D. Asprone, C. Ferone, F. Colangelo, A. Balsamo, A. Prota, R. Cioffi and G. Manfredi, "Use of geopolymers for composite external reinforcement of RC members," *Composites Part B: Engineering*, vol. 45(1), pp. 1667-1676, 2013.

[143] H. Y. Zhang, X. Hao and W. Fan, "Experimental Study on High Temperature Properties of Carbon Fiber Sheets Strengthened Concrete Cylinders Using Geopolymer as Adhesive," *Procedia Engineering*, vol. 135, pp. 47-55, 2016.

[144] P. Chindaprasirt, C. Jaturapitakkul, W. Chalee and U. Rattanasak, "Comparative study on the characteristics of fly ash and bottom ash geopolymers," *Waste Management*, vol. 29(2), pp. 539-543, 2009.

[145] P. Nath and P. K. Sarker, "Use of OPC to improve setting and early strength properties of low calcium fly ash geopolymer concrete cured at room temperature," *Cement and Concrete Composites*, vol. 55, pp. 205-214, 2015.

[146] X. G. Zhang, Corrosion and electrochemistry of zinc, Springer Science & Business Media, 2013.

[147] C. Carloni and K. V. Subramaniam, "Investigation of the interface fracture during debonding between FRP and masonry," *Advances in Structural Engineering*, vol. 12(5), pp. 731-743, 2009.

[148] C. Carloni and K. V. Subramaniam, "FRP-masonry debonding: numerical and experimental study of the role of mortar joints," *Journal of Composites for Construction*, vol. 16(5), pp. 581-589, 2012.

[149] C. Mazzotti, B. Ferracuti and A. Bellini, "Experimental bond tests on masonry panels strengthening by FRP," in *Proceedings of 6th international conference on FRP composites in civil engineering (CICE 2012)*, Rome, 2012.

[150] P. Carrara, D. Ferretti and F. Freddi, "Debonding behavior of ancient masonry elements strengthened with CFRP sheets," *Composites Part B: Engineering*, vol. 45(1), pp. 800-810, 2013.

[151] S. Briccoli Bati, M. Fagone and G. Ranocchiai, "The effects of mortar joints on the efficiency of anchored CFRP sheets reinforcements of brick-masonry," *Key Engineering Materials*, vol. 624, pp. 575-583, 2015.

[152] F. Ceroni, A. Garofano, M. Pecce and G. M. Procaccini, "Effect of the presence of mortar joints in the bond behaviour of tuff masonry elements," *Key Engineering Materials,* vol. 624, pp. 526-533, 2015.

[153] M. Panizza, E. Garbin, M. R. Valluzzi and C. Modena, "Experimental study of the bond of FRP applied to natural stones and masonry prisms," *Key Engineering Materials,* vol. 624, pp. 453-460, 2015.

[154] T. D'Antino, L. H. Sneed, C. Carloni and C. Pellegrino, "Bond behavior of the FRCM-concrete interface," in *Proceedings of the 11th international symposium*, Guimaraes, 2013.

[155] F. G. Carozzi and C. Poggi, "Mechanical properties and debonding strength of Fabric Reinforced Cementitious Matrix (FRCM) systems for masonry strengthening," *Composites Part B: Engineering,* vol. 70, pp. 215-230, 2015.

[156] A. D'Ambrisi, L. Feo and F. Focacci, "Experimental and analytical investigation on bond between Carbon-FRCM materials and masonry," *Composites Part B: Engineering,* vol. 46, pp. 15-20, 2013.

[157] G. P. Lignola, C. Caggegi, F. Ceroni, S. De Santis, P. Krajewski, P. B. Lourenço, M. Morganti, C. C. Papanicolau, C. Pellegrino, A. Prota and L. Zuccarino, "Performance assessment of basalt FRCM for retrofit applications on masonry," *Composites Part B: Engineering,* vol. 128, pp. 1-18, 2017.

[158] M. Santandrea, G. Quartarone, C. Carloni and X. L. Gu, "Confinement of Masonry Columns with Steel and Basalt FRCM Composites," *Key Engineering Materials,* vol. 747, pp. 342-349, 2017.

[159] M. Santandrea, G. Daissè, C. Mazzotti and C. Carloni, "An Investigation of the Debonding Mechanism between FRCM Composites and a Masonry Substrate," *Key Engineering Materials,* vol. 747, pp. 382-389, 2017.

[160] M. Santandrea, I. A. O. Imohamed, C. Carloni, C. Mazzotti, S. de Miranda and F. Ubertini, "A study of the debonding mechanism in steel and basalt FRCM-masonry joints," in *Brick and Block Masonry: Proceedings of the 16th International Brick and Block Masonry Conference, Padova, Italy, 26-30 June 2016*, Padova, 2016.

[161] S. De Santis, F. Ceroni, G. de Felice, M. Fagone, B. Ghiassi, A. Kwiecien, G. P. Lignola, M. Morganti, M. Santandrea, M. R. Valluzzi and A. Viskovic, "Round Robin Test on tensile and bond

behaviour of Steel Reinforced Grout systems," *Composites Part B: Engineering,* vol. 127, pp. 100-120, 2017.

[162] A. Razavizadeh, B. Ghiassi and D. V. Oliveira, "Bond behavior of SRG-strengthened masonry units: Testing and numerical modeling," *Construction and Building Materials,* vol. 64, pp. 387-397, 2014.

[163] F. Focacci, T. D'Antino, C. Carloni, L. H. Sneed and C. Pellegrino, "An indirect method to calibrate the interfacial cohesive material law for," *Materials & Design,* vol. 128, pp. 206-217, 2017.

[164] T. D'Antino, C. Pellegrino, C. Carloni, L. H. Sneed and G. Giacomin, "Experimental analysis of the bond behavior of glass, carbon, and steel FRCM composites," *Key Engineering Materials,* vol. 624, pp. 371-378, 2015.

[165] V. Corinaldesi, J. Donnini and G. Mazzoni, "Experimental study of adhesion between FRCM and masonry support," *Key Engineering Materials,* vol. 624, pp. 189-196, 2014.

[166] A. D'Ambrisi, L. Feo and F. Focacci, "Experimental analysis on bond between PBO-FRCM strengthening materials and concrete," *Composites Part B: Engineering,* vol. 44(1), pp. 524-532, 2013.

[167] G. Cardani, M. R. Valluzzi, M. Panizza, P. Girardello and L. Binda, "Influence of salt crystallization on composites-to-masonry bond evaluated on site by pull-off tests," *Key Engineering Materials,* vol. 624, pp. 338-345, 2015.

[168] D. Arboleda, S. Babaeidarabad, C. Hays and A. Nanni, "Durability of fabric reinforced cementitious matrix (FRCM) composites," *7th. International Conference of FRP Composites in Civil Engineering, International Institute for FRP in Construction,* pp. 1-6, 2014.

[169] J. Donnini, F. De Caso y Basalo, V. Corinaldesi, G. Lancioni and A. Nanni, "Fabric-reinforced cementitious matrix behavior at high-temperature: Experimental and numerical results," *Composites Part B: Engineering,* vol. 108, pp. 108-121, 2017.

[170] E. Franzoni, "Rising damp removal from historical masonries: a still open challenge," *Construction and Building Materials,* vol. 54, pp. 123-136, 2014.

[171] E. Franzoni, C. Gentilini, G. Graziani and S. Bandini, "Compressive behaviour of brick masonry triplets in wet and dry conditions," *Construction and Building Materials,* vol. 82, pp. 45-52, 2015.

[172] A. E. Charola, "Salts in the deterioration of porous materials: an overview," *Journal of the American institute for conservation,* vol. 39(3), pp. 327-343, 2000.

[173] G. W. Scherer, "Stress from crystallization of salt," *Cement and concrete research,* vol. 34(9), pp. 1613-1624, 2004.

[174] C. Rodriguez-Navarro, E. Doehne and E. Sebastian, "How does sodium sulfate crystallize? Implications for the decay and testing of building materials," *Cement and concrete research,* vol. 30(10), pp. 1527-1534, 2000.

[175] N. Tsui, R. J. Flatt and G. W. Scherer, "Crystallization damage by sodium sulfate," *Journal of cultural heritage,* vol. 4(2), pp. 109-115, 2003.

[176] F. Sandrolini and E. Franzoni, "Repair systems for the restoration of ancient buildings: dampness rise problem," *Restoration of buildings and monuments,* vol. 13(3), pp. 161-172, 2007.

[177] R. P. J. Van Hees and H. J. P. Brocken, "Damage development to treated brick masonry in a long-term salt crystallisation test," *Construction and Building Materials,* vol. 18(5), pp. 331-338, 2004.

[178] E. Sassoni, G. Graziani and E. Franzoni, "An innovative phosphate-based consolidant for limestone. Part 2: Durability in comparison with ethyl silicate," *Construction and Building Materials,* vol. 102, pp. 931-942, 2016.

[179] G. Graziani, E. Sassoni and E. Franzoni, "Experimental study on the salt weathering resistance of fired clay bricks consolidated by ethyl silicate," *Materials and Structures,* vol. 49(7), pp. 2525-2533, 2016.

[180] H. Derluyn, H. Janssen and J. Carmeliet, "Influence of the nature of interfaces on the capillary transport in layered materials," *Construction and Building Materials,* vol. 25(9), pp. 3685-3693, 2011.

[181] E. Franzoni, "The role of mortars in ancient brick masonries' decay: a study in the Pio Palace at Carpi (Italy)," *2nd Conference on Historic Mortars-HMC 2010 and RILEM TC 203-RHM final workshop,* pp. 483-490, 2010.

[182] C. Gentilini, E. Franzoni, S. Bandini and L. Nobile, "Effect of salt crystallisation on the shear behaviour of masonry walls: an experimental study," *Construction and Building Materials,* vol. 37, pp. 181-189, 2012.

[183] E. Franzoni, C. Gentilini, G. Graziani and S. Bandini, "Towards the assessment of the shear behaviour of masonry in on-site conditions: A study on dry and salt/water conditioned brick masonry triplets," *Construction and Building Materials,* vol. 65, pp. 405-416, 2014.

[184] RILEM TC 127-MS Recommendation MS-A.1 , "Determination of the resistance of wallettes against sulfates and chlorides.," *Mater Struct 31:2–4,* 1998.

[185] T. J. Wijffels and B. Lubelli, "Development of a new accelerated salt crystallization test," *Heron,* vol. 51 (1), pp. 63-79, 2006.

[186] A. Luque, E. Ruiz-Agudo, G. Cultrone, E. Sebastián and S. Siegesmund, "Direct observation of microcrack development in marble caused by thermal weathering," *Environmental Earth Sciences,* vol. 62(7), pp. 1375-1386, 2011.

[187] H. Böke and S. Akkurt, "Ettringite formation in historic bath brick–lime plasters," *Cement and Concrete Research,* vol. 33(9), pp. 1457-1464, 2003.

[188] F. Sandrolini, E. Franzoni, G. Cuppini and L. Caggiati, "Materials decay and environmental attack in the Pio Palace at Carpi: A holistic approach for historical architectural surfaces conservation," *Building and environment,* vol. 42(5), pp. 1966-1974, 2007.

[189] E. Franzoni, S. Bandini and G. Graziani, "Rising moisture, salts and electrokinetic effects in ancient masonries: from laboratory testing to on-site monitoring," *Journal of Cultural Heritage,* vol. 15(2), pp. 112-120, 2014.

[190] D. Benavente, L. Linares-Fernandez, G. Cultrone and E. Sebastian, "Influence of microstructure on the resistance to salt crystallisation damage in brick," *Materials and structures,* vol. 39(1), pp. 105-113, 2006.

[191] S. Yu and C. T. Oguchi, "Role of pore size distribution in salt uptake, damage, and predicting salt susceptibility of eight types of Japanese building stones," *Engineering Geology,* vol. 115(3), pp. 226-236, 2010.

[192] M. Saafi, H. A. Toutanji and Z. Li, "Behavior of concrete columns confined with fiber reinforced polymer tubes," *ACI materials journal*, vol. 96(4), pp. 500-509, 1999.

[193] P. Rochette and P. Labossiere, "Axial testing of rectangular column models confined with composites," *Journal of composites for construction*, vol. 4(3), pp. 129-136, 2000.

[194] S. P. Tastani, I. Balafas, A. Dervisis and S. J. Pantazopoulou, "Effect of core compaction on deformation capacity of FRP-jacketed concrete columns," *Construction and Building Materials*, vol. 47, pp. 1078-1092, 2013.

[195] T. Ozbakkaloglu and J. C. Lim, "Axial compressive behavior of FRP-confined concrete: Experimental test database and a new design-oriented model," *Composites Part B: Engineering*, vol. 55, pp. 607-634, 2013.

[196] S. Pessiki, K. A. Harries, J. T. Kestner, R. Sause and J. M. Ricles, "Axial behavior of reinforced concrete columns confined with FRP jackets," *Journal of Composites for Construction*, vol. 5(4), pp. 237-245, 2001.

[197] G. Campione and N. Miraglia, "Strength and strain capacities of concrete compression members reinforced with FRP," *Cement and Concrete Composites*, vol. 25(1), pp. 31-41, 2003.

[198] A. Mirmiran and M. Shahawy, "Behavior of concrete columns confined by fiber composites," *Journal of Structural Engineering*, vol. 123(5), pp. 583-590, 1997.

[199] L. De Lorenzis and R. Tepfers, "Comparative study of models on confinement of concrete cylinders with fiber-reinforced polymer composites," *Journal of Composites for Construction*, vol. 7(3), pp. 219-237, 2003.

[200] A. Prota, G. Manfredi, A. Nanni, E. Cosenza and M. Pecce, "Flexural strengthening of RC beams using emerging materials: Ultimate behavior," *Proc of CICE, Adelaide, Australia*, pp. 163-170, 2002.

[201] A. Balsamo, F. Nardone, I. Iovinella, F. Ceroni and M. Pecce, "Flexural strengthening of concrete beams with EB-FRP, SRP and SRCM: Experimental investigation," *Composites Part B: Engineering*, vol. 46, pp. 91-101, 2013.

[202] R. El-Hacha and K. Abdelrahman, "Slenderness effect of circular concrete specimens confined with SFRP sheets," *Composites Part B: Engineering*, vol. 44(1), pp. 152-166, 2013.

[203] A. Turkel and M. H. Ozkul, "Size and Wall Effects on Compressive Strength of Concretes," *ACI Materials Journal,* vol. 107, no. 4, pp. 372-379, 2010.

[204] Y.-. F. Wang and H.-. L. Wu, "Size Effect of Concrete Short Columns Confined with Aramid FRP Jackets," *Journal of Composites for Construction,* vol. 15, no. 4, pp. 535-544, 2011.

[205] J. H. Gonzalez-Libreros, L. H. Sneed, T. D'Antino and C. Pellegrino, "Behavior of RC beams strengthened in shear with FRP and FRCM composites," *Engineering Structures,* vol. 150, pp. 830-842, 2017.

[206] G. E. Thermou, K. Katakalos and G. Manos, "Concrete confinement with steel-reinforced grout jackets," *Materials and Structures,* vol. 48(5), pp. 1355-1376, 2015.

[207] G. E. Thermou, K. Katakalos and G. Manos, "Influence of the cross section shape on the behaviour of SRG-confined prismatic concrete specimens," *Materials and Structures,* vol. 49(3), pp. 869-887, 2016.

[208] C. Mazzotti and F. S. Murgo, "Numerical and experimental study of GFRP-masonry interface behavior: Bond evolution and role of the mortar layers," *Composites Part B: Engineering,* vol. 75, pp. 212-225, 2015.

[209] M. R. Valluzzi, M. Valdemarca and C. Modena, "Behavior of brick masonry vaults strengthened by FRP laminates," *Journal of Composites for Construction,* vol. 5(3), pp. 163-169, 2001.

[210] P. Foraboschi, "Strengthening of masonry arches with fiber-reinforced polymer strips," *Journal of composites for construction,* vol. 8(3), pp. 191-202, 2004.

[211] A. Baratta and O. Corbi, "Stress analysis of masonry vaults and static efficacy of FRP repairs," *International Journal of Solids and Structures,* vol. 44(24), pp. 8028-8056, 2007.

[212] L. De Lorenzis, R. Dimitri and A. La Tegola, "Reduction of the lateral thrust of masonry arches and vaults with FRP composites," *Construction and Building Materials,* vol. 21(7), pp. 1415-1430, 2007.

[213] D. V. Oliveira, I. Basilio and P. B. Lourenço, "Experimental behavior of FRP strengthened masonry arches," *Journal of Composites for Construction,* vol. 14(3), pp. 312-322, 2010.

[214] L. Rovero, F. Focacci and G. Stipo, "Structural behavior of arch models strengthened using fiber-reinforced polymer strips of different lengths," *Journal of Composites for Construction,* vol. 17(2), pp. 249-258, 2012.

[215] F. G. Carozzi, G. Milani and C. Poggi, "Mechanical properties and numerical modeling of Fabric Reinforced Cementitious Matrix (FRCM) systems for strengthening of masonry structures," *Composite Structures,* vol. 107, pp. 711-725, 2014.

[216] A. Incerti, A. Vasiliu, B. Ferracuti and C. Mazzotti, "Uni-Axial compressive tests on masonry columns confined by FRP and FRCM," *Proc. of the 12th International Symposium on Fiber Reinforced Polymers for Reinforced Concrete Structures & The 5th Asia-Pacific Conference on Fiber Reinforced Polymers in Structures, Joint Conference, Nanjing, China, 14–16 December 2015,* 2015.

[217] F. Ferretti, A. Incerti, B. Ferracuti and C. Mazzotti, "Diagonal compression tests on masonry panels strengthened by FRP and FRCM," *Proc. of the 10th SAHC Conference, Lueven, Belgium,* vol. 13, p. 15, 2016.

[218] A. Bellini, A. Incerti and C. Mazzotti, "Out-of-plane behavior of masonry walls strengthened by FRCM composites," *Proc. of the 10th SAHC Conference, Lueven, Belgium, 13-15 September 2016,* 2016.

[219] V. Alecci, F. Focacci, L. Rovero, G. Stipo and M. De Stefano, "Extrados strengthening of brick masonry arches with PBO–FRCM composites: Experimental and analytical investigations," *Composite Structures,* vol. 149, pp. 184-196, 2016.